THE UNIVERSITY *of* EDINBURGH

On abnormal microvascular phenotypes in a mouse model of glioblastoma and the effect of vessel compression on blood flow

Romain Enjalbert

THE UNIVERSITY *of* EDINBURGH

Doctor of Philosophy

THE UNIVERSITY OF EDINBURGH

January 2023

Abstract

Cancer is a major healthcare concern in the world, accounting for one in six deaths. Despite this, cancer patient survival rates have increased over the past decades as a result of healthcare improvement reforms and advances in medical research. Among the numerous areas of research in cancer, studying the tumour microenvironment and the physics of cancer has shown promising results for patient benefit, and will be the focus of this thesis.

A tumour is an abnormal cell growth, and is cancerous when it has the potential to metastasise. Tumours have their own microenvironment which presents numerous abnormalities compared to healthy tissue. In particular, as tumours grow they develop their own microvascular system to transport nutrients and oxygen to the cells. However, the tumour vasculature is abnormal and inefficient, leading to an abnormal microenvironment, with traits such as hypoxia. Hypoxia leads to more aggressive tumours and is a barrier to treatment, making it an undesirable trait. A better understanding of the causes of tumour hypoxia could thus benefit patient care.

One tumour vessel abnormality is vessel compression, which is the result of high solid stress in tumours. Studies have shown that vessel compression correlates with reduced survival rates, and increased hypoxia and oxygen heterogeneity. However, the biophysical mechanism which links compressed vessels to hypoxia is not clear. In addition, vessel compression has not been characterised in glioblastoma multiforme brain tumours, despite the correlation between vessel compression and reduced survival rates, and the low survival rates of glioblastoma patients.

As red blood cells transport oxygen in blood, the central hypothesis of this thesis is that vessel compression leads to abnormal transport of red blood cells, contributing to tissue hypoxia. Therefore, the aim of this work is to find a mechanistic link between vessel compression and abnormal red blood cell transport in compressed vascular networks and contextualise it to glioblastoma.

The first results chapter investigates the effect of a compression on the partitioning of red blood cells at a downstream bifurcation. The numerical experiment shows that, with a compressed parent branch, the higher flowing child branch is enriched in red blood cells compared to a control simulation. The abnormal partitioning of red blood cells is the result of a narrowing of the red blood cell cross-sectional distribution as they enter the compression. Indeed, in the compression the red blood cells undergo cross-streamline migration to more central streamlines as a result of the increased shear rate and shear rate gradient in the

compression. The results further show that the abnormal partitioning of red blood cells is present over a wide range of flow ratios to the child branches. The abnormal partitioning of red blood cells becomes less pronounced as the parent branch haematocrit increases, up to a critical threshold of around 30%, above which abnormal partitioning no longer occurs.

The second results chapter builds on to the first one and numerically investigates how the abnormal partitioning of red blood cells at a single bifurcation propagates at a network level. To do so, it adapts and validates an existing reduced-order model to accurately and efficiently calculate the abnormal partitioning of red blood cells when parent branches are compressed. At a network level, and compared to a control, vessel compression increases haematocrit heterogeneity, reduces the average haematocrit, and increases the number of plasma channels present. The mechanisms for these findings are investigated and show that both the increased resistance to flow and the abnormal partitioning of red blood cells at a bifurcation contribute to lowering the haematocrit in the networks, but that haematocrit heterogeneity is only the result of the abnormal partitioning of red blood cells. Finally, it is shown that the reduction in average haematocrit in the networks occurs over a wide range of inlet haematocrits, and that only a relatively small number of vessels need to be compressed for the reduction to be present.

The final results chapter phenotypes and compares the microvasculature in a mouse model of a glioblastoma to control mice. A pipeline is developed and validated to reconstruct the three-dimensional vessel surfaces from multiphoton microscopy images of the vasculature. The data show that the non-dimensional interbifurcation distance and the mean tissue-vessel distance are significantly lower in tumours, but that other phenotypes are not different. Notably, the tumour vessels were not compressed. Furthermore, the results show that there is a correlation between the mean tissue-vessel distance in a region of interest and the distance of the region of interest from the tumour core.

Taken together, these findings address the aim of this thesis and provide a mechanism for abnormal transport of red blood cells in compressed vessel networks. Due to the importance of red blood cells in the transport of oxygen, this work contributes to the knowledge of the causes of hypoxia in tumours with vessel compression. As hypoxia is an important trait adversely affecting patient prognosis, understanding the mechanisms leading to hypoxia has the potential, in the long term, to inform patient care.

Lay Summary

Cancer is a major healthcare concern in the world, and accounts for one death in six worldwide. As a consequence of its devastating impact, research in cancer is aimed at improving the survival rates of patients. One avenue of research is to better understand blood flow in cancer, which is what is investigated in this thesis.

Most cancers are solid tumours, which is an abnormal cell growth which has the potential to spread from the original location of the tumour to other parts of the body. As solid tumours grow, they need to develop new blood vessels to supply oxygen and nutrients to the growing tumour. However, the new blood vessels are abnormal, which has an adverse effect on blood flow in tumours. Blood carries oxygen in blood, through red blood cells, and because tumours have poor blood flow they have low oxygen levels. The low availability of oxygen in tumours makes them more difficult to treat and more aggressive to patients. As poor oxygenation of tumours is bad for patients, there is research to understand the link between abnormal blood vessels in tumours and their low levels of oxygen.

One specific abnormality in tumour blood vessels is that they are compressed and have a different shape compared to healthy blood vessels. The work in this thesis aims to understand what is the link between compressed vessels and blood flow, to ultimately better understand the role that vessel compression has for the oxygenation of tumours. Understanding how compressed vessels are linked to low levels of oxygen is important because there are various therapeutic avenues that can change the structure of vessels in tumours to make them more normal and improve oxygenation, or some therapies can be adapted to account for the low levels of oxygen in tumours.

The work in this thesis shows that when vessels are compressed, red blood cells are not transported in vessels in the same way as if vessels are not compressed. Indeed, when blood vessels reach a branching point, also called a bifurcation, one of the child branches will receive much fewer red blood cells than if it were not compressed, possibly not receiving any red blood cells at all. In compressed blood vessel networks, the reduced amount of red blood cells in one of the child branches compounds, and leads to a high number of vessels having a low amount of red blood cells or no red blood cells at all. As red blood cells transport oxygen in blood, the oxygenation of the neighbouring tissue is impaired. Finally, this thesis investigates how

prevalent vessel compression and other abnormalities are in animal models of a brain tumour. The results show that tumour vessels are not compressed in this animal model, and that the only abnormalities present are reduced branching distance and that the vessel networks are denser.

The work in this thesis furthers our understanding of how compressed vessels affect blood flow in tumours. In doing so, this work helps to understand one of the root causes of low levels of oxygen in tumours, and in better understanding poor oxygenation in tumours lies the hope that novel treatment avenues will adapt to this and improve patient survival rates.

Acknowledgements

Thank you to my supervisors, Miguel O. Bernabeu and Timm Krüger. Throughout the years they have always been present, and helpful, with the research undertaken in this thesis. In the process, they have made me a better researcher, and a better person.

Thank you to Professor Valerie Brunton, Dr. Martin Lee, and the various members of Valerie's group that have provided images to work with for the final research chapter of this thesis, the data and images that you generate are remarkable.

Thank you to Professor Sylvie Lorthois and Professor Prashant Valluri for examining this thesis. I am grateful for the time that they spent reading this thesis, for helping me see my work differently, and for challenging some of the assumptions that I have made. Their insights have helped me deepen the undertsanding of my work, and for that I am thankful.

Thank you to all the members, past and present, of Miguel's and Timm's research group. There are too many to name them all, but they accompanied me through this journey, both academically and humanly.

Thank you to my parents, Nathalie and Alain. You supported me throughout my undergraduate studies, and then through this thesis; you have made all of this possible.

Thank you to Viola Maria Periti, by having you in my life, fortune has smiled on me.

If your name is here, I could not have done it without you.

Romain Enjalbert

Edinburgh, September 29th 2023

Declaration

I declare that this thesis was composed by myself, that the work contained herein is my own except where explicitly stated otherwise in the text, and that this work has not been submitted for any other degree or professional qualification except as specified.

Romain Enjalbert

Romain Enjalbert

Publications

Journals

Enjalbert, R., Hardman, D., Krüger, T., Bernabeu, M.O.; Compressed vessels bias red blood cell partitioning at bifurcations in a hematocrit-dependent manner: Implications in tumor blood flow; *PNAS* 2021

Conferences

Enjalbert, R., Krüger, T., Bernabeu, M.O.; Vessel compression biases red blood cell partitioning at a bifurcation; International bio-fluid mechanics and vascular mechano-biology symposium; Tucson, Arizona 2020.

Enjalbert, R., Krüger, T., Bernabeu, M.O.; Impact of vessel compression on red blood cell partitioning at a bifurcation; WCCM-ECCOMAS congress; online 2021.

Enjalbert, R., Hardman, D., Krüger, T., Bernabeu, M.O.; Vessel compression biases the partitioning of red blood cells at a downstream bifurcation; Congress of the European society of biomechanics; online 2021.

Enjalbert, R., Hardman, D., Krüger, T., Bernabeu, M.O.; Impact of vessel compression on red blood cell partitioning at a downstream bifurcation; International school in HemoPhysics; Montpellier 2021.

Enjalbert, R., Krüger, T., Bernabeu, M.O.; Network effect of vessel compression on the partitioning of red blood cells at bifurcations in vascular networks; IOP workshop: Microrheology and transport in complex biological media; online 2022.

Enjalbert, R., Krüger, T., Bernabeu, M.O.; Vascular abnormalities lead to heterogeneous red blood cell partitioning at bifurcations, and its implications in tumour blood flow; World congress of biomechanics; online 2022.

Enjalbert, R., Krüger, T., Bernabeu, M.O.; Effect of vessel compression on red blood cell partitioning at vascular bifurcations in a vessel network; European conference on mathematical and theoretical biology; Heidelberg, 2022.

Contents

Figures and Tables

Figures

Tables

Chapter 1

Introduction

1.1 Motivation

Cancer is a major healthcare concern in the world, causing one death in six [131]. In the United Kingdom cancer caused close to 165,000 deaths in 2017, accounting for 28% of all deaths [25]. Despite accounting for a high fraction of deaths, the survival rate in the past 40 years has increased from 24% to 40% in the United Kingdom [26]. Increases in the survival rate have been driven by a combination of healthcare improvement reforms and medical progress, such as better diagnostic tools, patient care and treatment, and advances in cancer knowledge [5].

One particular area of research in cancer is the tumour microenvironment, which is abnormal compared to a healthy one. The abnormal microenvironment leads to negative physical traits such as impaired blood flow and tissue hypoxia [91, 186]. A direct consequence of tissue hypoxia is that tumours develop more aggressive phenotypes and are more resistant to treatments, such as chemotherapy, radiotherapy or immunotherapy [135]. There are existing therapeutic strategies that respond or adapt to the abnormal tumour microenvironment, such as normalisation therapy or precision medicine [43, 187]. However, these therapeutic strategies rely on knowledge of the physics of cancer, for example in blood flow and tissue oxygenation, to be optimised.

In recent years, the physics of tumours has developed into a field of its own [135]. This is because the mechanisms explaining how tumours respond to the aforementioned therapeutic strategies find some of their roots in the physical mechanics of tumours, rather than its biology [135]. The motivation of this thesis lies in the hope that a better understanding of the physics of tumours will lead to the development and improvement of therapeutic strategies to improve patient survival.

1.2 Tumour microenvironment abnormality: vessel compression

In the tumour microenvironment blood vessels have an abnormal shape and function [95]. One specific blood vessel abnormality is blood vessel compression [140]. Studies have demonstrated that blood vessels in solid tumours are heavily compressed [6, 56, 78, 192] and correlated the degree of vessel compression to reduced survival rates in patients [56]. In addition, studies have shown that therapeutically reducing solid stress, which has the effect of decompressing vessels, increases survival rates in animal models of tumours [33]. Vessel decompression was associated with improved tumour tissue oxygenation and reduced oxygen heterogeneity [33]. However, it is not clear what the biophysical mechanism is that links vessel decompression to improved oxygenation.

A previous study from our group has demonstrated that one tumour blood vessel abnormality, reduced interbifurcation distance, led to abnormal red blood cell transport at vascular bifurcations [18]. The study further showed that a direct consequence of this is an increased heterogeneity of red blood cells in a model vascular network, as well as a more heterogeneous oxygenation of the neighbouring tissue [18]. The question of whether other vessel structural abnormalities, such as vessel compression, lead to abnormal red blood cell transport at vascular bifurcations is not known.

Glioblastoma multiforme is a brain tumour with dismal survival rates, with 5% of patients surviving for five years or more [31]. Vessel compression, which has been quantified in several cancer types and is associated with reduced survival rates [6, 56, 78, 192], has not been thoroughly investigated in glioblastoma [38, 169], despite reports of other vascular abnormalities [38, 169]. The role that vessel compression could play in glioblastoma is therefore not elucidated.

1.3 Hypothesis, Aim, and Objectives

This thesis will investigate the effect that vessel compression has on blood flow in tumours and contextualise it to glioblastoma. The central hypothesis is that vessel compression leads to abnormal partitioning of red blood cells at vascular bifurcations, contributing to a high fraction of plasma channels in tumour networks and to tumour tissue hypoxia.

The aim of the thesis is to find a mechanistic link between vessel compression and abnormal red blood cell transport in vascular networks and contextualise it to glioblastoma. The aim leads to three objectives. Each objective will be addressed in a results chapter of this thesis.

1. Numerically investigate how vessel compression impacts partitioning of red blood cells at a single vascular bifurcation (chapter 4)
2. Numerically investigate how vessel compression impacts red blood cell distribution in vascular networks (chapter 5)

3. Quantify blood vessel phenotypes, including vessel compression, in a mouse model of a glioblastoma (chapter 6)

1.4 Outline

This thesis is divided into four parts.

The first part consists of the state of the art in chapter 2. The state of the art reviews the relevant aspects of tumours in section 2.1 and blood flow in section 2.2. Finally, section 2.3 summarises the state of the art and identifies the gap in the literature, and formulates the hypothesis, aim, and objectives of this thesis.

The second part contains the methods used in this thesis. Section 3.1 provides the method for the particulate blood flow simulations. Section 3.2 covers the method for the network blood flow simulations. Finally, section 3.3 gives the method for studying the microvasculature in a mouse model of a glioblastoma.

The third part contains the results of this thesis, each addressing one of the objectives. Chapter 4 presents the numerical study on how vessel compression impacts the partitioning of red blood cells at a single vascular bifurcation. Chapter 5 contains the study on how vessel compression impacts red blood cell distribution in vascular networks. Chapter 6 presents the quantification of vascular phenotypes in a mouse model of a glioblastoma.

The fourth and last part concludes this thesis with chapter 7 and contains the summary, conclusion, and outlook of this thesis.

Chapter 2

State of the art

This chapter aims to review the relevant literature for the research performed in this thesis, identify the gaps that will be investigated, and provide the background to investigate those gaps. Section 2.1 is a state of the art on the relevant aspects of cancer and tumours for this thesis. Section 2.2 is a state of the art on the microcirculation and microhaemodynamics, as it is through this lens that this thesis will study tumours. Finally, section 2.3 will identify the gaps in the literature, outline the hypothesis of this thesis, and formulate the aim & objectives.

2.1 Cancer, tumours, tumour hypoxia, & the abnormal tumour vasculature

This section aims to review the necessary knowledge of cancer for the work presented. Initially, section 2.1.1 broadly introduces cancer, followed by section 2.1.2 on hypoxia in tumours. Sections 2.1.3 and 2.1.4 review structural abnormalities in tumours due to deficient angiogenesis and solid stress, respectively. Section 2.1.5 reviews the benefits and vision associated with a better understanding of the effect of hypoxia and structural abnormalities in tumours. Finally, section 2.1.6 summarises the state of the art on cancer and tumours.

2.1.1 Introduction to cancer and solid tumours

Cancer is a major healthcare concern. Globally, it accounts for approximately one death in six [131], while in the UK it causes a quarter of all deaths [27]. In their life, it is estimated that one out of two people in the UK will be diagnosed with cancer, while at current survival rates, one out of two with a positive cancer diagnosis will die of cancer. See Figure 2.1 for a summary of UK cancer statistics. The average cancer survival rate of 50% hides disparity within the different types of cancer and stages of cancer. Early stages of some cancer, like breast or prostate cancer, show high survival rates with over 98% of patients surviving for five years or

more [29, 30]. On the other hand, cancers like glioblastoma multiforme[1] have a dismal survival rate, with fewer than 5% of patients surviving for more than five years [31]. Nevertheless, in the UK, cancer survival has doubled in the past 40 years, and is still improving [5]. The increased survival rate of cancer is attributed to progress in several factors, including diagnostic tools, treatment, and policies improving access to diagnosis and treatment [5].

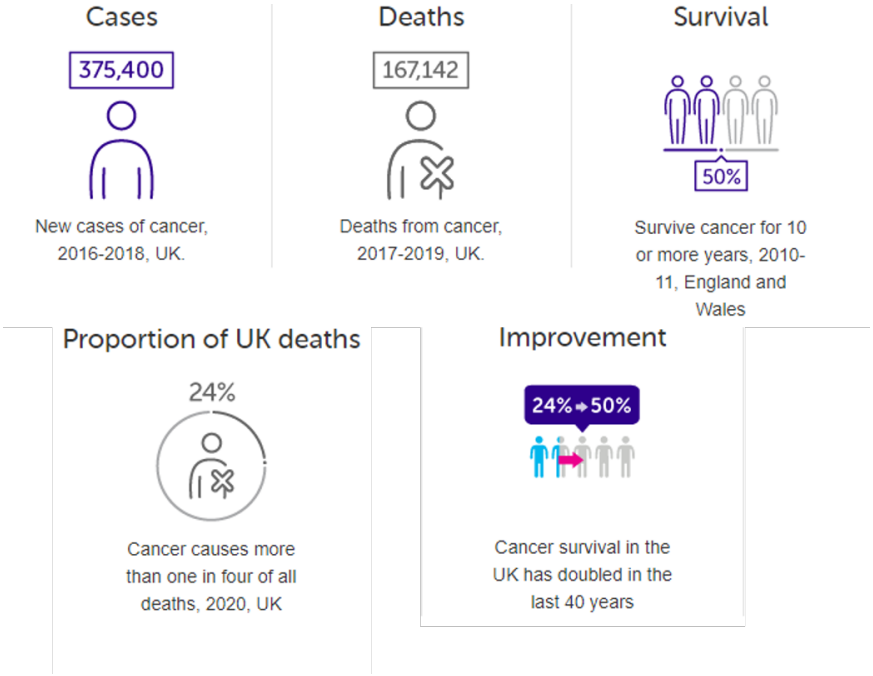

Figure 2.1: Illustration summarising cancer statistics in the United Kingdom. From top left to bottom right, it shows: annual new cases, annual deaths due to cancer, the ten year survival rate for cancer, the proportion of deaths due to cancer, and the improvement in cancer survival over time. Based on graphic created by Cancer Research UK [25–27].

Cancer is defined as an abnormal cell growth due to a cell mutation, where the cells have the potential to spread from the original location of the cancer to other parts of the body to form secondary cancers, called metastases [82]. The majority of cancers are solid tumours (the remaining cancers are blood cancers), also called neoplasms, which are a solid mass of abnormal cell growth. Solid tumours can be either benign or malignant. Cancers are malignant tumours, and they differ from benign tumours by their ability to invade their surroundings, see Figure 2.2 for an illustration, and spread to other parts of the body to form metastases [82]. Metastases are responsible for 90% of deaths due to cancer [82].

1. Glioblastoma multiforme is often referred to as glioblastoma.

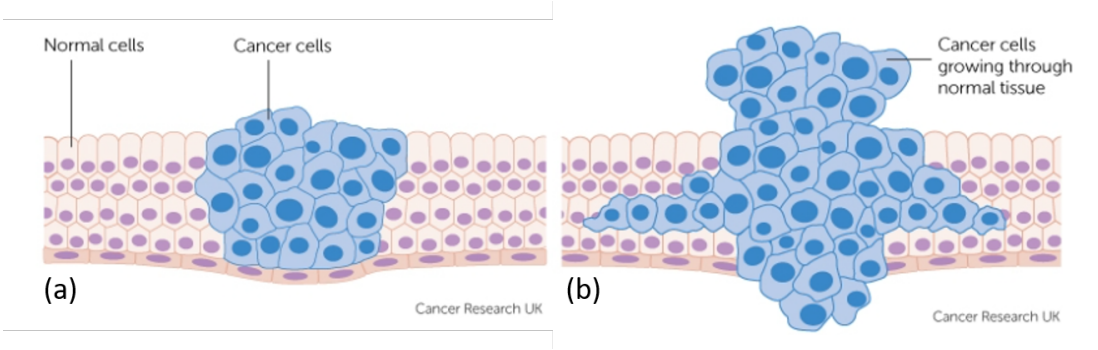

Figure 2.2: Illustration of cancer cells in healthy tissue. (a) shows cancer cells (in blue) grow in healthy tissue (in light red). (b) shows the proliferation of the cancer cells (in blue) in healthy tissue (in light red) which it is invading. Based on a graphic created by Cancer Research UK [28].

The causes of cancer is still a subject of research. Ultimately, cancer is the result of cell mutation going wrong, but the origin of the mutation is complex. At a high level, the causes are divided into external causes and internal causes. External causes are environmental factors, such as ultraviolet radiation, exercise, alcohol and tobacco consumption, and diet [82]. Internal causes are genetically inherited. Out of the two, research indicates that external causes dominate over internal ones, making many cancers avoidable through lifestyle changes [83].

There are several treatment paths for cancer, involving surgical removal of the tumour, radiotherapy, chemotherapy, and immunotherapy. In all cases, the aim of the treatment is to remove the cancerous cells, and avoid their spread to other parts of the body. Treatment is not always successful and cancer can kill in multiple ways. It can kill through the growth of the solid tumour against healthy tissue, for example, a brain tumour growing against the brain. However a majority of deaths are due to secondary causes such as infections, due to impaired immune systems of cancer patients, and cachexia, also known as wasting syndrome due to malnutrition and fatigue [82].

Cancer research is, in part, dedicated to improving the survival rate of patients with cancer. This is a complex task, for a complex disease, and the approaches to that are numerous and the literature is vast. Cancer presents numerous hallmarks and research challenges [79, 80]. However, given the broadness of the subject, this section will focus on the aspects of cancer relevant to the research in this thesis. Therefore, the state of the art will focus on the tumour hypoxia, and its link to both the tumour vasculature and tumour blood flow [135]. To the reader interested in other aspects of cancer, there are some high level papers regarding cancer [79, 80], and the citation trail therein will help to delve into specific areas.

2.1.2 Tumour hypoxia

Tumour tissue hypoxia is a common phenotype of solid cancers [202]. Hypoxia is defined as insufficient tissue oxygen concentration to sustain aerobic function, and is usually distributed in heterogeneous sub-regions in the solid tumour [10, 129]. Hypoxia is undesirable as it leads to poorer patient prognosis through two different mechanisms. Firstly, hypoxic tumours are more malignant and are more likely to metastasise [23]. As metastases are the cause of the majority of cancer deaths [82], this is a mechanism rendering hypoxic tumours more fatal. Secondly, hypoxic tumours are resistant to many treatments. Radiation therapy is three times more effective in oxygenated tissue than in hypoxic tissue [70]. Hypoxic tumours are also resistant to cytotoxic drugs [24, 43] and exhibit immunosuppression [124]. As hypoxic tumours are more difficult to treat, they are also more fatal to patients [24].

Seven mechanisms for regulation of tumour oxygenation have been identified in a review [41], see Figure 2.3 for an illustration.

(a) Steep longitudinal (along the vessel length) oxygen gradients
(b) Intravascular hypoxia
(c) Large diameter shunts depriving tissue of blood supply
(d) Low vascular density
(e) Inefficient vessel orientation
(f) High oxygen consumption rates
(g) Increase in blood viscosity due to stiffer red blood cells and red blood cell clustering

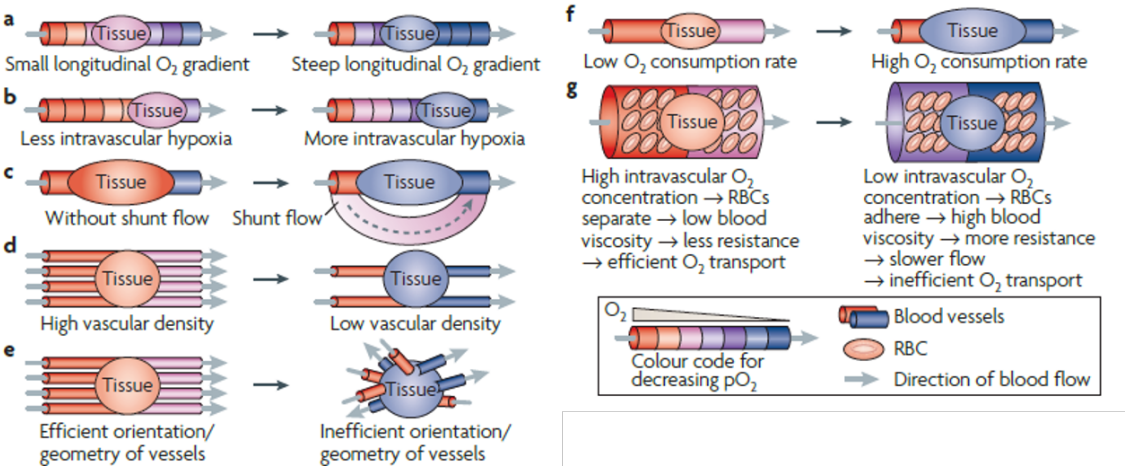

Figure 2.3: Illustration of seven identified mechanisms leading to tissue hypoxia in tumours. Image reproduced with permission from [41].

In turn, the mechanisms reported above feed into two different identified forms of hypoxia in solid tumours, they are chronic hypoxia and cycling hypoxia[2] [10, 129].

2. In the literature cycling hypoxia is also alternatively called intermittent, acute or transient hypoxia [10]. For clarity, this thesis will only use the term cycling hypoxia.

Chronic hypoxia is diffusion limited hypoxia: as an area of tissue is too distant from blood vessels, the oxygen is consumed prior to attaining the said tissue, thus rendering it hypoxic [129, 194]. It is called chronic as it occurs over long time periods [10, 129]. The diffusion distance of oxygen in tumours is reported to be of the order of 100 μm [194], although it varies according to individual tumour parameters [73]. Above the diffusion distance of oxygen, tissue becomes anoxic, which means there is no oxygen present at all. Regions of hypoxia/anoxia lead tumours to form both a necrotic core and hypoxic tissue regions in poorly vascularised regions when the tissue is too far away from blood vessels [129, 194]. Chronic hypoxia is therefore associated with an abnormal and sparse vascularisation of the tumour [129].

Cycling hypoxia is tissue hypoxia that fluctuates over two different timescales. The first timescale occurs over a period of minutes to hours. This timescale is associated with temporal fluctuations in red blood cell flow (including flow reversal and plasma channels[3]) and in haemoglobin saturation within red blood cells, where these fluctuations have been correlated to neighbouring tissue oxygenation [10, 44, 84, 103, 112, 141, 182]. The cause of the red blood cell flux and haemoglobin saturation fluctuation, however, is not settled yet with various hypotheses existing, including vasodilation, temporary vessel blockages due to blood cells or compressed vessels, and thermoregulation [42, 129]. The second timescale is much longer, over a period of days, and is associated with vascular remodelling [32, 129]. Experiments have shown that imaging of the tumour vasculature at the same position over several days shows an evolution in the vasculature, and is associated with changes in hypoxic regions [32]. Cycling hypoxia has also been shown to have a more pronounced effect on treatment resistance and on the malignancy of the tumour compared with chronic hypoxia due to the cyclical deoxygenation and reoxygenation of the cells [10].

In both chronic and cycling hypoxia, the abnormal tumour microvasculature and tumour blood flow are associated with hypoxia [65, 129, 170, 181]. The next two sections will look at the two different causes of microvascular structural abnormalities, namely excess angiogenesis and high solid stress, what the resulting abnormalities are, and the effect these abnormalities have on blood flow and oxygen transport in tumours.

---

3. Plasma channels are blood vessels without red blood cells.

2.1.3 Vascular structural abnormalities: excess angiogenesis and deficient vessels

The first cause of vessel structural abnormality is uncontrolled angiogenesis[4]. To grow above a critical size of 1-2 mm in diameter, tumours need to develop their own vasculature through angiogenesis [106]. In healthy tissue, vascular networks develop to form healthy and stable networks. The stability of networks is ensured by a balance of proangiogenic and antiangiogenic factors [88]. In tumours, proangiogenic factors dominate, leading to unstable and abnormal microvascular networks [88, 91]. Figure 2.4 shows, for illustration purposes, both a healthy microvasculature and an abnormal tumour microvasculature.

These structural abnormalities due to excessive angiogenesis take multiple forms and have been extensively investigated [8, 18, 89, 91, 97, 132, 137, 142, 154, 185, 187, 197]. The main ones are listed below:

1. Leaky blood vessels
2. Enlarged vessel diameters
3. Increased vessel tortuosity
4. High interstitial fluid pressure
5. Decreased vessel inter-bifurcation distance
6. General loss of network hierarchy, including vascular shunts
7. Areas of avascularity

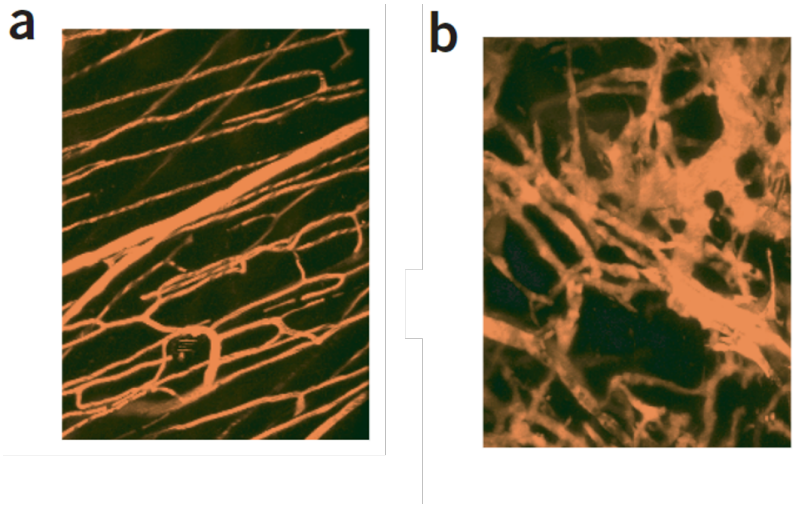

Figure 2.4: Illustration of a healthy microvasculature in (a) compared to an abnormal tumour microvasculature in (b). Image reproduced with permission from [88].

4. Angiogenesis is defined as the development of vascular networks.

Taken together, these structural abnormalities lead to an impaired function of the tumour microvasculature [95] and correlate with reduced survival rates [192]. There are two direct effects on microvascular function of the abnormal vasculature: a reduction in blood perfusion and oxygen transport, and an impediment to the delivery of therapeutic drugs to the patient [42].

The first effect of abnormalities is on tumour oxygenation. There is a reduced availability of oxygen to tumours due to an increased resistance to blood flow and a reduction in average haematocrit [5] in tumour vessels [42, 175]. This reduction in haematocrit shows large disparities between individual vessels, with some vessels being plasma channels [96] and therefore barely transporting oxygen at all. Structural abnormalities have been shown to be a cause of tumour tissue oxygen heterogeneity, through abnormal transport of red blood cells as a consequence of the structural abnormality [18]. In addition, avascular areas in the tumour lead to tissue hypoxia due to the diffusion distance of oxygen in tissue [194]. The abnormal nature of tumour vessel networks results in poor transport of oxygen to the tissue [113, 132, 137].In addition, shunts and increased blood resistance lead to poor perfusion to tumour tissue, and therefore they reduce the transport of oxygen to the tissue [132, 154, 173].

The second effect of vascular abnormalities is impeded drug delivery to the tumour tissue [42]. Similarly to the delivery of oxygen to tissue, areas of avascularity lead to poor drug transport to the tissue, as drugs are transported through the blood to the tissue [137]. In addition, high interstitial fluid pressure due to leaky vessels leads to low interstitial fluid flow, slowing the advection of drug molecules in the tissue [42]. However, leaky vessels also allow larger therapeutic molecules and blood cells to extravasate to the tumour tissue [42, 127], allowing some larger molecules to exploit the leakiness of the vessels [42]. In addition, the reduced and heterogeneous blood perfusion through the tumour also naturally reduces the delivery of drugs to the tumour tissue [42, 137].

Uncontrolled angiogenesis results in structural abnormalities in the tumour vasculature [91]. These structural abnormalities have been shown to impede both oxygen and drug delivery to the tumour [42], both of which are undesirable. Another cause of structural abnormalities in tumours is high solid stress [188], reviewed in the next section.

---

5. Haematocrit is the volume fraction of red blood cells in blood, section 2.2 will provide a more in depth definition of the term.

2.1.4 Vascular structural abnormalities: high solid stress and vessel compression

High solid stress in tumours is another cause of vessel structural abnormalities [33]. High solid stress in tumours is the result of two different mechanisms: growth induced solid stress and externally applied solid stress. Growth induced solid stress is caused by an excess proliferation of cells within the solid tumour and accounts for 30% of the solid stress in tumours [95]. Externally applied solid stress is the result of the tumour growing against surrounding organs in the body, and accounts for the remaining 70% of solid stress in tumours [95]. It has been demonstrated that solid stress is highest in the core of the tumour, and progressively decreases to a negligible amount at the surface of the tumour [188]. There are numerous consequences of high solid stress in tumours. Some of them have a direct effect on cells (e.g. solid stress inhibits tumour cell growth, induces apoptosis, increases metastatic potential, and reduces effective drug diffusivity [42, 95, 188]), however as this thesis focusses on the changes in the vasculature and in perfusion to the tumour due to solid stress, these consequences will be reviewed below. Figure 2.5 illustrates solid stress in a tumour and its effect on the vasculature.

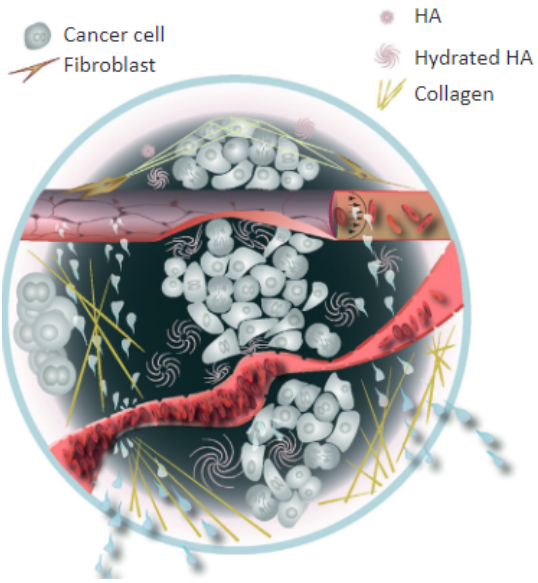

Figure 2.5: Illustration of solid stress in tumour tissue due to excessive cell proliferation, with a compressed vessel. Image reproduced with permission from [189].

A direct consequence of tumour solid stress is that both lymphatic and blood vessels are compressed [140]. The result of lymphatic vessel compression is that interstitial fluid cannot be drained, and it therefore contributes to elevated interstitial fluid pressure [21]. In addition, blood vessels can be compressed or totally collapsed, as illustrated in Figure 2.5. Blood vessel

compression and collapse reduces blood flow due to increased resistance, and therefore impedes the microvascular function [6, 33, 95, 205]. Vessel compression has been directly correlated to tissue hypoxia [33], impeded drug delivery [33], and correlates with reduced survival rates in animal models and human patients [33, 56, 192].

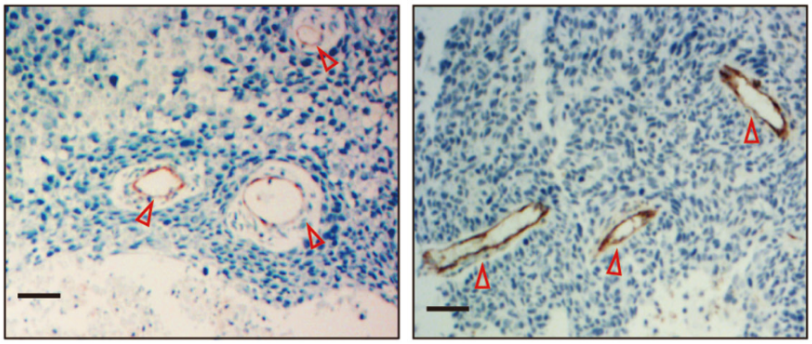

Figure 2.6: Illustration of compressed vessels in tumour tissue, red arrows point towards vessel cross-sections. Scale bar is 50 μm. Image reproduced through open license (CC BY 3.0) from [56].

As this thesis will require a quantitative value of the extent to which vessels are compressed in tumours, a summary of studies that quantify vessel compression is given in Table 2.1. The studies quantify vessel compression through a cross-sectional aspect ratio, where a high aspect ratio shows high vessel compression. These studies are all done through histological tissue slices and measure the vessel cross-section on the two-dimensional surface of the tissue slice. All the studies show that tumour blood vessels have a high aspect ratio [6, 56, 78, 192], and in cases where the studies have control vessels, they show that the tumour vessels are significantly more compressed than the control vessels [6, 78]. Figure 2.6 shows vessel cross-sections with high aspect ratios [56]. Finally, several studies quantifying vessel compression show that an increased degree of vessel compression correlates to a reduced survival rate [56, 192].

Study	Minimum AR	Mean AR	Maximum AR	Cancer
Fang *et al.* [56]	2.43	3.65	6.28	Non-small cell lung cancer
Aromando *et al.* [6]	1.10	2.50	7.60	Oral cancer
Hagendoorn *et al.* [78]	N/A	7.59	N/A	Skin squamous carcinoma
Tadeo *et al.* [192]	2.00	2.20	4.00	Neuroblastoma

Table 2.1: Summary of studies reporting aspect ratio (AR) for tumour vessels. Some values are read from figures in the papers and are thus approximations and rounded to the first decimal place.

Coupled with excess angiogenesis, high solid stress is characteristic of solid tumours [95]. Solid stress is the result of an excessive proliferation of cells in the tumour and the growth of the tumour against its surrounding [188], and it leads to vessel compression and collapse [95]. Studies demonstrate that compressed vessels correlate to lower survival rates and that they are the cause of poor perfusion to tumours [33, 56]. The next section will focus on why understanding tumour abnormalities is important.

2.1.5 Benefits of understanding structural abnormalities and tumour hypoxia

Vascular structural abnormalities are a hallmark of solid tumours, and are the result of both abnormal angiogenesis and high solid stress [95]. The abnormalities lead to poor blood perfusion to solid tumours, and therefore lead to poor drug delivery as well as tumour tissue hypoxia, both of which are undesirable [42, 93]. Understanding the abnormal tumour microvasculature is driven by research into therapeutic strategies to adapt or counteract these effects, which will be reviewed below.

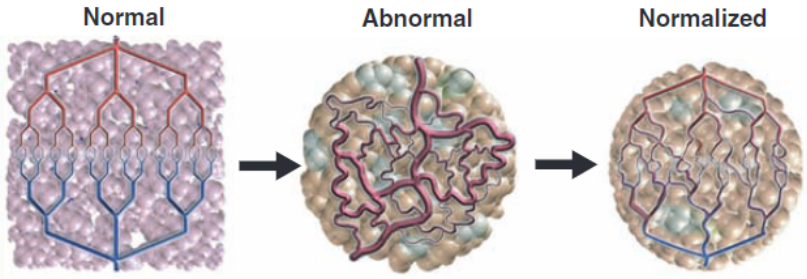

Figure 2.7: Illustration of normalisation therapy on the tumour vasculature. Image reproduced with permission from [90].

The first proposed strategy to counteract structural abnormalities in tumours is called normalisation therapy [91]. It consists of administering drugs that counteract the cause of the structural abnormality and temporarily transforms the abnormal microvasculature to a normalised one, where the functional properties of the microvasculature are improved, see Figure 2.7 for an illustration of normalisation therapy. As a consequence, tumour tissue oxygenation and drug delivery are both improved [91], which also helps radiation treatment work better due to the presence of more oxygen [91]. There are currently two proposed normalisation therapies, which are antiangiogenic therapy and stress alleviation therapy, to target excess angiogenesis and high solid stress, respectively [187]. Experiments in animal models have shown positive results [33, 197], which have in part translated to patient benefit [93]. There are multiple challenges associated with normalisation therapy, such as identifying the correct biomarkers for a normalised microenvironment or cancers response to normalisation, which have so far prevented normalisation therapy to be as efficient as expected [17, 92, 94].

The second proposed strategy is to adapt to structural abnormalities through personalised medicine [43]. Personalised medicine is a move away from a one size fits all therapeutic strategy, towards adapting treatment planning to individual patients [43]. For example, it is hypothesised that through improved biomarkers and functional imaging of tumours, to measure hypoxia for example, the targeting of radiation therapy can be improved and thus lead to patient benefit [16, 184]. For personalised medicine, better biomarkers and an understanding of the underlying mechanisms are necessary to improve the personalisation of the therapeutic treatment to patients [16, 43].

Taken together, normalisation therapy and personalised medicine provide a rationale for a better understanding of the effect that structural abnormalities have on tumour perfusion and oxygenation. Underlying these strategies is the hypothesis that a better understanding of the physics of cancer can improve patient survival [16, 42, 43, 135], and justifies further research in the field of the physics of cancer and its link to vascular structural abnormalities.

2.1.6 Summary: Cancer, tumours, tumour hypoxia, & the tumour abnormal vasculature

Cancer is a major healthcare concern in the world [131], where in the UK it is responsible for a quarter of all deaths [27]. Cancer is an abnormal cell growth in the body that has the potential to invade its surroundings and metastasize. Solid tumours, which form a majority of cancers, are complex and show a number of hallmarks, with tumour tissue hypoxia and vascular structural abnormalities being some key hallmarks [186].

Hypoxia occurs when cells have insufficient oxygen to function normally. In tumours, hypoxia leads to more aggressive tumour phenotypes and is a barrier to treatment [23, 43]. In solid tumours, there are two forms of hypoxia: chronic hypoxia and cycling hypoxia [10, 129]. Both types of hypoxia are the result of impaired blood perfusion to tumours and an abnormal tumour microvasculature [42, 65, 129, 181].

Structural abnormalities are the result of uncontrolled angiogenesis in tumours and high solid stress in tumours [186]. In both cases, they lead to blood vessels having an abnormal structure or network architecture, impairing their function to perfuse blood vessels and transport oxygen and other substances to tissue [186]. In the specific case of solid stress, compressed vessels correlate with reduced survival rate, increased hypoxia, and reduced drug delivery to the tissue [33]. Studies, therefore, show that structural abnormalities are undesirable phenotypes in tumours [93, 95].

Therapeutic strategies have been devised as a response to tumour tissue hypoxia and the abnormal tumour microvasculature [16, 43, 91]. Normalisation therapy aims to counteract the root causes of the structural abnormalities, rendering the tumour microvasculature temporarily more normal and therefore improving its function. Personalised medicine aims to use

biomarkers and functional imaging to adapt therapeutic strategies to individual patients [16, 43]. Underlying these strategies is the hypothesis that a better understanding of the physics of cancer can improve patient survival [16, 42, 43, 135], and justifies further research in the field of the physics of cancer and its link to vascular structural abnormalities.

2.2 Microcirculation & microhaemodynamics

This section aims to review the state of the art on the relevant research of microcirculatory blood flow for this thesis. Initially, section 2.2.1 introduces the circulatory system and the role of the microcirculation. Section 2.2.2 reviews the components of blood and their importance. Sections 2.2.3 and 2.2.4 review blood flow phenomena in straight microchannels and in compressed microchannels, respectively. Sections 2.2.5 and 2.2.6 review blood flow through bifurcations and networks. This is followed by a state of the art on blood flow through tumours in section 2.2.7. Finally, section 2.2.8 summarises the state of the art on microhaemodynamics.

2.2.1 Introduction to the microcirulatory system

The cardiovascular system in the human body is divided into two subcomponents, the pulmonary circulation and the systemic circulation, see Figure 2.8 for a schematic illustration. The pulmonary circulation flows blood through the lungs so that the blood is oxygenated and carbon dioxide removed. The systemic circulation distributes oxygenated blood to organs and tissues that require oxygen, nutrients, and waste removal. In the systemic circulation, the vessels leading out of the heart are called arteries, and have a size of the order of millimetres. At the end of the arteries, the microcirculatory system begins, which is embedded where the body needs the delivery of oxygen and nutrients [85]. After the microcirculation, blood flows through veins and back to the heart. The heart acts as a pump for both circulation systems, through a repetitive cycle of contraction and expansion, creating a pressure drop through the circulation systems. It is the microcirculation that is investigated in this thesis, so it is its structure, function, and blood flow phenomena in the microcirculation that is reviewed here.

The microcirculation is divided into three types of vessels[6] [85, 153]. The first, arterioles, are vessels between 10 μm to 100 μm in diameter and feed blood from the arteries to the capillaries. The capillaries are the smallest vessels in the body, and are of a comparable size to a red blood cell, ranging from 2 μm to about 10 μm. Finally, the venules drain the blood from the capillaries and back to veins, and have dimensions of several 10 μm to several 100 μm. Figure 2.9 shows an example of a microcirculatory network.

6. When it comes to the sizes of the three types of vessels in the microcirculation, the literature mentions different ranges of values for capillaries, arterioles, and venules. The key is that the capillaries are the smallest ones, of a comparable size to a red blood cell, that arterioles feed the capillaries, and that venules drain the capillaries, all in a hierarchical fashion.

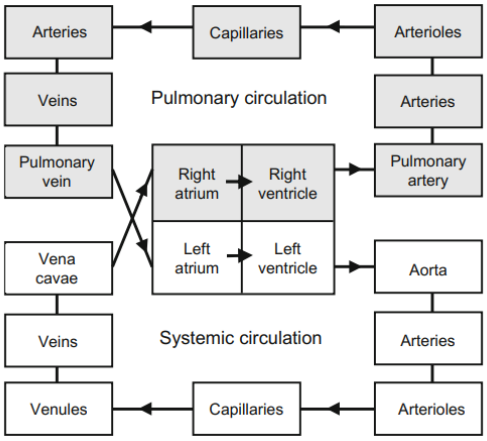

Figure 2.8: Schematic illustration of the cardiovascular system. Image reproduced with permission from [85].

The microcirculation has several purposes. Firstly, the capillary network serves as an exchange site for substances between the blood and the surrounding tissue, where these substances are oxygen, nutrients, and other molecules that the tissue requires [85, 153]. Secondly, waste molecules, such as carbon dioxide, are removed from the tissue into the blood [85, 153]. Capillaries, being of a similar size to red blood cells, are optimal for the transfer of oxygen from the red blood cells to the tissue [66, 119, 120, 130]. The microcirculation is crucial for the immune system, as it transports various cells and molecules, such as white blood cells and platelets. The microcirculation also acts as a thermoregulator, ensuring that the body temperature remains constant at 37 degrees Celsius. Finally, the microcirculation acts to balance fluid in various parts of the body, to ensure that the body can function properly [85].

The microcirculation has the ability to regulate blood flow through it. The regulation of blood flow mainly occurs through dynamic changes of vessel diameter, principally by expansion or contraction of arteriole smooth muscles [153].

To deliver its function, the microcirculation depends on blood flow, which is a complex fluid. The next sections will review current knowledge of blood and blood flow through the microcirculation.

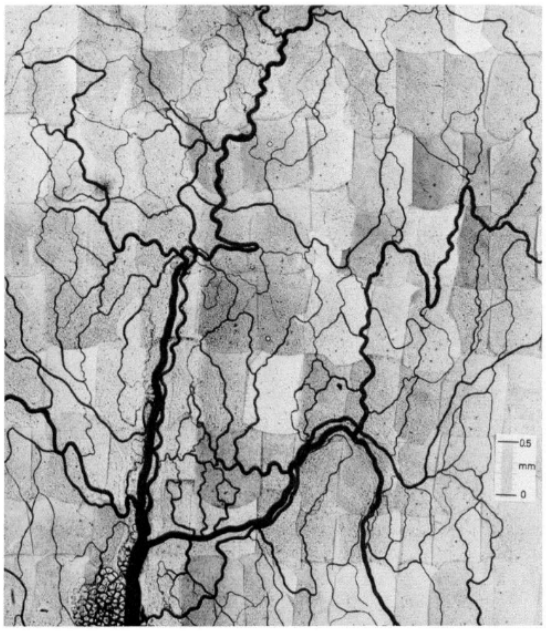

Figure 2.9: Example microcirculatory network from the rat mesentery. Image reproduced with permission from [149].

2.2.2 Blood and its components

Blood is a suspension of cells and other subcellular material in a fluid called plasma, and plays a crucial role in the microcirculatory function. The flow of blood in the microcirculation, called microhaemodyamics, exhibits specific behaviours due to the components within it. In this section, the various components of blood will be covered, with special attention on red blood cells due to their importance in microhaemodynamics and microcirculatory function. Figure 2.10 shows the components of blood in a vessel cross-section.

The most voluminous component of blood is plasma and makes up about 55% of human blood[7]. Plasma is an aqueous solution containing proteins, glucose, electrolytes, hormones, clotting factors, carbon dioxide, and oxygen [85]. Isolated plasma mostly behaves as a Newtonian fluid with a viscosity of 0.0012 Pa s, slightly higher than that of water due to its dissolved components, although under non-physiological high shear conditions it can exhibit viscoelastic behaviour [201].

Within the plasma are suspended white blood cells and platelets. These components account for less than 1% of blood volume, and have vital roles in the immune system and coagulation, respectively [164]. White blood cells range in diameter from 10 μm to 30 μm and platelets are plate-like with a diameter of 2 μm to 3 μm [85]. White blood cells and platelets play a lesser role than red blood cells in haemodynamics due to their low volume fraction [172].

7. The volume fraction of the components of blood varies according to several factors: environmental, genetic, and sex. The cited values are average ones for a human.

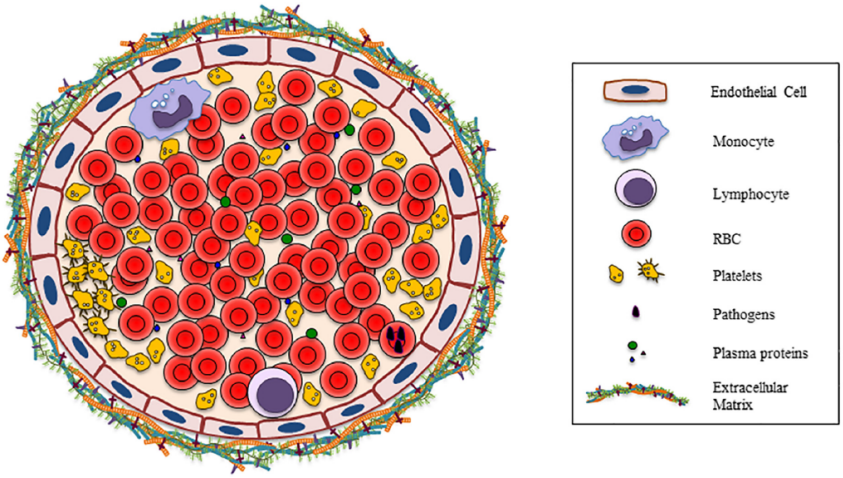

Figure 2.10: Illustration of the cross-section of a vessel, with the components in blood. Image reproduced through open license from [147].

Red blood cells are also suspended in the plasma and are the most abundant cell type in blood and are of primary importance for blood rheology and oxygen transport [67, 145, 172]. The volume fraction of red blood cells in blood, called haematocrit, is a key parameter defining the rheology of blood. Systemic haematocrit for a healthy adult is on average 45%, however, this value changes locally within the body. In the microvasculature the average haematocrit is 20%-25%, this value hides further local disparities within the microcirculation [153].

A red blood cell has the shape of a biconcave disk of $\sim 8\ \mu m$ in diameter, see Figure 2.11 for an illustration of its shapes and dimensions. Red blood cells' shape give it a high surface area to volume ratio [196], which is what allows them to deform despite having an incompressible cytoplasm[8]. Red blood cell cytoplasm is mainly composed of haemoglobin. Haemoglobin is an iron containing protein which has binding sites for oxygen and is what gives red blood cells their extraordinary oxygen carrying capacity. Although plasma does contain dissolved oxygen, up to 95% of oxygen in blood is bound in the red blood cells' haemoglobin [48, 66, 146]. The presence of iron within haemoglobin is what gives red blood cells, and ultimately blood, its distinctive red colour. The viscosity of the cytoplasm, at 0.006Pa s, is about five times higher than that of plasma [172]. Red blood cell cytoplasm is encapsulated within a membrane, about 4 nm thick, containing a lipid bilayer and a cytoskeleton, see Figure 2.11 for an illustration. The membrane behaves like an incompressible fluid, and therefore makes red blood cells deform while preserving their surface area.

8. Cytoplasm is the liquid within a cell.

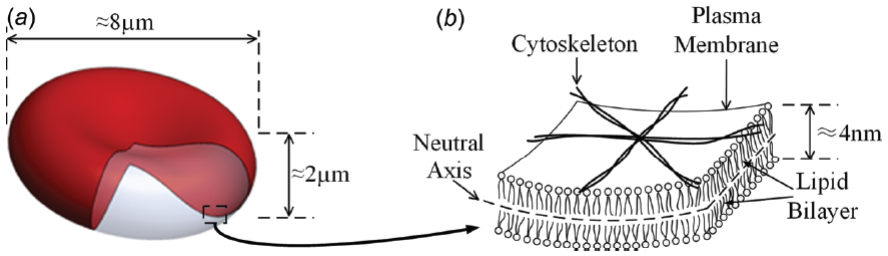

Figure 2.11: (a) drawing and dimensions of a red blood cell. (b) focus on the red blood cell membrane and its components. Image reproduced with permission from [34].

Red blood cells play a key role in microhaemodynamics due to their high volume fraction, deformability, and comparable size to the blood vessels in which they flow. The presence of red blood cells leads to blood flow having some unique properties which are critical in the function of the microcirculation. The next sections will review what these phenomena are, and review the state of the art regarding their study.

2.2.3 Blood flow through microvascular vessels

In straight microchannels, where red blood cells have a comparable dimension to that of red blood cells, blood flow exhibits some unique phenomena. In the microcirculation blood flow has a very low Reynolds number[9], $\ll 1$, indicating that inertial forces are negligible [172]. This is highlighted as, in some cases, the phenomena and mechanisms described below would be different in inertial flows [45]. This section will review these phenomena and their underlying mechanisms.

Red blood cells, under low shear, can form aggregates and rouleaux, which is when groups of cells clump together through a biochemical mechanism. Vessels in the microcirculation are generally too small, and shear rates too high, for rouleaux and aggregates to form. Therefore, although in some diseased conditions they can be present [89], rouleaux and aggregates tend to not have a leading order effect on microhaemodynamics [153].

Red blood cells under flow have different motions and can deform into different shapes depending on the flow conditions and the geometry [109, 111, 161]. Under low shear, they undergo a tumbling motion, and as shear rate increases they change motion to tank-treading, parachute, and polylobe like shapes depending on confinement ratio[10] [161]. The change in the motion and deformation of red blood cells under flow is responsible for its shear-thinning behaviour [111], see Figure 2.12 for an illustration. The shear-thinning behaviour of blood is also induced by the breaking down of red blood cell aggregates at higher shear rates [111].

9. The Reynolds number quantifies inertia in flow, with a high Reynolds number meaning high inertia. It will be more formally defined in section 3.1.
10. The confinement ratio is the ratio of the red blood cell diameter to the diameter of the channel.

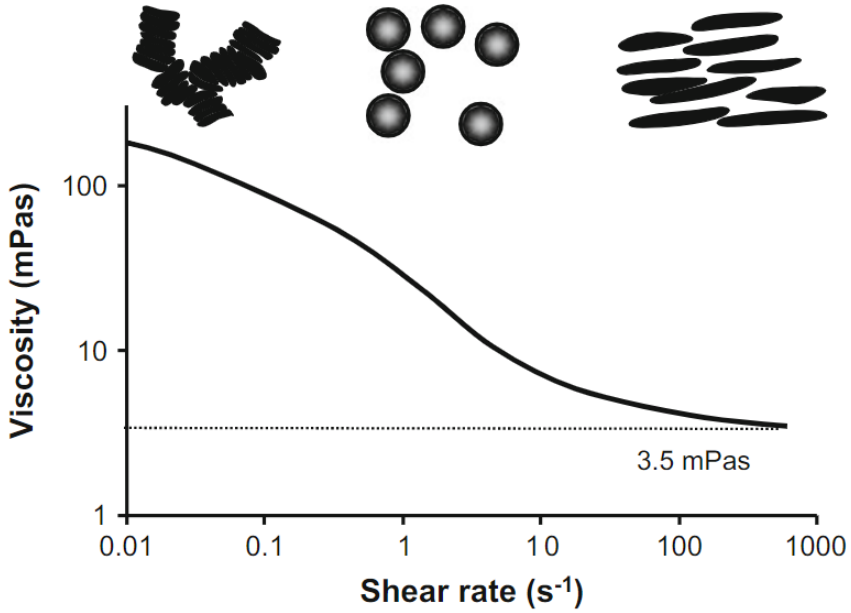

Figure 2.12: Shear thinning behaviour of blood, with illustrations of how changes in apparent viscosity result from changes in red blood cell flow/deformation. Image reproduced with permission from [85].

In small straight channels of $\sim 6\ \mu m$ red blood cells flow in a single file. As the diameter of the channel increases, there is a change from a single file motion to a multifile motion in a haematocrit dependant manner [172]. When red blood cells flow in microchannels, there is a combination of mechanisms that leads to the presence of a cell-free layer, which is the region between the vessel wall and the red blood cells that contains solely plasma. The phenomenon is observed both in physical experiments and in numerical simulations [11, 12, 172, 199, 210], and is the result of the particulate nature of blood and red blood cells' tendencies to flow towards the centre of channels.

There are several mechanisms leading to the equilibrium position of red blood cells in channels, illustrated in Figure 2.13, which preferentially flow towards the centre and lead to the cell-free layer. Firstly, a red blood cell's centre of mass cannot get closer than about 1 μm from the vessel wall, due to its finite size. This is in addition to the exclusion zone created by the endothelial surface layer, which is a layer of macromolecules present in vivo in vessel walls, excluding the presence of red blood cells [152, 172]. In addition to this size exclusion effect, there are two mechanisms leading red blood cells to migrate away from walls. The first mechanism is due to boundary interactions with the vessel wall [37, 46]. The second mechanism is due to the curvature of the velocity profile. In a numerical simulation, a deformable particle was suspended in an unbounded (without a wall) Poiseuille flow, and it was demonstrated that the red blood cell migrated towards the centre of the channel [98]. In both of these mechanisms described, increased cell deformation favours quicker migration towards

the centre of the channel [37, 98]. On the other hand, there is cell-cell interaction between red blood cells, which prevents all of the red blood cells from flowing in the centre of the channel and pushes some red blood cells towards the vessel wall [69, 172]. All of these mechanisms are illustrated in Figure 2.13 and result in the cell-free layer. Finally, more recent studies show that a high degree of leakage of plasma from a vessel can lead to red blood cells migrating towards the wall, rather than the centre of the vessel [178, 190].

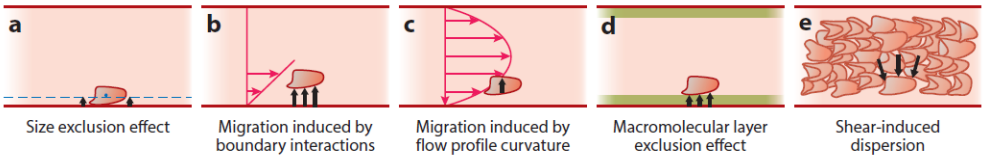

Figure 2.13: Mechanisms for red blood cell equilibrium position leading to the cell-free layer. Image reproduced with permission from [172].

As a final note on the cell-free layer, when dilute blood flows through larger vessels, of the order of several 10 μm, the cell-free layer is ill defined as red blood cells do not flow in a bulk, but independently of each other [177, 211]. In those circumstances red blood cells migrate towards the channel centre over very long distances [117].

As red blood cells flow towards the centre of the channel and form a cell-free layer, there are two interesting phenomena that appear in straight microchannels: the Fahraeus effect and the Fahraeus-Lindqvist effect.

The Fahraeus effect is defined by the flowrate fraction of red blood cells in blood being higher than the volume fraction of red blood cells in blood [52, 53]. In effect, as the red blood cells flow preferentially towards the centre of the channel, the average flowrate of red blood cells is higher than the average flowrate of the blood in the channel. This leads to two different definitions of haematocrit: the tube haematocrit, which is the volume concentration of red blood cells; and the discharge haematocrit, which is the flowrate concentration of red blood cells [153, 172]. From now on, unless stated otherwise, the term haematocrit will refer to the discharge haematocrit.

The Fahraeus-Lindqvist effect relates to the viscosity of blood in narrow tubes [54]. Below vessels of about 300 μm in diameter, the apparent viscosity of blood decreases as the vessel diameter decreases. The apparent viscosity of blood reaches a minimum at a vessel diameter of 5-7 μm, after which it sharply increases with further decreases in diameter. The mechanism

for this phenomenon is largely attributed to the cell-free layer acting as a lubrication layer, but it remains incompletely understood [153, 172]. To illustrate the Fahraeus-Lindqvist effect Figure 2.14 shows the relation between relative apparent viscosity[11] and tube diameter at a discharge haematocrit of 45%.

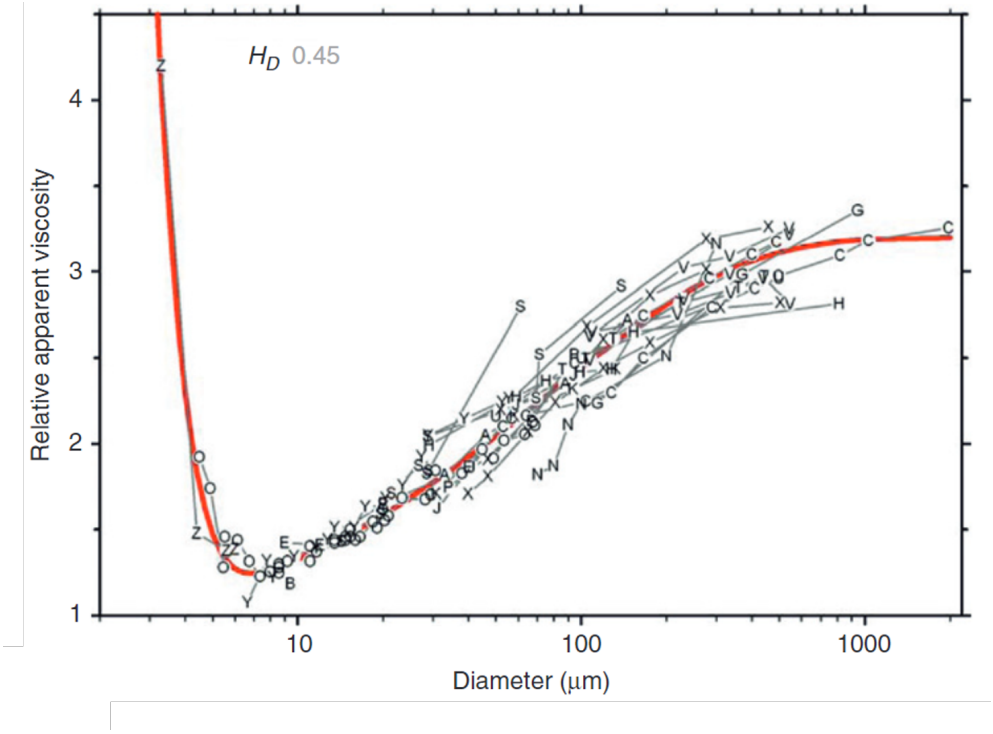

Figure 2.14: Fahraeus-Lindqvist effect for a discharge haematocrit of 45%. The red line is a fit to the experimental data, in grey. The relative apparent viscosity is the ratio of the apparent viscosity of blood to that of the viscosity of plasma. Image reproduced with permission from [153].

This concludes the relevant phenomena of blood flow in straight channels. Prior to reviewing the dynamics of blood flow at bifurcations, the next section will review studies of blood flow through compressed channels, as they are relevant to the work completed in this thesis.

2.2.4 Blood flow studies through compressed channels

As this thesis will investigate the effect of compressed vessels on blood flow, this section is dedicated to studies on particulate blood flow through compressed channels.

There have been multiple studies investigating blood flowing through a compression at the microscale. These studies are a mixture of both experimental and numerical studies and cover a broad spectrum. Several of these studies are direct investigations of blood flowing through a compression at a low Reynolds number, and due attention will be provided to them in this

11. The relative apparent viscosity is the apparent viscosity of blood divided by that of the plasma.

section [9, 55, 61, 199, 208]. There are numerous additional studies of blood flowing through a constriction at higher Reynolds number [1, 101, 102, 198]. A brief summary will be provided of these studies but they are less relevant due to the presence of inertia, although they provide an insight into the physics, which will lead one towards a better understanding of how blood flows through a compression.

Faivre *et al.* [55] flow a dilute suspension of blood, 0.1% and 2.6% tube haematocrit, through an in vitro geometrical constriction at a Reynolds number of 0.01, see Figure 2.15a for an illustration. They report that there is a marked increase in the cell-free layer of the blood after the constriction compared to before, and observe a symmetry in the cell-free layer when comparing the top to the bottom cell-free layer. They also measure the cell-free layer much further down the constriction (1cm, equivalent to a length of 100 channel heights in their geometry) and see that it is mostly unchanged. They then proceed to vary multiple parameters within their system to understand the effect it has on the cell-free layer, reported in Table 2.2 [55].

Parameter	Parameter change	Effect on downstream cell-free layer
Flowrate	Increase	Weak
Length of constriction	Increased	Increased
Width of constriction	Decreased	Increased
Haematocrit	Increased	Increased
Suspending fluid viscosity	Increased	Increased
Cell deformability	Increased	Increased
Cell volume	Increased	Increased

Table 2.2: Summary of the impact of varying parameters within the study performed by Faivre *et al.* [55].

Their discussion attributes the increase of the cell-free layer to cross streamline migration of red blood cells in the constriction towards more central streamlines. They add that this occurs due to the increase in shear rate within the constriction [55]. Lastly, they perform the same experiment with rigid spherical particles and show that the cell-free layer is symmetric before and after the constriction. They attribute the change in the cell-free layer as the red blood cells flow through the compression to a combination of the non-spherical shape and deformability of the red blood cells [55].

Fujiwara *et al.* [61] conducted a similar in vitro experiment with a semi-dilute suspension of blood, 10% and 20% haematocrit[12], in an asymmetric stenosis at a Reynolds number of 0.005, see Figure 2.15b for an illustration. They start by flowing pure water with 1 μm tracer particles, and observe a quasi-symmetry in the position of the particles before and after the stenosis. They then proceed to flow a suspension of blood at 10% haematocrit and observe that red blood cells located near the walls of the stenosis moved away from the wall as they

12. It is not explicit in this study if the haematocrit is a tube or a discharge haematocrit.

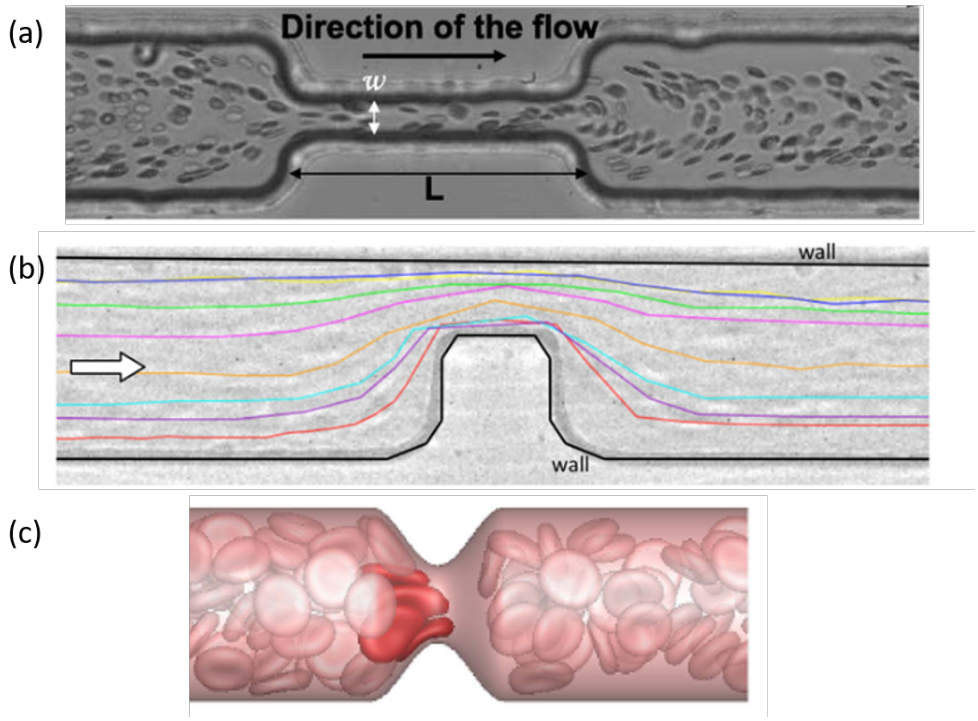

Figure 2.15: Illustration of key blood flow through constriction studies for visualisation purposes. (a) shows geometry for study by Faivre *et al* [55]. Channel dimensions are 75 μm and 25 μm for the compressed region. (b) shows geometry for study by Fujiwara *et al* [61]. Channel dimensions are 50 μm and 15 μm for the compressed region. (c) shows study by Vahidkhah *et al* [199]. Channel dimensions are 25 μm and an area blockage of 50% for the compressed region. Images reproduced with permission and through open license from [55, 61, 199].

flow through the stenosis, that the cell-free layer is increased after the stenosis, and that the cell-free layer is top/bottom symmetric. They attribute this behaviour to the deformability of the cells and confirm this by performing the same experiment with hardened red blood cells. With the hardened red blood cells, they see that the cell-free layer downstream of the compression changes negligibly, contrarily to the soft red blood cells. They further explain that the red blood cells experience higher deformation within the stenosis than in the non-stenosed section, as the channel dimensions through the stenosis are reduced and the peak velocity is increased to conserve mass [61].

Lastly, Fujiwara *et al.* [61] increase haematocrit to 20% and perform the same experiment. They see that red blood cells tend to move away from the wall as they flow through the stenosis, similarly to the experiment with soft red blood cells at 10% haematocrit, however, they observe that this is much less pronounced than at 10% haematocrit [61]. An increase in haematocrit leading to a smaller change in the cell-free layer as blood flows through the stenosis is opposite to the observation from Faivre *et al.*'s study [55], where they see an

increase in the cell-free layer at higher haematocrits. Fujiwara *et al.* discuss this difference and attribute it to the different haematocrits used, arguing that within the 10%-20% haematocrit range, cell-cell interaction is high, therefore the cell-free layer increase is opposed by this interaction and is smaller at 20% than at 10% haematocrit [61].

Vahidkhah *et al.* [199] present a numerical study of blood flowing through a stenosis, where they vary numerous parameters within their simulation in the Stokes flow regime, see Figure 2.15c for an illustration. They start by observing that, when the channel is 11 μm and at 23% tube haematocrit without the stenosis, the red blood cells flow in multifile, however, the stenosis causes a switch from multifile to single file motion in the same channel diameter. This in turn impacts the distribution of red blood cells within the channel cross-section. Indeed, they observe that when the channel diameter is 11 μm the red blood cells flow in a single file, and that the cell-free layer upstream of the stenosis is wider than downstream of the stenosis. In larger vessels where red blood cells no longer flow in a single file, they observe the opposite effect, i.e. the cell-free layer is wider downstream of the stenosis than upstream of the stenosis. They also report that in all cases the cell-free layer is narrower at the throat of the stenosis [199].

Bächer *et al.* [9] numerically investigate blood flow through a stenosis with microparticles, at 16.7% and 23.7% tube haematocrit, with a Reynolds number $\mathcal{O}(10^{-3})$. Their study focusses on the microparticles, however, they report a transient increase in the cell-free layer following the stenosis [9]. The transient increase suggests the non-permanence of this change. In a similar numerical study with blood and microparticles flowing through a stenosis, Yazdani *et al.* [208] report an enhancement of the cell-free layer after the compression, which increases as the degree of compression increases, and observe that the cell distribution after the compression eventually recovers its upstream distribution after an estimated length of 2 channel heights [208]. They expect that distance to be longer as the flowrate in the channel increases, although they provide no data or argument towards that expectation [208].

In addition, multiple experimentalists have studied blood flowing through a constriction at higher Reynolds number $\mathcal{O}$(1–10). For example, Abay *et al.* [1] study dilute blood flowing through an in vitro experimental setup with a dilute blood suspension of 1% and 5% tube haematocrit. They see an increase in the cell-free layer following the constriction, which is larger for deformable red blood cells than rigid ones [1]. This increase in the cell-free layer has been observed and exploited in microfluidic devices for blood plasma separation [101, 102, 198]. The increased Reynolds number however leads to the formation of vortices following the constriction [1] which are not reported, nor expected, at lower Reynolds number [55, 61, 199]. In addition, the presence of inertia in the system induces inertial lift forces, which are not present at low Reynolds number, therefore different mechanisms are at play making higher Reynolds number studies less relevant to the microvasculature, which is limited to Reynolds number $\ll 1$ [172].

To summarise, it has been established in experiments and numerical simulations that laminar blood flow through a compression increases the cell-free layer post compression [9, 55, 61, 199, 208]. The mechanism for this change in the cell-free layer is the increased lift force experienced by red blood cells as the shear rate and shear rate gradient increases in the compression [55, 61]. However, in dilute suspensions this change is reported to be present after a length of 100D [55], whereas at higher haematocrits the change in the cell-free layer disappears after a length of 2 channel heights [208]. In addition, geometry asymmetry is shown to have a negligible effect, and increasing haematocrit reduces the change in the cell-free layer [61]. Lastly, more rigid red blood cells are shown to have a smaller change in the cell-free layer [55, 61].

2.2.5 Blood flow through microvascular bifurcations

Thus far, microhaemodynamics has been reviewed in straight channels. However, blood flows through networks of interconnected vessels, and it is at vascular bifurcations that the individual vessels are connected. An interesting phenomenon, called phase separation[13], occurs at diverging microvascular bifurcations [172]. This section will review the current state of the art knowledge on phase separation.

At diverging bifurcations, blood flow experiences phase separation of the plasma phase and the red blood cell phase [57, 62], see Figure 2.16 for an illustration. Due to the particulate nature of blood and the cell-free layer, the higher flowing child branch has a tendency to be enriched in haematocrit compared to the lower flowing child branch [172]. It is the result of the red blood cell cross-sectional distribution prior to the bifurcation, and the curvature of the flow separation line to each child branch, that leads to this effect [172]. Phase separation at a bifurcation can lead the lower flowing child branch to be entirely depleted of red blood cells, and thus to become a plasma channel. Studies have demonstrated that the leading order parameters for this phenomenon are parent branch haematocrit, the diameter of the vessels, and the flow ratio to the child branches [57].

Phase separation at bifurcations is the subject of many studies, both numerical and experimental. Some studies use red blood cells, while others use particles, where the particles can be proxies for red blood cells. The effect of a single suspended red blood cell/particle is investigated to better understand the underlying physics [47, 203, 204], whereas other studies look at denser suspensions or particles or red blood cells, which are relevant for more physiological blood flow settings [18, 35, 36, 86, 105, 122, 123, 128, 139, 155, 165, 177–179, 206, 207, 209, 212, 213].

---

13. The literature refers to this phenomenon in a myriad of different ways: Zweifach-Fung effect, plasma skimming, phase separation, partitioning of red blood cells at vascular bifurcations, and others. In this thesis, the terms phase separation or partitioning of red blood cells will be used.

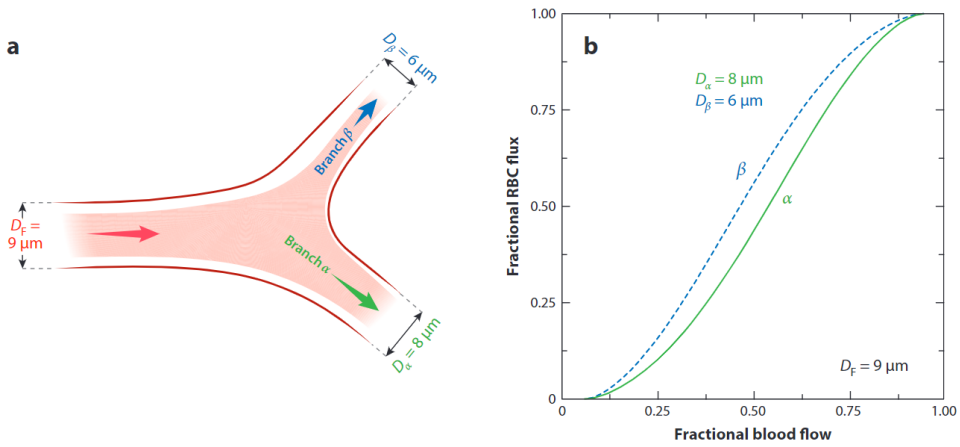

Figure 2.16: Illustration of phase separation at diverging bifurcations. (a) shows a diverging bifurcation, the shaded red showing the red blood cell distribution. (b) shows the fraction of red blood cells flowing in each branch (blue and green curves) at a given blood fraction flowing in the branches. The curve shows that the higher flowing branch is typically enriched in red blood cells. Image reproduced with permission from [172].

At the single particle scale, the path selection of a particle is the result of the position of the particle prior to the bifurcation in relation to the separating streamlines[14] [47, 203, 204]. If the particle is far enough from the separating streamlines, the particle flows to the child branch to which its underlying streamlines flow to. However, when a particle is close to the separating streamline, which naturally happens for channel diameters comparable to that of a red blood cell, the path selection of a particle is more complex [47]. On the one hand, as fluid streamlines in the centreline are more likely to flow to the higher flowing child branch and particles migrate to the centre of the channel, there is an attraction to the higher flowing child branch [172]. On the other, when red blood cells approach the lower flowing child branch they may flow there through an obstruction effect, even if the underlying streamline of the red blood cell centre of mass does not [47].

In the case of suspensions, cell-cell interaction for particles at the vicinity of the separating streamline plays a role as well [14], rendering the study of the mechanisms more complex. However, the collective outcome is generally that the higher flowing child branch is enriched in haematocrit. The higher flowing child branch being enriched in haematocrit is the result of the cell-free layer representing a lower fraction of the blood flowing to the higher flowing child branch. However, more recent studies have shown certain circumstances under which the lower flowing child branch can be enriched in haematocrit, sometimes called reverse partitioning, contrary to normal circumstances [11, 18, 177].

14. The separating streamline is the streamline separating point particles flowing from one child branch to the other child branch.

The first case of reverse partitioning is the result of asymmetry in the diameters of the two child branches at a bifurcation [172]. When the asymmetry in diameters is present, and the flowrate to each branch is similar, there is a range of flow ratios where the lower flowing child brannch is enriched in haematocrit, and the higher flowing child branch is impoverished in haematocrit [172]. For illustration purposes, this is visible in Figure 2.16b, where at a fractional blood flow near 0.5, the smaller branch has a higher fractional flux of red blood cells than the larger branch.

Another example of reverse partitioning occurs when two successive vascular bifurcations are within a length of 10D from each other [18, 128, 156]. When blood flows through a bifurcation, the symmetry of the cell-free layer in both child branches is disturbed and the cell-free layer becomes asymmetric. In the child branches, the cell-free layer on the side of the apex of the bifurcation is smaller than on the other side [18, 139], see Figure 2.17 for an illustration. This asymmetry in the cell-free layer takes 10-25 diameter lengths to fully recover. If another diverging bifurcation is reached before the disturbance in the cell-free layer recovers, the partitioning of red blood cells will be altered and there may be reversed partitioning [18, 87, 128, 148, 212].

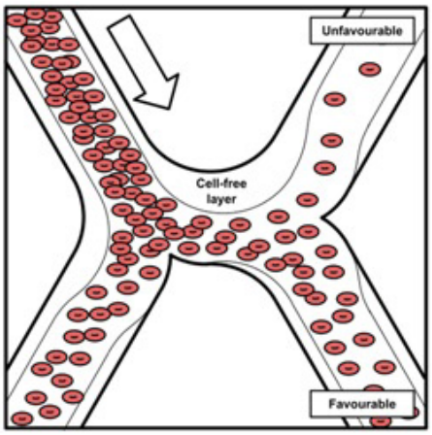

Figure 2.17: Illustration of cell-free layer disturbance following a bifurcation. The top right branch is labelled as unfavourable, as the preceding branch has the cell-free layer biased to reduce red blood cell flow to the unfavourably labelled branch. Image reproduced with permission from [18].

A third case of reverse partitioning has been studied by Shen *et al* [177]. They show that reverse partitioning is associated to conditions where the cross-sectional distribution of red blood cells is both non-uniform and altered compared to common physiology [177]. The reverse partitioning can lead to the lower flowing child branch being fed by a section of the parent branch containing a higher concentration of red blood cells, leading to a reverse partitioning effect [177].

The current state of the art on phase separation at diverging vascular bifurcations has been reviewed. At bifurcations, the higher flowing child branch is usually enriched in haematocrit [172], although some mechanisms can lead to a reverse partitioning effect [11, 177]. However, vascular networks are formed by many bifurcations where network effects are present. The next section will review blood flow in networks.

2.2.6 Blood flow in microvascular networks

It is through microvascular networks as a whole that their function is achieved. This section will review a specific phenomenon, the network Fahraeus effect, which occurs at a network level, and is relevant to understand blood flow dynamics in networks.

One direct consequence of phase separation of plasma and red blood cells in networks is that the average haematocrit continues to decrease after consecutive bifurcations. This has been coined the network Fahraeus effect [149], see Figure 2.18 for an illustration. The network Fahraeus effect is the result of phase separation at bifurcations, where there is a non-linear and positive correlation between higher flowing child branches and higher haematocrit in the child branches [153]. As a result, the average discharge haematocrit of child branches at a bifurcation is lower than that of the parent branch discharge haematocrit [153]. The network Fahraeus effect has been shown to have a higher effect on the reduction in haematocrit when phase separation is more pronounced at bifurcations [149].

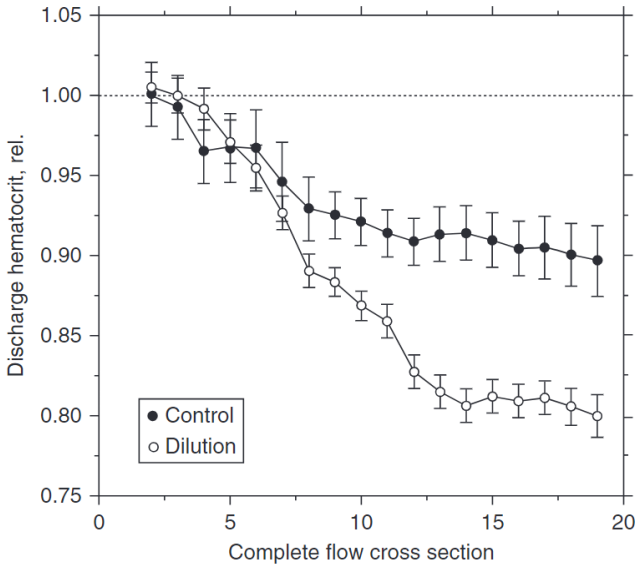

Figure 2.18: Network Fahraeus effect. Shows relative average vessel haematocrit as a function of bifurcation generation (referred to as complete flow cross-section in the graph). This illustrates the network Fahraeus effect as after each successive generation the haematocrit is reduced. It also illustrates that enhanced phase separation, in the dilution case (lower inlet haematocrit), enhances the network Fahraeus effect. Image reproduced with permission from [153].

In addition to the network Fahraeus effect, there are numerous works investigating blood flow through microvascular networks, see the following references for examples [68, 115, 116, 170]. This thesis, however, focusses on blood flow through tumours and will therefore specifically look at the dynamics of blood flow in tumours and tumour vascular networks, which will be reviewed in the next section.

2.2.7 Blood flow in tumours

This section will now revisit tumours, specifically blood flow in tumours, now that microhaemodynamics has been reviewed. The knowledge gained in haemodynamics from sections 2.2.1-2.2.6 provides the necessary knowledge to delve into more technical aspects of tumour blood flow.

Blood perfusion through tumour networks is reduced through both an increase in geometric resistance and an increase in viscous resistance [89, 95, 174, 175]. Combined, these increases in flow resistance reduce the blood perfusion of tumours and therefore reduce oxygen availability flowing through the tumour [41, 89, 95, 106].

An increase in geometric resistance refers to changes in the vascular network which reduce the flow of blood through it, as it increases resistance to flow [89, 174]. Increases in geometric resistance in tumours are the result of vessel tortuosity [106] and vessel compression [33, 95, 169]. Tortuosity increases the distance blood travels, and therefore increases resistance, whilst vessel compression reduces the available cross-sectional area available for blood to flow through [89].

An increase in viscous resistance is the result of an increase in the apparent viscosity of blood in tumours. There are various mechanisms leading to this increase in apparent viscosity of blood [89, 175]. Firstly, red blood cells can deform less in tumours than in healthy tissue (mechanisms include lower flowrates leading to less shear deformation, and acidic environment in tumours leading to stiffer red blood cells [89]). As red blood cells deform less, they have a higher apparent viscosity due to the shear thinning nature of blood [111]. Secondly, blood vessels in tumours are leaky and let plasma seep from them [89, 96, 175]. As plasma leaks from the vessels, the haematocrit in the vessels increases, and so does the apparent viscosity of blood in it [96, 175]. Finally, in tumours, blood vessels are enlarged compared to healthy vessels. Due to the Fahraeus-Lindqvist effect, as the vessels are larger the apparent viscosity of blood increases [89, 175], all other things being equal. Increases in viscous resistance are partly counterbalanced by the reduction of systemic haematocrit in tumours, which can include plasma only channels [96, 175].

In addition to increases in flow resistance, and therefore a reduced perfusion through tumours, tumour blood flow is highly heterogeneous [39, 42, 96, 191]. There is a high heterogeneity of blood flow between vessels within the same tumour [96], which can also include temporary flow reversal in vessels [112]. This heterogeneity in blood perfusion can correlate to spatial locations, for example in some tumours blood flow is higher at the periphery than the core [39]. The blood flow heterogeneity is also linked to the presence of shunts that can capture a large fraction of blood flow and deprive other areas of blood [154], see Figure 2.19 for an illustration of a shunt. In addition to heterogeneity in blood flow, there is a highly heterogeneous haematocrit distribution in tumour networks [18, 96]. Some vessels can have haematocrits higher than systemic haematocrit, attributed to vessels leaking plasma [96, 175], while other vessels can be devoid of red blood cells, almost 30% of vessels in some cases [96], see Figure 2.20. In Figure 2.20, control vessels also appear to have some red blood cell free vessels, however, they are much less common, by a factor of 4 [96]. These heterogeneities in blood flow also lead to heterogeneity in tissue oxygenation [41].

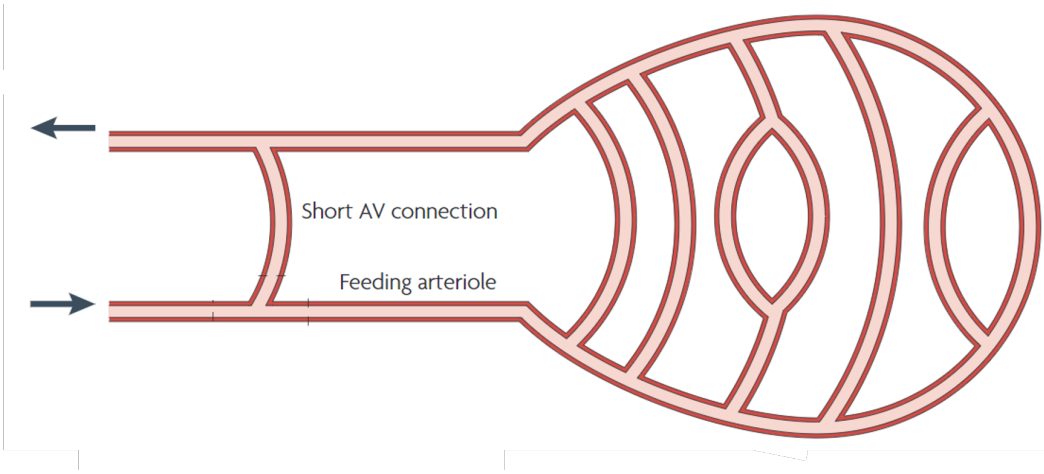

Figure 2.19: Illustration of a vascular shunt, labelled short AV (arterio-venous) connection. The short AV connection leads blood to bypass the capillary vessels on the right hand side of the network. Image reproduced with permission from [154].

The mechanisms leading to blood vessels being devoid of red blood cells are not well understood. A more recent study links reduced interbifurcation distance in tumours, a structural abnormality, to abnormal red blood cell partitioning at vascular bifurcations [18]. It is the disturbance of the cell-free layer at a bifurcation, which is not relaxed by the time the next bifurcation is reached, which alters the partitioning of red blood cells at the second bifurcation, see Figure 2.17. This mechanism for abnormal red blood cell partitioning leads to haematocrit heterogeneity and tissue oxygen heterogeneity in tumours [18]. The abnormal partitioning due to reduced interbifurcation distance, however, does not appear to lead to plasma channels [18].

In addition to the reduced-interbifurcation distance, there are a number of phenomena in tumour blood flow that alter red blood cell flow, or red blood cell cross-sectional distribution in a vessel. Changes in red blood cell stiffness due to acidity [89], can change the motion of red blood cells [161], which in turn will change the cell-free layer [100]. Compression has also been shown to change the cell-free layer in straight channels [55, 61], and so has leakage of plasma from vessels [178]. Finally, clustering of red blood cells in tumours [89] will not only have an effect on the apparent viscosity of blood, but also on the cell-free layer development, and therefore partitioning of red blood cells [179]. Given the role of the cell-free layer in the partitioning of red blood cells at bifurcations [172], these can be important phenomena in tumour blood flow.

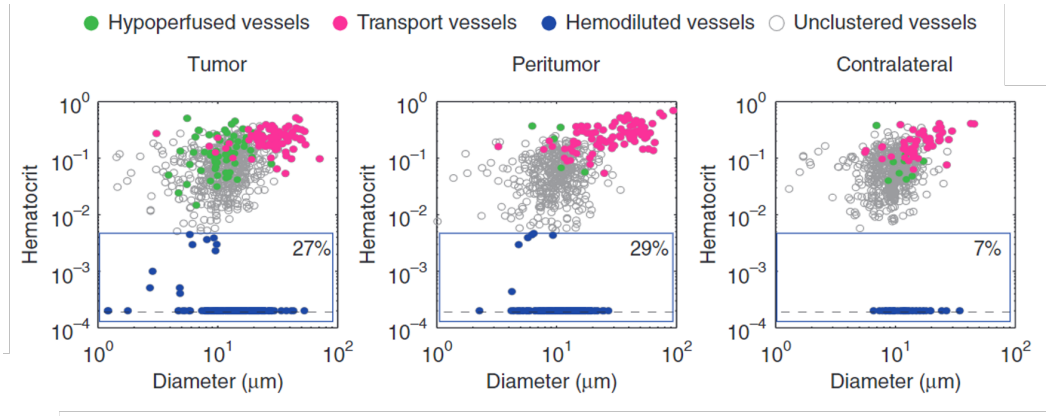

Figure 2.20: Shows vessel tube haematocrit as a function of vessel diameter in tumour, peritumor and contralateral vessels. The Figure shows that tumour vessels have a much higher fraction of haemodiluted vessels. Image reproduced with permission from [96].

Blood flow through tumours differs from blood flow in healthy networks through various mechanisms, which lead to reduced perfusion, and heterogeneities in blood perfusion and in tube haematocrit in tumour networks [95, 96]. The consequence of these heterogeneities is the presence of plasma channels and hypoxia, and therefore more fatal tumours [18, 41, 95, 129]. The link between blood flow, tissue oxygenation, and prognosis justifies further research in the field of blood flow in tumours.

2.2.8 Summary: Microcirculation & microhaemodynamics

The microcirculation, a subset of the circulatory system containing the smallest vessels, is the area where the majority of substance and fluid exchange between the blood vessels and the tissue occurs. As such, it plays a key role in regulating the body and distributing oxygen.

Blood flow is highly affected by its most common suspended cell, the red blood cell, which occupies 45% of the fraction of blood. In channels where blood vessels are of a comparable size to the red blood cells, such as in the microcirculation, their presence leads to a cell-free layer between the red blood cells flowing in the centre of the channel and the vessel wall.

The Fahraeus effect, a reduced volume fraction of red blood cells compared to the flowrate fraction of red blood cells, and the Fahraeus-Lindqvist effect, decreasing apparent viscosity with decreasing vessel size in the microcirculation, are key phenomena in microcirculatory blood flow.

A review of blood flow studies through compressed microchannels shows that the cell-free layer is increased as a result of blood flowing through the compression. The change in the cell-free layer is a result of the deformable and non-spherical nature of red blood cells, as well as the increased shear rate through the compressed channels.

At vascular bifurcations, red blood cell partitioning leads to the higher flowing child branch being enriched in red blood cells whilst the lower flowing child branch is impoverished. An inverse effect, called reverse partitioning, is possible in circumstances reviewed in this chapter. Red blood cell partitioning at bifurcations leads to the network Fahraeus effect, where in a network the average haematocrit decreases at consecutive bifurcations.

Blood flow in tumours differs from healthy blood flow due to increased geometric and viscous resistances to blood flow. In addition, tumours have heterogeneities in blood flowrate and in haematocrit, with some vessels being devoid of red blood cells while others have very high haematocrits. Through these mechanisms, blood flow in tumours participates in tumour tissue hypoxia. The link between blood flow, tissue oxygenation, and prognosis justifies further research in the field of blood flow in tumours.

2.3 Gaps, hypothesis, and aim & objectives

This section will join pieces of knowledge from sections 2.1 and 2.2 to identify gaps in the literature. Once these gaps are identified, the underlying hypothesis of this thesis will be formulated, followed by the aim & objectives.

Section 2.2.7 reviewed several reports of heterogeneous haematocrit distributions in tumour vascular networks. The mechanism for high haematocrit vessels, plasma leaking into the interstitium, is identified. However, it is unclear what mechanism leads to vessels having no red blood cells flowing through them. Reflecting on vascular networks, section 2.2.1, and how red blood cells are transported in them, sections 2.2.5 and 2.2.6, one could hypothesise that it is phase separation that would lead to vessels having no red blood cells. However, a comparison of healthy networks and tumour networks shows that tumour networks have more plasma channels. As phase separation is also present in healthy networks, tumour networks would require another mechanism to explain the higher number of plasma channels.

Sections 2.2.5 and 2.2.7 discuss a more recent study [18] that has shown that one vascular abnormality present in tumours, namely reduced interbifurcation distance, leads to abnormal partitioning of red blood cells at vascular bifurcations. There are two key observations here. The first is that it identifies a mechanism which is not present in healthy vasculature for red blood cell heterogeneity in networks. However, the abnormal red blood cell partitioning identified in the study, from the results, does not seem to be enough to explain the high fraction of plasma channels in tumour networks. The second observation is that the underlying mechanism for the abnormal partitioning of red blood cells is a change in the cell-free layer in the blood.

Section 2.2.4 reviews several studies of blood flowing through compressed microchannels, all of which report an increase in the cell-free layer as blood flows through the compressed region. Given the prevalence of compressed vessels in tumours, section 2.1.4, and the previously identified abnormal partitioning of red blood cells as a result of a change in the cell-free layer, section 2.2.5, it naturally follows that vessel compression could also have an effect on the partitioning of red blood cells at microvascular bifurcations. However, how vessel compression effects the partitioning of red blood cells at a downstream bifurcation is not investigated in the literature. The effect of a compression on the partitioning of red blood cells at a bifurcation would be in addition to the reduced perfusion when vessels are compressed as a result of the increased geometric resistance, section 2.2.7.

Section 2.1.4 summarises reports of vessel compression in cancer. Table 2.1 shows that the aspect ratio of compressed vessels has been quantified in lung cancer, oral cancer, skin cancer, and neuroblastoma. However, the literature does not report on aspect ratio in glioblastoma. Given the poor survival rate of glioblastoma patients, section 2.1.1, and the association between vessel compression and survival rate, section 2.1.4, quantifying vessel compression in glioblastoma would contribute to the knowledge of the glioblastoma microenvironment.

From the identified gaps in the literature, I formulate the central hypothesis of this thesis:

Vessel compression leads to abnormal partitioning of red blood cells at vascular bifurcations, contributing to a high fraction of plasma channels in tumour networks and to tumour tissue hypoxia.

The aim of the thesis is to find a mechanistic link between vessel compression and abnormal red blood cell transport in vascular networks, and contextualise it to glioblastoma. The aim leads to three objectives. Each objective will be addressed in a results chapter of this thesis.

1. Numerically investigate how vessel compression impacts partitioning of red blood cells at a single vascular bifurcation (methods in section 3.1, results in chapter 4)
2. Numerically investigate how vessel compression impacts red blood cell distribution in vascular networks (methods in section 3.2, results in chapter 5)

3. Quantify blood vessel phenotypes, including vessel compression, in a mouse model of a glioblastoma (methods in 3.3, results in chapter 6)

Chapter 3

Methods

This chapter describes the methods used in this thesis to perform the research. Section 3.1 gives the method for the particulate blood flow model, section 3.2 provides the method to solve for blood flow in networks, and section 3.3 covers the method for the animal models and the imaging technique to obtain the vascular marker images from the animal models.

3.1 Particulate blood flow model

This section covers the model for particulate blood flow, used in chapters 5 and 6. Blood is treated as a suspension of deformable particles in a continuous liquid phase, which are models for red blood cells (RBCs) and plasma, respectively. This section is subdivided into the physical model, section 3.1.1, which contains a description of the physics that is modelled, with the equations and assumptions for the physics; and the numerical model, section 3.1.2, which shows how the numerical solution for the physical model is obtained. For illustration purposes, Figure 3.1 shows a snapshot of what a simulation looks like, with deformed red blood cells flowing through a channel.

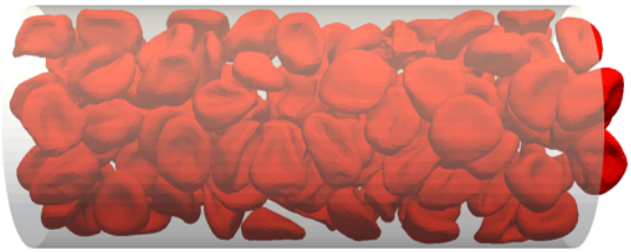

Figure 3.1: Snapshot of a simulation of red blood cells flowing through a channel using the particulate blood flow model outlined in this section.

3.1.1 Physical model

The physical model for particulate blood flow is detailed in this section. This section contains three parts, one for the fluid model, one for the particle model, and one for the boundary conditions.

Fluid model

The fluid model for particulate blood flow models the plasma phase, in which the RBCs are suspended. The plasma is treated as an incompressible and continuous Newtonian fluid using the continuity equation, equation (3.1), and the Navier-Stokes equation, equation (3.2) [107, 108, 195]. Respectively, the equations read [107],

$$\nabla \mathbf{u} = 0, \tag{3.1}$$

$$\rho \frac{D\mathbf{u}}{Dt} = -\nabla p + \eta \triangle \mathbf{u} + \mathbf{F}, \tag{3.2}$$

where ρ is the density, t is time, p is the pressure, η is the shear viscosity, $\mathbf{u}$ is the fluid velocity, and $\mathbf{F}$ is an external force acting on the fluid (e.g. gravity). Plasma can have viscoelastic behaviour due to the presence of substances within it, such as proteins [201]. However, the viscoelasticity of plasma is only present at high shear rates, beyond that which will be investigated in this thesis, therefore a Newtonian approximation is sufficient. Additionally, the effect of gravity is neglected, as in the conditions investigated in this thesis the effect of gravity is not relevant for the sedimentation of the RBCs within the channel [3].

The Reynolds number is used in this thesis to characterise the flow in channels. The Reynolds number is a non-dimensional number which quantifies the ratio of the time scales between the diffusive timescale of momentum to the advective timescale of momentum. Higher Reynolds number flows have higher inertia, and can have turbulence. Lower Reynolds number flows are momentum diffusion dominated, and contain low inertia to no inertia in Stokes flow (Stokes flow is when Reynolds number $\ll 1$). Typically, in the microcirculation the blood flow Reynolds number is $\ll 1$ making inertial effects negligible [172]. The channel Reynolds number is defined as:

$$Re = \frac{u_{max} D \rho}{\mu}, \tag{3.3}$$

where D is the channel diameter, and u_{max} is the maximum velocity in the channel.

Particle model

In flow, red blood cells deform under shear and therefore it is necessary to have a model which captures the deformation of the red blood cells. In this thesis, I use a continuum based model, which assumes an isotropic and hyperelastic membrane. The hyperelastic model assumes that the red blood cell membrane has no viscous behaviour, this assumption is sufficient at low Reynolds number flows, such as the ones investigated in this thesis [157]. The model assumes that any shear or bending energy increases the free energy of the red blood cell membrane, E, through [195],

$$E = E_S + E_B, \tag{3.4}$$

where E_S is the membrane shear energy, which quantifies the energy stored in the membrane when it experiences shear deformation; and E_B is the membrane bending energy, which quantifies the energy stored in the membrane when it experiences bending deformation.

The membrane shear energy is defined by Skalak's model [183],

$$E_S = \oint dA\varepsilon^s, \tag{3.5}$$

$$\varepsilon^s = \frac{\kappa_s}{12}(I_1^2 + 2I_1 - 2I_2) + \frac{\kappa_\alpha}{12}I_2^2, \tag{3.6}$$

where A is the surface area of a red blood cell, ε^s is the strain energy, κ_s is the elastic modulus of the red blood cell, κ_α is the area dilation modulus. I_1 and I_2 are the strain invariants. For additional information on the strain invariants the interested reader is directed towards [74, 195].

The bending energy is defined from Helfrich's model as [74],

$$E_B = \oint dA\frac{\kappa_b}{2}\left(H - H^{(0)}\right)^2, \tag{3.7}$$

where κ_b is the bending modulus of the red blood cell, H is the trace of the surface curvature tensor and $H^{(0)}$ is the spontaneous curvature. For additional information on the surface curvature the interested reader is directed towards [195].

The interior of a red blood cell, the cytoplasm, is filled with a solution containing mostly haemoglobin, which binds and transports oxygen in blood [66, 172]. The dynamic viscosity of red blood cell cytoplasm is about 5 times higher than the dynamic viscosity of plasma [172]. The ratio of the dynamic viscosity of the cytoplasm to the dynamic viscosity of plasma is called the viscosity ratio. In this thesis, however, the viscosity ratio is assumed to be 1. This is because the effect of a realistic viscosity ratio on particulate blood flow is not a leading order effect on particulate blood flow [40].

The capillary number is used within this thesis to characterise the deformability of the red blood cells [195]. The capillary number is the ratio of the timescale for a red blood cell to recover from a deformation to the timescale for a red blood cell to deform from the shear flow. In effect, at low capillary numbers the recovery timescale is dominant and red blood cells experience low deformation, whereas at high capillary numbers the deformation timescale is dominant, and red blood cells experience higher deformation. The capillary number is calculated through,

$$Ca = \frac{\mu \gamma r_{rbc}}{\kappa_s}, \tag{3.8}$$

where μ is the dynamic viscosity of the suspending fluid, γ is a typical shear rate of the system, r_{rbc} is the rest radius of the red blood cell, and κ_s is the elastic modulus of the red blood cell. As the shear rate within a channel is not uniform, I use a characteristic shear rate to calculate the capillary number which is defined as,

$$\gamma = \frac{2u_{max}}{r_{vessel}}, \tag{3.9}$$

where u_{max} is the peak velocity within the vessel of radius r_{vessel}. It is possible to use other characteristic shear rates to define the capillary number, however different equations for calculating the characteristic shear rate will merely cause the different capillary numbers to scale linearly with each other, and not add additional physical insight to the capillary number. Therefore, it will just lead to red blood cells and red blood cell suspensions having the same behaviour, but at different values due to the different definitions. In addition, the elastic modulus is related to the bending modulus, κ_b through the following relation [136],

$$\kappa_b = \frac{\kappa_s r_{rbc}^2}{400}, \tag{3.10}$$

which is an experimentally determined relationship specific to red blood cells [136].

Boundary conditions

Boundary conditions are necessary to solve the physical model, see Figure 3.2 for an illustration of labelled boundaries. The no-slip boundary condition is imposed at boundaries separating the fluid from solid objects, the solid objects include the vessel wall and the red blood cells. The boundary conditions at the open boundaries can be modelled through a pressure or a velocity boundary condition. In the case of a velocity boundary condition, a fully developed Poiseuille velocity profile is imposed at the boundary [15].

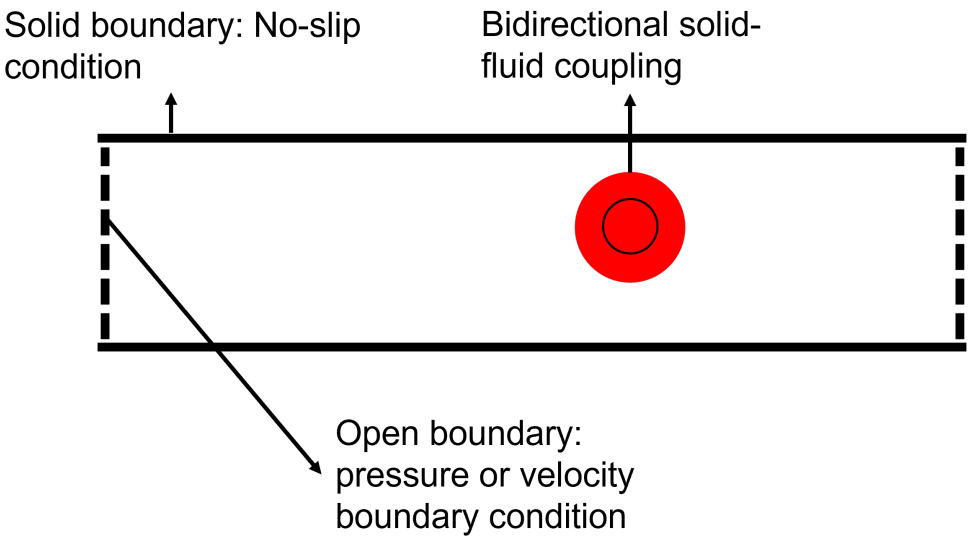

Figure 3.2: Illustration of boundary conditions for cellular blood flow in a straight channel. The solid black boundaries are a wall, the dotted lines are open boundaries, and the red particle is a red blood cell.

As the red blood cells are suspended in the plasma phase, there is an interaction between the red blood cells and the plasma which needs to be modelled. This coupling is bidirectional, which means that the red blood cells have an effect on the plasma, and that the plasma has an effect on the red blood cells [195].

The effect of the fluid on the red blood cell is modelled with the no-slip boundary condition at the fluid-solid surface. In effect, this means that at the boundary where the red blood cell and the plasma are in contact, the two move at the same velocity.

In addition, as the red blood cells deform, they exert a stress on the fluid as they resist the deformation. This stress at the RBC-fluid interface needs to be imposed.

3.1.2 Numerical model

This section shows how the physical model for particulate blood flow in Section 3.1.1 is numerically solved. The numerical methods are explained, an overview of the entire algorithm is covered, and the codes that were used for this thesis are shared. As the aim of this thesis does not consist in developing a new method, an overview will be given of it which is sufficient to introduce the method, and the interested reader will be directed to the relevant literature for more detailed information and analyses of the method.

The lattice-Boltzmann method

The lattice-Boltzmann method (LBM) is a numerical method which solves a discretised and truncated Boltzmann equation on a lattice grid [107]. By doing so, one can mathematically recover a solution to the Navier-Stokes equation through a relationship between the microscopic properties of the particle based LBM to the macroscopic properties of a fluid[1]. In this section, the Boltzmann equation is briefly introduced, after which the necessary components of the lattice-Boltzmann method for this thesis are covered.

One of the key variables in the Boltzmann equation is the distribution function, $f(\mathbf{x},\xi,t)$. The distribution function quantifies the density of particles at position $\mathbf{x}$ and time t moving with velocity ξ.

The Boltzmann equation reads,

$$\frac{\partial f}{\partial t}+\xi_\beta\frac{\partial f}{\partial x_\beta}+\frac{F_\beta}{\rho}\frac{\partial f}{\partial \xi_\beta}=\Omega(f), \tag{3.11}$$

where t is time, ξ_β is the particle velocity, x_β is the particle position, f is the distribution function, and $\Omega(f)$ is the collision operator. Conceptually, the Boltzmann equation can be read as an advection equation for the distribution function, with the second term being an advection of the distribution function, the third term being forces affecting the distribution function, and the right hand side denoting changes due to collisions of particles. It is then possible, through the known distribution function, to calculate the properties of a continuous fluid, such as density and velocity, which provide a solution to the Navier-Stokes equation [107].

The Boltzmann equation is difficult to solve analytically, therefore it is discretised into the lattice-Boltzmann equation to find a numerical solution. It is this discretised form of the Boltzmann equation that is at the core of the lattice-Boltzmann method.

---

1. In the context of the LBM, the word particle refers to molecules in a fluid, microscopic refers to the particles, and macroscopic refers to a continuous fluid.

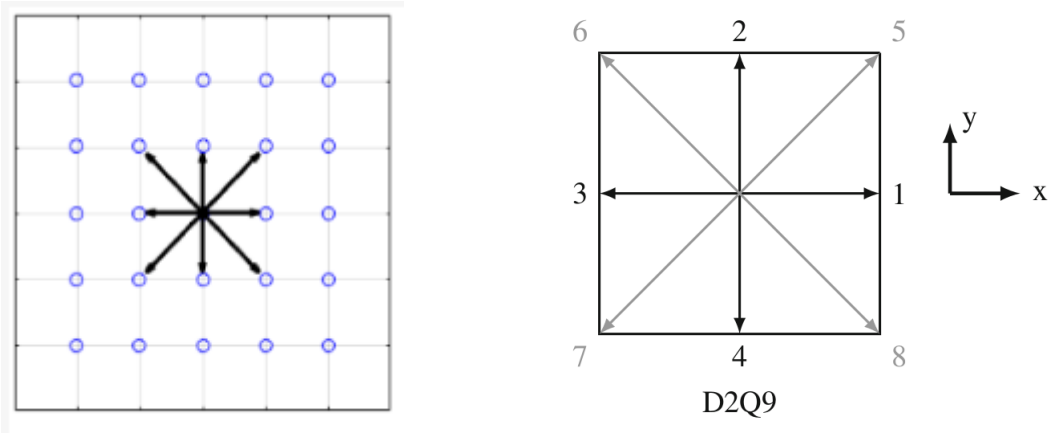

(a) (b)

Figure 3.3: (a) Illustration of the uniform grid for the LBM. The blue points represent the discrete points, (b) Illustration of the 2-dimensional D2Q9 velocity set, the ninth velocity is not shown and is stationary. Images reproduced through an open license (a) and with permission (b) from [20, 107].

As the continuous distribution function is a function of three variables, velocity, space, and time, the LBM discretises all three of these variables, and solves for a discretised distribution function, f_i. The detailed derivation of the LBM from the Boltzmann equation can be found within the literature [107].

Space is discretised into a lattice grid, shown in Figure 3.3a. This means that in the LBM, the distribution function is no longer known everywhere in space, but only at the given discrete positions in the grid (shown as blue points in Figure 3.3a), which in 3-dimensions is a cubic lattice. The spacing of each point in the grid is known as the lattice spacing, Δx.

The time discretisation means that the distribution function is no longer known at any point in time, but only at given discrete intervals, Δt.

Finally, velocity is discretised into velocity sets, denoted $\mathbf{c}_i$, where the subscript i is for the number of discrete velocities. Concretely, this means that the particles can no longer move in an infinite number of directions, but only in specific, discrete velocities within the lattice, denoted as DdQq. The variable d denotes the number of dimensions within the system (for example a 3-dimensional domain would have d=3) and q denotes the number of discrete velocities with which the particles can move with. An example of the D2Q9 velocity set is shown in Figure 3.3b (a 2D rather than a 3D set is shown for ease of visualisation). Each velocity set is associated with a set of weighting coefficients, w_i, which inform what fraction of particles move with a specific velocity. In this thesis, the D3Q19 velocity set is used, meaning that the system is 3-dimensional, and particles can move in 18 directions with an additional rest velocity. The velocity sets can be found in the literature [107].

With a known discrete distribution function $f_i(\mathbf{x},t)$, it is possible to calculate the macroscopic density and momentum of the fluid through the following equations,

$$\rho(\mathbf{x},t) = \sum_i f_i(\mathbf{x},t), \tag{3.12}$$

$$\rho\mathbf{u}(\mathbf{x},t) = \sum_i \mathbf{c}_i f_i(\mathbf{x},t), \tag{3.13}$$

where $\rho(\mathbf{x},t)$ is the macroscopic density of the fluid at position $\mathbf{x}$ and time t, and $\mathbf{u}(\mathbf{x},t)$ is the macroscopic velocity of the fluid at position $\mathbf{x}$ and time t. The velocity $\mathbf{u}$ at any point and time can be obtained through the division of equation (3.13) by equation (3.12).

The missing ingredient to use the LBM is to know how the discretised distribution function evolves in space and time. This is done through the lattice Boltzmann equation,

$$f_i(\mathbf{x}+\mathbf{c}_i\Delta t, t+\Delta t) = f_i(\mathbf{x},t) + \Omega_i(\mathbf{x},t), \tag{3.14}$$

where $\Omega_i(\mathbf{x},t)$ is the collision operator, and $f_i(\mathbf{x}+\mathbf{c}_i\Delta t, t+\Delta t)$ is the distribution function at timestep $t+\Delta t$ and position $\mathbf{x}+\mathbf{c}_i\Delta t$. For the work undertaken in this thesis, the collision operator used is the Bhatnagar-Gross-Krook (BGK) operator, the simplest one, which reads [19],

$$\Omega_i(\mathbf{x},t) = -\frac{f_i - f_i^{eq}}{\tau}\Delta t, \tag{3.15}$$

where f_i^{eq} is the equilibrium population that the population relaxes towards, and τ is the relaxation time. The equilibrium population is defined by,

$$f_i^{eq}(\mathbf{x},t) = w_i\rho\left(1 + \frac{\mathbf{u}\cdot\mathbf{c}_i}{c_s^2} + \frac{(\mathbf{u}\cdot\mathbf{c}_i)^2}{2c_s^4} - \frac{\mathbf{u}\cdot\mathbf{u}}{2c_s^2}\right), \tag{3.16}$$

where c_s is the lattice speed of sound. In this thesis both Δx and Δt are systematically set to 1, leading to $c_s^2 = \frac{1}{3}$. The relaxation time, τ, is determined from the macroscopic kinematic viscosity, ν, through the following relation,

$$\nu = c_s^2\left(\tau - \frac{\Delta t}{2}\right). \tag{3.17}$$

LBM boundary conditions, initial conditions and additional LBM requirements The LBM described above provides a solution to the Navier-Stokes equation within the bulk of the fluid. However, the boundary conditions for the Navier-Stokes equation need to be numerically implemented within the LBM to solve the LBM within the simulation domain.

The no-slip boundary condition is enforced through the bounce back method [107]. For open boundaries, a velocity boundary condition is implemented through a bounce back scheme for a moving wall [110, 133]. Pressure boundary conditions are imposed through an anti-bounceback scheme [107].

In addition to the boundary conditions, initial conditions need to be set for the simulations. Apart for the lattice sites corresponding to boundaries, the lattice sites were set to have a velocity, at time zero, of zero [195]. The simulations are then left to reach the steady state flow solution prior to inserting red blood cells.

A final consideration is the addition of forces in the LBM. This external force can correspond to a gravity force, for force driven flows, or may locally be the force that an immersed particle exerts on a fluid. There are various schemes in the LBM to impose an external force on the fluid. In this thesis, the Guo forcing scheme is used as it has been shown to satisfactorily recover the desired physics for particulate blood flow [76, 107, 108].

Fluid compressibility The LBM as stated above solves for a weakly compressible fluid. Therefore, the compressibility of the fluid in the simulation needs to be controlled and monitored to ensure that it is kept sufficiently small to be negligible. There are two sources of fluid compressibility.

The flow compressibility of a fluid is determined by the Mach number,

$$Ma = \frac{u}{c_s}, \tag{3.18}$$

where Ma is the Mach number. One can therefore control the compressibility of the fluid by controlling the Mach number within the simulations. This is ensured by keeping the $Ma \ll 0.3$.

The second source of compressibility is due to large pressure drops through the domain, changing the density of the fluid. This is controlled by keeping simulation domains to an appropriate size, and compressibility is monitored for each simulation. As long as the compressibility is only of a few percentage points, it is considered negligible.

Simulation acceleration LBM simulations can be computationally costly. To reduce the cost, one has the possibility of speeding up the simulation by increasing the Reynolds number of the simulation, and by doing so reducing the number of timesteps required to complete a simulation. There are two important considerations when accelerating a simulation.

The first consideration is that by increasing the Reynolds number one changes the inertia present in the fluid, and therefore contains the risk of changing the outcome of a simulation. This can be controlled through benchmarking or varying the Reynolds number to see the effect it has on the outcome of a simulation [107].

The second consideration is that increasing the Reynolds number has an effect on shear rate, and therefore the deformation of suspended red blood cells. This is controlled by adapting the elastic modulus in the capillary number, equation (3.8), to keep the capillary number constant while increasing the Reynolds number [18].

The finite element method

The particle physical model in Section 3.1.1 is numerically solved with the finite element method. The first step is to discretise the particle membrane so that the continuous physical model can be discretised and numerically solved on the membrane.

The membrane is discretised into an unstructured mesh containing N_f triangular facets i, where each facet i is defined by three vertices (also called nodes) and their connectivity, illustrated in Figure 3.4. The membrane mesh is generated for an undeformed RBC, whose shape is parameterised by the equation [51],

$$z(q) = \pm\sqrt{1-\left(\frac{q}{r}\right)^2}\left(C_0 + C_2\left(\frac{q}{r}\right)^2 + C_4\left(\frac{q}{r}\right)^4\right), \tag{3.19}$$

$$q = \sqrt{x^2+y^2}, \tag{3.20}$$

where r is the RBC radius, x, y are the coordinates of the RBC, C_0, C_2, and C_4 are parameters specific to RBCs [51].

The continuous equations from the membrane physical model can now be discretised using the finite element method onto the mesh and solved numerically. The strain and bending energies, respectively, are calculated over each facet i,

$$E_S = \sum_{i=1}^{N_f} A_i^{(0)} \varepsilon_i^s, \tag{3.21}$$

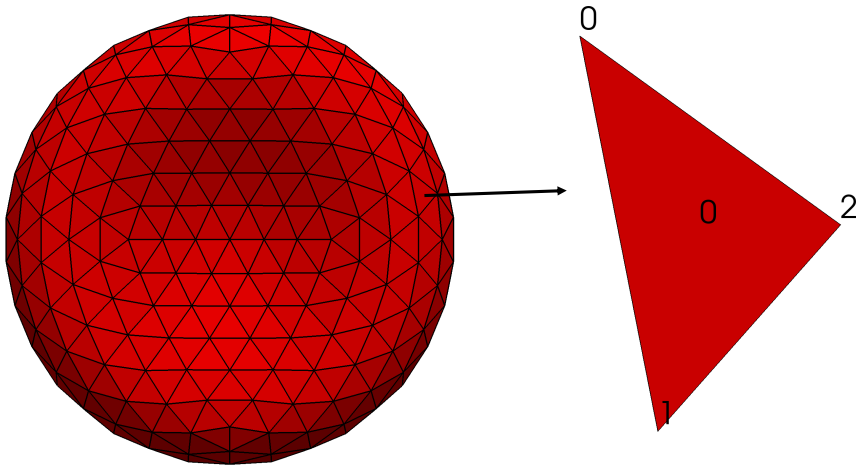

Figure 3.4: Example of undeformed RBC mesh used in simulations, with 720 faces. Shows a single facet, here facet 0 as labelled in the centre of the triangular facet, with its three vertices, 0, 1, 2.

$$E_B = \sqrt{3}\kappa_b \sum_{\langle i,j>i\rangle} \left(\theta_{i,j} - \theta_{i,j}^{(0)}\right)^2, \tag{3.22}$$

where $A_i^{(0)}$ is the undeformed surface area of facet i, ε_i^s is the strain energy in facet i, $\theta_{i,j}$ is the angle between the normal vectors of facets i and j, and $\theta_{i,j}^{(0)}$ is the angle between the normal vectors of facets i and j of the undeformed RBC membrane.

When RBCs deform, they conserve both their volume and surface area, due to the incompressibility of both the cytoplasm and the bilayer. As the volume and surface area of a RBC may numerically drift, a penalty is imposed on deviations of the volume and surface area of a RBC compared to its rest state [108, 195], defined by:

$$E_{\mathrm{V}} = \frac{\kappa_V}{2} \frac{(V - V^{(0)})^2}{V^{(0)}}, \tag{3.23}$$

$$E_{\mathrm{A}} = \frac{\kappa_A}{2} \frac{(A - A^{(0)})^2}{A^{(0)}}, \tag{3.24}$$

where E_V is the volume energy, κ_V is the volume modulus, V is the volume of the current RBC state, $V^{(0)}$ is the volume of rest RBC state, E_A is the surface energy, κ_A is the area modulus, A is the surface area f the current RBC state, and $A^{(0)}$ is the surface area of the rest RBC state. The volume and surface area of the RBC membrane can be calculated by summing up the volume contribution and surface area contribution, respectively, of each facet [108].

The membrane energy at each facet i can be calculated through,

$$E = E_S + E_B + E_V + E_A, \tag{3.25}$$

where E is the sum of the energy contributions at each facet. The membrane energy at a facet can be converted to a force, through the principle of virtual work, at each vertex of the membrane mesh with,

$$\mathbf{F}_i = -\frac{\delta E(\mathbf{x}_i)}{\delta \mathbf{x}_i}, \tag{3.26}$$

where $\mathbf{F}_i$ is the force at vertex i, which has a coordinate position $\mathbf{x}_i$. The derivatives for each energy contribution can be analytically calculated to save the computational time to numerically calculate them. The analytical solutions can be found in the literature [195]. The force at each vertex can then act on the fluid to couple the RBC to the fluid, this is done with the immersed boundary method.

The immersed boundary method

The immersed boundary method, originally developed by Peskin in the 1970s, provides bi-directional coupling between a fluid, and a body suspended in the fluid. The bidirectional coupling implements a no-slip condition between the body and the fluid, and makes forces acting on the body also act on the fluid. These two components are identified in the physical model boundary conditions in section 3.1.1. In this section the distinction between Eulerian and Lagrangian systems is initially explained, followed by the discretised immersed boundary method equations, the reader is referred to the literature for the continuous equations [72, 143]. The implementation of the IBM within the LBM is discussed as a final point, for full integration within the numerical method used in this thesis.

The immersed boundary method works at the interface of an Eulerian mesh and a Lagrangian mesh, illustrated in Figure 3.5. The Eulerian mesh is a fixed mesh representing the fluid, on which the Navier-Stokes equation is resolved. In practice within this numerical framework, the Eulerian mesh is the lattice of the lattice-Boltzmann method. The Lagrangian mesh on the other hand is the points on the mesh of the moving body. In practice within this numerical framework, the Lagrangian mesh is the vertices of the RBC unstructured mesh. The Lagrangian mesh is effectively able to move and deform, and the two meshes interact with each other through the immersed boundary method, but they are two distinct entities.

The fundamental idea of the immersed boundary method is that the immersed boundary, at a given position, moves at the same velocity as the fluid at the said point. This effectively enforces the no-slip boundary condition on the immersed body. This is written as,

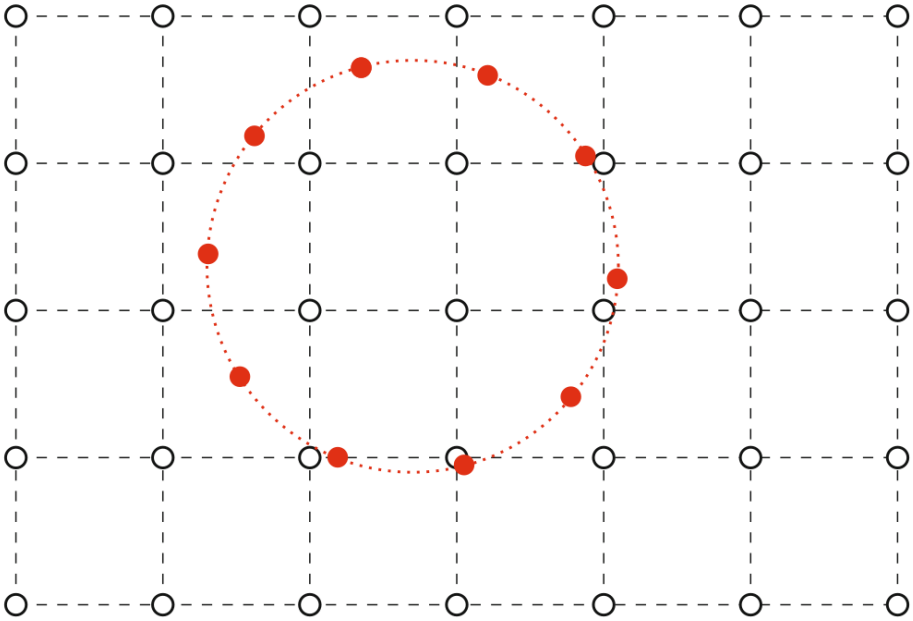

Figure 3.5: Illustration of the Eulerian and Lagrangian meshes for the immersed boundary method. The white points are the fluid sites for the LBM. The red points are the vertices for the immersed body. There are two main steps in the IBM. Firstly, the forces on the Lagrangian mesh vertex are spread to the Eulerian fluid sites. Secondly, the velocity at the Lagrangian mesh vertex is interpolated from the velocity of the neighbouring Eulerian fluid sites. Image reproduced with permission from [195].

$$\dot{\mathbf{r}}(t) = \mathbf{u}(\mathbf{r}(t), t) \tag{3.27}$$

where $\dot{\mathbf{r}}(t)$ is the velocity of a point (of the immersed body) at a given time t, and $\mathbf{u}(\mathbf{r}(t), t)$ is the velocity of the fluid at the same point and at the same time, t. Following discretisation, this leads to,

$$\mathbf{u}_i(t + \Delta t) = \sum_{\mathbf{X}} \mathbf{u}(\mathbf{X}, t + \Delta t)\delta(\mathbf{X} - \mathbf{x}_i(t)) \tag{3.28}$$

where $\mathbf{u}_i$ is the interpolated velocity at the Lagrangian vertex i, $\mathbf{u}$ is the velocity on the Eulerian grid, $\mathbf{X}$ is the position of the Eulerian fluid mesh, and $\mathbf{x}_i$ is the position of the Lagrangian vertex i. Equation (3.28) interpolates the velocity from the Eulerian fluid mesh to the Lagrangian mesh of the moving particle, ensuring the no-slip condition, and is done with the help of the interpolation function, $\delta(\mathbf{X} - \mathbf{x}_i(t))$.

There are multiple interpolation functions available from the literature, and the different ones are, for the most part, a trade off between accuracy on the one hand, and computational tractability on the other [108]. For the purpose of this thesis, the three point stencil is chosen, which was shown to have the desired balance of accuracy and efficiency [108], it reads,

$$\phi_3(x) = \begin{cases} \frac{1}{3}(1+\sqrt{1-3x^2}) & 0 \leq |\mathrm{x}| \leq \frac{1}{2}\Delta x, \\ \frac{1}{6}(5-3\mid x\mid -\sqrt{-2+6\mid x\mid -3x^2}) & \frac{1}{2}\Delta x \leq |\mathrm{x}| \leq \frac{3}{2}\Delta x, \\ 0 & \frac{3}{2}\Delta x \leq |\mathrm{x}| \end{cases} \tag{3.29}$$

The next core equation of the immersed boundary method is the spreading of forces from the immersed body onto the ambient fluid, which is done through,

$$\mathbf{f}(\mathbf{X},t) = \sum_i \mathbf{F}_i(t)\delta(\mathbf{X}-\mathbf{x}_i(t)), \tag{3.30}$$

where $\mathbf{f}(\mathbf{X},t)$ is the force acting on the Eulerian fluid mesh, and $\mathbf{F}_i(t)$ is the force from the Lagrangian mesh at vertex i. The spreading of forces takes the local forces acting on the Lagrangian mesh of the particles to spread it to the neighbouring Eulerian mesh of the fluid, so that it may act on the fluid. This force is added to the LBM fluid solver as an external force acting on the fluid, coupling the fluid to the membrane.

Finally, to implement the no-slip boundary condition on the membrane vertex, the membrane vertex is advected by the velocity of its ambient fluid through,

$$\mathbf{x}_i(t+\Delta t) = \mathbf{x}_i(t) + \mathbf{u}_i(t+\Delta t)\Delta t. \tag{3.31}$$

The advection of the membrane vertices by the fluid, in equation (3.31), reevaluates the deformation of the membrane, as each membrane vertex is advected with a different velocity.

Cell-cell and cell-wall repulsion force

In the simulations, there is a risk that the membranes of two different cells overlap with each other, or that a cell membrane overlaps with the wall boundaries in a simulation. To prevent that from happening, a repulsion force is introduced, which takes the form,

$$\mathbf{F}_{ij}(\mathbf{d}_{ij}) = \begin{cases} \kappa_{int}[1-(\frac{\Delta x}{d_{ij}})^2] & d_{ij} < \Delta x, \\ 0 & d_{ij} \geq \Delta x, \end{cases} \tag{3.32}$$

where $\mathbf{F}_{ij} = -\mathbf{F}_{ji}$ is the repulsion force acting on node i, d_{ij} is the distance between node i and j, κ_{int} controls the magnitude of the repulsion force, and Δx is a lattice spacing. This repulsion force effectively prevents red blood cells from getting closer than one lattice spacing from each other or to a wall. In practice in the simulations, for cell-cell interaction $\kappa_{int} = \kappa_b$, and for cell-wall interaction $\kappa_{int} = 10\kappa_b$, where κ_b is the bending modulus.

Red blood cell insertion

In addition to the numerical solution to the model for the red blood cell membrane and its coupling to the fluid flow, the insertion of red blood cells into the simulation needs to be treated. Initially, the simulations reach flow steady-state without the presence of red blood cells. When the flow steady state is reached, the red blood cells are inserted at the flow inlets. The insertion of cells is done in concentric rings at the inlet, and they are inserted at a frequency which is calculated to give the desired inlet haematocrit. At the point of insertion, the red blood cells are at their rest state shape.

Algorithm implementation

Given the different components of the model for particulate blood flow, their integration with one another needs to be covered. The algorithm repeatedly follows the below sequence, up to the point that the final timestep of the simulation is reached.

1. At this stage, the position of the membrane mesh and the fluid velocity/density is known, either from the initial conditions at the first timestep or from the previous timestep, at any other time of the simulation. The forces acting on the membrane are calculated from equation (3.26)
2. The forces from the membrane are spread to the fluid through equation (3.30)
3. The LBM is solved through equation (3.14), which includes forces acting on it from the membrane
4. The velocity at the membrane nodes is calculated through interpolation, equation (3.28)
5. The vertices of the RBC membrane are advected through equation (3.31)
6. The current time step is complete, the time step is incremented and the loop is repeated

The described numerical method is implemented in HemeLB, which is the software I use in this thesis. HemeLB is a highly efficient and parallelised open source (https://github.com/hemelb-codes/hemelb) implementation of the algorithm, with tools enabling it to be used in arbitrary geometries [126].

3.2 Network model for blood flow

This section covers the network model for blood flow used to solve for blood flow in vascular networks, used in chapter 5 of this thesis. In this model, blood is treated as a continuous fluid with an apparent viscosity, allowing one to calculate blood flow and haematocrit through a network of vessels when the geometrical properties of the network are known. Figure 3.6a shows what an input network can look like, with the outputs, flowrate and haematocrit, shown in Figure 3.6b-c.

This section is subdivided into the physical model, section 3.2.1, which contains a description of the physics that is modelled, with the equations and assumptions for the physics; and the numerical model, section 3.2.2, which shows how the numerical solution for the physical model is obtained.

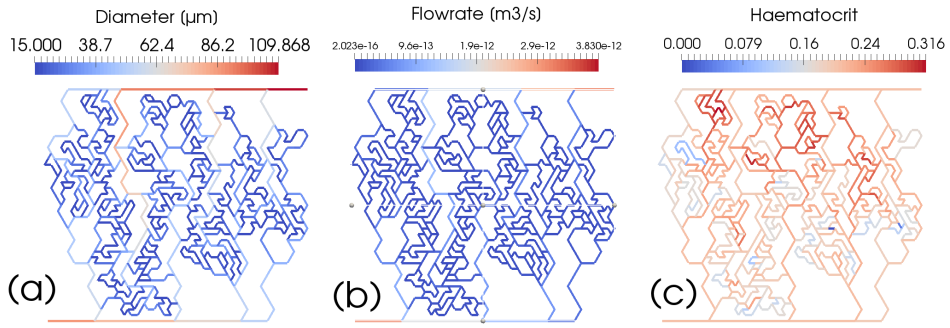

Figure 3.6: Illustration of input and output of the network model for blood flow. (a) shows the geometrical properties of the network, which is an input to the model. (b) shows the flowrate in every vessel of the network, which is an output of the model. (c) shows the haematocrit in every vessel of the network, which is an output of the model.

3.2.1 Physical model

The physical model for blood flow through a vascular network is detailed here. This section contains two parts, one for the fluid model, and one for the boundary conditions for the model.

Fluid model

In the network model blood flow through a vessel is treated in one-dimension as a continuous and incompressible fluid with an apparent viscosity, modelled through Poiseuille's law [77, 144]. Figure 3.7 shows a vessel segment with the notation for Poiseuille's law, equation (3.33), which reads for a circular cross-section,

$$Q_{0,1} = \frac{(p_0 - p_1)\pi D^4}{128 L \mu_{app}}\,, \tag{3.33}$$

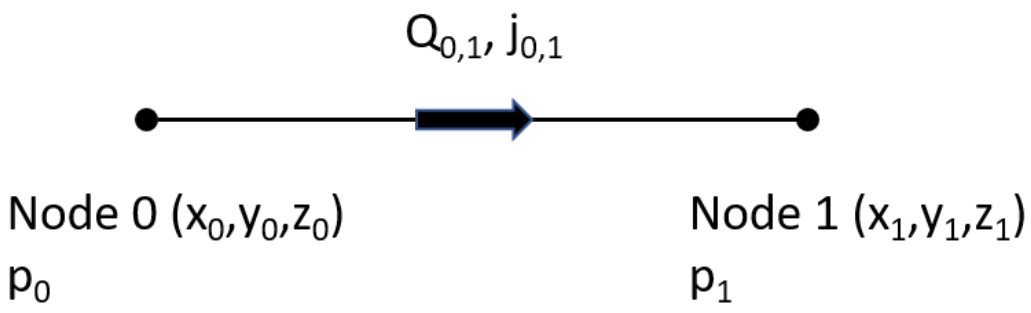

Figure 3.7: Shows a vessel segment in which equation (3.33) is applied. The vessel is defined by its two nodes, 0 and 1 with coordinates (x, y, z), that form the endpoints of the vessel segment. Each node has a pressure, p, with the subscript denoting the node. $Q_{0,1}$ and $j_{0,1}$ are the flowrate and conductance going from node 0 to node 1, respectively.

where $Q_{0,1}$ is the volumetric flowrate of blood, p_0 and p_1 are the pressure values at the end of the vessel segment of length L, D is the diameter of the vessel, and μ_{app} is the apparent viscosity of blood. The subscripts 0 and 1 are the points, see Figure 3.7, of the vessel where Poiseuille's law is applied. Poiseuille's law can also be generalised for an elliptical cross-section, and reads,

$$Q_{0,1} = \frac{\pi(p_0 - p_1)a^3b^3}{4L\mu_{app}(a^2+b^2)}, \tag{3.34}$$

where a and b are the major and minor radii of an ellipse. If $a = b$, this recovers Poiseuille's law for a circular cross-section.

For both the elliptical or circular formulation of Poiseuille's law, it can be rewritten for convenience as,

$$Q_{0,1} = j_{0,1}\Delta p_{0,1}\ , \tag{3.35}$$

where $j_{0,1}$ is the conductance, defined through the parameters in equations (3.33) or (3.34). Modelling blood this way makes a set of assumptions [153]:

1. Entrance and exit effects are negligible in the scale of the vessel length
2. Blood flow is laminar
3. Blood flow is in steady state
4. The vessel is uniform with a circular or elliptical cross-section
5. The vessel does not leak blood
6. Blood can be treated as an incompressible continuous Newtonian fluid and has an apparent viscosity within the relevant vessel, defined as the viscosity of a Newtonian fluid that would have the same flowrate given the same vessel diameter and pressure drop

Although blood is treated as a continuous Newtonian fluid in Poiseuille's law, blood is a shear thinning fluid [111], meaning its apparent viscosity decreases with increased shear rate. Numerous experiments have been performed to establish the apparent viscosity of blood in narrow glass tubes [153], which were compiled in a single data set. From that data set, an empirical fit for blood apparent viscosity as a function of haematocrit and vessel diameter was generated [151, 172]. The equations for the fit read,

$$\mu_{app} = \mu_{rel}\mu_{plasma} \,, \tag{3.36}$$

$$\mu_{rel} = 1 + (\mu_{45} - 1)\frac{(1-H_D)^C - 1}{(1-0.45)^C - 1} \,, \tag{3.37}$$

$$\mu_{45} = 220e^{-1.3D} + 3.2 - 2.44e^{-0.06D^{0.645}} \,, \tag{3.38}$$

$$C = (0.8 + e^{-0.075D})\Big(-1 + \frac{1}{1+10^{-11}D^{12}}\Big) + \frac{1}{1+10^{-11}D^{12}} \,, \tag{3.39}$$

where μ_{app} is the apparent dynamic viscosity of blood, μ_{rel} is the relative dynamic viscosity of blood with regards to plasma, and μ_{plasma} is the dynamic viscosity of plasma (taken as 0.0012Pa s [172]), μ_{45} is the relative apparent blood viscosity for a discharge haematocrit of 45%, D is the vessel lumen diameter in microns, and H_D is the discharge haematocrit within the vessel. This empirical relation was determined from glass tube experiments and therefore ignores the effect of the endothelial surface layer, and it assumes that the shear rate is sufficiently high that the apparent viscosity is no longer a function of the shear rate, which is a suitable approximation for the microcirculation [172]. This empirical relation accurately captures the Fahraeus-Lindqvist effect [172].

Furthermore, one must model the phase separation of blood at microvascular bifurcations, where the flowrate fraction of red blood cells in each child branch is not the same as the fraction of blood in the said child branches. There are numerous models available within the literature to model partitioning of red blood cells at a bifurcation [50, 68, 75, 138, 148], however the one proposed by Pries *et al.* [148, 152] is chosen for this thesis, due to its extensive use in the literature to simulate blood flow though large networks [67, 172], and because it has been extensively investigated in fully resolved numerical simulations and in microfluidic devices [18, 50, 86, 122, 150, 160, 165, 179, 180, 206, 212, 213]. The model is a semi-empirical relation derived from data obtained in the microcirculation of the rat mesentery, and later updated for more robust results when using extreme haematocrits and diameters [148, 152]. The phase separation model at microvascular bifurcations reads,

$$FQ_E = 0 \qquad \text{if } FQ_B \leq X_0 \,, \tag{3.40}$$

$$\text{logit}(FQ_E) = A + B\text{logit}\Big(\frac{FQ_B - X_0}{1-2X_0}\Big) \qquad \text{if } X_0 \leq FQ_B \leq 1-X_0\,, \tag{3.41}$$

$$FQ_E = 1 \qquad \text{if } 1-X_0 \leq FQ_B\,, \tag{3.42}$$

where FQ_e is the fractional flowrate of red blood cells to the child branch, and FQ_b is the fractional flowrate of blood to the same child branch. The fractional flowrate to a child branch is the flowrate in the said child branch divided by the flowrate of the parent branch. The remaining parameters, A, B, and X_0 are calculated through the following equations,

$$\text{logit}(x) = \ln\Big(\frac{x}{1-x}\Big)\,, \tag{3.43}$$

$$A = -13.29\frac{\frac{D_\alpha^2}{D_\beta^2}-1}{\frac{D_\alpha^2}{D_\beta^2}+1}\frac{1-H_D}{D_P}\,, \tag{3.44}$$

$$B = 1 + 6.98\frac{1-H_D}{D_P}\,, \tag{3.45}$$

$$X_0 = 0.964\frac{1-H_D}{D_P}\,, \tag{3.46}$$

where D_α and D_β are the diameters of the two child branches in microns, D_P is the diameter of the parent branch in microns, and H_D is the discharge haematocrit of the parent branch. With equations (3.40)–(3.42) one can calculate the discharge haematocrit in both child branches through,

$$H_D = \frac{Q_e}{Q_b}\,. \tag{3.47}$$

where Q_e is the flowrate of red blood cells, and Q_b is the flowrate of blood. With the known haematocrit in all vessels from equation (3.47), the physical model contains all of the ingredients to calculate blood flowrate and haematocrit in all vessels of a microvascular network.

Boundary conditions

The flow boundary conditions at the open boundaries of the vessel network need to be imposed to solve the model, and can be imposed in one of two ways. One may either impose a pressure boundary condition at the end of the vessel which constitutes the open boundary. Or one may impose a flux boundary condition, either a velocity or flowrate, in the vessel segment that is the vessel leading to or leading from the open boundary. In addition, one must impose a discharge haematocrit value to the vessels flowing into the network, which is referred to as the inlet haematocrit in this thesis.

Initial conditions

In addition to the boundary conditions, the initial conditions for the haematocrit in the vessels need to be set. This is done by setting a uniform haematocrit throughout the network [150], in this case 0%. The haematocrit then propogates from the inlet to the vessels in the networks. No other initial conditions, other than the boundary conditions, are necessary for the network simulations.

3.2.2 Numerical model

This section shows how the physical model for blood flow through a vascular network, described in section 3.2.1, is numerically solved. The numerical method is explained, followed by some additional considerations for the solver. I implemented the numerical scheme in Python2.7.

Iterative scheme solver

The numerical solution of this physical model is that proposed by Pries et al. [150], and has since extensively been used in the literature [18, 60, 63, 67, 68, 115, 116, 128, 170]. Figure 3.8 shows a flow diagram of the method used, which is followed by additional details for the numerical implementation where required. It is an iterative scheme, as one needs to know the haematocrit to calculate the flowrates, but one cannot know the haematocrit in each vessel without knowing the flowrates.

The first step sets the boundary and initial conditions. The inlet haematocrit is set at all the inflow vessels to the network, the other vessels in the network are set to have a haematocrit of 0%. The pressure, or flux, boundary conditions are set at the open boundaries.

Next, equation (3.36) calculates the apparent viscosity at every every vessel segment.

One can then apply a mass balance at every bifurcation within the network, Figure 3.9 illustrates such a bifurcation. The direction of flow can be determined from the pressure values at the nodes. The sum of the flowrates leading into the bifurcation is equal to the sum of the flowrates leading out of the bifurcation,

$$Q_{0,1} = Q_{1,2} + Q_{1,3} \ , \tag{3.48}$$

and substituting the flowrates, Q, with equation (3.35), one obtains,

$$j_{0,1}(p_1 - p_0) + j_{1,2}(p_1 - p_2) + j_{1,3}(p_1 - p_3) = 0 \ . \tag{3.49}$$

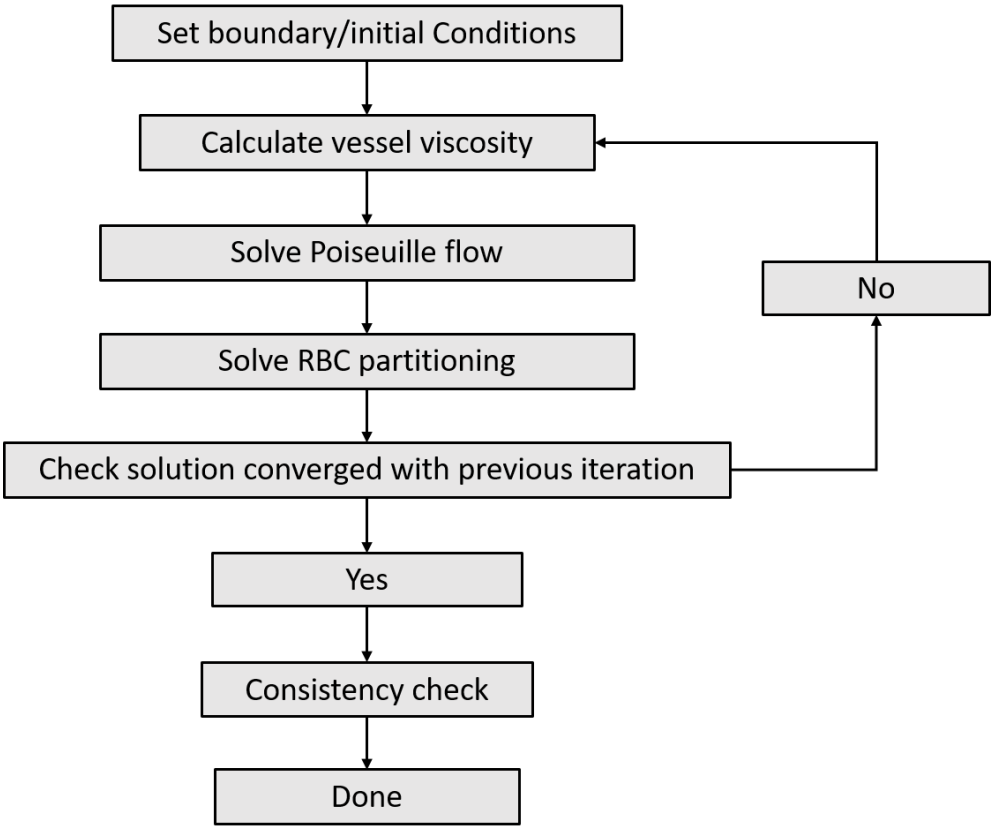

Figure 3.8: Flowchart of solver used to calculate flowrates and haematocrits within the vascular networks.

Applying equation (3.49) at every bifurcation in the network leads to a system of linear equations, where the unknowns are the pressure values at the end of each vessel segment. With known boundary conditions the solution for the pressure values can be found. In the framework of this thesis, a linear equation matrix is created and solved using numpy's linear algebra package, linalg. This leads to a solution containing the pressure values at both ends of every vessel segment within the network. One can then calculate the flowrate in every vessel segment by substituting the now known pressure values into equation (3.35).

With known flowrates, one can predict the haematocrit within the vessels of the network. If a bifurcation is diverging (one inlet and two outlets), Pries's phase separation model is used, equations (3.40)–(3.42), to calculate the RBC flowrate in all vessels, and from that calculate the haematocrit in all vessels. In the event that a bifurcation converges, the out-flowing child branch merely has an RBC flowrate which is the sum of the two in-flowing RBC flowrates.

Upon knowing the haematocrit in all vessels, one can check whether the current iteration of the solver has converged with the previous iteration of the solver [150]. The criteria for convergence is that the flowrate of blood and red blood cells in all vessels is within .001% of the previous iteration,

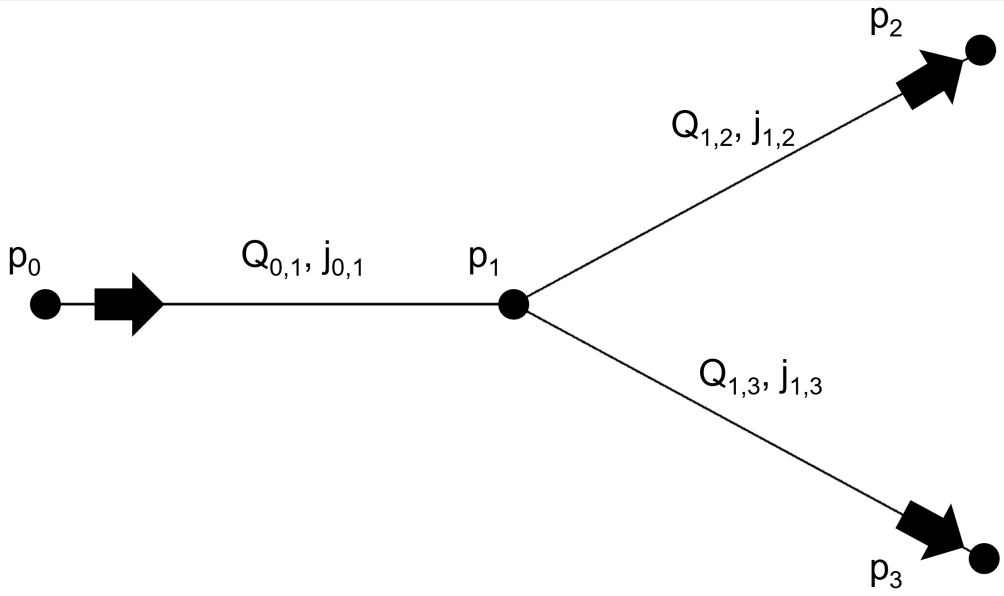

Figure 3.9: Illustration of a bifurcation within a network. p is the pressure at the end of the vessel segments, Q is the flowrate of blood through the vessel segments, and j is the conductance of the vessel segments according to equation (3.35). In this simple case, nodes 0, 2, and 3 would be open boundaries.

$$\left| \frac{Q_{current} - Q_{previous}}{Q_{current}} \right| \leq 0.00001, \tag{3.50}$$

where $Q_{current}$ is the flowrate in a vessel, for either blood or red blood cells, for the current iteration, and $Q_{previous}$ is the flowrate in a vessel for the previous iteration.

Once the solution has converged a consistency check is performed on the result of the simulation. A mass balance on RBC flowrate and blood flowrate at each bifurcation is performed, where the sum of in-flowing flowrates should be within 1% of the sum of out-flowing flowrates,

$$0.99 \leq \frac{\sum |Q_{in}|}{\sum |Q_{out}|} \leq 1.01, \tag{3.51}$$

where Q_{in} is the flowrate of blood or RBCs flowing into the bifurcation, and Q_{out} is the flowrate of blood or RBCs flowing out of the bifurcation. As previously, the absolute values of the flowrates are necessary, as depending on the direction of the flow the flowrate may be negative or positive. This mass balance step is a check to ensure that the convergence criteria, and the simulation output are suitable. Upon completing the mass balance check, the simulation is complete.

Additional considerations

For the iterative scheme solver to work, some additional considerations needed to be implemented.

While calculating the flowrate, the linear equation matrix solver can set the flowrate in a branch to very low values, without setting the flowrate to zero. Setting flowrate near-zero, but non-zero values, leads to numerical difficulty for the solver to converge, as negligible changes in the value of the flowrate lead to large percentage changes, which is what the convergence criteria is based on. To address this issue, vessels with a flowrate $Q < 10^{-20}$ m^3 s^{-1} were set to zero, and so was their discharge haematocrit [115].

The model developed by Pries can lead to abnormally high haematocrits when networks are very large [68, 115], which would in fact be non-physical. To avoid non-physical haematocrits one can impose a threshold above which a haematocrit within a vessel cannot go [115]. Mass is conserved by balancing the mass with the other child branch at the bifurcation [115]. This method was not imposed within my iterative solver as the networks were not large enough to observe non-physical haematocrit values, but it is highlighted as a consideration if one wishes to perform such simulations in very large networks.

3.3 Method: animal models, image reconstruction, and phenotyping

This section presents the methods for chapter 6 of this thesis, which is the result of a collaborative work with Professor Val Brunton's research group at the University of Edinburgh. The experiments and imaging of the microvasculature were performed by Dr. Martin Lee. My work starts with the data provided by them, where I take the raw images to reconstruct the three-dimensional microvasculature, and then quantify the relevant phenotypes. As such, the methods for the animal models and imaging, section 3.3.1, will be an overview, and more details will be given on the reconstruction of the vasculature, section 3.3.2, and on the phenotype quantification, section 3.3.3.

3.3.1 Animal model of a tumour & imaging

This section will cover the animal model of a tumour, and how the vasculature is imaged. The information provided will be sufficient to know what was done, however as I did not perform the experiments, it will not include details, and relevant references will be provided. I thank Professor Val Brunton and Dr. Martin Lee for performing the experiments and sharing these images.

Animal model

The experiments used modified mice to express the tdTomato fluorescent protein in endothelial cells [58, 71]. The tdTomato reporter is necessary as it enables the imaging of the vasculature by imaging the tdTomato fluorescent protein.

The mice were separated into two groups, the tumour group and the control group. The experimental data were not blinded for the control versus the tumour. The tumour mice were intracranially injected [22] with Cre-loxP–controlled lentiviral vectors expressing oncogenes, which causes the development of a brain glioblastoma [125]. Through this method, the tumour cells also express a green fluorescent protein, which enables imaging of the tumour cells [125]. The control mice did not have an intracranial injection of the oncogenes, and therefore the control mice did not have a tumour.

Once the glioblastoma bearing mice develop neurological symptoms, such as ataxia, the mice were perfusion fixed, culled, and the brains were collected and stored in formaldehyde. The same process is applied to the control mice. Each mouse was identified using three digits, which will be used to identify the images later.

Imaging

All of the imaging was done through multiphoton microscopy [81]. The vasculature was imaged through the red tdTomato fluorescent reporter expressed by the endothelial cells, and the tumour cells were imaged through the green fluorescent proteins in the tumour cells. The resolution of the multiphoton microscope is 0.994 μm by 0.994 μm, and the depth of the imaging was incremented in steps of 1 μm.

Once the brains were collected, they were sliced into 1 mm thick sections, each brain slice section was numbered and associated with the three digit identifier of the mouse. Figure 3.10a shows an image of the green fluorescent protein of the cross-sectional surface of one of these brain slices. Each of these surface images of the brain cross-section is divided into tiles, similarly to a chessboard, as in Figure 3.10a, which will be used to locate further images taken from the slices.

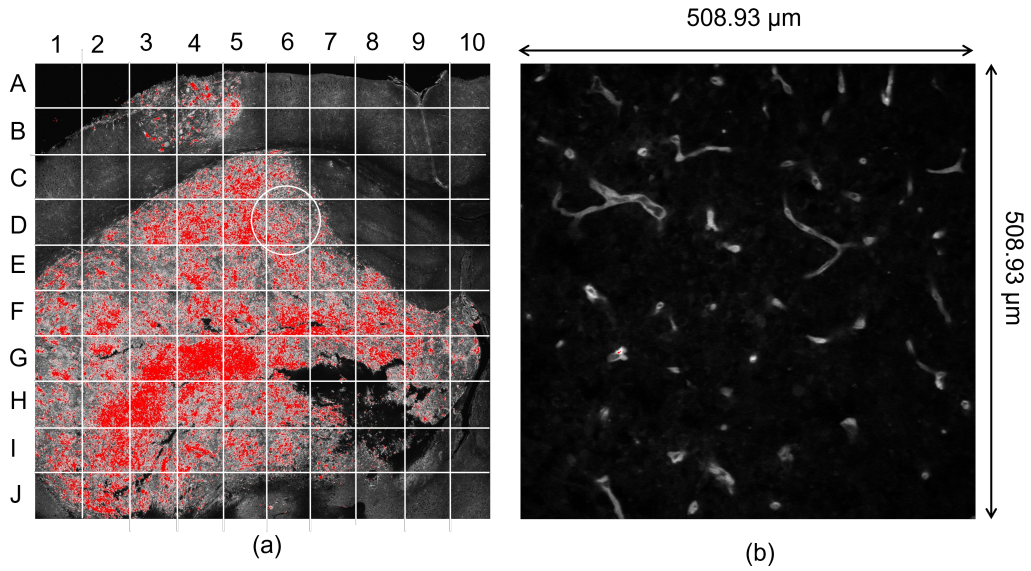

Figure 3.10: (a) shows the tumour cell fluorescence in the cross-section of one of the brain slices. The entire cross-section of the brain slice is a single image and does not image into the depth of the brain. In this case, it is of mouse 324 and slice 3, so is referred to as 324-3. (b) One of the two-dimensional images of the tdTomato reporter in the stack obtained from tile D6, circled in (a). The imaging of the tiles is done in stacks, and images into the depth of the brain. As this is tile D6 in mouse 324 and brain slice 3, it is referred to as 324-3-D6.

Some of the tiles were further imaged with the multiphoton microscope. Each tile was 508.93 μm by 508.93 μm (512 pixels by 512 pixels), and imaged 150 μm (or 151 μm) in depth in steps of 1 μm, providing a stack of 150 (or 151) two-dimensional images, where the superposition of the stack represents three-dimensional data. Figure 3.10b shows an image of the vascular reporter for one of the tiles, circled in Figure 3.10a. Each stack of images for the tiles imaged the vascular and the tumour cell reporter. With the known tile, the images can be identified based on a mouse-brain-tile format, see the caption in Figure 3.10.

3.3.2 Reconstruction of the vascular surface and centreline extraction

The stack of two-dimensional images of the vasculature needs to be reconstructed into a three-dimensional surface of the vessel wall with centrelines. As part of the work undertaken in this thesis, I have put together a pipeline of various existing image processing methods to reconstruct the vessel surfaces from the stack of images. Chapter 6 contains a validation, comparing the reconstructed surface to the raw images, to evaluate the pipeline. The surface reconstruction is done through two key steps. Firstly, the stack of images is thresholded, secondly, the thresholded stack is reconstructed into a three-dimensional surface of the vessel walls. Within these key steps, there are several image processing methods that are used to remove noise and improve the final quality of the image. Finally, the centrelines through the centre of the three-dimensional surface are generated as they will be used to phenotype the vasculature. This section will give the details of the reconstruction pipeline and share which software were used to perform it. Figure 3.11 shows a pipeline of the entire process as a flow diagram and an example of a final reconstructed three-dimensional vascular surface with its centreline.

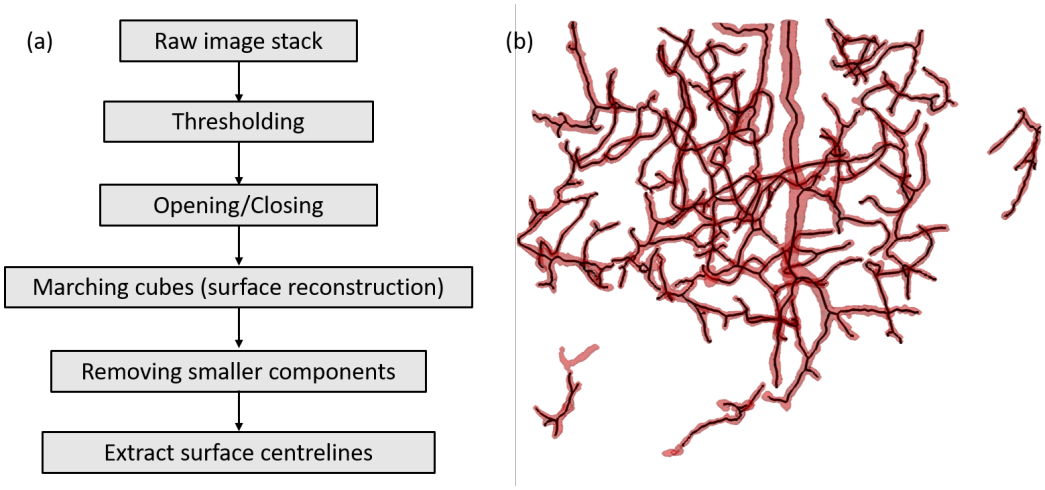

Figure 3.11: (a) pipeline used to reconstruct the three-dimensional vascular surface and extract the centrelines from the raw image stack. (b) One of the reconstructed three-dimensional vascular surfaces with its centrelines.

Thresholding

The first step of the process is to threshold the stack of images. Thresholding consists in taking an image with a colour histogram, and binarising it so that below a certain threshold pixels are black and above they are white (or vice versa). Thresholding is useful when the object of interest is distinguishable from its background [2, 176]. The thresholding algorithm used is the Kapur-Sahoo-Wong maximum entropy thresholding method [99] implemented in FIJI (Fiji Is Just imageJ) [167].

The Kapur-Sahoo-Won maximum thresholding method, with default parameters in FIJI, was chosen based on a heuristic approach. One can threshold a stack of images using various thresholding algorithms, and FIJI will generate the thresholded output images of all the algorithms, see Figure 3.12 for an image with a montage corresponding to the thresholded image with 16 thresholding algorithms and their default FIJI parameters. The choice of the Kapur-Sahoo-Won method was self-evident, as the other methods outputted poorly thresholded images in various parts of the stack, in Figure 3.12b for example there are numerous algorithms that do not output useable binarised images.

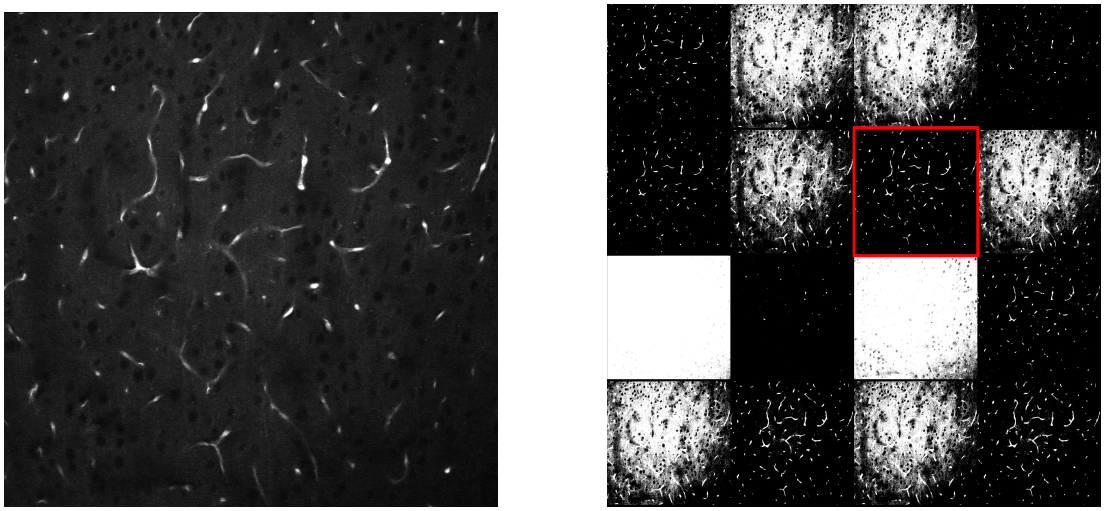

(a) **(b)**

Figure 3.12: (a) is the raw data of the vascular reporter as shared by experimentalists of a single image in a stack. (b) shows a montage of different thresholding techniques, with their default FIJI parameters, applied to that image. The montage of this specific image shows that many thresholding techniques output noisy or poorly thresholded images. The thresholding technique used is outlined in red.

Opening and closing

Once the image is thresholded, two morphological operations, called opening and closing, are sequentially performed on the thresholded images, Figure 3.13 illustrates these operations. Those operations were performed in FIJI [167].

Both opening and closing use erosion and dilation, which will be defined first. Erosion is the removal of a pixel that interfaces between the foreground and the background. Dilation is the opposite, and consists of adding a pixel that interfaces between the foreground and the background. Figure 3.13 illustrates erosion and dilation.

Opening is an operation consisting of erosion followed by dilation. Opening aims to open gaps between touching features. Closing is an operation consisting of dilation followed by erosion, and aims to close features [166]. Both opening and closing are illustrated in Figure 3.13, and the sequence of operations was chosen as it yielded the best results.

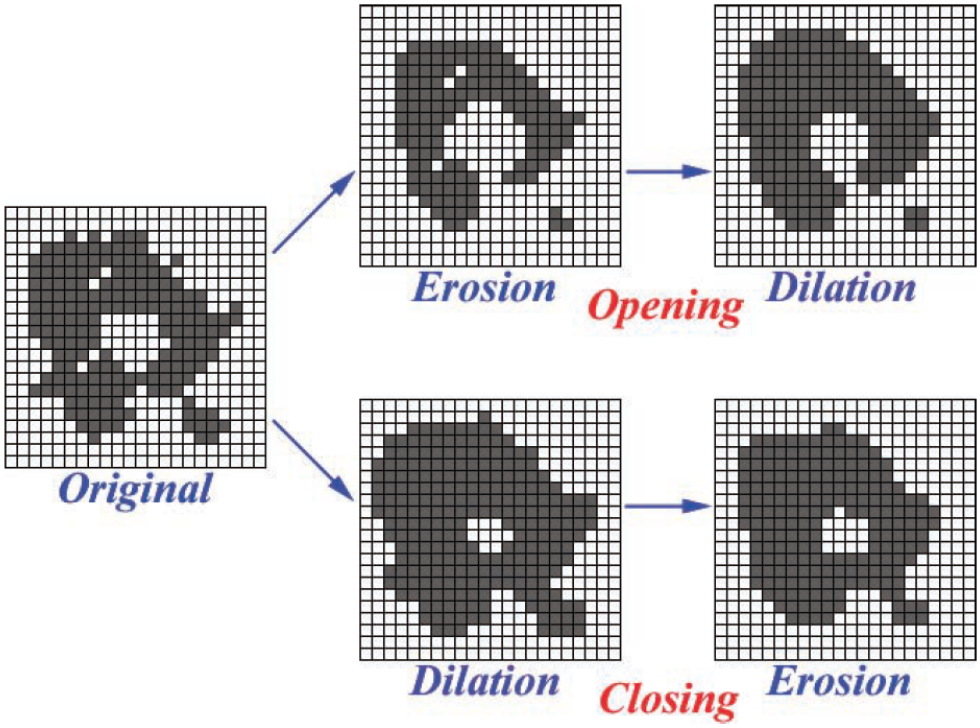

Figure 3.13: Illustration of opening and closing procedures on an image, and its substeps erosion and dilation. Image reproduced with permission from [166].

Marching cubes

The next step is to reconstruct the stack of two-dimensional images into a three-dimensional surface of the vasculature. The reconstruction is done through the marching cubes algorithm [114], implemented in VTK [168], which takes the set of points in the images and generates a triangular surface around the points [114]. Figure 3.14 illustrates the marching cubes algorithm in two-dimensions (sometimes called marching squares, but uses the same principle, the two-dimensional form is used for ease of visualisation) with an explanation.

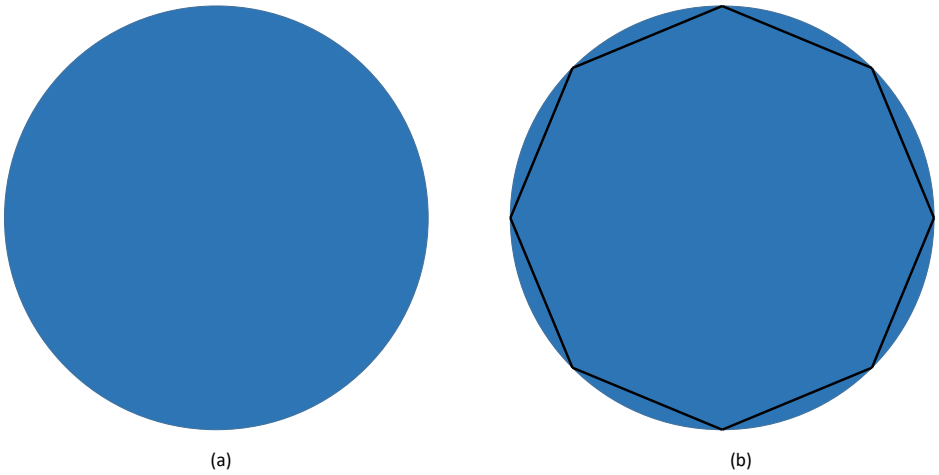

Figure 3.14: Two-dimensional illustration of the marching cube algorithm. (a) shows the shape the marching cube algorithm will work on. (b) shows the original shape, with the output of the marching cube algorithm, which is the black lines. In effect, it takes the shape and outputs the boundary of the shape. Here, in two-dimensions, the input is a surface and the output is a line at the boundary of the surface. In three-dimensions, the input is a volume and the output is a triangular mesh forming a surface at the boundary of the volume. The coarseness of the surface depends on the resolution of the initial volume.

Removing smaller components

The final step in the reconstruction process is to remove the remaining noise in the vasculature. This step is achieved through the removal of small components that are disconnected from the larger components of the vascular surface. It removes any isolated component that has a volume smaller than 1% of the total volume in the reconstructed surface. Figure 3.15 illustrates a vascular network prior to and after the implementation of this step.

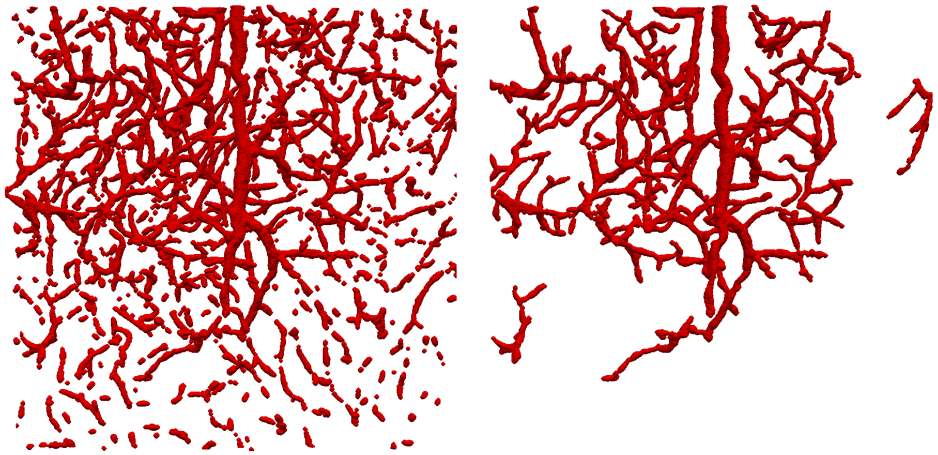

Figure 3.15: Illustrates the step of removing the smaller components in the vasculature. (a) shows the vasculature prior to the smaller components being removed, containing a lot of noisy and non-usable data. (b) shows the same vasculature after the smaller components have been removed.

Extracting centrelines

Following the reconstruction of the surface, the centrelines of the vascular surface are required for calculating phenotypes from the networks. The centrelines are extracted using an existing centreline extractor, called "vmtkNetworkExtractor" and implemented in the open-source VMTK software [4]. Figure 3.16 illustrates the centrelines in a network that is fully reconstructed.

3.3.3 Automatic quantification of vascular phenotypes

To phenotype the microvasculature within the mouse models, a series of vascular phenotypes were automatically quantified through an algorithm. The choice of phenotypes was guided by the literature and the technical feasibility of quantifying them, and are:

1. Vessel diameter
2. Vessel aspect ratio
3. Vessel tortuosity
4. Non-dimensionalised interbifurcation distance (referred to as λ)
5. Distribution of tissue-vessel distances

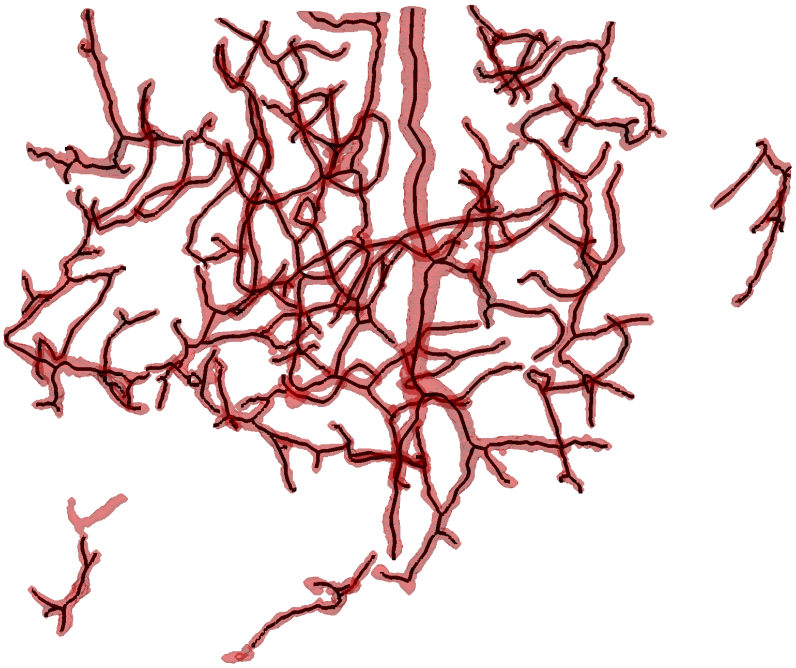

Figure 3.16: Shows the surface of the vasculature in red, and in black inside the vasculature is the centreline of the vascular surface.

This section provides the method to quantify the phenotypes from the reconstructed surface and centreline, where the surface and the centreline are the ones outlined in section 3.3.2. Four of these phenotypes (diameter, aspect ratio, tortuosity, and λ) are calculated for each vessel segment. The final phenotype, distribution of tissue-vessel distances, is calculated for each vascular network.

Phenotypes of vessel segments

The four phenotypes calculated at each vessel segment are vessel diameter, aspect ratio, tortuosity, and λ. A segment is defined through the centreline, as the set of lines connecting two degree three nodes. Figure 3.17 illustrates a vessel segment.

The aspect ratio is a quantification of how circular or oval the cross-section of a vessel is. It is quantified by taking a cross-sectional slice at each point in the vessel segment with a vector in the direction of the vessel centreline. The general ellipse equation is then fitted to the cross-sectional slice of the vessel. In doing so, I obtain the major and minor diameters of the ellipse for the said cross-section, which also provides me with the diameter values for each point. The aspect ratio is then the major axis of the ellipse divided by the minor axis of the ellipse. As the aspect ratio and diameters are evaluated at every point in the vessel

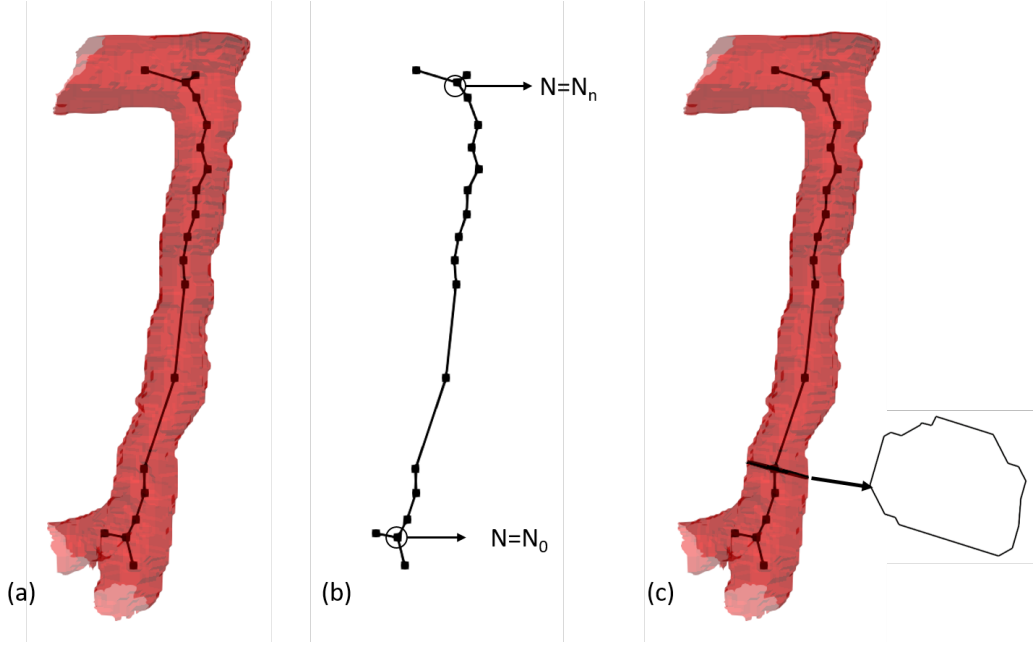

Figure 3.17: Illustration of a vessel segment in which the phenotypes are quantified. A segment is defined through the centreline as the lines connecting two degree three or more nodes. (a) shows the centrelines of a segment (with the neighbouring points of the segment for illustrative purposes) in the vessel surface. (b) isolates the centreline, going from point 0 to point n. (c) shows the aspect ratio calculation at a given point. A slice (the solid black line perpendicular to the vessel) is taken in the direction of the vessel to obtain the vessel cross-section at a given point, which is then used to calculate the aspect ratio by fitting the equation of an ellipse to it.

segment, the value retained is the maximum aspect ratio in the vessel segment as it is the most important value affecting blood flow [50], and the corresponding values for the major and minor diameters are retained. The points inside a bifurcation were ignored, as the diameter and aspect ratio at points inside the bifurcation are ill defined.

λ is the length of the vessel segment non-dimensionalised by the diameter of the vessel segment. The diameter used is the diameter of a circle with the same area as the ellipse previously defined. Using the notation in Figure 3.17b, the interbifurcation distance can be calculated through

$$\lambda = \frac{\sum_{i=0}^{n-1} \text{distance}(N_i, N_{i+1})}{D}, \tag{3.52}$$

where the distance is the euclidean distance between two points and D is the equivalent circle diameter of the vessel segment.

The vessel tortuosity, τ, is determined through

$$\tau = \frac{\sum_{i=0}^{n-1} \text{distance}(N_i, N_{i+1})}{\text{distance}(N_0, N_n)}. \tag{3.53}$$

Listing 1 shows the python pseudocode for calculating the aspect ratio, diameter, tortuosity and λ in the vessel segments.

Distribution of tissue-vessel distances

The final metric calculated is the distribution of tissue-vessel distances, where the tissue-vessel distance is the distance from a point in the tissue to the closest vessel surface. This metric is not calculated for each vessel segment, contrary to the previous metrics, and is a distribution for each vascular network. 500 random points are generated in the convex hull of the vascular network, and at each point the shortest distance to a vessel surface is calculated. The convex hull ensures that the sampled points are within the vascular network. Different numbers of points were tested, and eventually the distribution of distances converges and remains unchanged with an increased number of random points, the value of 500 points was chosen as it is above this convergence. Listing 2 shows the python pseudocode to calculate the distribution of distances from the tissue to the vessel surface.

Listing 1 Code to calculate phenotypes in vessel segments

```
# Initialise empty lists
aspect_ratios = []
major_axes = []
minor_axes = []
interbifurcation_distance = 0.

# Loop through points in vessel segment
for point in vessel_segment:

    # Increment interbifurcation distance according to the equation
    if point != last_point:
        interbifurcation_distance += distance(point, next_point)

    # Ignore points that form the bifurcation for aspect ratio
                                        calculation
    if point is inside(bifurcation):
        continue

    # Calculate the direction of the vessel segment, done through vector
                                         between previous point and next
                                         point in centreline
    vector = find_vector(previous_point, next_point)

    # Take slice of vessel at given point with the vector
    slice = slice_vessel_surface(point, vector)

    # Fit generalised equation of ellipse to slice
    ellipse = fit_ellipse(slice)

    # Calculate aspect ratio from ellipse fit
    aspect_ratio = ellipse.major_axis / ellipse.minor_axis

    # Append values to lists
    aspect_ratios.append(aspect_ratio)
    major_axes.append(ellipse.major_axis)
    minor_axes.append(ellipse.minor_axis)

# The aspect ratio used is the maximum aspect ratio in a vessel segment
aspect_ratio = max(aspect_ratios)

# Use major and minor axis corresponding to the maximum aspect ratio in
                                        segment
index = aspect_ratios.index(aspect_ratio)
major_axis = major_axes[index]
minor_axis = minor_axes[index]

# Calculate lambda from the interbifurcation distance and the segment
                                        diameter
lambda = interbifurcation_distance / equivalent_circle_diameter(
                                        minor_axis, major_axis)

# Calculate tortuosity from the equation
tortuosity = interbifurcation_distance / distance(first_point,
                                        last_point)
```

Listing 2 Code to calculate distance from tissue to vessel

```
# Initialise empty list for distances
distances = []

# Sample 500 points in the convex hull of the vessel network surface
points = sample(500, convex_hull_vessel_network_surface)

# Loop through points
for point in points:

  # Measure distance from point to closest vessel surface
  distance = measure_distance(point, closest_vessel_surface)

  # Add distance to list of distances
  distances.append(distance)
```

Chapter 4

Effect of a vessel compression on the partitioning of red blood cells at a downstream bifurcation

This results chapter addresses the first objective of this thesis, to numerically investigate how vessel compression impacts the partitioning of red blood cells at a single vascular bifurcation. The key finding is that, at a bifurcation downstream of a vessel compression, the higher flowing child branch in further enriched in haematocrit. The abnormal partitioning of red blood cells is the result of a narrowing of the red blood cell cross-section distribution in the compressed region, due to an increased shear rate and shear rate gradient. The abnormal partitioning of red blood cells occurs up to a critical threshold of 30% haematocrit in the parent branch. Finally, the results are contextualised within the broader question of how vessel compression has an effect on tissue hypoxia.

The results of this chapter were published in the Proceedings of the National Academy of Sciences (PNAS), in 2020 under the title "Compressed vessels bias red blood cell partitioning at bifurcations in a haematocrit-dependent manner: Implications in tumor blood flow" (https://doi.org/10.1073/pnas.2025236118). This chapter is an adaptation of the publication, for which the rights were obtained. Professor Bernabeu, Dr. Krüger, and Dr. Hardman contributed to the paper.

This chapter is divided into three main sections. Section 4.1 summarises the methods used in this chapter, section 4.2 presents the results of this chapter, and section 4.3 contains a discussion and conclusion for the work presented.

4.1 Methods

This section outlines the method used to investigate the effect of a vessel compression on the partitioning of red blood cells (RBCs) at a downstream bifurcation. I use a computational model with high fidelity blood flow simulations and physiologically relevant geometries to investigate the effect of a compression at vascular bifurcations.

4.1.1 Blood flow model

In this chapter, I model blood flow as a suspension of deformable RBC particles in a continuous plasma phase, as described in section 3.1.

I characterise the RBC deformability with the capillary number,

$$Ca = \frac{\mu \gamma r}{\kappa_s}, \tag{4.1}$$

where μ is the fluid dynamic viscosity, γ is a characteristic shear rate, r is a characteristic length (the RBC radius) and κ_s is the strain modulus of the RBCs. The capillary number is set to 0.1, unless stated otherwise, and will be varied to investigate its effect on the partitioning of red blood cells. The parameters used for the red blood cell model are summarised in Table 4.1.

Table 4.1: Parameters used for the red blood cell model. Variables with a tilde are in lattice units.

Parameter	Symbol	Value
Strain modulus	κ_s	depends on capillary number
Dilation modulus	$\tilde{\kappa_\alpha}$	0.5
Bending modulus	κ_B	depends on capillary number
Surface area modulus	$\tilde{\kappa_A}$	1
Volume modulus	$\tilde{\kappa_V}$	1
Föppl-von Kármán number	$\Gamma = \kappa_B/(\kappa_S r_{RBC}^2)$	1/400
Number of faces in RBC mesh	N_f	720
RBC radius	r_{RBC}	4 μm

The fluid parameters for the simulation are summarised in table 4.2.

Table 4.2: Simulation parameters used for the lattice-Boltzmann method.

Parameter	Symbol	Unit	Value
Voxel size	Δx	μm	0.6667
Timestep	Δt	s	7.41×10^{-8}
Relaxation time	τ	lattice units	1
Fluid viscosity	μ	mPa s	1
RBC cytoplasm viscosity	μ	mPa s	1
Fluid density	ρ	kg/m^3	1000

4.1.2 Geometry

I produced four geometries representing a vessel with diameter D and a downstream bifurcation. The first geometry is a control geometry (no compression, Figure 4.1a), while the remaining three geometries feature a single compression upstream of the bifurcation. The first compression model (Figure 4.1b) contains a long compression without a recovery length between compression and bifurcation. In the second compression model (Figure 4.1c), the compression is short, and there is a short recovery length between the compression and bifurcation. The last geometry (Figure 4.1d) features a short compression followed by a long recovery segment. The relevant geometrical parameters of all four geometries are summarised in Table 4.3.

Table 4.3: Dimensions of the geometry (D is channel diameter).

Geometry name	compression length	distance between compression and bifurcation
Control	N/A	N/A
Long-compression-no-recovery	$4D$	0
Short-compression-short-recovery	D	$2D$
Short-compression-long-recovery	D	$25D$

I set the channel diameter to $D = 33$ μm, a typical value for the tumour microvasculature [96]. I assume the cross-section of the channel to be circular, except for the section that is compressed, where it takes an elliptical form. I assume the perimeter of the cross-section to be constant along the channel, setting the ellipse perimeter to the same value as the uncompressed circular cross-section. The segment with an elliptical cross-section has an aspect ratio of 4.26, following reports from the literature [56]. The assumption of an elliptical cross-section within the compression is in line with observations from tumour histological slices where vessel compression is commonly reported as the aspect ratio of the elliptical shape of the vessel cross-sections [6, 56, 78, 192].

My aim is to focus on the effect of the compression. Therefore, I remove any effect from the slope leading to the compression by having a steep transition to and from the compression. I also remove the effect of a bifurcation asymmetry by having both child branches at the same diameter and angle from the parent branch.

4.1.3 Inlet and outlet boundary conditions

I set the outflow boundary conditions at the child branches as a Poiseuille velocity profile with an imposed maximum velocity. The flow ratio to the child branches is initially set to 80:20, and is varied as part of the study. Unless specified otherwise, the inlet branch has an average velocity of 600 μm/s, a typical value for the tumour microvasculature [96].

The inlet boundary condition is an arbitrary pressure value that has no impact on the simulation result. In order to reduce any memory effects and establish a quasi steady-state distribution of RBCs, the cells flow through a straight tube with a length of 25 tube diameters before entering the compression [100]; I call this length the initialisation length.

I vary the value of haematocrit within the system from 10% to 30%, covering a wide range which is physiologically present within the tumour microvasculature [96].

The Reynolds number of the system is 0.04. Therefore, viscous forces dominate and the system is in the Stokes flow regime. For computational tractability, I set the numerical Reynolds number to 1, where inertial forces still do not play a significant role, see section 3.1.2 for more details.

4.1.4 Processing results

All haematocrits reported are discharge haematocrits. I calculate the discharge haematocrit, H_d, by calculating the fraction of RBC flow to total blood flow at any channel cross-section normal to the direction of flow,

$$H_d = \frac{Q_{RBC}}{Q_{blood}}, \tag{4.2}$$

where Q_{RBC} is the volumetric flow rate of RBCs and Q_{blood} is the volumetric flow rate of blood, i.e. plasma and RBCs. The flow rate of RBCs is calculated by counting the RBCs crossing a plane normal to the direction of flow over a given period of time, Δt. Knowing the volume of an RBC, $V_{RBC} = 100\ \mu\text{m}^3$, one can calculate the RBC flow rate,

$$Q_{RBC} = \frac{NV_{RBC}}{\Delta t}, \tag{4.3}$$

where N is the number of cells that have crossed the plane.

In order to quantify the distribution of the RBCs in a cross-section, I measure the root mean squared distance (RMSD) of the RBC centres of mass with respect to the channel centreline,

$$RMSD = \sqrt{\frac{1}{N}\sum_{i=1}^{N}(\mathbf{x}_i - \mathbf{x}_0)^2}, \tag{4.4}$$

where $\mathbf{x}_i$ is the i^{th} RBC position, and $\mathbf{x}_0$ is the channel centre, both taken on a cross-section normal to the direction of flow at points of interest. Figure A.1 illustrates how I obtain the positions $\mathbf{x}_i$ in practice.

I non-dimensionalise length by the vessel diameter D, unless stated otherwise. By definition, I set the downstream end of the compression as the reference point with an axial position of 0. Axial positions are positive in the downstream direction ($l > 0$) and negative in the upstream direction ($l < 0$).

As part of the analysis, I use the separatrix, which is defined as an imaginary surface separating fluid particles going to one child branch from those going to the other child branch. It is an important tool for the investigation of RBC partitioning at a bifurcation [203]. I determine the separatrix by completing a simulation without RBCs to obtain streamlines unperturbed by RBCs, see Figure A.2 for details.

4.2 Results

4.2.1 At 10% haematocrit, vessel compression alters RBC partitioning at a downstream bifurcation

I initially investigate the effect that a compression has on the model geometries in Figure 4.1a-d at an inlet discharge haematocrit of 10%, a flow ratio of 80:20 and a capillary number of 0.1. Simulation results for a long compression at 10% haematocrit, Figure 4.1b, show that the RBC partitioning at the bifurcation is strongly affected by the compression. Figure 4.1e shows that, for a long compression with no recovery, the child branch with the lower flow rate is almost depleted of RBCs and has approximately 0.5% haematocrit, whereas the control simulation indicates that the same branch has $\sim$8% haematocrit in the absence of a compression. The control simulation is in agreement with the standard plasma skimming model, see Figure A.3.

The short-compression-short-recovery geometry, Figure 4.1c, shows a smaller effect on the RBC partitioning than the long compression. With $\sim 3.5\%$ haematocrit in the child branch with the lower flow rate, this is still less than half of the haematocrit in the control simulation.

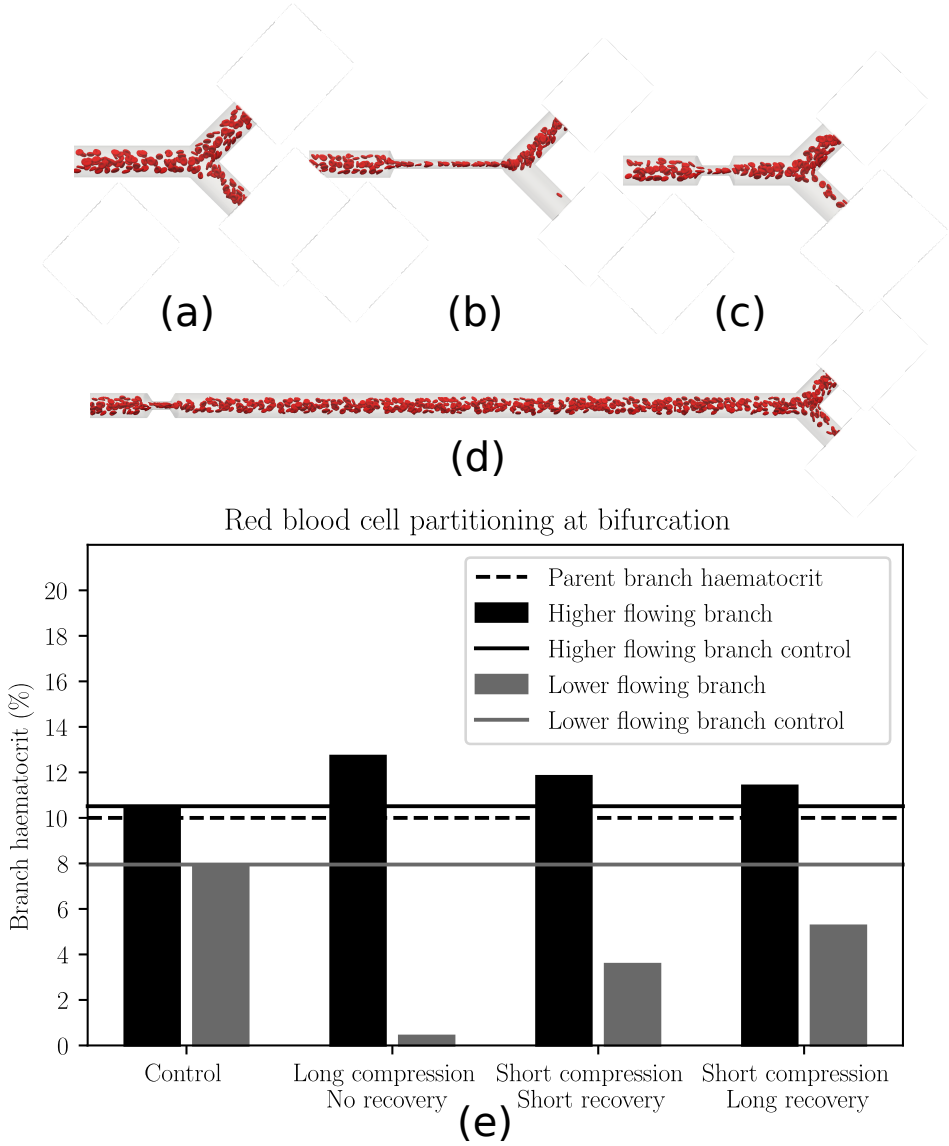

Figure 4.1: Phase separation in child branches after a bifurcation at $H_d = 10\%$. (a–d) are snapshots of the control, long-compression-no-recovery, short-compression-short-recovery and short-compression-long-recovery, respectively. (e) shows the haematocrit in the child branches for these four cases. Black/grey indicates the higher/lower flowing child branch, respectively. Solid lines are the control discharge haematocrits. The dotted line illustrates the discharge haematocrit of the parent branch.

In all of the geometries the increase in haematocrit of the higher flowing child branch is less pronounced than the decrease in haematocrit of the lower flowing child branch, Figure 4.1e, leading to non-conservation of haematocrit. The non-conservation of haematocrit is because at the bifurcation the conserved quantity is RBC flowrate, and not haematocrit. When there is disproportional partitioning of RBCs compared to flow, as is the case here, the lower flowing child branch is more impoverished than the higher flowing child branch is enriched [149].

In order to test whether the symmetry of the compression has an effect on the partitioning of the RBCs at the downstream bifurcation, I investigated an asymmetric compression, Figure 4.2. The simulation results are similar to those obtained with a symmetric compression. This indicates that, under the present conditions, the asymmetry of the compression does not have an important effect on the downstream partitioning of RBCs.

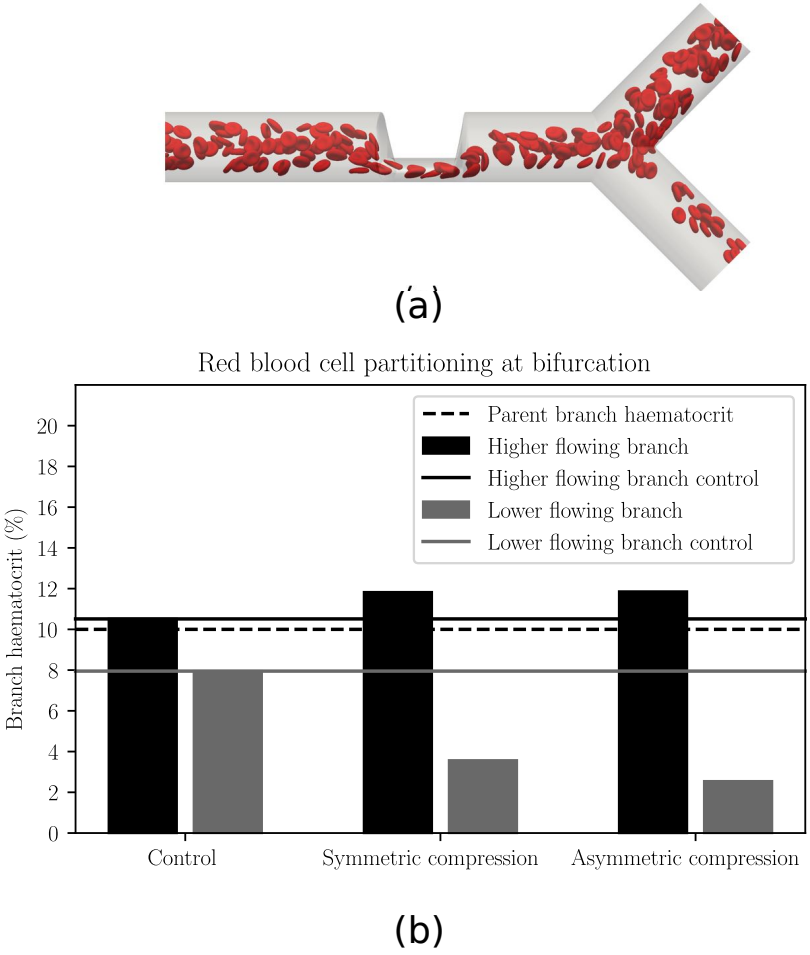

Figure 4.2: Phase separation of child branches after bifurcation at $H_d = 10\%$ comparing effect of compression asymmetry. (a) Snapshot of the asymmetric short geometry with the same dimensions as the short geometry. (b) From left to right are the haematocrit of the child branches for a control geometry, a symmetric compression, and an asymmetric compression (a). Results show a negligible difference between a symmetric and asymmetric geometry. In black is the higher flowing child branch and in grey the lower flowing child branch. The solid lines are the control discharge haematocrits. The dotted line illustrates the discharge haematocrit of the parent branch.

I also investigated the effect of flow rate on RBC partitioning. By changing the flow rate, I change the capillary number, which quantifies the deformation of the RBCs. I performed two additional simulations at a capillary number of 0.02 and 0.5, to cover the RBC tumbling and tank-treading regimes and the range of flow rates typical for the tumour microvasculature [96, 109]. The numerical Reynolds number is kept constant as the change in the physical Reynolds number is negligible (ranging from 0.008-0.2). Figure 4.3 shows that the RBC partitioning does not change with capillary number, i.e. RBC deformability, which implies that the flow rate and capillary number are not important parameters for RBC partitioning in the presence of a compression at 10% haematocrit within the studied range of flow rates and at a low Reynolds number.

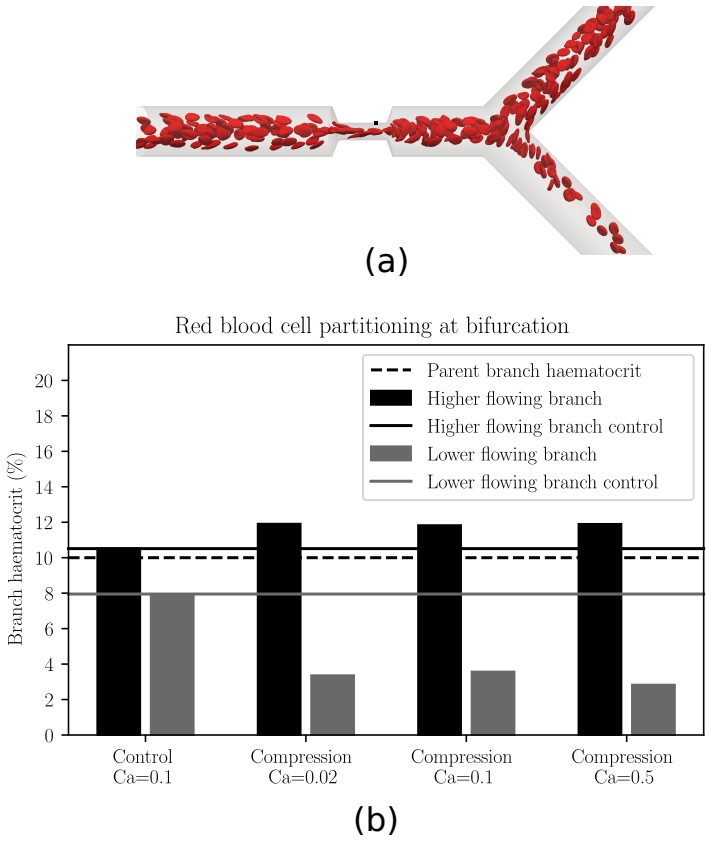

Figure 4.3: Phase separation of child branches after bifurcation at $H_d = 10\%$, comparing the effect of different channel flow rates (increasing capillary number denotes increasing flow rate). (a) Snapshot of the short compression with a higher channel flow rate and a capillary number of 0.5. (b) haematocrit of the child branches for a control geometry, on the left, and a compression geometry (a) at three different capillary numbers. In black is the higher flowing child branch and in grey the lower flowing child branch. The solid lines are the control discharge haematocrits. The dotted line illustrates the discharge haematocrit of the parent branch.

4.2.2 Narrowing of cell distribution alters partitioning of RBCs

Next, I investigated which mechanism leads to the observed changes in partitioning, and why the different geometries have different effects.

As blood flows through the compression, the shear rate increases since the fluid velocity within the compression is larger due to mass conservation (the elliptical cross-sectional area is reduced compared to the circular cross-sectional area), and the width of the channel along the compression axis is reduced. The simulations show that RBCs situated close to the wall prior to the compression migrate across streamlines towards the channel centre. After leaving the compression, RBCs do not immediately migrate back towards the position they had prior to the compression. As a consequence, the RBC distribution downstream of the compression is narrower than upstream of the compression. This explanation is in line with prior findings from experimentalists [61]. Figure 4.4a–d illustrates this mechanism.

To quantify the narrowing of the RBC distribution, I plot the RMSD of the RBC centres of mass along the compression axis. Figure 4.4e–g shows that, for all geometries, there is a narrowing of the distribution of cells in and after the compression compared to the region before the compression. However, in the short recovery geometries, Figure 4.4f–g, the RBC distribution partially recovers before the cells reach the bifurcation. This explains why the RBC partitioning is more affected when there is no recovery length between compression and bifurcation, Figure 4.4e. Previous studies report an increase of the cell-free layer (CFL) post compression compared to the CFL thickness pre compression, here seen as a narrowing of the RBC distribution, which leads to a partitioning bias of RBCs towards the higher flowing branch [14].

To investigate the behaviour of the RBC distribution after the compression, I increased the distance between the compression and the bifurcation from $2D$ to $25D$, as shown in Figure 4.1d. Figure 4.4g shows a gradual recovery of the RBC distribution between the compression and bifurcation, although 25 channel diameters are not sufficient to reach the same RMSD as before the compression.

While the data imply that a mechanism exists that leads to the recovery of the RBC distribution, it is not clear a priori what the underlying mechanism is. I assume that, given enough channel length after the compression, the RBC distribution will fully recover eventually. given the progression seen between Figure 4.4f and 4.4g. Katanov *et al.* [100] demonstrated that, from an initially uniform distribution of RBCs in a channel, the formation of a stable CFL is governed by the shear rate time scale and takes a length of about 25 vessel diameters to form, independently of flow rate, haematocrit or vessel diameter within the range of parameters they investigated. The data here suggest that the opposite effect, the recovery of an initially heterogeneous RBC distribution where most of the RBCs are close to the channel centre,

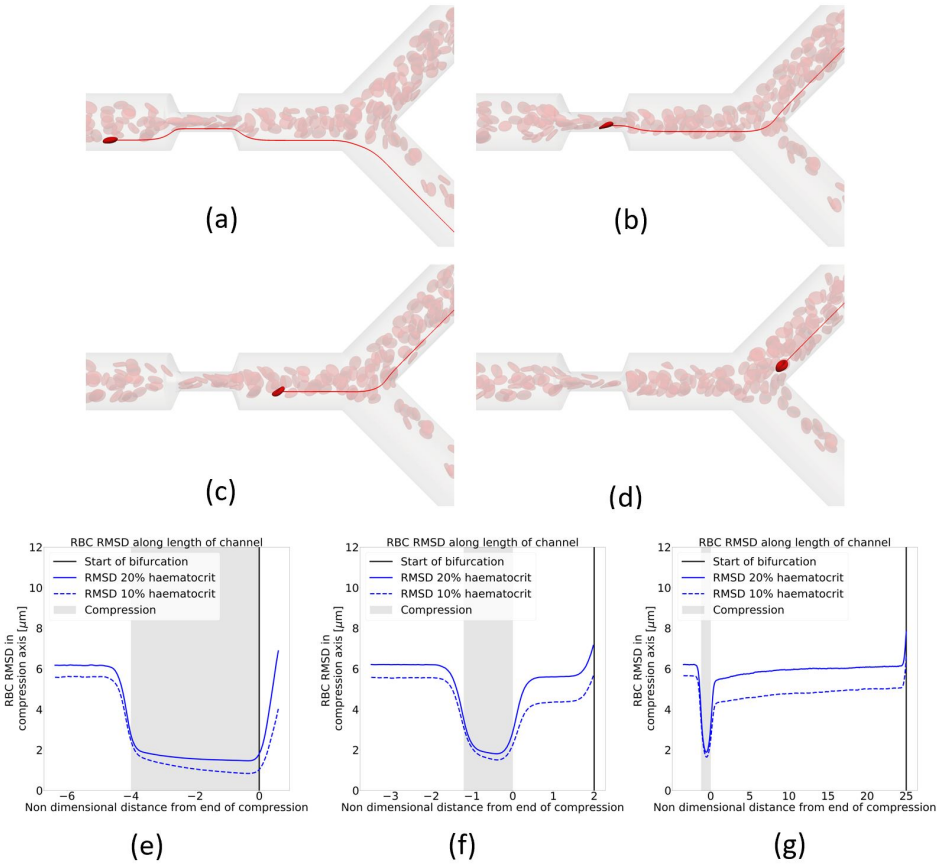

Figure 4.4: Narrowing of RBC distribution in compression. (a–d) In red are the streamlines of the underlying fluid. In bright red is an RBC of interest. (a) An RBC situated prior to the compression and near to the vessel wall. (b) The same RBC after it has crossed streamlines within the compression. (c) The RBC exits the compression on a more central streamline than the one on which it entered the compression. (d) The RBC goes to a different branch than the pre-compression streamline it was on. (e–g) RBC RMSD along the vessel length, rigid line at $H_d = 20\%$ and dashed line at $H_d = 10\%$. The blue line is the RMSD, the black vertical line is the point of bifurcation, and the shaded grey zone is the compression area. Geometries are (e) Long-compression-no-recovery, (f) short-compression-short-recovery, and (g) short-compression-long-recovery. The child branch flow ratio is 80:20 in all cases.

cannot be described in the same way since a length of 25 channel diameters is not sufficient for recovery. The shear rate is lower and cells move faster near the channel centreline, which should lead to a weaker shear-induced recovery of the cell distribution along a distance of $25D$. I hypothesise that cell-cell interactions are the dominant driver for the recovery.

4.2.3 Abnormal partitioning is present in a large range of flow ratios

I next investigate the effect of the flow ratio on the abnormal partitioning of RBCs downstream of the compression. I varied the flow ratio from 50:50 to 90:10 in five steps and measured the difference between the compression geometry and the control geometry. Figure 4.5 reveals that abnormal partitioning is present over a wide range of flow ratios, except for the 50:50 case. Since the compression is symmetric (Figure 4.1b) and both downstream branches behave identically in the 50:50 case, the overall symmetry is retained and an equal number of RBCs enter both branches. Therefore, the 50:50 flow ratio does not lead to abnormal partitioning. The presence of a small difference between the compression and the control for the 50:50 case in Figure 4.5 is attributable to the finite number of RBCs in the simulations.

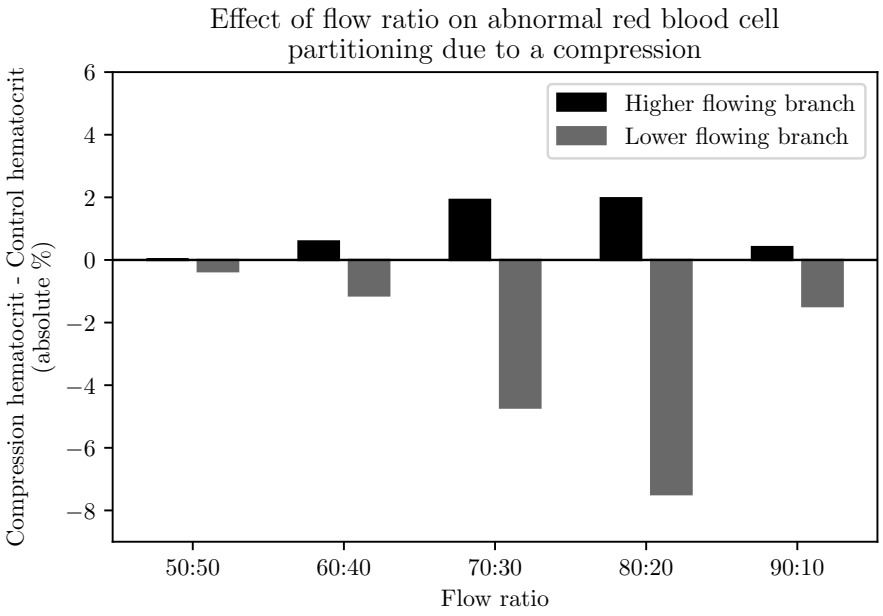

Figure 4.5: Effect of flow ratio on phase separation of blood downstream of a compression at $H_d = 10\%$. The difference between the control geometry (Figure 4.1a) and the compression geometry (Figure 4.1b) is an absolute haematocrit value. A positive value denotes a haematocrit enrichment compared to the control geometry, a negative value denotes a haematocrit reduction compared to the control geometry. Note that the flow ratios X:Y and Y:X would give the same results due to the symmetry of the geometry.

I also observe that the degree of abnormal partitioning is largest for the 80:20 case and sharply decreases for the 90:10 case. When the flow ratio in a bifurcation increases, the low flow branch has a decreasing discharge haematocrit, until the branch eventually becomes a pure plasma branch [172], even in uncompressed geometries. Therefore, in the 90:10 case, the discharge haematocrit in the low flow branch is already small, and any change due to abnormal partitioning will also be small. Eventually, when the flow ratio is sufficiently high, there will be no difference in RBC partitioning between the compression and control geometries, as they will both be plasma branches without RBCs.

4.2.4 Increasing haematocrit reduces bias in RBC partitioning

To test the hypothesis that cell-cell interactions drive the recovery of the narrowed RBC distribution, I investigate blood flow at an increased haematocrit of 20%. Figure 4.6 shows that the long-compression-no-recovery geometry still leads to a deviation from the control simulation. However, the deviation is smaller than at 10% haematocrit, Figure 4.1. This observation can be explained by Figure 4.4e–g which reveals that the narrowing of the RBC distribution is less pronounced at higher haematocrit compared to lower haematocrit. I conclude that, as the haematocrit increases, hydrodynamic cell-cell interactions become more relevant, leading to a smaller narrowing of the cell distribution by the compression as well as a faster decay of the narrowed RBC distribution after the compression.

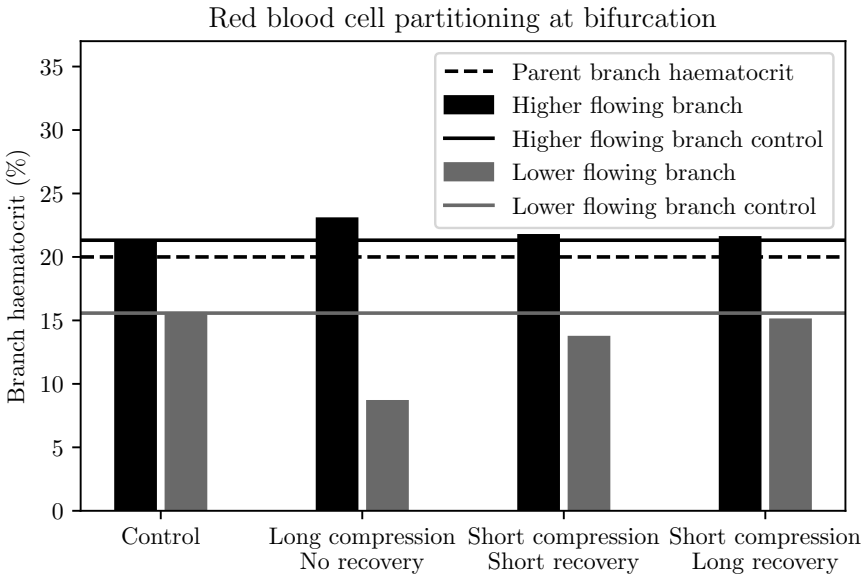

Figure 4.6: Phase separation in child branches after a bifurcation at $H_d = 20\%$. Black/grey indicates the haematocrit in the higher/lower flowing child branch, respectively. Solid lines are the control discharge haematocrits. The dotted line illustrates the discharge haematocrit of the parent branch. The child branch flow ratio is 4:1 in all cases.

For the short-compression-long-recovery geometry, the deviation from the control is almost non-existent at $H_d = 20\%$, Figure 4.6. Whilst the control simulation shows 15.6% haematocrit in the lower flowing child branch, the compression merely alters that value to 13.7%. As can be seen from Figure 4.4f, not only is the narrowing of the RBC distribution in the compression smaller, but after exiting the compression the RBC distribution is much closer to its pre-compression counterpart.

I also investigated the role of the distance between the short compression and the bifurcation by increasing it from $2D$ to $25D$. Figure 4.4g shows that the RBC distribution with $H_d = 20\%$ eventually recovers and goes back to its pre-compression level, contrary to the simulation at 10% haematocrit. This further suggests that cell-cell interaction is the dominant mechanism for the post compression distribution to recover its pre compression value.

The decreasing effect of the constriction on the RBC distribution at increasing haematocrit raises the question of whether there is a critical haematocrit above which the RBC partitioning is not modified by the presence of an upstream constriction. To that end, I increased the haematocrit in the parent branch to 30% and revisited the long compression geometry that has no recovery length between compression and bifurcation. Figure 4.7 shows that there is no significant difference in RBC partitioning when compared to the control without compression, indicating that the critical haematocrit value lies near 30%.

(a)

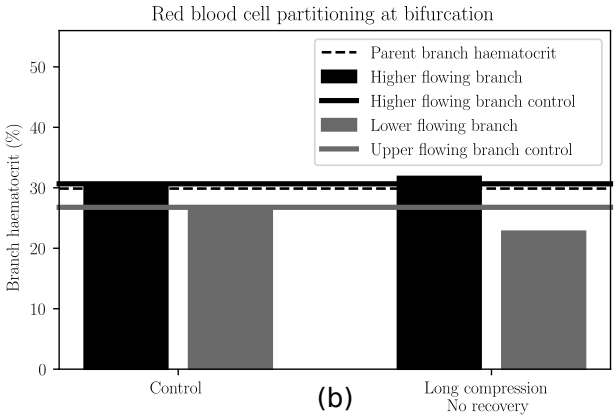

(b)

Figure 4.7: Phase separation in child branches after a long bifurcation at $H_d = 30\%$. (a) shows the haematocrit of the child branches. Black/grey indicates the higher/lower flowing child branch, respectively. Solid lines are the control discharge haematocrits. The dotted line illustrates the discharge haematocrit of the parent branch. (b) shows the snapshot of the simulation in the long compression. The child branch flow ratio is 4:1.

4.2.5 Reduced-order model

Numerically and theoretically investigating RBC transport in large networks is challenging due to the high computational expense associated with the simulations [12, 108, 210]. For this reason, several authors have proposed the use of reduced-order models to quantify the partitioning of RBCs at bifurcations. The most common model existing for partitioning of RBCs is that presented by Pries et al. [148, 152], although others exist, e.g. [68].

I have demonstrated that vessel compression indeed has an impact on the partitioning of RBCs at a downstream bifurcation and that this is not captured by a state-of-the-art reduced-order model, as seen in Figure A.3. To investigate how this effect propagates on a network level, I propose a novel reduced-order model that captures this phenomenon. I make four main assumptions for the reduced-order model:

1. An RBC's centre of mass will go to the same child branch as its underlying streamline. This assumption relies on the low Reynolds number of the system, which is true for the microcirculation, where the Reynolds number is $\ll 1$ [172]. Similarly to reports of RBCs crossing the separatrix prior to a bifurcation [14, 47, 203], in the simulations I observed $< 5\%$ of RBCs near the separatrix crossing streamlines. Due to this small fraction, I deem the assumption appropriate.
2. A curved separatrix independent of the Reynolds number is used, whereas the curvature of the separatrix generally depends on the Reynolds number [49, 203]. Since blood flow in the microvasculature is in the low-Reynolds regime, a small change in Reynolds number has a negligible effect on the separatrix.
3. The cross-sectional distribution of RBC centres of mass can be approximated by a step function, whereas the distribution profile of RBCs tends to quickly, but not instantaneously, reduce at the edge of the RBC distribution as is often reported [177, 180] and indeed observed in the simulations. The step function, however, is a good fit and simplifies the model considerably. I assume the step function to take the shape of an ellipse on any given cross-section of the channel, Figure 4.8a–c. The fraction of RBCs ending up in the top and bottom child branch is $A/(A+B)$ and $B/(A+B)$, respectively, defined by the areas A and B above and below the separatrix. Since the separatrix is a consequence of the geometry and flow ratio to each child branch, the model is applicable to all cases for which the separatrix is known.
4. The cross-section that determines which child branch an RBC enters is located about $2D/3$ upstream of the bifurcation. The simulations show that this is the upstream perturbation length after which the streamlines start to curve in order to enter the child branches. The length $2D/3$ is similar to that found in other studies [203]. Therefore, the reduced-order model needs to be able to predict the cross-sectional distribution of the RBCs up to a point $2D/3$ upstream of the bifurcation.

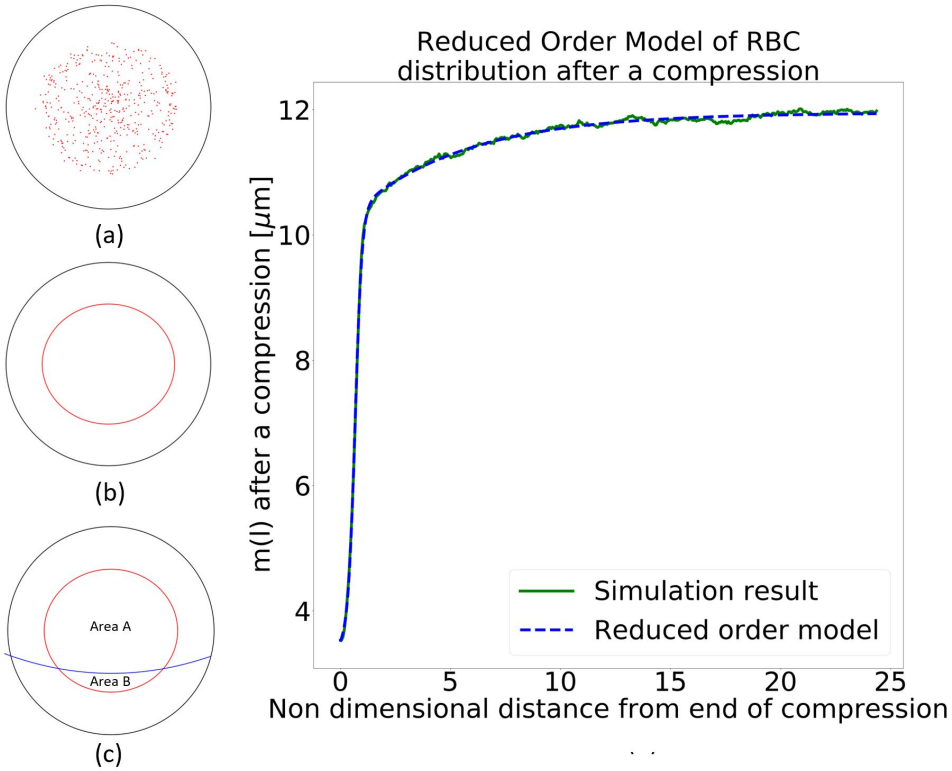

Figure 4.8: Reduced-order model. (a) The RBCs' centres of mass are shown on a cross-section. (b) An ellipse is used to represent the distribution of the RBCs. (c) The curved separatrix is added. Any RBC above the separatrix is assumed to go to the top branch, and any RBC below it to go to the bottom branch. (d) $m(l)$ from the reduced-order model in Eq. (4.5) with parameters from Table 4.4 for 20% haematocrit compared to simulation data.

The step function that approximates the RBC distribution in a channel cross-section has the form of an ellipse. Therefore, the major and minor semi-axes of this ellipse, a and b, need to be defined. I found that the best results are obtained when

1. the aspect ratio of the ellipse is determined by the ratio of the RMSD along the width and height directions (where the height direction is the axis of the compression),
2. the ellipse encloses 90% of the RBCs' centres of mass.

Next, I propose a function that describes the development of the radius m, along the compression axis, of the step function along the channel length l between the end of the compression (defined as $l = 0$) and the point $2D/3$ upstream of the bifurcation. The area of the ellipse is given by $A = \pi ab$ where a and b are the major and minor semi-axis of the ellipse for the step function. Once the minor axis b, which is $m(l)$, and the aspect ratio $\varepsilon(l) = a(l)/b(l)$ are known, the model can predict the number of RBCs entering either child branch.

The simulations show that there are three key mechanisms governing the lateral RBC distribution when entering and leaving the compression. The first is that the RBC distribution is suddenly narrowed by the compression. Secondly, upon exiting the compression, the RBC distribution sees a quick but only partial lateral recovery due to the expansion of the streamlines. Lastly, cell-cell interactions lead to a slow recovery of the RBC distribution to its pre-compression distribution via cross-streamline migration if given sufficient length. I model the flow expansion of the RBC distribution with a logistic term and the cross-streamline recovery with an exponential decay:

$$m(l) = m_c + \frac{m_{sl}}{1 + e^{-(l-l_g)/l_s}} + m_d \left(1 - e^{-l/l_r}\right). \tag{4.5}$$

For $l = 0$, at the downstream end of the compression, the equation returns the ellipse radius inside the compression, which is within 5% of m_c, due to the second term becoming very small when $l = 0$, but not vanishing. m_{sl} is the change in RBC distribution due to the flow expansion which occurs over a length scale $2l_g$. The length l_s determines the steepness of the slope. m_d is the change in RBC distribution due to cell-cell interaction, which occurs over a longer length scale $l_r \gg l_g$. For long distances, $l \to \infty$, I have $m(l) = m_c + m_{sl} + m_d$ which is the width of the fully recovered RBC distribution and the width of the unperturbed RBC distribution before the compression. If l is not sufficiently large, the RBC distribution is still affected by the compression, and the RBC partitioning at the bifurcation tends to be biased accordingly. Although it may be possible to construct a reduced-order model with fewer parameters, the advantage of equation (4.5) is that all parameters have a physical meaning and can potentially be predicted by separate models.

I obtained the numerical values of the parameters in the reduced-order model by fitting $m(l)$ to the simulation data for 10% and 20% haematocrit, respectively. The parameters are listed in Table 4.4, and Figure 4.8d shows an excellent agreement between $m(l)$ and the simulation data at $H_d = 20\%$. In particular, I find that $l_g \approx 0.66D$, independently of the chosen haematocrit. This value corresponds to the characteristic length which describes the streamline recovery after a distortion. I find that the cross-streamline recovery length l_r reduces by a factor of about 2 when the haematocrit is increased from 10% to 20%. This is in line with literature reporting that shear-induced diffusion is directly proportional to the particle concentration [69, 104, 193].

Table 4.4: Parameter values for equation (4.5) obtained by fitting the reduced-order model to simulation data.

haematocrit	m_c	m_{sl}	m_d	l_s	l_g	l_r
10%	1.62 μm	6.40 μm	2.19 μm	$0.17D$	$0.69D$	$13.8D$
20%	2.75 μm	7.41 μm	1.79 μm	$0.16D$	$0.67D$	$5.1D$

With the reduced-order model being calibrated, I can now predict the RBC partitioning at the downstream bifurcation and compare these results with actual RBC simulation data. I apply the separatrix model to the cross-sectional RBC distribution predicted by the reduced-order model at the length l that marks the distance between the compression and the point of bifurcation.

Table 4.5 compares the absolute difference in discharge haematocrit obtained from the HemeLB simulations and the reduced-order model. I find that the reduced-order model accurately predicts the impact of the compression on the RBC partitioning at the downstream bifurcation within 1% on average. Notwithstanding the assumptions underlying the reduced-order model, the error is low. This approach, therefore, provides a means of modelling the disturbance caused by a compressed vessel in network simulations, which has not been possible using established empirical models [68, 148]. Despite this success, further simulations are necessary to extend the applicability of the reduced-order model to a larger parameter space.

Table 4.5: Absolute differences of the discharge haematocrit in both child branches between the results of the HemeLB simulations and the predictions of the reduced-order model. In each box, the top left is the difference for the higher flowing child branch, whereas the bottom right is the difference for the lower flowing child branch. See Figure 4.1a–d for the respective geometries.

haematocrit	Control	Long compression no recovery	Short compression short recovery	Short compression long recovery
10%	-0.02% / 2.02%	0.22% / 0.42%	0.00% / 0.84%	0.29% / -0.25%
20%	0.89% / -2.70%	-0.62% / 3.23%	0.29% / -0.61%	0.96% / -2.54%

4.2.6 At 10% haematocrit, a converged suspension of RBCs requires a long development length

I observed that, at 20% haematocrit, the RMSD of the RBCs after $25D$ downstream of the compression has recovered to 98% of its original value prior to the compression, Figure 4.9a. However, at 10% haematocrit in the same geometry, the RMSD recovery is incomplete after the $25D$. In fact, equation (4.5) predicts a partial recovery of the RMSD at $50D$ to only 91% of its pre-compression value, Figure 4.9b.

Given the results in Figure 4.9b, I hypothesise that, at 10% haematocrit, details of the RBC initialisation in the simulation play a role. An RBC distribution that has not reached steady state upstream of the compression might affect the overall outcome of the simulation. To confirm this, I increased the length of the periodic tube that is used to generate the RBC distribution fed into the compression geometry from $25D$ (Figure 4.9b) to $100D$ (Figure 4.9c). I observed that the longer tube leads to a narrowing in the pre-compression distribution of the RBCs

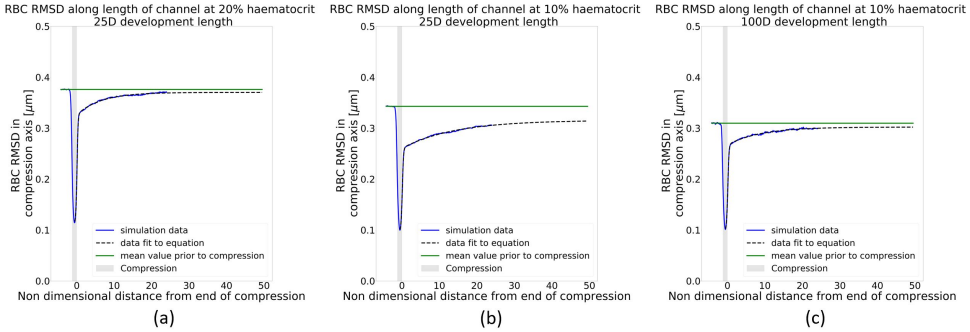

6

Figure 4.9: Recovery of RBC distribution after short compression. (a) Simulation at $H_d = 20\%$, (b–c) simulations at $H_d = 10\%$. (a) and (b) are simulations with the cells inserted after $25D$ of initialisation length. (c) is a simulation with cells inserted after an initialisation length of $100D$. The blue line is the simulation data, the black line is the prediction of the reduced-order model, and the green line is the mean value of the RMSD prior to the compression.

(Figure 4.9c). At 10% haematocrit, when the initialisation length is $100D$, I can assume that the RBC distribution has reached a steady state. In fact, Figure 4.9c shows that after $50D$ the RMSD of the RBCs has recovered to 98% of its pre-compression value. Despite the sensitivity of the pre-compression distribution on the cell initialisation strategy at $H_d = 10\%$, I found that the RBC dynamics after the compression is quantitatively and qualitatively similar for both RBC initialisation lengths used.

4.3 Discussion and conclusion

4.3.1 Discussion

The tumour microvasculature is abnormal and linked to tumour tissue hypoxia [95], which is a known biomarker for poor prognosis [129] and a barrier to recent promising immunotherapeutic approaches [124]. One such vascular abnormality is vessel compression [140]. Previous studies have shown that decompressing tumour vessels leads to increased survival rates [56], via increased perfusion [56, 95] and oxygen homogenisation [33], and that the degree of vascular compression correlates with reduced survival time [56]. However, the mechanism linking tumour decompression to increased oxygen homogeneity is unclear. Oxygen binds to haemoglobin in red blood cells (RBCs) and is transported through the vasculature with the RBCs. Previous work identified the reduced inter-bifurcation distance associated with the pro-angiogenic tumour environment as a source of oxygen heterogeneity via its impact on RBC partitioning at bifurcations [18]. However, the impact that other tumour vascular phenotypes, such as vessel compression, play on this process is not known.

In this chapter, I investigate the hypothesis that a vessel compression changes the partitioning of RCBs at a downstream bifurcation using a computational model. The numerical simulations show that a vessel compression enhances the disproportional partitioning of RBCs at a downstream bifurcation in favour of the higher flow rate child branch, occurring over a wide range of flow ratios. This is a consequence of the previously identified narrowing of the RBC distribution within the vessel cross-section [61].

Similarly to previous studies [55, 61], I identify the mechanism leading to this narrowing as RBC cross-streamline migration towards the vessel centre due to an increased shear rate within the compression. Once the RBCs leave the compression, their cross-sectional distribution gradually goes back to their pre-compression configuration in a haematocrit-dependent manner. This process is significantly slower at 10% haematocrit, where the dynamics occur over a length of ~ 50 vessel diameters. However, at 20% haematocrit, there is an almost instantaneous recovery, and after 2 vessel diameters in length, the difference in RBC partitioning compared to a control simulation is negligible. Furthermore, I show that at 30% haematocrit, the difference between the compressed and control simulation is negligible. The similarity between the control and compressed geometry at 30% haematocrit suggests the presence of a critical haematocrit above which vessel compression no longer alters the partitioning of RBCs at a bifurcation. I hypothesise that the different dynamics at 10%, 20% and 30% haematocrit are caused by cell-cell interaction which increases with haematocrit. I also show that an asymmetric compression does not lead to a measurable difference in the partitioning of RBCs compared to a symmetric compression. Likewise, a reduction and increase in flow rate by a factor of 5, respectively, do not significantly change the RBC partitioning.

This study focusses on a single vessel diameter of 33 μm. As the abnormal partitioning of RBCs is attributed to a narrowing of the cross-sectional distribution of RBCs in the vessel, it follows that for single file RBC flow in the microvasculature, the abnormal partitioning will be reduced or negligible. Therefore, I expect the abnormal partitioning to be of significance in channels with a diameter larger than ~ 8 μm, the typical diameter of an RBC.

I propose a reduced-order model to approximate the partitioning of RBCs at a bifurcation downstream of a compression, which I show has an error of 1% compared to the fully resolved numerical simulations, in the range of parameters studied. This model has the potential to overcome the computational tractability limitations associated with simulating RBC flow in large computational domains. The reduced-order model will help to understand the network effects arising from the abnormal partitioning of RBCs, such as haematocrit heterogeneity at a network level and compensatory mechanisms due to changes in vessel resistance with haematocrit. This will contribute to unravelling the dynamics of oxygen transport in large vascular tumour networks. In addition, the reduced-order model supports the hypothesis that

the recovery of the RBC distribution post compression is driven by cell-cell interaction. This is supported by the term modelling the post compression recovery in the reduced-order model being close to proportional to haematocrit, which is in line with RBC diffusion coefficients scaling linearly with haematocrit [69, 104].

The development of the cell-free layer, reported here as the cross-sectional distribution of red blood cells, is crucial for the findings in this work. As such, the presence of a repulsion force between red blood cells as they come to close to each other, or to a wall, needs to be discussed. In the dilute regime (10% haematocrit or lower), the repulsion force is negligeable as the immersed boudnary method resolves hydrodynamic interactions [195]. At higher haematocrits, the repulsion force is non-zero [100], however with the choice of parameters used, the literature [159] has shown good agreement between experiment and simulations, indicating it is not a leading order factor in the development of the cell-free layer.

The implications of the findings in this chapter are multiple. First, the results show that the effect of vessel compression on the downstream partitioning of RBCs is only apparent when discharge haematocrit and the distance between the compression and the bifurcation is sufficiently low. Another study showed that two consecutive bifurcations within a short distance can also alter the partitioning of RBCs at the downstream bifurcation [18]. Furthermore, a study showed that interbifurcation distances are much reduced in the tumour micro-environment [18], and Kamoun *et al.* [96] showed that hemodiluted vessels are more common and are present across a larger range of diameters in tumour networks than in controls. Taken together, this suggests that healthy vascular networks are structurally adapted to protect themselves from mechanisms leading to RBC transport heterogeneity, and that this may be compromised in diseased networks.

Second, previous studies have shown that decompressing tumour vessels leads to increased survival rates [33, 56]. This effect has been attributed to increased tumour perfusion due to reduced vessel resistance [56, 95] and reduced hypoxia fraction and increased oxygen homogeneity [33]. My results of anomalous RBC partitioning being unaffected by increases in flow rate support the view that increasing total perfusion through the network may not be sufficient to homogenise oxygenation if it is not accompanied by vessel decompression (or other forms of structural remodelling normalising RBC partitioning). This finding is further supported by recent work demonstrating that haematocrit plays a more important role in the delivery of oxygen to tissue than the speed of the RBCs [118], indicating that haematocrit normalisation can play a more critical role than increased perfusion for improved tissue oxygenation. As the simulation results in this chapter are steady-state, hypoxia resulting from the abnormal partitioning of red blood cells would be chronic hypoxia, and not cycling hypoxia.

Third, Kamoun *et al.* found that up to 29% of tumour vessels in an animal model of glioma experience hemodilution (defined as having haematocrits below 5%) and proposed a mechanism whereby extravasated plasma from leaky vessels would be reabsorbed by other vessels and lead to hemodilution [96]. Along similar lines, recent studies have reported findings of tissue hypoxia near perfused vessels [129]. The results demonstrate that, in the presence of vessel compression and uneven flow ratio at bifurcations, haematocrit can decrease from 20% to nearly 0% following two consecutive bifurcations without contributions from interstitial fluid. The present findings, therefore, provide an alternative explanation of the occurrence of hemodilution and plasma channels in tumour networks. Future work should elucidate the relative importance of these two mechanisms.

Lastly, I identified that, in the semi-dilute regime of 10% haematocrit, achieving convergence in an RBC suspension that has been disturbed requires longer distances than previously thought. Katanov *et al.* [100] reported that it takes a length of 25 diameters for the CFL of a randomly initialised suspension in a straight channel to converge. However, the data suggest that up to $100D$ of length is required for an initially compacted RBC distribution to expand and reach a steady distribution when the haematocrit is 10%. This finding supports the view that the cross-sectional distribution of RBCs at low *in vivo* haematocrits may be away from equilibrium not only in diseased vascular networks, as previously shown in tumours [18], but also under physiological conditions where inter-bifurcation lengths average fewer than $100D$. Further research into the network-level dynamics arising from these results is warranted.

As a final comment, these results should be considered for *in vitro* experiments that need to carefully consider the design of microfluidic devices if full convergence of RBC suspensions is required in the semi-dilute regime. It is also an additional challenge for *in silico* studies with open boundary conditions, where not only the insertion of cells needs to be considered [121], but also their cross-sectional distribution.

4.3.2 Conclusion

In this work, I have demonstrated that vessel compression can alter RBC partitioning at a downstream bifurcation, where the higher flowing child branch is further enriched in haematocrit compared to the lower flowing child branch. The altered red blood cell partitioning happens in a haematocrit-dependent and flow rate-independent manner. This chapter addressed the first objective of this thesis, to numerically investigate how vessel compression impacts the partitioning of red blood cells at a single vascular bifurcation. I argue that these findings contribute to the mechanistic understanding of haemodilution in tumour vascular networks and oxygen homogenisation following pharmacological solid tumour decompression. Further-

more, I have formulated a reduced-order model that will help future research elucidate how these effects propagate at a whole network level. Unravelling the causal relationship between tumour vascular structure and tissue oxygenation will pave the way for the development of new therapeutic strategies.

Chapter 5

Effect of vessel compression on blood flow in a model microcirculatory network

This results chapter addresses the second objective of this thesis, to investigate how vessel compression impacts red blood cell distribution in vascular networks. The key finding is that vessel compression both reduces the average haematocrit, and increases haematocrit heterogeneity, in vessels in the network. The mechanisms for these changes in haematocrit distribution are unravelled, and a parameter sweep shows that networks with lower inlet haematocrits are most susceptible to haemodilution from vessel compression over a wide range of compressed fraction of a network. Finally, the results are contextualised within the broader research of tumour tissue hypoxia, and blood flow. The results of this chapter are being written into a manuscript format to be published.

The chapter is divided into three main sections. Section 5.1 summarises the methods used in this chapter, section 5.2 presents the results of this chapter, and section 5.3 contains a discussion and conclusion for the work in this chapter.

5.1 Methods

This section outlines the methods used to investigate the effect of a vessel compression on blood flow at a network level. I initially use a computational model with high fidelity particulate blood flow simulations outlined in section 5.1.1, and then move towards a reduced-order model approach to blood flow modelling to investigate blood flow in a large network outlined in section 5.1.2. Section 5.1.3 explains how the model vascular networks are generated, and finally section 5.1.4 provides information on how the more complex data processing is performed in this chapter.

5.1.1 Particulate blood flow

In the first part of this chapter, I model blood flow as a suspension of deformable RBCs in a continuous plasma phase, as described in section 3.1. The simulation parameters for the particulate red blood cell model and the LBM are in Table 5.1 and Table 5.2, respectively. In the inlet channel, I set the numerical Reynolds number to 1 for numerical tractability, and the red blood cell capillary number to 0.1, as per the previous chapter results showing capillary number is not a leading order parameter, see section 4.2.

(a) (b)

Figure 5.1: (a) Snapshot of a fully resolved cellular blood flow simulation. (b) Rotated snapshot of same simulation to show compression has an elliptical cross-section.

As in section 4.1, I assume the cross-section of the vessels to be elliptical. The perimeter of the cross-section is assumed to be constant along the channel, setting the ellipse perimeter to the same value as the uncompressed circular cross-section. The segment with an elliptical cross-section has an aspect ratio of 4.26, following reports from the literature [56]. Preceding the elliptical cross-section, I have an initialisation length of 25 vessel diameters, to initialise the distribution of the red blood cells [100], followed by the compression which is 4 vessel diameters long. Figure 5.1 shows an image of one of the simulations for illustration purposes.

The outlet boundary conditions are set as velocities, according to each simulation described in section 5.2, and the inlet boundary is set as an arbitrary pressure condition, which has no effect on the simulation outcome. The inlet haematocrit is set for each simulation as described in section 5.2

Table 5.1: Parameters used for the red blood cell model. All values are given in simulation units, unless specified otherwise.

Parameter	Symbol	Value
Strain modulus	κ_s	depends on shear rate for $Ca = 0.1$
Dilation modulus, lattice units	$\tilde{\kappa}_\alpha$	0.5
Bending modulus	κ_B	depends on shear rate for $Ca = 0.1$
Surface area modulus, lattice units	$\tilde{\kappa}_A$	1
Volume modulus, lattice units	$\tilde{\kappa}_V$	1
Föppl-von Kármán number	$\Gamma = \kappa_B/(\kappa_S r_{RBC}^2)$	1/400
Number of faces in RBC mesh	N_f	720
RBC radius	r_{RBC}	4 μm

Table 5.2: Simulation parameters used for the lattice-Boltzmann method.

Parameter	Symbol	Unit	Value
Voxel size	Δx	μm	0.6667
Timestep	Δt	s	7.41×10^{-8}
Relaxation time	τ	Lattice units	1
Fluid viscosity	μ	mPa s	1
RBC cytoplasm viscosity	μ	mPa s	1
Fluid density	ρ	kg/m^3	1000

5.1.2 Network blood flow

In the second part of this chapter, I model blood flow as a continuous fluid on a set of 1-dimensional vessels, as described in section 3.2.

This chapter studies blood flow through networks with compressed vessels, and the vessel compression has to be accounted for in two ways. The first one is the abnormal partitioning of red blood cells, as identified in section 4.2, and the second one is a change in vessel resistance due to the altered cross-section.

The abnormal partitioning of red blood cells is dealt with by adapting the plasma skimming model, equation (3.40)-(3.42), for compressed vessels. The method for adapting the plasma skimming model for compressed vessels forms part of the results of this chapter. Chapter 4 presents a reduced-order model for predicting red blood cell partitioning in compressed vessels. However, this chapter will adapt an existing reduced-order model, equations (3.40)-(3.42), due to its efficiency and accuracy.

The increased resistance due to the changed cross-section is dealt with using Poiseuille's law for an elliptical cross-section [15], see equation (3.34) in section 4.2 for details.

When vessels are treated as compressed, The effect of abnormal partitioning of red blood cells and increased resistance can be numerically isolated, as they are separate steps in the numerical scheme, see section 3.2.2 for details. Separating the two effects allows me to study the effect of increased resistance without abnormal partitioning, called increased resistance case (IR); and the effect of abnormal partitioning of RBCs without increased resistance, called abnormal partitioning case (AP). This leads to four different types of simulation cases, shown in Table 5.3.

Table 5.3: Table summarising four possible scenarios for how vessels are treated in network simulations. This determines how the compressed vessels, in red in Figure 5.2, are treated.

Name	Description	Flow Solver	Phase separation model
Control case	Vessels are treated as non-compressed for a control	Equation (3.33), Poiseuille circular	Equations (3.40)-(3.42)
Increased resistance and abnormal partitioning case (IR+AP), fully compressed model	Vessels are treated as having an increased resistance due to reduced cross-section, and abnormal partitioning at bifurcations	Equation (3.34), Poiseuille elliptical	Updated as part of results
Increased resistance case (IR)	Vessels are just treated as having an increased resistance due to reduced cross-section	Equation (3.34), Poiseuille elliptical	Equations (3.40)-(3.42)
Abnormal partitioning case (AP)	Vessels are just treated as having abnormal partitioning at bifurcations	Equation (3.33), Poiseuille circular	Updated as part of results

The networks in which the blood flow is simulated are conveniently set to have a single inlet and a single outlet. This leads to the flow boundary conditions not being relevant to calculate the haematocrit distribution in the network, as only the flow ratios at the bifurcations matter, and not the absolute flowrate. Thus, a pressure of 0 is set at the outlet, and an inlet velocity is set according to typical values from the microcirculation, but without consequence on the result of the simulations. The inlet boundary condition for haematocrit is first set at 20%, a typical value for the microcirculation [153], and is then varied as part of the study.

5.1.3 Artificial network generation

The networks are generated using the open source software Tumorcode [59, 162, 163]. It uses an algorithm to randomly generate vessel networks on a mesh. The algorithm is based on Murray's law and geometrical properties for capillaries, arterioles, and venules. Tumorcode also has the ability to reproduce the evolution of a tumour vessel network in the *in silico* generated network. However, for the purpose of the research here only the healthy networks are used, to isolate the network from other structural abnormalities. An example of a generated network is depicted in Figure 5.2. I use the two-dimensional default network generator, with a single inlet and a single outlet. The two-dimensional networks are generated within a square surface of 5000μm by 5000μm.

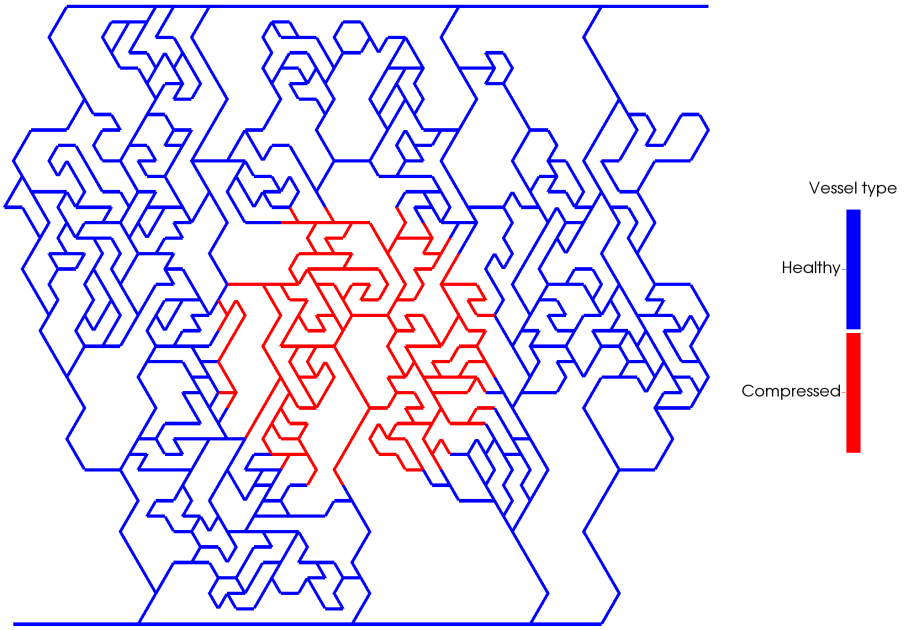

Figure 5.2: Depiction of the network in which the blood flow simulations are performed. The blue vessels are treated as normal blood vessels, the red vessels are treated as compressed vessels, also called compressed region. The inlet is at the bottom left, and the outlet is at the top right.

Within the network, I treat some vessels differently, detailed in Table 5.3, which I call the compressed vessels or compressed region. Initially, the compressed vessels are in the centre of the network and are vessels that have both ends within a 1000μm radius of the centre of the vessel network, shown in red in Figure 5.2. I also vary the fraction of compressed vessels, using a radial model and a random model. The radial model is a model for tumours where the solid stress is higher in the centre, thereby compressing vessels more in the centre of the tumour [188]. In the radial model, the compressed vessels are the vessels closest to the centre of the network, Figure 5.3a-f illustrates the radial model. The random model is an alternative model where compressed vessels are not deterministically situated. In the random model, a random fraction of vessels are compressed, Figure 5.3g-l illustrates the random model.

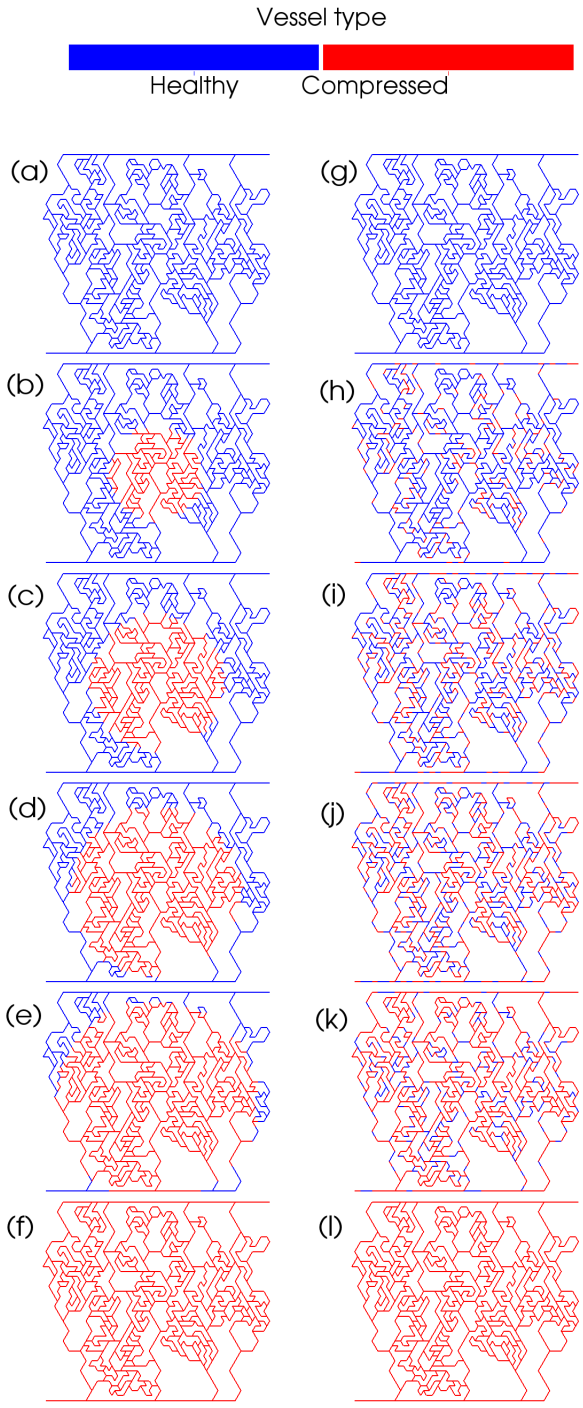

Figure 5.3: Illustration for fraction of compressed vessels in the network. (a)-(f) illustrates the radial model from 0% to 100% of compressed vessels in steps of 20%. (g)-(l) illustrates the random model from 0% to 100% of compressed vessels in steps of 20%.

5.1.4 Processing results

To process the results, I also define a set of critical bifurcations. A critical bifurcation is defined as a diverging bifurcation where:

1. One of the child branches has to have every possible path emanating from it flow through the compressed region
2. The other child branch has to have at least one path emanating from it not flowing through the compressed region

Figure 5.4 illustrates one of these critical bifurcations.

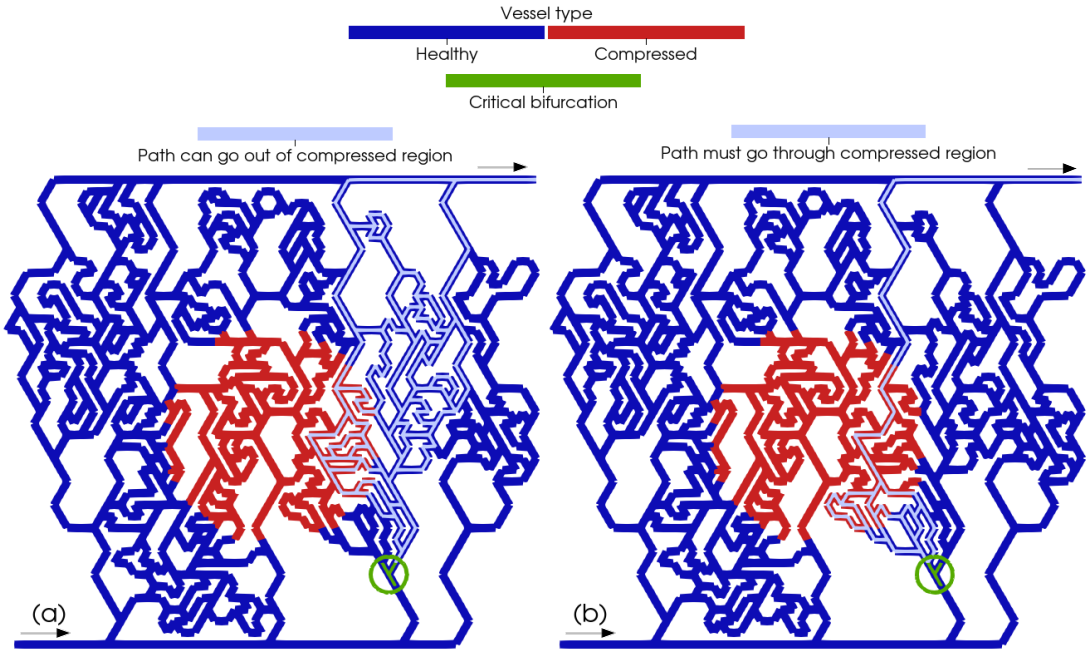

Figure 5.4: Illustration of one critical bifurcation. In dark blue are the vessels which are treated as non-compressed, and in red the vessels treated as compressed. The green vessels are the vessels in the identified critical bifurcation, and are circled in green for visibility. The arrows at the inlets and outlets indicate the direction of flow. (a) the vessels in light blue are all the paths from one of the child branches of the critical bifurcation, where at least one path can flow outside of the compressed region. (b) the vessels in light blue are all the paths from one of the child branches of the critical bifurcation, where all paths must flow through the compressed region.

In addition, to quantify the effect that vessel compression has on the reduction of haematocrit in the networks, I define metrics which are all proxies to quantify haematocrit reduction in a network. All of the metrics use the basic form,

$$F_{haemodiluted} = \frac{N_{haemodiluted}}{N_{total}}, \tag{5.1}$$

where $F_{haemodiluted}$ is the fraction of haemodiluted vessels in the network, N_{total} is the total number of vessels in the network, and $N_{haemodiluted}$ is the number of haemodiluted vessels in the network. The metric effectively expresses the fraction of haemodiluted vessels in a network, and only what constitutes haemodilution needs to be defined. I define three different conditions for a vessel to be haemodiluted, which are that a vessel is haemodiluted if:

1. the haematocrit in a given vessel has a value of 50% or less of the haematocrit of the same vessel in the control case.
2. the haematocrit in a given vessel has a value of 50% or less of the inlet haematocrit to the network.
3. the haematocrit in a given vessel is below 1%.

5.2 Results

5.2.1 Updating the phase separation model to account for vessel compression

To model the partitioning of red blood cells in compressed vessels at a network level, I need a reduced-order model due to the high computational cost of fully resolved simulations. Pries and coworkers developed a model for the partitioning of red blood cells, described in section 3.2.1, which works well for non-compressed vessels [148, 150], but is not adapted for compressed vessels [50]. I start by adapting Pries' model for the partitioning of RBCs in compressed vessels. I choose to adapt Pries' model due to its robustness and ubiquity in the literature, see section 3.2.1 for more details.

I hypothesise that I can adapt Pries' model to account for vessel compression by changing the functional form for X_0. I choose to adapt X_0 for a vessel compression for two reasons. The first one is that X_0 is understood as a proxy for the cell-free layer [115], and the previous chapter identifies a narrowing of the RBC distribution as the mechanism for abnormal RBC partitioning, Figure 4.4, which is akin to an increase in the cell-free layer. Secondly, in the previous chapter, the flow ratio was varied to understand its effect on the abnormal partitioning of RBCs. This provided me with data to demonstrate that X_0 is the suitable term to adapt. I plot the data in Figure 4.5 as data points, and produce plasma skimming curves with the original phase separation model and with an updated X_0 term, fitted to the data, in the phase separation model. Figure 5.5 demonstrates that, solely by changing the X_0 term, the plasma skimming curve closely fits the RBC partitioning due to a compression.

Supported by this evidence, I set out to find a new functional form for X_0 for when vessels are compressed. Figure 5.6 is a flowchart illustrating the method I use to update X_0.

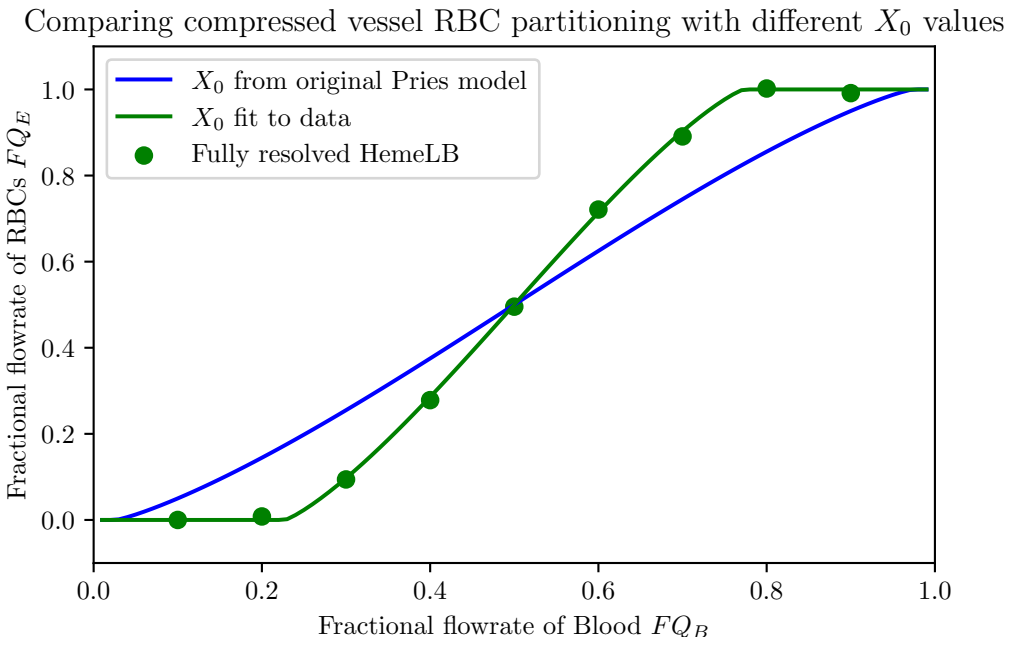

Figure 5.5: Plots the data from Figure 4.5 (green points) and compares how well the original phase separation empirical model works (blue line), and how changing solely the X_0 term improves the fit (green line). The X_0 term for the green line is obtained through a fit to the data in Figure 4.5 using the non-linear least squares method.

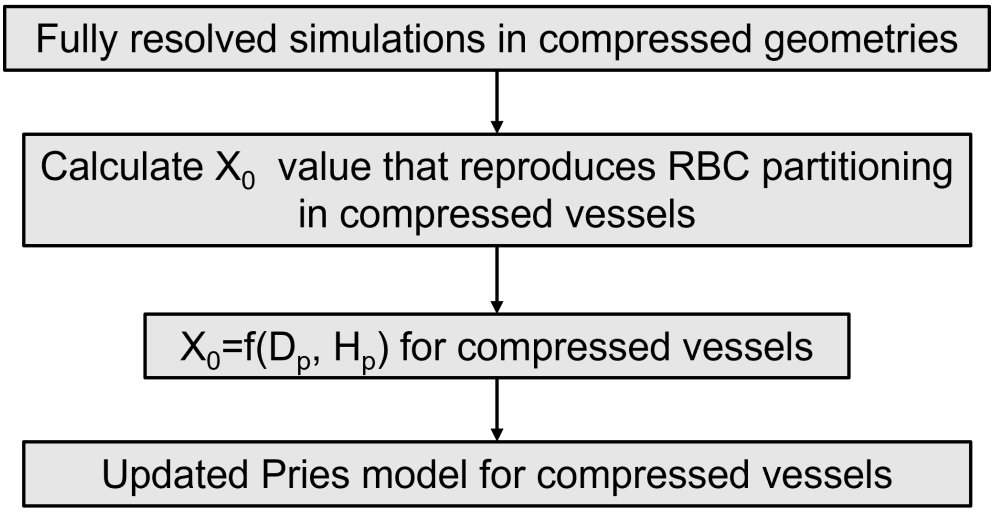

Figure 5.6: Flow chart of the process to calculate the new X_0 values for red blood cell partitioning in compressed vessels.

I fully resolve a set of 24 bifurcations with HemeLB simulations, see table 5.4 for a summary of the bifurcations, and Figure 5.1 for an illustration of one of these simulations. The flow ratios, haematocrits, and diameters in Table 5.4 were taken from the diverging bifurcations in the network within the compressed region, Figure 5.2, to be representative of the bifurcations

that the updated phase separation model will resolve. The haematocrit and flow ratio in these bifurcations was resolved by solving the Poiseuille flow through the entire network using the standard phase separation model for phase separation. The parent branch diameters in Table 5.4 is the undeformed diameter, the deformed one is calculated as described in the method in section 4.1 with an aspect ratio of 4.26, as per literature reports [56].

Four simulations were excluded from the calculation, in table 5.4 they are simulation numbers 12, 13, 17, and 19. These simulations were excluded as in each of those bifurcations one of the child branches had a 0% haematocrit value, and due to the nature of the model having three equations, equations (3.40)-(3.42), when a 0% haematocrit is calculated in the child branch only a range of values can be calculated for X_0, and not a unique value.

Next, I need to find the X_0 values for the results of these simulations that match the child branch haematocrits from the fully resolved simulations. I analytically invert the main equation of the model, equation (3.41), to make X_0 the subject of the equation,

$$X_0 = \frac{FQ_B + FQ_B e^{\alpha} - e^{\alpha}}{1 - e^{\alpha}}, \tag{5.2}$$

where α is defined as,

$$\alpha = \frac{\text{logit}(FQ_E) - A}{B}, \tag{5.3}$$

where A and B are terms defined in the original empirical model, see section 3.2.1.

I can now calculate what value of X_0 reproduces the partitioning of red blood cells through a compressed bifurcation, which is known from the fully resolved simulations. This is done by having a known FQ_E value, calculated from the haematocrit values in table 5.4, and solving for X_0 in equation (5.2). The new X_0 value calculated for compressed vessels will henceforth be referred to as X_0^c, where the superscript c denotes a compression.

The next step is to derive a new functional form for X_0^c. As in the original phase separation model $X_0 = f(D,H)$, the simplest assumption is that the updated X_0^c functional form will depend on the same parameters, $X_0^c = f(D,H)$. I plot X_0^c against H, Figure 5.7a, and X_o^c against D, Figure 5.7b. Although the data are three-dimensional, I plot two two-dimensional plots for ease of visualisation. Figure 5.7 shows that, similarly to the original functional form for X_0, X_0^c is inversely proportional to D and decreases linearly with H. Therefore, I keep the original functional form, and update the pre-factor,

$$X_0^c = C\frac{1 - H_D}{D_P}, \tag{5.4}$$

Simulation	$D_{PB}[\mu m]$	$D_{CB1}[\mu m]$	$D_{CB2}[\mu m]$	$Q_{fraction}$	$H_{PB}[\%]$	$H_{CB1}[\%]$	$H_{CB2}[\%]$
1	46.08	45.00	18.89	0.90	21.70	23.24	6.39
2	47.62	46.60	18.89	0.92	20.36	22.02	2.11
3	43.26	18.89	42.03	0.14	22.89	15.06	25.36
4	45.00	43.86	18.89	0.91	22.73	24.63	4.51
5	48.59	47.62	18.89	0.93	19.67	21.45	2.32
6	15.00	15.00	15.00	0.48	3.72	3.27	3.70
7	41.38	37.79	25.64	0.82	25.04	26.82	16.43
8	21.63	18.89	15.00	0.67	18.11	20.55	13.46
9	46.60	46.08	15.00	0.92	20.67	22.57	1.08
10	43.86	43.26	15.00	0.94	22.93	24.32	1.01
11	18.89	15.00	15.00	0.54	12.96	13.75	11.80
12	42.03	41.38	15.00	0.98	24.91	25.52	0.00
13	25.64	21.63	28.89	0.90	16.61	18.21	0.00
14	15.00	15.00	15.00	0.49	9.03	8.34	9.56
15	18.89	15.00	15.00	0.41	13.03	8.62	15.69
16	18.89	15.00	15.00	0.52	6.03	0.23	8.49
17	15.00	15.00	15.00	0.76	9.53	12.54	0.00
18	18.89	15.00	15.00	0.62	10.85	13.92	5.46
19	15.00	15.00	15.00	0.87	17.67	19.30	0.00
20	21.63	15.00	18.89	0.48	23.61	24.01	23.05
21	18.89	15.00	15.00	0.68	15.89	19.66	7.18
22	18.89	15.00	15.00	0.23	17.61	1.28	21.90
23	15.00	15.00	15.00	0.30	18.75	8.37	23.08
24	23.81	21.63	15.00	0.68	16.88	18.52	13.46

Table 5.4: Parameters of the fully resolved simulations to calculate an updated X_0 parameter for compressed vessels. All parent branches are compressed with an aspect ratio of 4.26. D_{PB} is the parent branch diameter, D_{CB1} is the diameter of the first child branch, D_{CB2} is the diameter of the second child branch, $Q_{fraction}$ is the flowrate fraction to the first child branch, H_{PB} is the parent branch haematocrit, H_{CB1} is the haematocrit of the first child branch, and H_{CB2} is the haematocrit of the second child branch.

where C is the pre-factor to be determined for the new functional form for X_0^c. I use a non-linear least squares method to fit the pre-factor, C, and obtain a value of 4.16, yielding,

$$X_0^c = 4.16\frac{1-H_D}{D_P}\,. \tag{5.5}$$

I now verify that the updated X_0^c functional form accurately captures the RBC partitioning from the fully resolved simulations. Figure 5.8a plots the analytically predicted X_0^c value from equation (5.2) against X_0^c from the new functional form from equation (5.5). Figure 5.8b plots the haematocrits predicted from the updated X_0^c functional form using equation (5.5) against the haematocrit of the child branches from the fully resolved simulations in Table 5.4. Assuming a perfect fit, one would expect the points to land on the diagonal line in Figure 5.8.

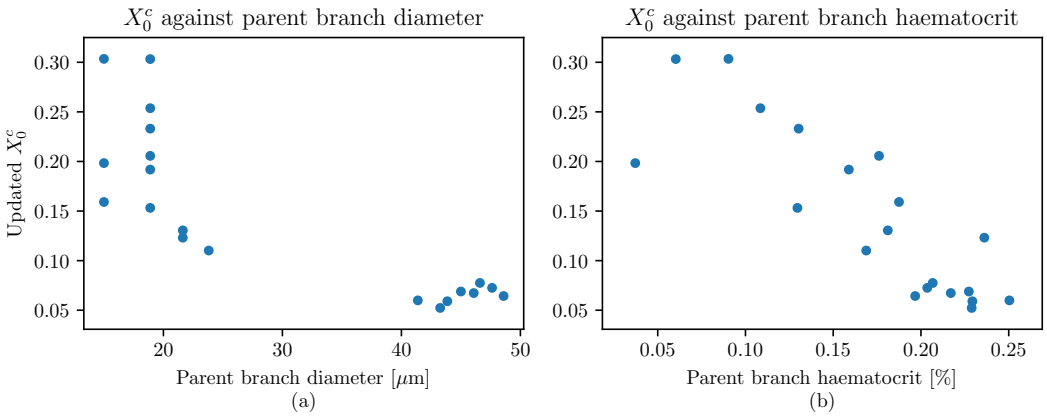

Figure 5.7: (a) The value of X_0^c calculated from the fully resolved simulations with equation (5.2) against the parent branch diameter. (b) The value of X_0^c calculated from the fully resolved simulations with equation (5.2) against the parent branch haematocrit. The data suggest that in (a) X_0^c is inversely proportional to D, and in (b) X_0^c decreases linearly with H.

Figure 5.8a shows that the functional form for X_0^c does not perfectly capture the analytically calculated X_0^c term. However, Figure 5.8b shows that the haematocrit in the child branches, the desired output of the model, is well predicted by the updated X_0^c term with an R^2 value of 0.96, and fits the data much better than the original model, with an R^2 value of 0.81.

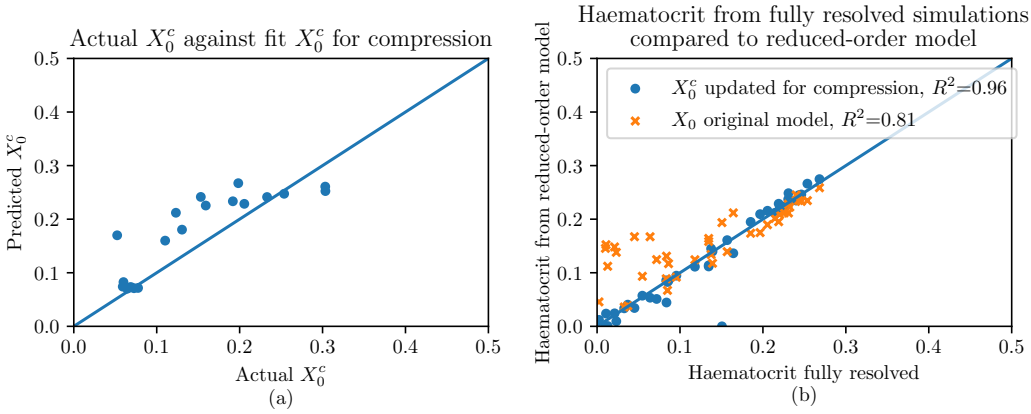

Figure 5.8: (a) Plot of the predicted X_0^c from equation (5.5) against the actual X_0^c as calculated from fully resolved simulations. (b) Plot of the predicted haematocrit (using the updated X_0^c in blue and the original X_0 in orange) against the fully resolved haematocrit. The diagonal line in (a) and (b) is a visual aid to see how close the predicted values are to the values obtained from fully resolved simulations.

There is one outlier in Figure 5.8b, it corresponds to simulation 3 in Table 5.4, which has an extreme flow ratio and child branch diameter ratio. The extreme flow ratio is very sensitive to X_0^c, as it may predict the depletion of a branch when that is not the case. Haematocrits of the child branches come in pairs, and it is worth noting that although one of the child branches poorly predicts haematocrit, the other child branch haematocrit is well predicted. There is a single outlier, and not two, due to the non-linear relationship between the flow ratio of blood and the flow ratio of RBCs.

I conclude that the updated functional form, equation (5.5), is suitable to predict RBC partitioning at a bifurcation when the parent branch is compressed. This is the tool I will use to investigate the effect of vessel compression on RBC dynamics at a network level.

5.2.2 Vessel compression reduces average haematocrit and increases haematocrit heterogeneity in a network

I start by investigating how the compressed vessels alter the distribution of RBCs, and therefore haematocrit, at a network level. I run the network model for blood flow in an artificially generated network, shown in Figure 5.2, where I treat the vessels in red as being compressed according to the description in Table 5.3.

Figure 5.9 shows that when the vessels are treated with the fully compressed model, there is a reduction in the average haematocrit of the compressed vessels compared to the control. The average haematocrit within the compressed vessels is reduced from 19.19% to 8.75%. Figure 5.9 also shows that the distribution of haematocrit within the compressed vessels is wider, ranging from [0.0%, 26.78%] in the control and increasing to [0.0%, 32.92%] in the fully compressed case. The frequency of 0% haematocrit vessels in the compressed vessels is increased from 1 vessel in the control case to 11 vessels in the fully compressed case, showing that in the fully compressed case, there are also more vessels that are depleted of RBCs, gravely impairing their oxygen transport capability.

Next, I separately investigate the effect of increased resistance and of abnormal partitioning. This is rendered possible as the model is numerical, and can thus individually deactivate these effects. Figure 5.9 shows the distribution of haematocrits when simulating the increased resistance case, and the abnormal partitioning case.

When comparing the increased resistance and the control cases, one initially sees that the haematocrit values are lower, but that the nature of the distribution is largely unchanged, Figure 5.9. Indeed, the distribution remains normal, with a slight skew, when comparing the increased resistance and the control cases. On the other hand, the resistance case haemato-

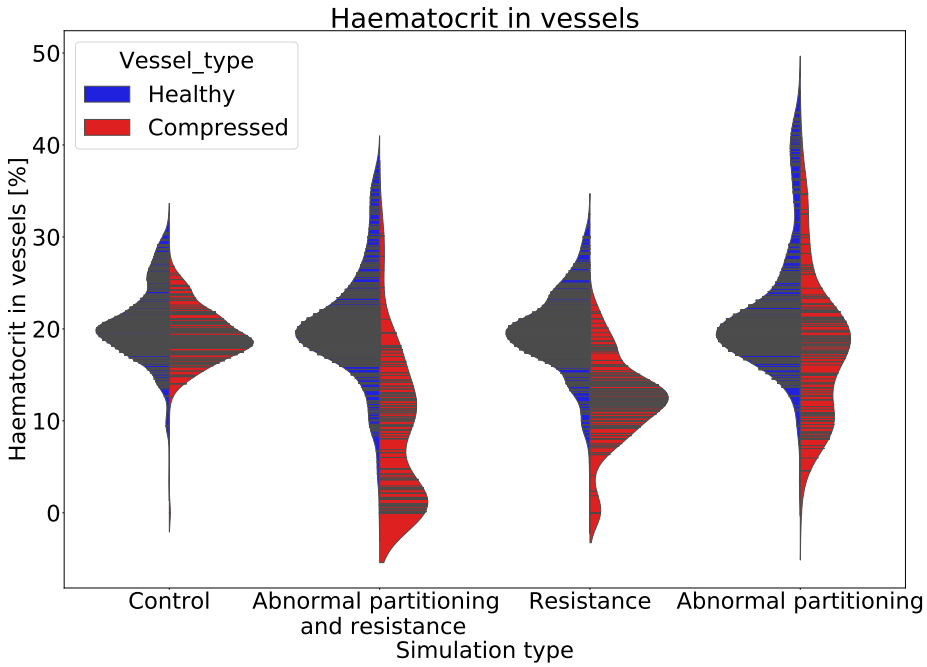

Figure 5.9: Violin plots of haematocrit distribution within the vessel network. Blue corresponds to the blue vessels, in Figure 5.2, and treats vessels as healthy and non-compressed. Red corresponds to the red vessels, Figure 5.2, and denotes the compressed region, treated as described in Table 5.3. The control case treats all vessels as normal vessels. Abnormal partitioning and resistance case treats compressed vessels as having an increased resistance and abnormal partitioning. The abnormal partitioning case treats compressed vessels as having just abnormal partitioning. Resistance case treats compressed vessels as having just increased resistance.

crit distribution bears no resemblance to the distribution of the abnormal partitioning of RBCs case, which appears bimodal. The bimodal distribution for the case with abnormal partitioning indicates that increased haematocrit heterogeneity is the result of abnormal partitioning of RBCs, and not the increased resistance.

Finally, one sees that both the increased resistance and abnormal partitioning reduce the average haematocrit in the compressed region, down to 12.11% and 17.68% respectively, compared to 19.19% in the control. The reduction in average haematocrit in both cases indicates that they each contribute to reducing the average haematocrit compared to the control. Interestingly, both the increase in resistance and the abnormal partitioning have non-negligible effects on the reduction in haematocrit, indicating that to understand haematocrit distribution in compressed networks, one must account for both increased flow resistance

and abnormal partitioning of red blood cells due to the compression of the vessel. This also suggests that when the full model is applied, there are two separate mechanisms reducing the average haematocrit in the compressed vessels, one due to the increased resistance and one due to the abnormal partitioning. I will next investigate those mechanisms.

5.2.3 Mechanism for the effect of increased resistance in compressed vessels

I start by investigating the effect that the increased flow resistance has on haematocrit within the network. I numerically remove the effect of abnormal partitioning, giving the opportunity to study the effect of increased flow resistance isolated from the abnormal partitioning. I hypothesise that the effect of increased resistance in the compressed vessels results from diverting flow away from the compressed vessels. As the phase separation effect disproportionally favours red blood cell flow to the higher flowing child branch, this disproportionally reduces the red blood cell flow going through the compressed region and therefore reduces the haematocrit of the compressed vessels.

The first step is to identify a set of critical bifurcations. The definition of a critical bifurcation is detailed in section 5.1.4 and illustrated in Figure 5.4. There are 11 critical bifurcations in the network.

I then compare the flowrate ratio at these critical bifurcations between the control case and the increased resistance case. Figure 5.10a shows that the flow ratio is always reduced in the child branch which necessarily flows through the compressed region in the increased flow resistance case. These results demonstrate that flow is diverted away from the paths that lead to the compressed region when flow resistance is implemented. This is expected as according to Poiseuille's law, flow follows the path of least resistance, with a dependency on the radius of the channel to the fourth power, equation (3.33).

Next, I show how the reduction in flow ratio to the compressed region leads to a reduction in haematocrit to the compressed region. I calculate how the haematocrit in the child branches differs with the altered flow ratio to the child branches. I take the geometrical properties of the critical bifurcations and take the parent branch haematocrit of the increased resistance case. I then resolve the haematocrit in the child branches using the original phase separation model, using the flow ratio with and without the increased resistance. Figure 5.10b shows that the change in flow ratio reduces the haematocrit in the child branch with the reduced flow ratio. This is explained by the partitioning of RBCs to a child branch being a function of flow ratio, with a disproportionate marginal loss in RBC flow with decreasing flow ratio. As the child branch that must flow through the compressed region has a reduced flow ratio, this is a mechanism explaining the reduction in haematocrit within the compression due to increased flow resistance.

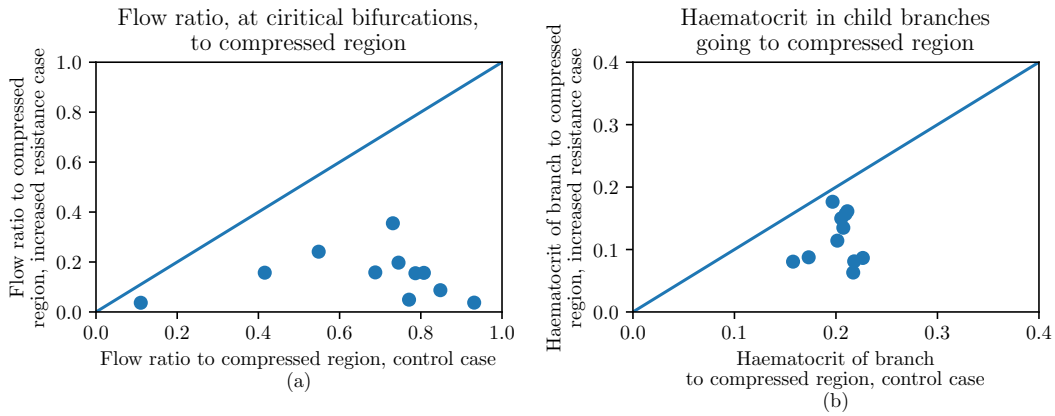

Figure 5.10: Effect of increased resistance at critical bifurcations in the vascular network. (a) Plots the flow ratio into the compressed region at critical bifurcations of the control case against the increased resistance case, showing a reduced flow ratio into the compressed region when compressed vessels have an increased resistance. (b) Plots the haematocrit of the child branch at a critical bifurcation flowing into the compressed region in the control case and the increased resistance case, showing a reduced haematocrit in the branch flowing into the compressed region when there is an increased resistance. The diagonal line in (a) and (b) is a visual aid to see how close the values in the increased resistance case are to the control case.

In summary, the increased flow resistance diverts flow away from the compressed region as flow follows the path of least resistance. This leads critical bifurcations to have a reduced flow ratio to the child branch flowing uniquely through the compressed region. Due to the RBC partitioning mechanism at bifurcations, this reduces the haematocrit of the branches leading to the compressed region when there is increased flow resistance, and mechanically leads to a reduced haematocrit of all the downstream vessels which are situated within the compressed region.

5.2.4 Mechanism for the effect of abnormal partitioning in compressed vessels

Next, I investigate the effect that the abnormal partitioning has on haematocrit within the network. I numerically remove the effect of the increased flow resistance due to a vessel compression, giving the opportunity to study the effect of abnormal partitioning isolated from the effect on increased flow resistance. I hypothesise that the reduced average haematocrit in the compressed region caused by abnormal partitioning alone is due to an enhanced network Fahraeus effect. The network Fahraeus effect contributes to the reduction of av-

erage haematocrit at each successive bifurcation as the average haematocrit of the two child branches at a bifurcation is lower than the haematocrit of the parent branch [149]. I hypothesise that this effect is exacerbated by the increased haematocrit heterogeneity at a bifurcation due to the abnormal partitioning.

To investigate this hypothesis, I start by showing that when there is phase separation of blood and red blood cells, the average haematocrit of the two child branches is lower than the parent branch haematocrit. At individual bifurcations, it is possible to show mathematically, with some assumptions, that the average haematocrit of the child branches is lower than the haematocrit of the parent branch. One can start with a mass balance on the blood flow, and the red blood cell flow, using Figure 3.9 as a sketch for the system,

$$Q_0 = Q_1 + Q_2 \,, \tag{5.6}$$

$$Q_0 H_0 = Q_1 H_1 + Q_2 H_2 \,. \tag{5.7}$$

One can then express the haematocrit in the child branches as a deviation from the parent branch haematocrit where one assumes branch 1 to be the enriched branch,

$$H_1 = H_0 + \Delta H_1 \,, \tag{5.8}$$

$$H_2 = H_0 - \Delta H_2 \,, \tag{5.9}$$

Combining equation (5.6) with equation (5.7) and substituting in equations (5.8) and (5.9), one can simplify the result to,

$$Q_1 \Delta H_1 = Q_2 \Delta H_2 \,. \tag{5.10}$$

If one assumes unequal partitioning of blood flow, such that $Q_1 > Q_2$, then to satisfy equation (5.10) it must follow that $\Delta H_2 > \Delta H_1$.

One may then calculate the average haematocrit of the child branches,

$$\overline{H}_{child} = \frac{H_0 + \Delta H_1}{2} + \frac{H_0 - \Delta H_2}{2} \,, \tag{5.11}$$

which simplifies to

$$\overline{H}_{child} = H_0 + \frac{\Delta H_1 - \Delta H_2}{2} \,, \tag{5.12}$$

and as, previously showed, $\Delta H_2 > \Delta H_1$, then it follows that,

$$\frac{\Delta H_1 - \Delta H_2}{2} < 0\,, \tag{5.13}$$

and therefore that

$$\overline{H}_{child} < H_0\,, \tag{5.14}$$

as the fraction on the RHS of the inequality in equation (5.12) must be negative, to satisfy equation (5.13). This inequality indicates that the average haematocrit of the child branches must be lower than the haematocrit of the parent branch, due to the non-linear relation between blood flow ratio and red blood cell flow ratio. This implies a reduction in average haematocrit in child branches, and the larger the heterogeneity of haematocrit at a bifurcation, the larger the reduction in average haematocrit. It follows that the average reduction in haematocrit at a divergent bifurcation is dependent on the degree of heterogeneity of RBC partitioning at the bifurcation, with increased haematocrit heterogeneity leading to greater average haematocrit reduction.

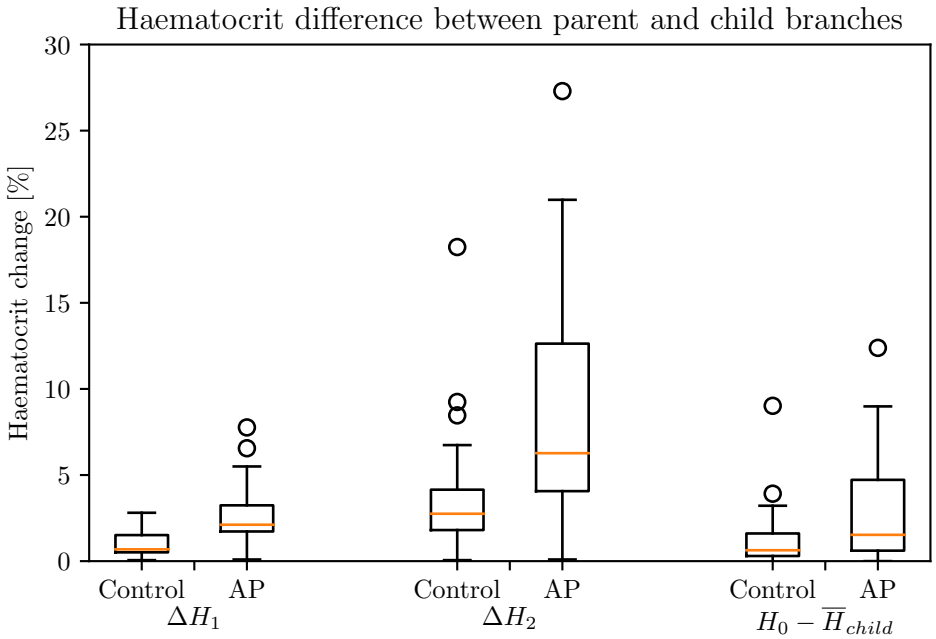

Figure 5.11: Shows the enrichment, ΔH_1, and impoverishment, ΔH_2, of the compressed vessels for the control and abnormal partitioning (AP) case. Also shows the reduction in average haematocrit between the parent branch and the average of the child branches, $H_0 - \overline{H}_{child}$, at a bifurcation for the control case and the abnormal partitioning case.

Using the terminology of ΔH_1 and ΔH_2 from above, I plot the data from bifurcations in the compressed portion of the network for the control case and the abnormal partititoning case, Figure 5.11. Figure 5.11 effectively shows that ΔH_1 and ΔH_2 are higher in the abnormal partititoning case compared to the control case, and that the mean reduction in haematocrit is increased in the abnormal partititoning case compared to the control. As the reduction in mean haematocrit in the two child branches with abnormal partitioning is more pronounced, it evidences a stronger network Fahraeus effect. In turn, the enhanced heterogeneity in haematocrit due to the abnormal partitioning suffices to explain the wider distribution of haematocrits within the compressed portion of the network observed in Figure 5.9.

5.2.5 Conditions for haematocrit reduction in compressed networks

Finally, I investigate under what conditions networks are susceptible to haemodilution when vessel compression is present. To that end, I perform a parameter sweep over a wide range of relevant inlet haematocrits to the network, and over the entire range of fraction of compressed vessels, using the fully compressed model. As described in section 5.1 and in Figure 5.3, I used two models for the fraction of compressed vessels in a network, one where the more central vessels are compressed first, and one where random vessels are compressed. Haemodilution is defined in three different ways, see section 5.1.

Figure 5.12a shows the fraction of haemodiluted vessels in the radial model, using the first definition for haemodilution (i.e. a vessel is haemodiluted if it has a haematocrit less than half of the same vessel in the control case). The results show that haemodilution generally increases with increasing fraction of compressed vessels, and with reducing inlet haematocrit. 5.12a also indicates that, although haemodilution is experienced over the entire parameter range, it is most pronounced when the inlet haematocrit to the network is relatively low, i.e. below 15%. In addition, this haemodilution effect is observed over a wide range of fraction of compressed vessels, suggesting that a low fraction of compressed vessels is sufficient for the network to experience haemodilution. Lastly, when vessels are randomly compressed, Figure 5.12b, it is interesting to see that the overall haemodilution is not very different compared to the radial model of compressed vessels.

I also observe, from Figure 5.12, that the highest fraction of haemodiluted vessels is not when the fraction of compressed vessels is highest. Indeed, at a fraction of compressed vessels of around 80%, haemodilution decreases as the fraction of compressed vessels continues to increase. I attribute this to the mechanism for haematocrit reduction in the networks. I previously identified that increased vessel resistance has the most pronounced effect on haematocrit reduction, and that it depends on flow redirection. However, when a very high fraction of the network is compressed, the opportunity for flow redirection is reduced, leading to a decrease in the effect of flow resistance within the network, thus reducing the effect of compression on haematocrit reduction.

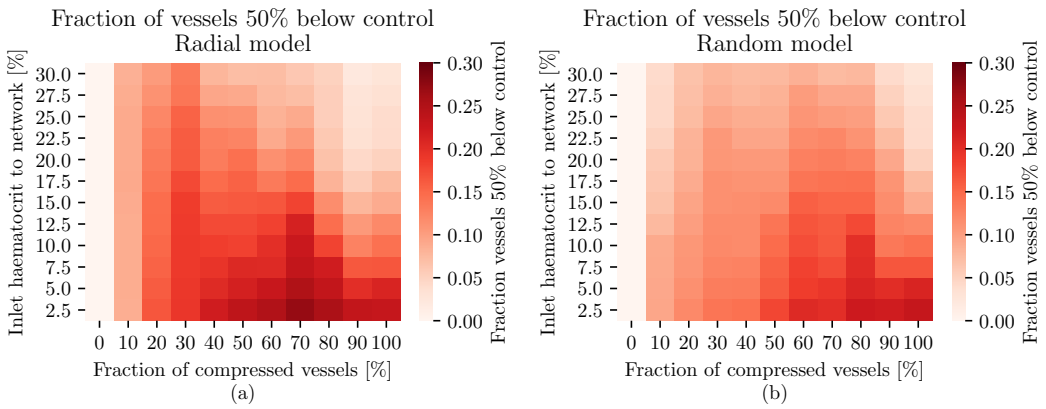

Figure 5.12: Heat map plot showing the fraction of haemodiluted vessels in the network, while varying inlet haematocrit and the fraction of compressed vessels in the network. Haemodiluted vessels are defined as vessels with a haematocrit of less than half of the haematocrit of the same vessel in the control case. (a) Radial model for the network, (b) random model for the network. See Figure 5.3 for an illustration of the radial and random models for the networks.

I next check that the observed haemodilution is not the result of:

1. The definition of haemodilution used
2. The specific network investigated

To that end, I test the additional two haemodilution metrics defined in section 5.1 in the radial model of a compression. Figure 5.13 shows that although the degree of haemodilution varies, the trends observed remain the same, regardless of the used haemodilution metric. I additionally generate four additional networks. shown in Figure B.1, and apply the radial model of compression to them to quantify haemodilution in these networks, the results are shown in Figure B.2. Similarly to using different haemodilution metrics, using different networks shows that the general trends observed remain the same. These findings suggest the robustness of the observation that networks experience haemodilution when their inlet haematocrit is sufficiently low, and even at a relatively low fraction of compressed vessels in the network.

5.3 Discussion and conclusion

5.3.1 Discussion

In this chapter, I investigate the hypothesis that a vessel compression has an effect at a network level on the transport of red blood cells in microvascular networks. To that end, I update an existing reduced-order model to calculate red blood cell partitioning at vascular bifurcations, to account for vessel compression of the parent branch. I demonstrate that the updated reduced-order model suitably predicts the partitioning of red blood cells in compressed vessels.

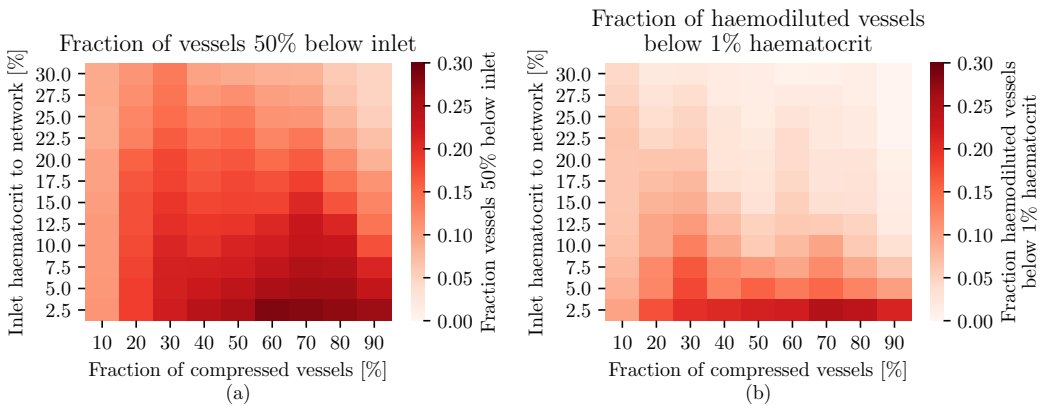

Figure 5.13: Heat map plot showing the fraction of haemodiluted vessels in the network, while varying inlet haematocrit and the fraction of compressed vessels in the radial model network. (a) Haemodiluted vessels are defined as vessels with a haematocrit of 50% or less of the inlet haematocrit to the network. (b) Haemodiluted vessels are defined as vessels with a haematocrit of less than 1%.

I next apply the reduced-order model for red blood cell partitioning at compressed bifurcations in artificially generated model networks. The results show that vessel compression leads to both an increased heterogeneity of haematocrit in the vessels, as well as a reduced average haematocrit in the vessels. Due to the numerical nature of the model, I isolate the two effects of vessel compression; namely increased resistance due to reduced vessel cross-section, and abnormal partitioning of red blood cells at a compressed bifurcation; to study the underlying mechanisms at hand. I show that increased resistance is responsible for a higher portion of the haematocrit reduction, and that this is done through flow redistribution away from the compressed vessels. As red blood cells disproportionally flow to the higher flowing child branch, diverting flow away from compressed vessels also reduces their haematocrit. The abnormal partitioning of red blood cells, on the other hand, is responsible for the increased heterogeneity of haematocrit in the child branches at bifurcations, as was shown in the previous chapter. This work further demonstrates how the increased heterogeneity at vascular bifurcations leads to an enhanced network Fahraeus effect, reducing average haematocrit in the network.

Finally, I investigate under what conditions microvascular networks undergo haemodilution due to vessel compression. The results show that networks experience varying degrees of haemodilution under a wide range of: inlet haematocrits to the network, and fraction of compressed vessels. However, lower inlet haematocrit networks are more susceptible to haemodilution, and haemodilution peaks when 80% of the network is compressed. Above 80% of compressed vessels, the mechanism for reducing haematocrit through increased resistance is less effective, therefore the network experiences less haemodilution.

There are several limitations in this study that I address here. The reduced-order model which was updated was originally developed from data obtained in rats. Red blood cells in rats are slightly smaller than human ones, and the new functional form for X_0^c, for compressed vessels, was obtained with red blood cells of a human dimension. However, I assume that the difference in red blood cell size would not have a leading order effect on the simulation results, as the difference in size is small. In addition, the abnormal partitioning of red blood cells is only one mechanism leading to the observed effects in this chapter, the other being increased resistance. Another limitation is that the reduced-order model is updated for the specific vessel orientation. In addition to different vessel orientations, one could also generalise equation 5.4 to make the pre-factor, C, a function of the aspect ratio of the compression.

An additional limitation of the reduced-order model is the range of parameters for which X_0 is fitted, and the choice of updating the reduced-order model by changing solely the X_0 term. The parameters for the simulations in Table 5.4 come from resolving the network, seen in Figure 5.2, without assuming vessel compression, and taking the boundary conditions and geometry from the vessels in red, which will then be compressed. Therefore, the range of parameters (diameters, haematocrits, and flow ratios) were chosen to be representative of what the reduced-order model will then resolve. The reduced-order model is still limited to the range of parameters present in the studied network, and using X_0^c outside of the range for which it was parameterised could lead to errors. Choosing to update the reduced-order model solely by changing the X_0 term was made due to the good fit seen in Figure 5.5, in a symmetric bifrucation. However, asymmetric bifurcations are known to show a different behaviour to symmetric ones [172], governed by the term A in the reduced-order model [115]. An additional consideration would be parameterise the reduced-order model by changing the other terms, to improve the fit of the model. Nevertheless, the updated reduced-order model shows a good match with the fully resolved HemeLB simulations, which include a number of asymmetric bifurcations.

The implications of the research in this chapter are numerous.

Firstly, it provides a theoretical underpinning to explain reports from the literature, where animal models are shown to have higher tissue hypoxia and tissue oxygen heterogeneity when vessels are compressed [33]. As the simulations in this study are steady-state and the abnormal partitioning of red blood cells is not due to temporal fluctuations in boundary conditions nor due to vascular remodelling, the findings pertain to the causes of chronic hypoxia. The findings in this chapter effectively show a higher degree of haematocrit heterogeneity as well as lower average haematocrit as a consequence of vessel compression. As red blood cells are responsible for the transport of oxygen in blood [172], the change in haematocrit due to vessel compression provides a mechanism for the observation in animal models of changes in tissue oxygenation due to vessel compression. The results further support the hypothesis in the

previous chapter that in a few successive bifurcations, vessels can be severely haemodiluted as a consequence of vessel compression [50]. Future work is warranted to model the oxygen transport from the vessels to the tissue, to fully understand how the reduction in haematocrit, and change in RBC transport in the vessels translates to tissue hypoxia [171].

Secondly, this work forms part of a larger corpus in the literature studying how tumour vascular abnormalities affect blood transport in tumour microvascular networks [18, 39, 50, 128, 191, 205]. Previously, inter-bifurcation distance and increased vessel diameter have been studied [18, 39, 50, 128, 191, 205], and with the results of this chapter, for the first time vessel compression has now been studied. Previous authors have identified and modelled structural abnormalities, but did not have the data to identify a) which abnormalities are the most relevant b) under what conditions the most relevant abnormalities present an issue to transport c) which abnormality is the most prevalent *in vivo* and how it can evolve with time and treatment. By investigating how vessel compression reduces haematocrit at a network level, this study addresses the relevance of vessel compression with regard to blood flow in tumour networks. However, future work is necessary to identify the relative effect on blood flow, and tissue oxygenation, of the different structural abnormalities. Identifying the most relevant structural abnormalities in tumour microvascular networks could be helpful for diagnosis and patient treatment planning, as that would help determine which abnormalities to focus on. Diagnosis could be improved through phenotyping tumours based on their structural abnormalities, as structural abnormalities correlate with survival rates [56, 192]. Treatment planning could be improved through optimising treatment based on the present structural abnormalities, to improve treatment delivery or efficacy [42, 91].

Thirdly, the results support the notion, hypothesised in the previous chapter [50], that healthy vessels are protected against structural abnormalities as they have higher haematocrits. Diseased networks are at higher risk of haemodilution as they have lower haematocrit vessels [96], which are susceptible to haemodilution from structural abnormalities, such as vessel compression. The idea that compressed networks are more susceptible to haemodilution when they have a lower haematocrit is supported by the parameterisation of the reduced-order model, Figure 5.8b, where at higher haematocrits compressed vessels and non-compressed vessels lead to a similar partitioning of red blood cells at the bifurcation. The results similarly show that higher inlet haematocrit networks are less susceptible to haemodilution. Nevertheless, even at higher inlet haematocrits to the network, the network experiences haemodilution, although to a lesser degree. This can be explained by the increased resistance still playing a role in diverting flow away from compressed vessels, and therefore reducing haematocrit through this mechanism.

Finally, by modifying a reduced-order model for calculating red blood cell partitioning at vascular bifurcations and validating the updated model, this chapter offers a new tool to the research community. Researchers interested in further studying structural abnormalities now have access to an RBC partitioning model for the case where vessels are compressed. Future work could parameterise the reduced-order model so that it is also a function of the aspect ratio of the compression, and could also parameterise the model for other structural abnormalities. This would pave the way to a better understanding of how structural abnormalities alter blood flow, and ultimately tissue oxygenation and treatment.

5.3.2 Conclusion

This chapter addressed the second objective of this thesis, to investigate how vessel compression impacts red blood cell distribution in vascular networks. I start by adapting an existing reduced-order for red blood cell partitioning at bifurcations for compressed vessels. I next demonstrate that vessel compression, at a network level, reduces average haematocrit and increases haematocrit heterogeneity in vessels. I unravel the mechanisms behind how compressed vessels reduce haematocrit in vascular networks. I show haematocrit reduction due to compressed vessels increases with reducing inlet haematocrit to the network, and increased fraction of compressed vessels, with a peak at 80% of vessels being compressed. I discuss how these findings provide mechanisms for the evidence of improved tumour tissue oxygenation following vessel decompression. Finally, I hypothesise how studying various vessel structural abnormalities, and their relative effect, could provide insight into diagnostics and treatment planning for patients.

Chapter 6

Quantifying vascular phenotypes in animal models of a glioblastoma

This results chapter addresses the third objective of this thesis, to quantify blood vessel phenotypes, including vessel compression, in a mouse model of a glioblastoma. This study is performed using images from an animal model of a glioblastoma multiforme. The key findings of this chapter are that a successful pipeline for the reconstruction of the three-dimensional microvasculature is validated, and that there are no major differences in most vascular phenotypes except interbifurcation distance and tissue-vessel distances, both being lower in the glioblastoma. Furthermore, the mean tissue-vessel distance correlates with the distance of the vessel network to the tumour core. Finally, the results show that, in the three-dimensional vessels of this animal model of a glioblastoma, vessel compression does not appear to be present.

This chapter is the fruit of a collaboration with a research group, led by Professor Val Brunton, at the Institute of Genetics and Cancer (IGC) at the University of Edinburgh. Dr. Martin Lee performed the experiments and shared the data presented in this chapter. They generated the animal models and did the imaging of the vasculature. I then worked to reconstruct the three-dimensional microvascular surfaces to phenotype the vasculature, and did the data processing. Any mistakes present in this chapter are mine, and not theirs.

This chapter is divided into three main sections. Section 6.1 summarises the methods used in this chapter, section 6.2 presents the results of this chapter, including the validation of the surface reconstruction, and section 6.3 contains a discussion and conclusion for the work in this chapter.

6.1 Method

This section outlines the methods used for the research in this chapter. Section 6.1.1 provides the information on the acquisition of the images, section 6.1.2 is about the reconstruction of the vascular surfaces from the images, and section 6.1.3 covers how the data was processed.

6.1.1 Data acquisition

The acquisition of the data was done by Dr. Martin Lee, who shared the raw images. The details of the method are in section 3.3. There were nine mice in total, divided into three groups. Group A was a control group without glioblastomas, group B was the glioblastoma bearing group that had a hypoxia marker injected in them, and group C was a glioblastoma bearing group that did not have the hypoxia marker injected in them. The experimental data were not blinded for the control versus tumor. As the acquisition of the hypoxia data was problematic and not usable, the hypoxia data is not presented in this thesis. Groups B and C were combined in a single tumour bearing group as the hypoxia marker was injected hours before culling the mice, and advice from the experimentalists stated that it would not affect the microvasculature. The combined groups B and C will be referred to as GB (for glioblastoma) in the results. In addition, some of the data provided were not used as the reconstruction of the vascular networks was not of a sufficient quality. Table 6.1 summarises the data that were used.

Group	Mouse-brain slice	Location	Figure
Control (A)	929-2	B5	Figure C.1
Control (A)	323-3	B6	Figure C.2
Control (A)	323-3	F6	Figure C.3
Tumour (B)	324-6	E6	Figure C.4
Tumour (B)	324-3	D6	Figure C.5
Tumour (B)	324-3	E7	Figure C.6
Tumour (C)	325-1	J12	Figure C.7
Tumour (C)	325-2	B2	Figure C.8
Tumour (C)	343-4	B4	Figure C.9
Tumour (C)	343-4	C7	Figure C.10
Tumour (C)	343-5	C7	Figure C.11

Table 6.1: Summary of raw data as shared by the experimentalists. The first number in the mouse-brain slice is the mouse identification number, and the second is the brain slice. The location is the tile in which the networks were imaged. See section 3.3 for more details. The Figures in the appendix show the reconstructed three-dimensional vasculature, and its location in the tumour.

6.1.2 Surface reconstruction

The raw images provided to me by the experimentalists were reconstructed into surfaces of the microvascular vessels for further processing. The method to reconstruct the three-dimensional vessel surfaces is detailed in section 3.3, and Table 6.1 refers to the appendix, where all of the reconstructed networks are shown. The first part of the results in this chapter will be dedicated to validating the surface reconstruction, to see if the final results are comparable to manually obtained data from the images.

6.1.3 Processing results

Measurements to validate reconstruction

To validate the reconstruction I compare measurements in the reconstructed surfaces and the thresholded images. I start by measuring the width of a vessel in one of the two-dimensional thresholded images, Figure 6.1a. The thresholded images are used rather than the raw images as the thresholded images have a clear separation between vessel and tissue. I then take a slice of the reconstructed surface at the same height as the thresholded image is in, and measure the same vessel at the same position, see Figure 6.1. The two vessels can be co-localised through their coordinates, and the co-localisation is visually verified, which is visibly the case in Figure 6.1.

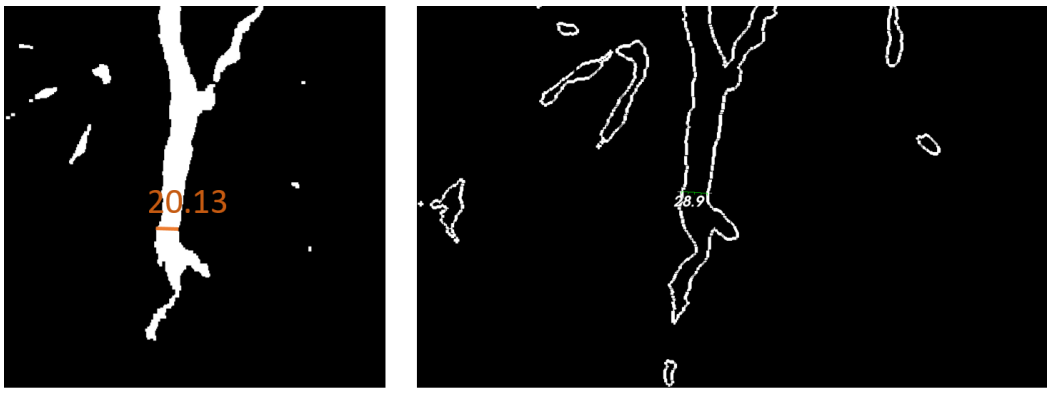

Figure 6.1: (a) shows the thresholded image of a two-dimensional image in a stack. The measurement is done in FIJI using the measurement tool. (b) shows a slice of the reconstructed surface at the same position as in (a). The measurement is done in Paraview using the ruler tool.

Quantitative phenotyping

The phenotypes of interest, namely non-dimensionalised interbifurcation distance (referred to as lambda, λ), the vessel aspect ratio, the vessel diameter, the vessel tortuosity and the tissue-vessel distance, were automatically quantified according to the method in section 3.3.3. As the major and minor diameters are obtained from the aspect ratio of the vessel cross-section, there are two diameter values per vessel segment. As both the minor and major diameters show similar trends, the results in this chapter present just the minor diameter data.

Tumour parameters

As part of the analysis, the surface area of the tumour in the slices and the normalised distance from the network to the tumour core are used.

The surface area of the tumour was obtained by drawing a closed shape around the reporter for the tumour cells, and FIJI was used to calculate the surface area of the closed shape. Figure 6.2a shows an illustration of the process to find the surface area of the tumour.

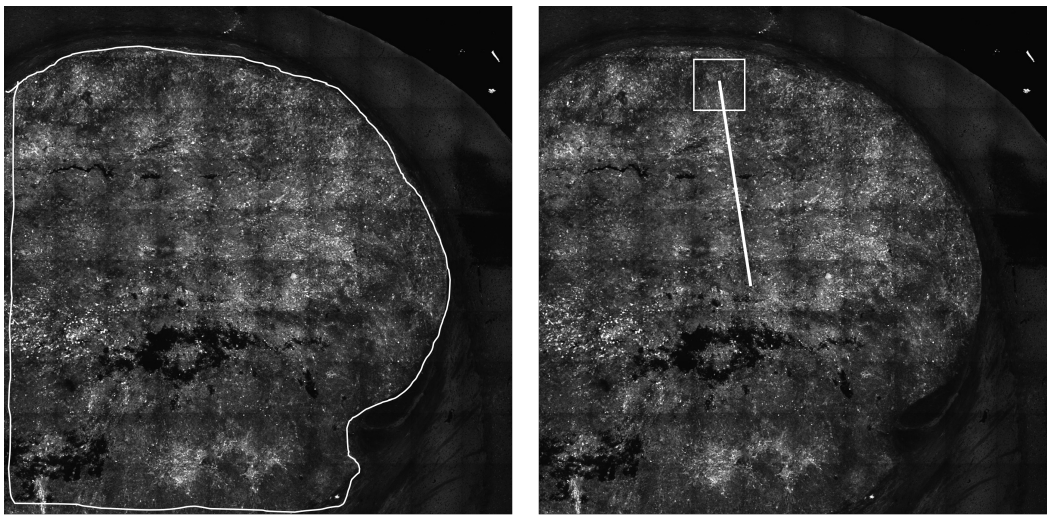

(a) (b)

Figure 6.2: (a) and (b) show the tumour cell reporter for 343-4. (a) shows the selection to calculate the surface area of the tumour (b) shows the measurement from the tumour centre (determined by counting tiles and taking the central one) and the centre of the tile in which the network is reconstructed, B4 in the image.

The normalised distance to the tumour core is calculated by measuring the distance from the centre of the tumour to the centre of the tile in which the network is situated. The distance is then normalised by the radius of a circle with the same surface area as the surface area of the tumour. Figure 6.2b shows an illustration of a measurement from the tumour centre to the centre of a tile.

6.2 Results

6.2.1 Validating the vessel surface reconstruction

The pipeline, outlined in section 3.3.2, to reconstruct the surface of the vascular networks was developed as part of the work done for this thesis. Therefore, the first step of the results is to demonstrate that the process is suitable and provides a reliable reconstructed network.

To that end, I take manual measurements of two vessels per network in the reconstructed surface and in the thresholded images, as described in section 6.1. In the pair of vessels in each network, I pick one from the smaller vessels, and the other from the larger vessels. The manual measurement is done on the thresholded image, and not on the raw images, as the delimitation between vessel and tissue in the raw images is unclear, due to the intensity gradient separating the two, whereas in the thresholded image the separation between vessel and tissue is clear. Figure 6.3 shows the measurements taken in the reconstructed surface plotted against the measurements in the thresholded image, showing a strong correlation with a Pearson's correlation coefficient of 0.967. The strong correlation does not prevent the measurements in the reconstructed surface to be an average of 51% higher than in the thresholded images, visible in Figure 6.3. However, the consistency of the higher measurement values in the reconstructed surfaces, present in all networks, indicates that although the absolute values may be incorrect, they scale by a nearly constant value, and comparison between networks is still suitable.

Furthermore, the reconstruction pipeline also removes smaller disconnected components, as shown in Figure 3.15. It is likely that some of these removed components are not just noise, but vessels that have failed to be reconstructed into connected segments. To identify if removing these smaller disconnected components has an effect on the quantified phenotypes, I check if there is a correlation between the phenotypes in the networks, and the volume fraction of removed vessels in the aforementioned step. Table 6.2 shows Pearson's correlation coefficient of the various phenotypes with the fraction of removed vessels, and indicates that there is no strong correlation between the phenotypes and the volume fraction of removed vessels.

Table 6.2 also shows the correlation between the number of vessel segments in each network, and the phenotypes of the network. There is only one phenotype, λ, which shows a strong correlation between the number of vessels and the phenotype itself. However, the β value for the correlation is very weak, 0.07, indicating that although there is a correlation, the effect it has on λ is minimal.

In summary, to demonstrate the suitability of the surface reconstruction pipeline, measurements in the final reconstructed surface are compared to measurements in the thresholded images, and show a strong correlation with each other. In addition, the correlation of the phenotypes with the fraction of volume removed and the number of segments in each network is verified. Removal of data during the reconstruction of the surface shows no correlation

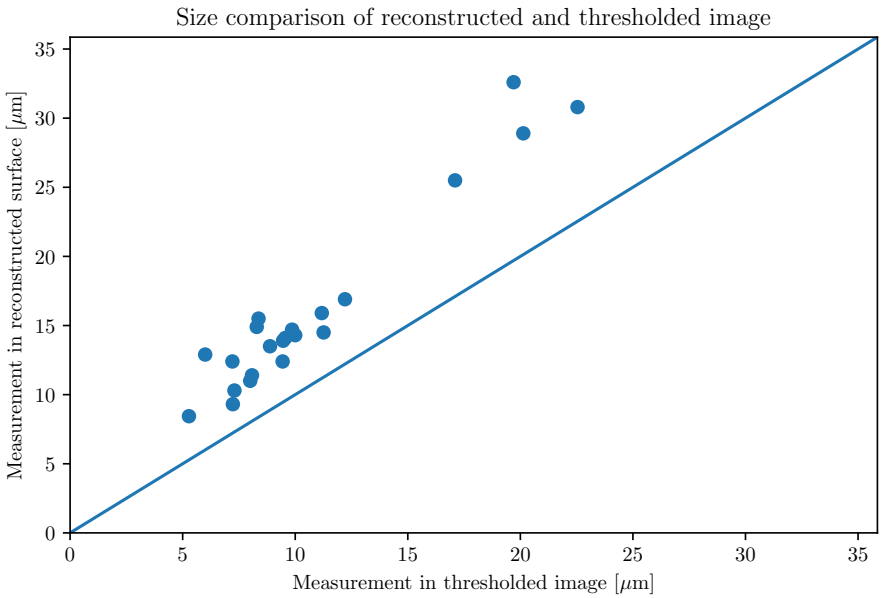

Figure 6.3: Comparison of manual measurements done in the reconstructed surface with manual measurements done in the thresholded images. The Pearson's correlation coefficient of the two measurements is 0.967. The diagonal line is a visual aid to see how close the reconstructed measurements are to the thresholded measurements. If they were a perfect match, the points would be on the diagonal line.

Parameter	Fraction of vessels removed		No. vessel segments in network	
	r	β	r	β
Aspect ratio	0.238	0.30	-0.12	-0.001
Minor diameter	0.605	10.79	-0.26	-0.03
λ	-0.320	-4.3	0.86	0.07
Tissue-vessel distance	-0.060	-2.46	0.6	0.15

Table 6.2: Pearson's correlation coefficient, r, and β values of phenotypes with respect to: the fraction of vessel volume removed during the process to reconstruct the vessel surfaces, and the number of vessel segments in the reconstructed networks.

with the calculated phenotypes. One phenotype, λ, shows a strong correlation but a weak effect with the number of vessel segments in networks. These validation steps demonstrate that the pipeline reconstructs the surfaces in a useful way. The suitability of the pipeline to reconstruct the vessel surface having been evaluated and deemed suitable, I next present the quantification of the phenotypes in the vascular networks.

6.2.2 Non-dimensionalised interbifurcation distance is significantly lower in tumours

The first phenotype I report is the non-dimensionalised interbifurcation distance, referred to as λ. Figure 6.4a shows λ in the combined control networks and in the combined tumour networks. λ is significantly higher in the control networks, with a p-value <0.05. With an average λ of 8.15 and 5.71 in the control and tumour networks, respectively, the control λ is on average 42.7% higher than the tumour one. The λ values reported show that the tumour networks branch more frequently than the control networks.

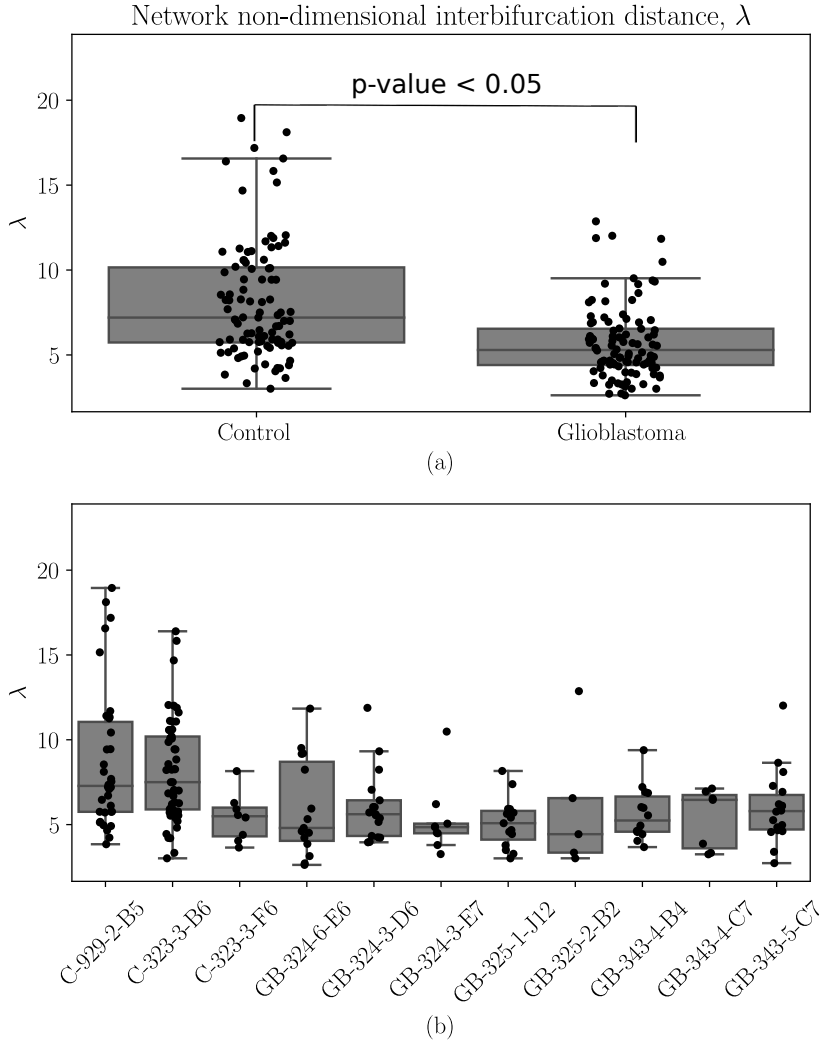

Figure 6.4: (a) Box plot of non-dimensionalised interbifurcation distance, λ, in the control networks and in the tumour networks. The two distributions are significantly different, with a p-value <0.05. (b) Box plot of non-dimensionalised interbifurcation distance, λ,in each individual networks. In the network names, C and GB refer to networks that are in control mice and in glioblastoma mice, respectively. The p-values for every pair in (b) can be found in Table C.1.

Finally, the distribution of λ is broken down into each individual reconstructed network, shown in Figure 6.4b. The individual networks show variability within the control networks and the tumour networks. Notably, one of the control networks, C-323-3-F6, is significantly lower than the other two control networks, while not having a significant difference with any of the tumour networks.

6.2.3 Distribution of tissue-vessel distances is significantly lower in tumours

The next phenotype I report is the distribution of tissue-vessel distances, shown in Figure 6.5. The mean value in the combined control networks and the combined tumour networks is 23.99 μm and 19.95 μm, respectively. The mean tissue-vessel distance in the control networks is 20% higher than in the tumour networks, with a p-value <0.05 indicating a significant difference. The distribution of the tissue-vessel distances is a proxy for vascular density, and the data suggest that the tumour networks are denser than the control networks.

Figure 6.5b plots the distribution of tissue-vessel distances for the individual networks. Similarly as for λ, the control network C-323-3-F6 is significantly lower than the other control networks, consistent with λ in showing that C-323-3-F6 has a different behaviour to the other two control networks. The highest mean of tissue-vessel distances in the tumour networks corresponds to 325-2-B2, which is significantly higher than most of the other tumour networks. It is interesting to note that 325-2-B2 is also the only tumour network imaged in a tile not situated within the tumour, although it is taken from a tumour bearing mouse, see Figure C.8.

6.2.4 Diameter, aspect ratio, and tortuosity are not significantly different in tumours

Next, I report the distribution for the other quantified phenotypes in the tumour networks, namely vessel diameter, vessel aspect ratio, and the vessel tortuosity.

Figure 6.6 shows the data for the vessel diameter. The results show that there is no significant difference between the control networks and the tumour networks, with a mean value of 12.68 μm and 13.5 μm respectively. The mean values of the diameters indicate that the vessels measured are in the microvasculature, and a majority of them are in the size range expected of capillary vessels. Figure 6.6b further plots the individual diameter distributions in each network, which shows variability. It is interesting to note that two control networks, C-929-2-B5 and C-323-3-B6, have some higher diameter vessels, between 25 μm and 30 μm, which could indicate the presence of hierarchy. Network c-929-2-B5, shown in Figure C.1, visibly has a larger vessel to illustrate this.

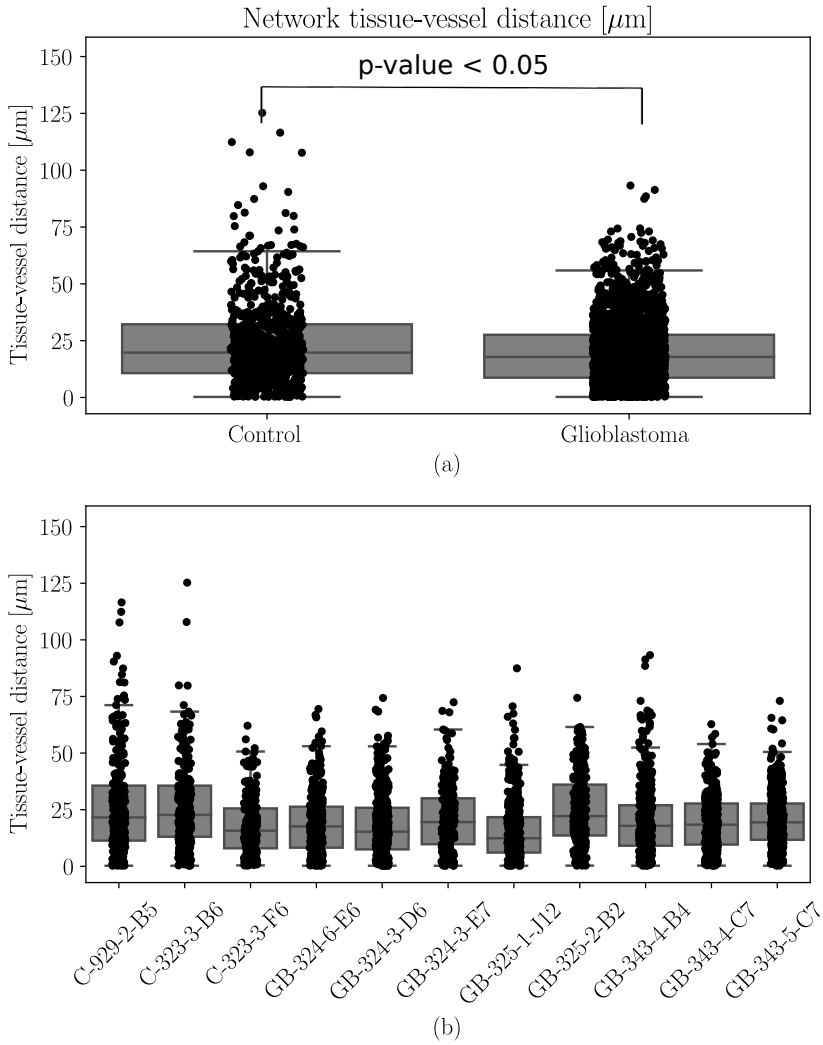

Figure 6.5: (a) Box plot of tissue-vessel distances in the control networks and in the tumour networks. The two distributions are significantly different, with a p-value <0.05. (b) Box plot of tissue-vessel distances in each individual network. In the network names, C and GB refer to networks that are in control mice and in glioblastoma mice, respectively. The p-values for every pair in (b) can be found in Table C.1.

Figure 6.7 reports the data for the aspect ratio. The data show that there is no significant difference between the control networks and the tumour networks, with mean values of 1.41 and 1.46, respectively. Although one would expect healthy capillaries to be circular, there are reports of them being slightly elliptical, and the mean aspect ratios reported here are in line with those reports for capillary vessels. Figure 6.7b shows the distribution of aspect ratios for each individual network, which shows only small variations across the mean aspect ratio values.

Finally, Figure 6.8a shows the tortuosity data in the control and tumour groups, with mean values of 1.18 and 1.19. There is no significant difference between the control and tumour groups. Figure 6.8b plots the distribution of tortuosities for each individual network and, similarly to the aspect ratios, shows only small variations in the mean values across the different networks.

The main finding here is that there is no statistically significant difference in the diameter, aspect ratio, and tortuosity between the control networks and the tumours networks, Figures 6.6-6.8.

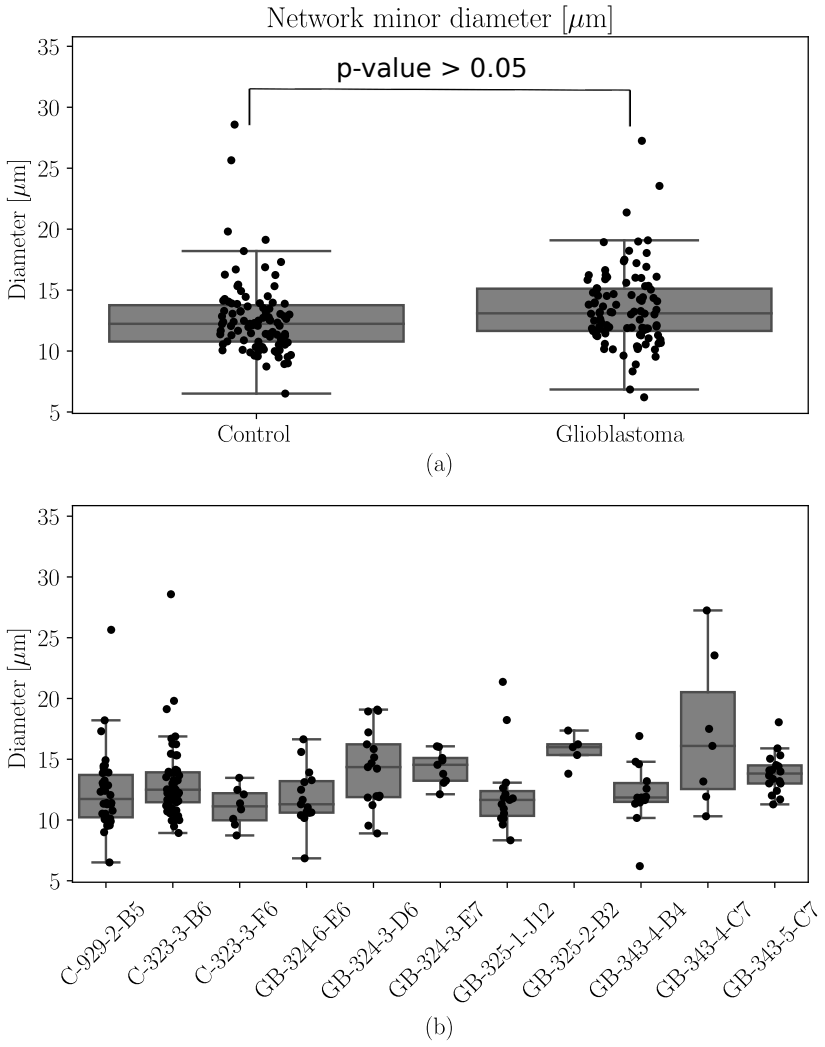

Figure 6.6: (a) Box plot of diameters in the control networks and in the tumour networks. The two distributions are not significantly different, with a p-value >0.05. (b) Box plot of diameters in each individual network. In the network names, C and GB refer to networks that are in control mice and in glioblastoma mice, respectively. The p-values for every pair in (b) can be found in Table C.1.

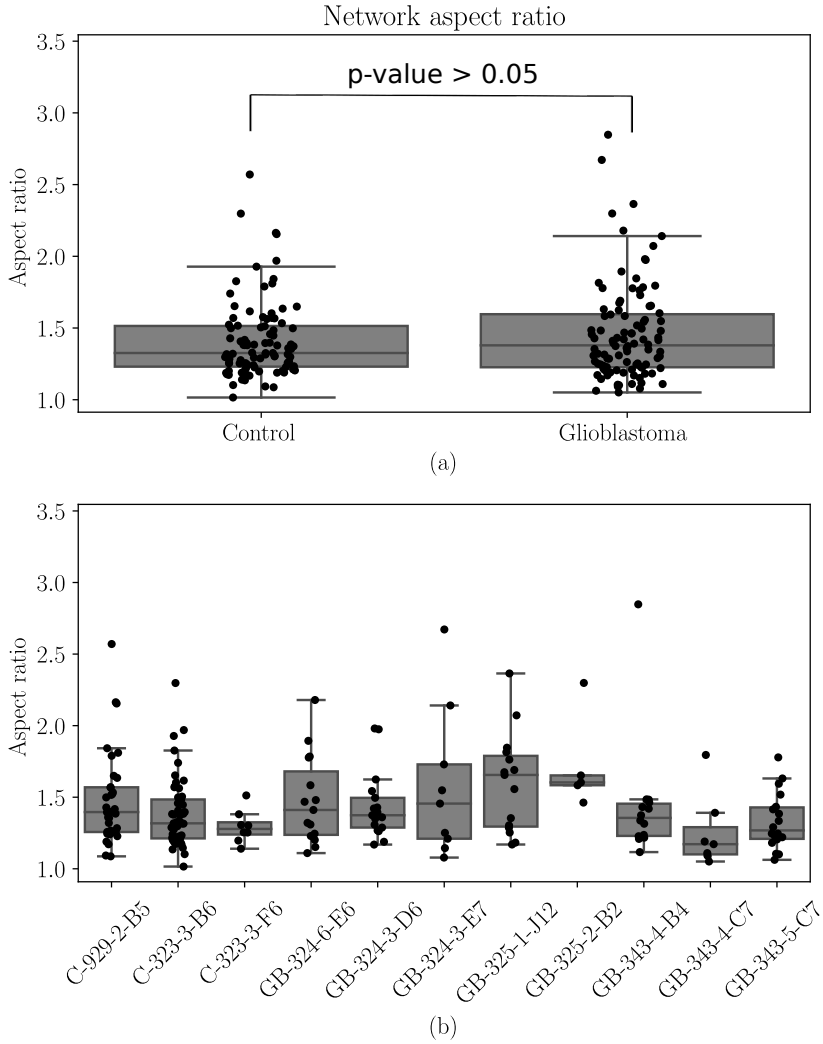

Figure 6.7: (a) Box plot of aspect ratios in the control networks and in the tumour networks. The two distributions are not significantly different, with a p-value >0.05. (b) Box plot of aspect ratios in each individual network. In the network names, C and GB refer to networks that are in control mice and in glioblastoma mice, respectively. The p-values for every pair in (b) can be found in Table C.1.

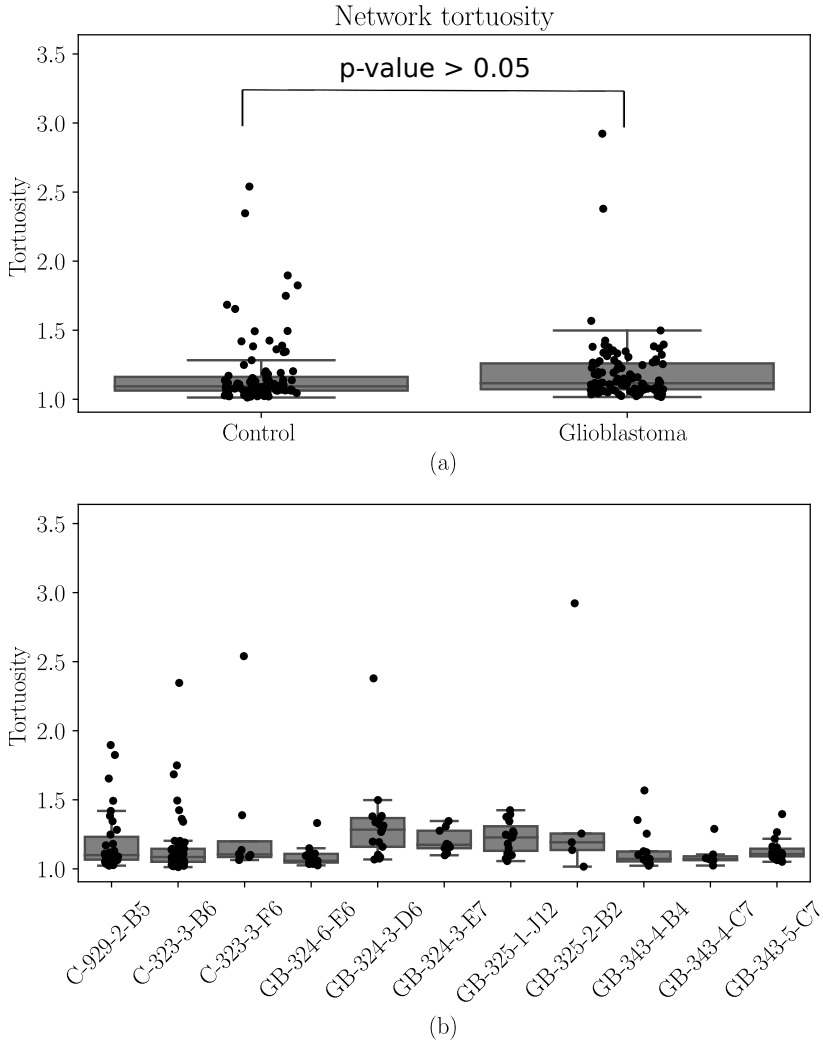

Figure 6.8: (a) Box plot of tortuosities in the control networks and in the tumour networks. The two distributions are not significantly different, with a p-value >0.05. (b) Box plot of tortuosities in each individual network. In the network names, C and GB refer to networks that are in control mice and in glioblastoma mice, respectively. The p-values for every pair in (b) can be found in Table C.1.

6.2.5 Mean of tissue-vessel distances correlates with the normalised distance to tumour core

Next, I investigate if the vascular phenotypes previously quantified correlate with the quantification of some tumour parameters. The tumour parameters are the surface area of the tumour in which the vessel network is situated, and the normalised distance of the vessel network to the core of the tumour. The method to calculate these parameters is provided in section 6.1.3.

Table 6.3 shows that the only phenotype that has a correlation with the surface area of the tumour in each slice is the aspect ratio, with a Pearson's correlation coefficient of -0.66. The correlation coefficient is not very high, and in addition, the β value of -0.014 demonstrates that the effect of the correlation is weak.

Parameter	Tumour surface area		Normalised distance to tumour core	
	r	β	r	β
Aspect ratio	-0.660	-0.014	0.73	0.15
Minor diameter	-0.372	-0.102	0.85	2.36
λ	-0.024	-0.001	0.478	0.311
Tissue-vessel distance	-0.166	-0.07	0.929	3.99

Table 6.3: Pearson's correlation coefficient, r, and β values of phenotypes with respect to: the surface area of the tumour, and the distance from the vessel network to the core of the tumour.

Table 6.3 also shows the correlation of the phenotypes with the normalised distance to the tumour core. One phenotype, which is the mean of the distribution of tissue-vessel distances, correlates with the normalised distance of the network to the tumour core with a Pearson's correlation coefficient of 0.929, Table 6.3. The positive value of the correlation indicates that the further a network is from the tumour core, the larger the mean tissue-vessel distance is. The β value of 3.99 indicates that in addition to the correlation, the effect is important. Figure 6.9 shows the mean of the distribution of tissue-vessel distances plotted against the distance of the network to the tumour core. Figure 6.9 confirms the findings from Table 6.3 indicating that the two parameters correlate with each other. It is interesting to note that the longest mean tissue-vessel distance in Figure 6.9 corresponds to network 325-2-B2, which is taken in a mouse with a brain tumour, but the network is situated outside of the tumour, Figure C.8, which is why its normalised distance is above 1. The minor diameter and aspect ratio also have a high Pearson's correlation coefficient with the normalised distance to the tumour core, but they are lower than the tissue-vessel distance one and the β values are lower, indicating the effects are not as strong.

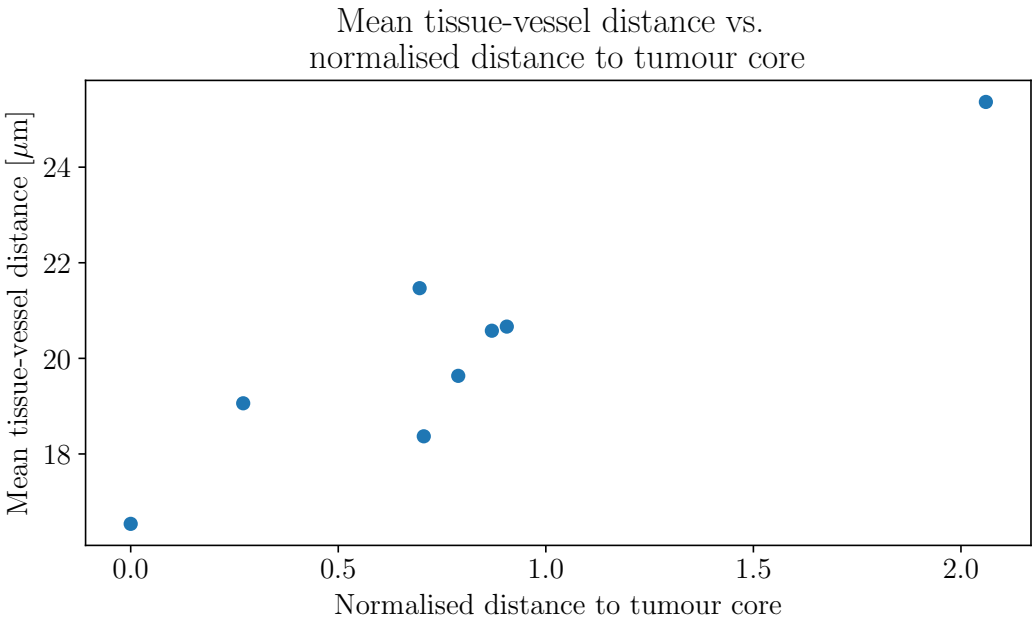

Figure 6.9: Plots the mean tissue-vessel distance in each tumour network against the normalised distance of the network to the tumour core.

6.3 Discussion and conclusion

6.3.1 Discussion

In this work, experimental collaborators shared images of the brain vasculature for control mice and mice intracranially injected with glioblastoma cells. The images of the vasculature were stacks of two-dimensional images, which in effect provide three-dimensional data. I developed and validated a pipeline to reconstruct the three-dimensional vascular surfaces of the vessels in the images, and to extract the centrelines of the vessels. Following that, I automatically extracted a set of vascular phenotypes from the images, namely non-dimensionalised interbifurcation distance (λ), tissue-vessel distances, vessel diameter, vessel aspect ratio, and tortuosity. The results show that the main difference between the control and tumour vessel networks is that both λ and the mean tissue-vessel distance were higher in the control compared to the tumour mice. There was no significant difference in the other phenotypes, including vessel aspect ratio, indicating that vessels were not compressed in the reported networks. Finally, I investigated correlations between properties of the network in relation to the tumour, such as the area of the tumour in the brain and the normalised distance of the vessels to the tumour core. The results showed that in the tumour mice, the mean tissue-vessel distance positively correlated with the normalised distance to the tumour core.

The work on the reconstruction of the three-dimensional surfaces posed numerous challenges and required a validation to ensure the quantified phenotypes were reliable. The consistency in the measurement differences between the reconstructed surfaces and the two-dimensional images indicates that although the absolute measurement values reported in the results are not reliable, they just require a scaling factor to be accurate.

The consistency throughout the networks also indicated that the comparison of the quantified phenotypes between the networks does not suffer from this scale difference. The validation demonstrated that there is no correlation between phenotypes and the removal of smaller disconnected components during the reconstruction. The lack of correlation between phenotypes and the reconstruction process is important, as one could assume that at least some of the disconnected components are vessels that are not reconstructed for various reasons. The fact that phenotypes did not correlate with the volume of removed components shows that no information is lost through this step. Future work to improve the reconstruction, particularly to have a better match between the three-dimensional reconstructed data and the two-dimensional mesurements, is warranted.

Despite evidence of the validity of the reconstruction, further work can be done to improve the quality of the segmentation of the raw images, as segmentation variability can lead to variability in the final results [200]. In this work, the default parameters for the segmentation methods in FIJI were used [167], and an exploration of the parameter space could lead to improved segmentation outputs. In addition, novel machine learning techniques have demonstrated better segmentation results than conventional segmentation algorithms [64]. There have also been recent publications of open source segmentation packages [7, 13], with the ability to manually and iteratively annotate images to train machine learning algorithms, which are promising methods to improve segmentation of images [64].

One of the main results of this chapter shows that the non-dimensionalised interbifurcation distance, λ, in the tumour networks is lower than in the control networks. Previous studies have shown that, in the microvasculature, shorter λ values alter red blood cell transport at bifurcations [18, 148] and increase red blood cell heterogeneity in vascular networks [18]. In addition, shorter λ values have also been shown to cause tissue oxygen heterogeneity [18]. Taken together, this finding corroborates other reports from the literature that λ values are shorter in tumours than in healthy tissue, with the added value of having a control to demonstrate that. The difference in λ between the control and the tumour networks could be indicative of an angiogenic response in the tumour [18, 32].

An additional finding of this chapter shows that the mean tissue-vessel distance, used as a proxy for vascular density, is higher in tumour networks than in control networks. This is in line with the literature, where glioblastoma networks are reported as denser than control ones [38]. In addition, the mean tissue-vessel distance correlates with the normalised distance from

the tumour core. Both of these findings could be an angiogenic response to the presence of hypoxia. Indeed, tumours are more hypoxic than normal tissue [91], and the rim of tumours is more oxygenated than the core [158], so the reduced tissue-vessel distance could be an angiogenic response to improve the oxygenation of the tissue.

As part of the initial hypothesis of this work was the assumption that the glioblastoma networks would have compressed vessels. This was supported by literature reports of high aspect ratio vessels in lung cancer [56], oral cancer [6], skin cancer [78], and neuroblastoma [192]. The literature does not explicitly report aspect ratios for glioblastomas, although there are reports of compressed vessels in them [169]. The results of this chapter show that this is not the case in the animal model used in this study, despite numerous reports that tumour vessels are compressed [6, 56, 78, 192], and that glioblastomas have high solid stress [169]. The results pose the question as to why vessel compression was not observed. One could speculate as to why this is not the case, for example, that these specific animal models do not have high solid stress or that smaller vessels, such as the ones measured here, do not deform. However, future work is warranted to better understand why the data reported does not show high aspect ratios and therefore vessel compression.

Finally, the initial objective for this chapter was to correlate hypoxia to the vascular phenotypes. Experimental difficulties have prevented the obtention of the tissue oxygenation data. However, the work presented here provides a pipeline to reconstruct the vascular surfaces which can be used in the future, if and when tissue oxygenation data are obtainable. Future work can therefore continue to work on the objective of correlating vascular phenotypes to tissue oxygenation data. Correlating vascular phenotypes to tissue oxygenation data is of interest to identify the relative contribution of various, potentially abnormal, phenotypes to tissue hypoxia in tumours.

6.3.2 Conclusion

In this chapter, I use images of a vascular marker in a mouse model of a glioblastoma, shared by experimental collaborators, to quantify the vascular phenotypes present in the glioblastoma and compare them to a control. This chapter addressed the third objective of this thesis, to quantify blood vessel phenotypes, including vessel compression, in a mouse model of a glioblastoma. I develop a pipeline to reconstruct the three-dimensional surfaces of the vessels and validate the pipeline. Next, I show that, in control mice, the non-dimensionalised inter-bifurcation distance and the tissue-vessel distances are higher than in glioblastoma bearing mice. Other phenotypes, the vessel diameter, vessel aspect ratio, and vessel tortuosity are not significantly different in control mice compared to tumour bearing mice. The data also show that the mean tissue-vessel distance in tumours correlates with the normalised distance of the network to the tumour core. Finally, I discuss the implications of these findings.

Chapter 7

Conclusion & Outlook

Section 7.1 reiterates the motivation, hypothesis, and aim & objectives of this thesis. Section 7.2 summarises the results of this thesis. Finally, 7.3 looks at possible future work.

7.1 Motivation, hypothesis, aim & objectives

Cancer is a major healthcare concern in the world, causing one death in six. Cancer research, in diagnostics and treatments for example, has improved survival rates of patients over the past decades. One field of research that has recently attracted attention is the tumour microenvironment and the physics of cancer. Interest in the physics of cancer stems from the fact that some aspects of cancer are driven by physical processes, rather than biological ones. The motivation of this thesis lies in the hope that a better understanding of the physics of tumours will lead to the development and improvement of therapeutic strategies to improve patient survival.

One specific tumour microenvironment abnormality is vessel compression. Studies have demonstrated that blood vessels in solid tumours are heavily compressed, and correlated the degree of vessel compression to reduced survival rates in patients. In addition, studies have shown that therapeutically reducing solid stress, which has the effect of decompressing vessels, increases survival rates in animal models of tumours. Vessel decompression was associated with improved tumour tissue oxygenation and reduced oxygen heterogeneity. However, it is not clear what the biophysical mechanism is that links vessel decompression to improved oxygenation. In addition, vessel compression has been quantified in various cancers, but not in glioblastoma. Given the correlation between vessel compression and survival rate, and that glioblastoma has a low survival rate, quantifying the presence of vessel compression in glioblastoma is important.

The central hypothesis of this study is that vessel compression leads to abnormal partitioning of red blood cells at vascular bifurcations, contributing to a high fraction of plasma channels in tumour networks and to tumour tissue hypoxia.

The aim was to find a mechanistic link between vessel compression and abnormal red blood cell transport in vascular networks, and contextualise it to glioblastoma. The aim leads to three objectives. Each objective was addressed by a results chapter.

1. Numerically investigate how vessel compression impacts partitioning of red blood cells at a single vascular bifurcation (chapter 4)
2. Numerically investigate how vessel compression impacts red blood cell distribution in vascular networks (chapter 5)
3. Quantify blood vessel phenotypes, including vessel compression, in a mouse model of a glioblastoma (chapter 6)

7.2 Summary

Chapter 4 numerically investigates how vessel compression impacts the partitioning of red blood cells at a single vascular bifurcation. The results show that an upstream compression introduces an abnormal partitioning of red blood cells, where the higher flowing child branch is further enriched in haematocrit. The further enrichment in red blood cells of the higher flowing child branch is present over a wide range of flow ratios. The abnormal partitioning of red blood cells is the result of a narrowing of the red blood cells' cross-sectional distribution as they experience a higher shear rate and shear rate gradient in the compressed region. The narrowing of the red blood cell distribution is less pronounced as the parent branch haematocrit increases, and at a critical threshold of around 30% haematocrit, the partitioning of red blood cells is very similar in compressed vessels and in non-compressed vessels.

Chapter 5 numerically investigates how vessel compression impacts red blood cell distribution in vascular networks. It builds on to chapter 4 by adapting and validating an existing reduced-order model to accurately and efficiently calculate the partitioning of red blood cells in compressed vessels. The results of the study show that, in microvascular networks, vessel compression introduces haematocrit heterogeneity, reduces average haematocrit, and increases the number of plasma channels. Next, the mechanisms are explored by numerically separating the increased resistance due to vessel compression, and the abnormal partitioning of red blood cells at bifurcations. Both the increased resistance and abnormal partitioning contribute to reducing the average haematocrit in the networks, but only the abnormal partitioning of red blood cells at bifurcations increases haematocrit heterogeneity. Finally, a parameter sweep is

performed on the fraction of compressed vessels in the network and the inlet haematocrit. The results of the parameter sweep show that the reduction in haematocrit is more pronounced with lower inlet haematocrits to the network, and that a low fraction of compressed vessels is sufficient to affect haematocrit throughout the network.

Finally, chapter 6 addresses the third objective, to quantify blood vessel phenotypes, including vessel compression, in a mouse model of a glioblastoma. Experimentalists shared images of the microvasculature of mouse models of a brain glioblastoma as well as control data from mice without tumours. Initially, a pipeline to reconstruct the three-dimensional vessel surfaces is developed and validated. Next, the phenotypes of the tumour bearing and control mice are compared. The tumour networks have a significantly lower non-dimensional interbifurcation distance and mean tissue-vessel distance. However, the other phenotypes do not show a significant difference, and notably the vessels in the tumour networks are not compressed. Lastly, the results show that in the tumour mice, the mean tissue-vessel distance correlates with the distance of the vessel network to the tumour core.

Taken together, these findings address the aim of this thesis and provide a mechanism for abnormal transport of red blood cells in compressed vessel networks, as well as providing quantitative vascular phenotypes in an animal model of a glioblastoma. Due to the importance of red blood cells in the transport of oxygen and its link to abnormal vascular phenotypes, this work contributes to the knowledge of the causes of chronic hypoxia in tumours with an abnormal vasculature, and more specifically compressed vessels.

7.3 Future work

The first two results chapters of this thesis investigate the hypothesis that vessel compression leads to abnormal partitioning of red blood cells at vascular bifurcations using numerical methods. The results of the simulations showing a narrowing of the red blood cell distribution post-compression are in good agreement with experimental works. However, the effect of the change in red blood cell distribution on the partitioning of the red blood cells at a downstream bifurcation could be verified experimentally to support the findings of this thesis. In addition, investigating how this propogates at a network level experimentally could validate the finding that vessel compression leads to a reduction in average haematocrit in networks, as well as an increase haematocrit heterogeneity. This experimental validation could be done using microfluidic devices.

The underlying hypothesis of this thesis was that vessel compression leads to abnormal partitioning of red blood cells at vascular bifurcations, contributing to a high fraction of plasma channels in tumour networks and to tumour tissue hypoxia. The first part of the hypothesis, that vessel compression leads to abnormal partitioning of red blood cells and leads to plasma

channels, is addressed in chapters 4 and 5. However, the second part of the hypothesis, which is that the abnormal transport of red blood cells contributes to tissue hypoxia, is not investigated in this thesis. Future work can test this hypothesis through various studies. Firstly, the results in chapter 5 do not include oxygen transport simulations, although there are existing methods to do that [63, 66]. Future work could use the model in chapter 5 to simulate blood flow through compressed networks, and study the ensuing tissue oxygenation. Secondly, the initial intention of the experiments with the animal models in chapter 6 was to have access to tissue hypoxia data, and co-localise tissue hypoxia with the vascular imaging data. Future work could use the pipeline developed in chapter 6 and similar experimental data, with additional tissue hypoxia data, to correlate vascular phenotypes with tissue hypoxia. To associate tissue hypoxia specifically with vessel compression would also require further understanding of why the vessels in the animal models were not compressed, and to use tumour models that have compressed vessels. Furthermore, there are animal models where compression is mechanically induced, allowing one to study the effect of vessel compression in the absence of a tumour [134]. Using such an animal model would provide an insight into the link between vessel compression and tissue hypoxia, while isolating vessel compression from the effects of a tumour.

The results in chapters 4 and 5 show that vessel compression, a vessel structural abnormality, has an effect on the transport of red blood cells in vascular networks. A previous study shows that another vascular abnormality, reduced interbifurcation distance, also alters red blood cell transport [18]. Future work could be targeted at identifying what other diseased vessel structures change the transport of red blood cells. It would also be interesting to study which of these abnormalities has a leading order effect on red blood cell transport, or if they all have a relevant contribution. Finally, the prevalence of these phenotypes in diseases, such as tumours, is also of relevance, and can be studied with animal models.

This study focussed on the effect that vessel compression has on the transport of red blood cells. However, numerous studies also show that the transport of drugs is abnormal in the tumour vasculature [42]. Further work could investigate how vessel compression, and other structural abnormalities, affect the transport of drugs. These studies can also compare the transport of drugs with the transport of oxygen, as some drugs do not function in hypoxic conditions [24].

As a final note, the collaboration undertaken in chapter 6 with experimentalists is a rich avenue for research as it helps bridge the gap between theoretical and experimental works. Bridging that gap, and mutually informing theory with experiments, is difficult. However, if the task were unidisciplinary and simple it would no longer be an avenue for research. Rising up to the challenge is exciting, and rewarding.

Appendix A

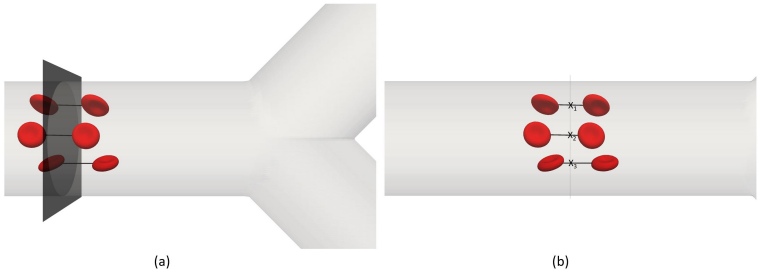

Figure A.1: (a) Three RBCs before and after a plane of interest. Lines indicate RBC trajectories, assumed as straight. (b) Side view as each cell crosses the plane at a given coordinate (x, y, z). The RMSD is calculated in the compression axis (here seen as height of channel) by setting x_0 as the channel centreline (always zero) and x_i as the height coordinate of the RBC as it crosses the plane. This measures the distribution in the height of the channel. For illustration purposes only three cells are shown, whereas several hundred are accounted for.

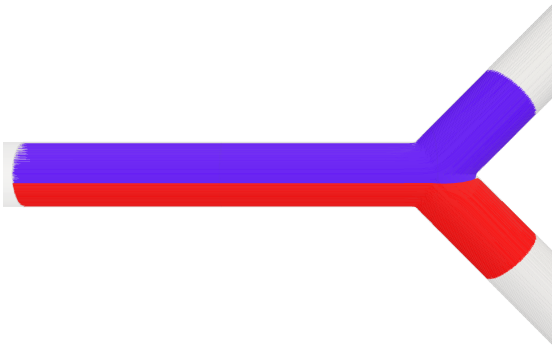

Figure A.2: Intuition for separatrix. Blue/red lines are streamlines ending in the top/bottom child branch, respectively. The separatrix is the surface separating the blue from the red streamlines on the plane.

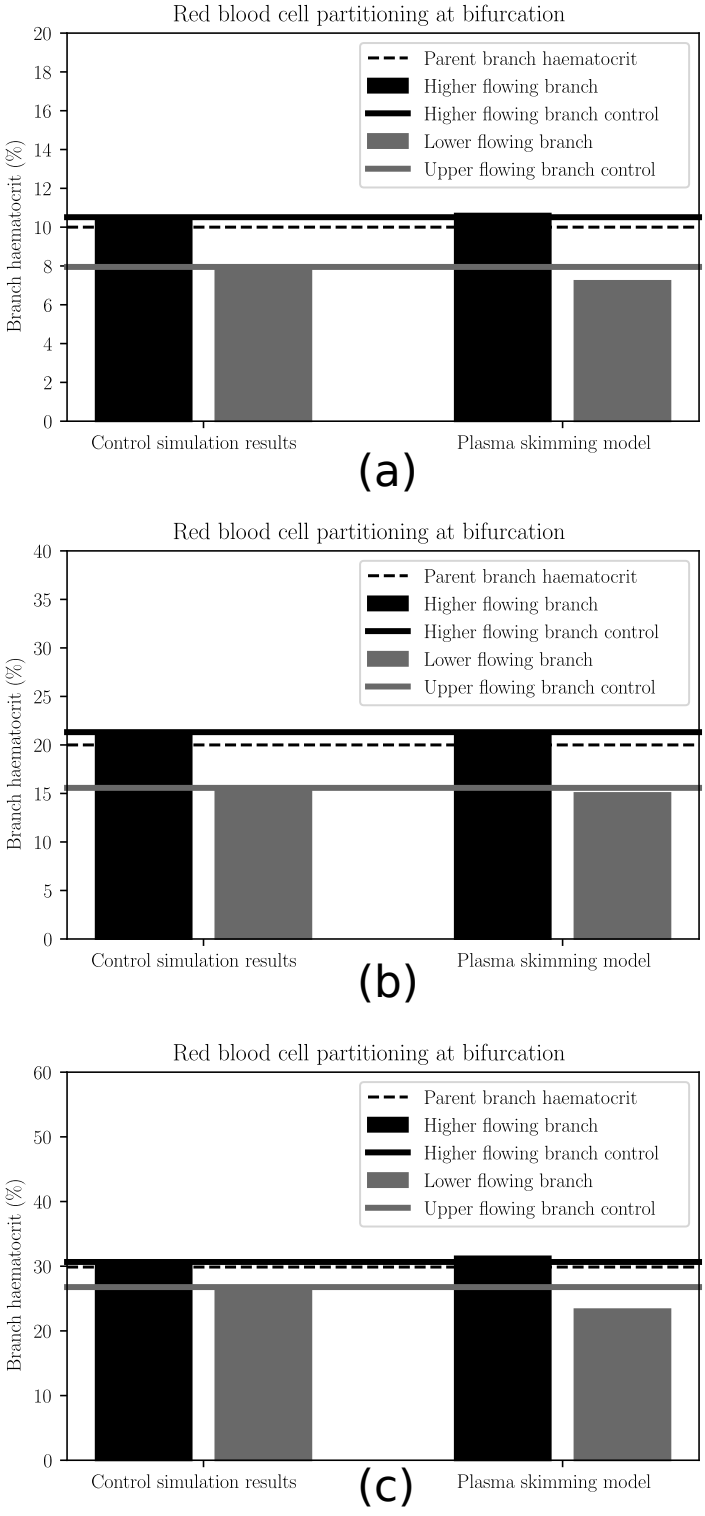

Figure A.3: Comparison of simulation control data with empirical plasma skimming model [148, 152] with a flow ratio of 4. (a) Simulation at $H_d = 10\%$. (b) Simulation at $H_d = 20\%$. (c) Simulation at $H_d = 30\%$.

Appendix B

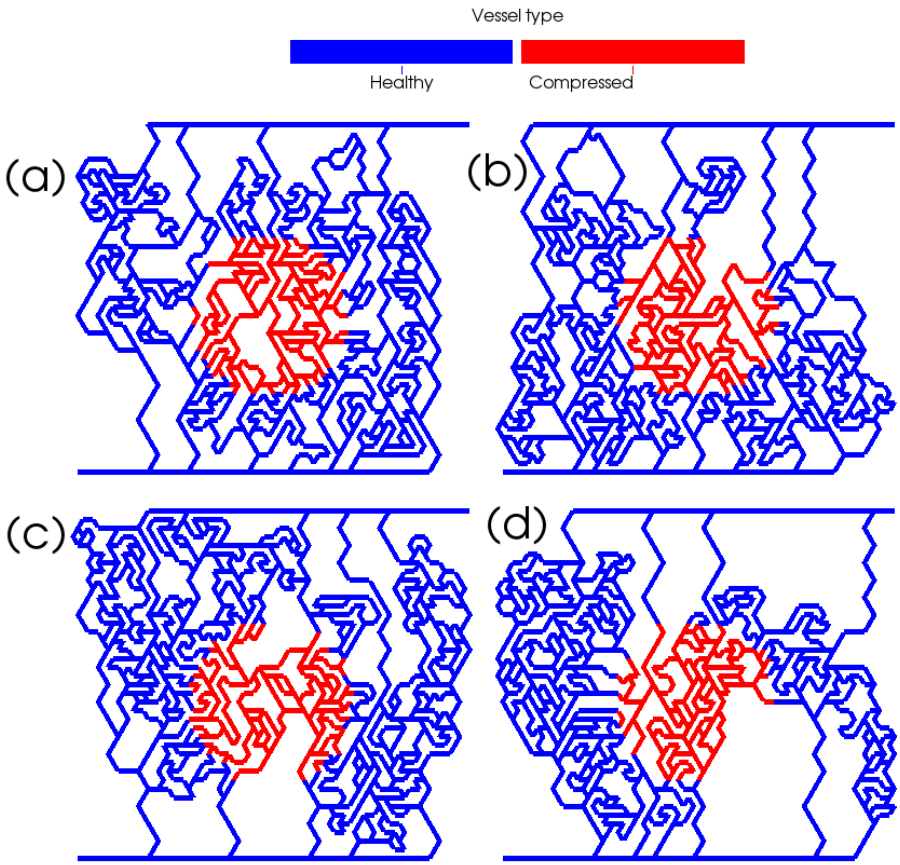

Figure B.1: Snapshot of additional four networks, generated according to the same rules and conditions as the network in Figure 5.2. The fraction of compressed vessels in all four networks is 20%.

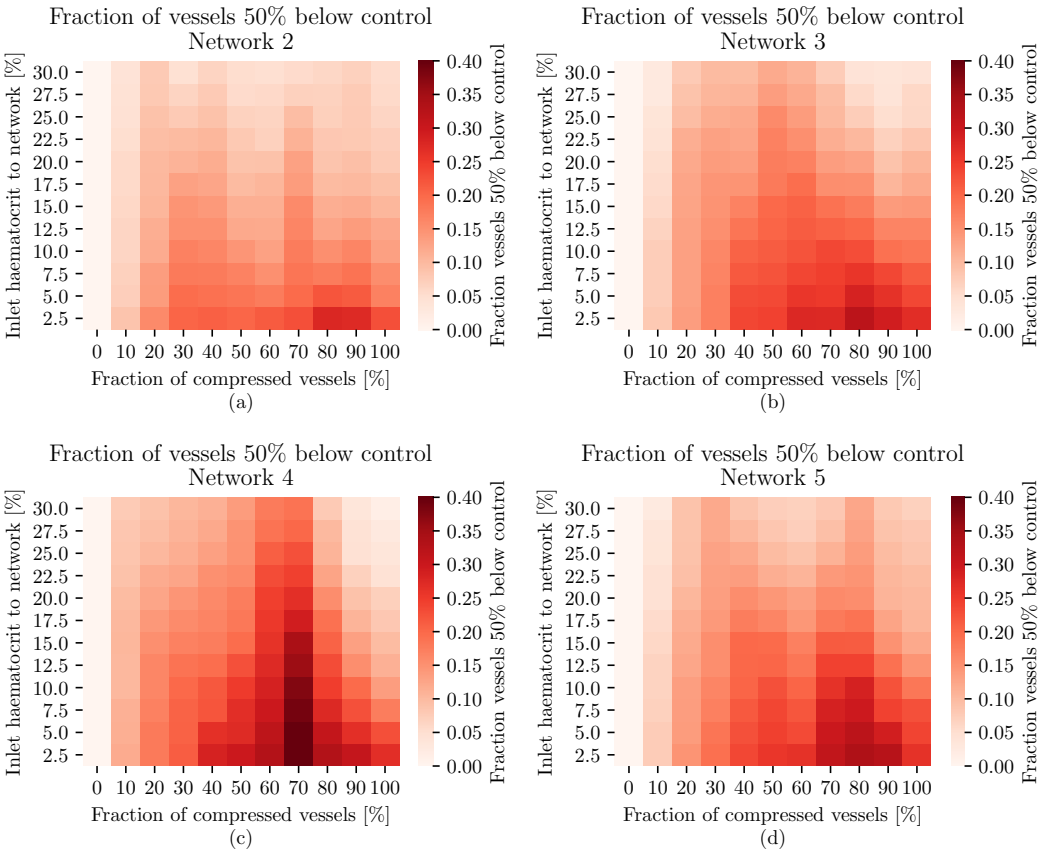

Figure B.2: Heat map plot showing the fraction of haemodiluted vessels in the networks, while varying inlet haematocrit and the fraction of compressed vessels in the network, according to the radial model. (a)-(d) corresponds to the networks in Figure B.1(a)-(d), respectively.

Appendix C

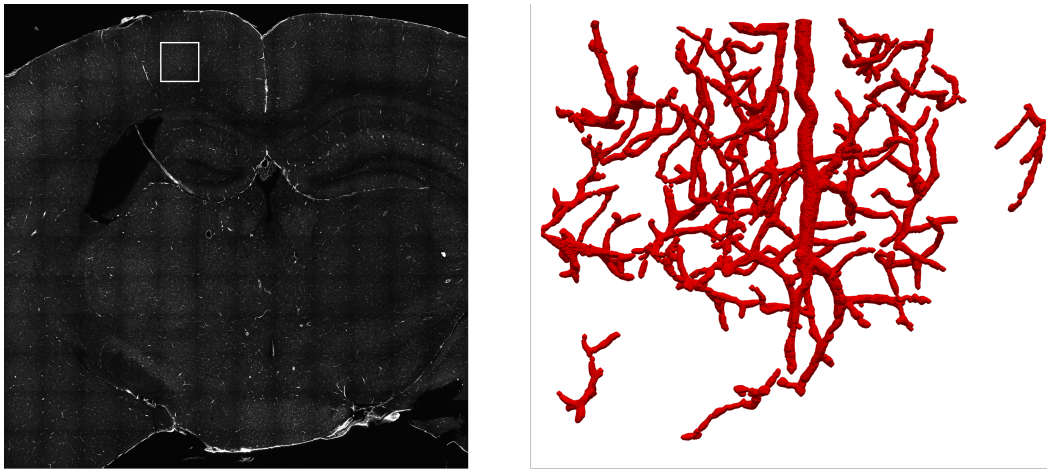

(a) (b)

Figure C.1: (a) shows the cross-sectional surface of the vascular reporter for the second slice of mouse 929 (control) with the tile B5 circled. (b) shows the reconstructed network at tile B5.

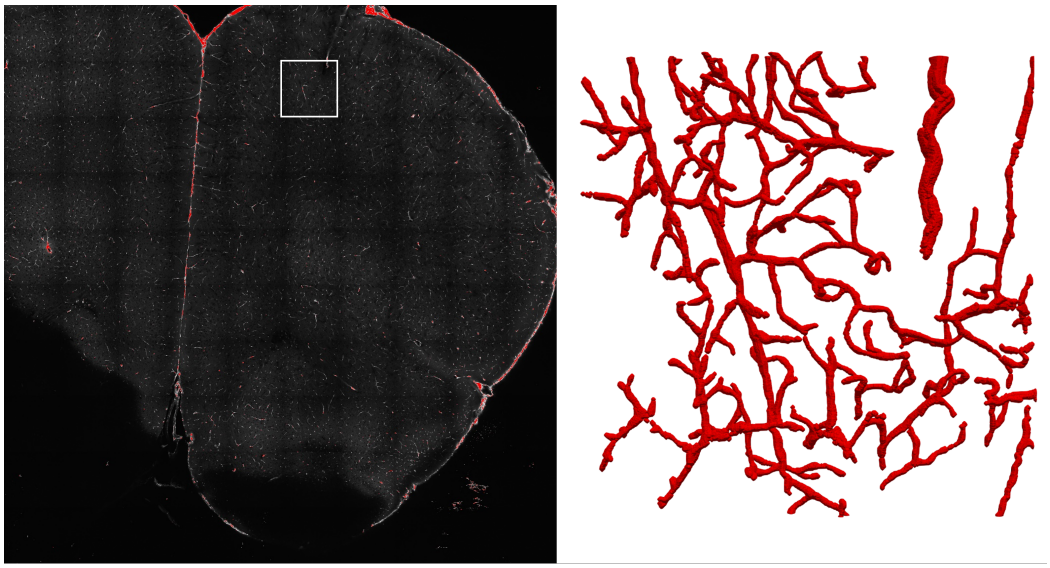

(a) (b)

Figure C.2: (a) shows the cross-sectional surface of the vascular reporter for the third slice of mouse 323 (control) with the tile B6 circled. (b) shows the reconstructed network at tile B6.

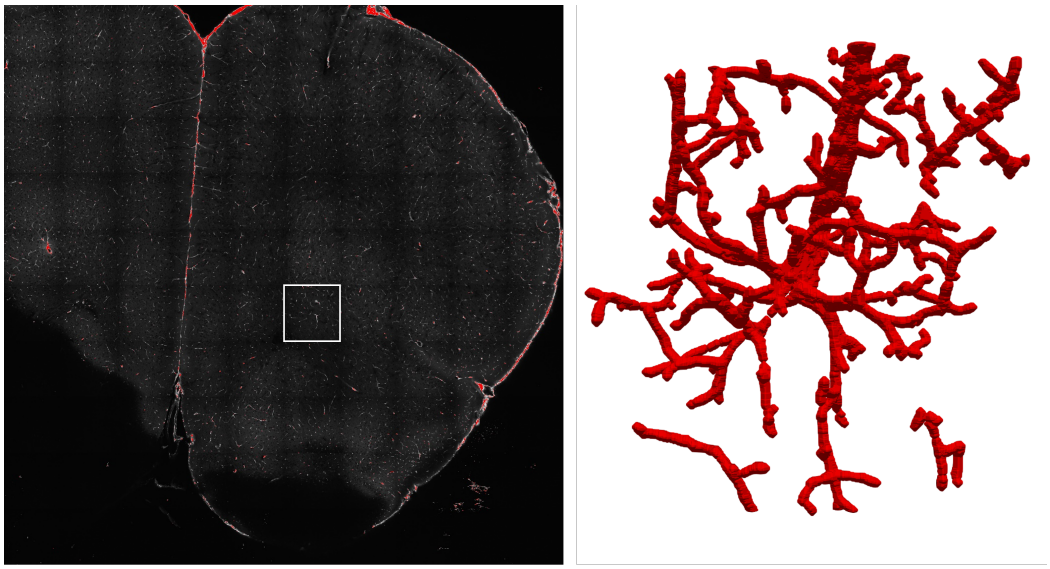

(a) (b)

Figure C.3: (a) shows the cross-sectional surface of the vascular reporter for the third slice of mouse 323 (control) with the tile F6 circled. (b) shows the reconstructed network at tile F6.

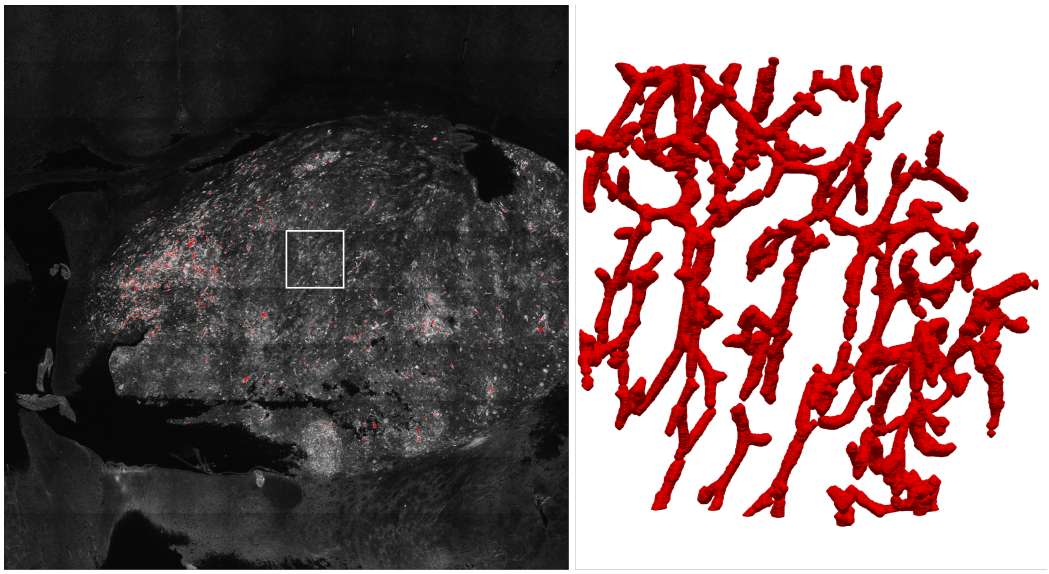

(a) (b)

Figure C.4: (a) shows the cross-sectional surface of the tumour cell reporter for the sixth slice of mouse 324 (tumour) with the tile E6 circled. (b) shows the reconstructed network at tile E6.

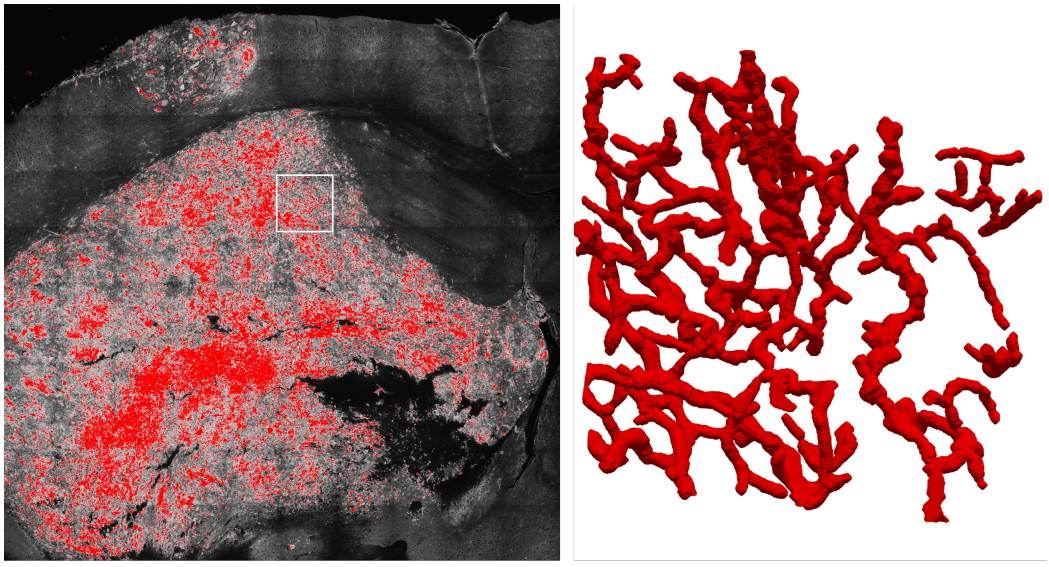

(a) (b)

Figure C.5: (a) shows the cross-sectional surface of the tumour cell reporter for the third slice of mouse 324 (tumour) with the tile D6 circled. (b) shows the reconstructed network at tile D6.

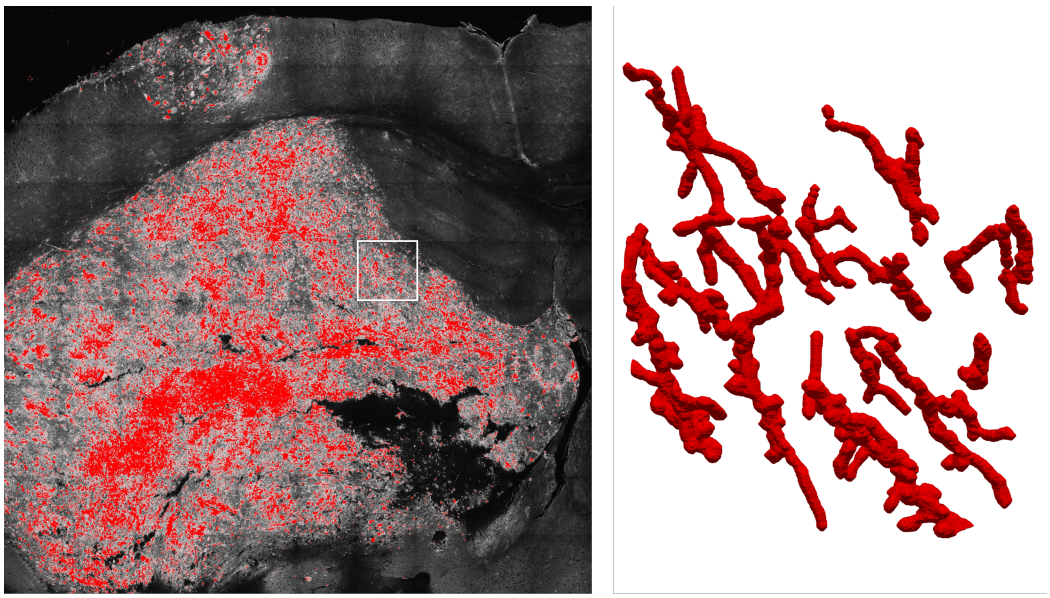

(a) (b)

Figure C.6: (a) shows the cross-sectional surface of the tumour cell reporter for the third slice of mouse 324 (tumour) with the tile E7 circled. (b) shows the reconstructed network at tile E7.

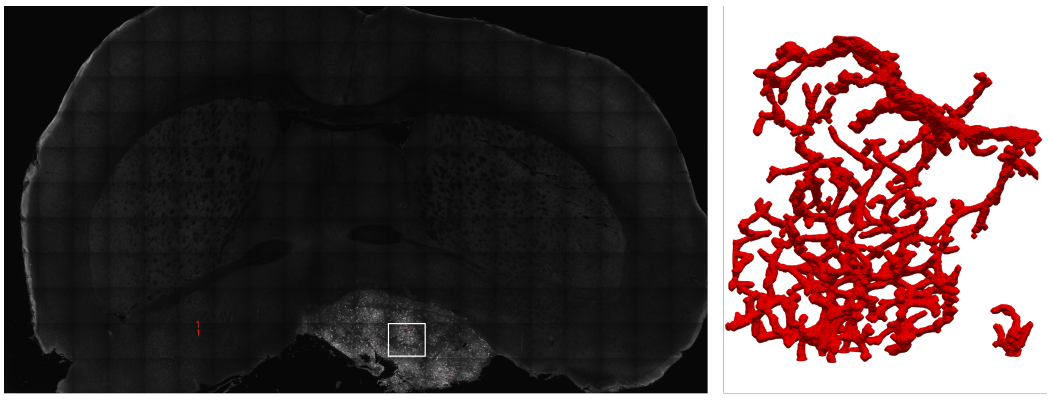

(a) (b)

Figure C.7: (a) shows the cross-sectional surface of the tumour cell reporter for the first slice of mouse 325 (tumour) with the tile J12 circled. (b) shows the reconstructed network at tile J12.

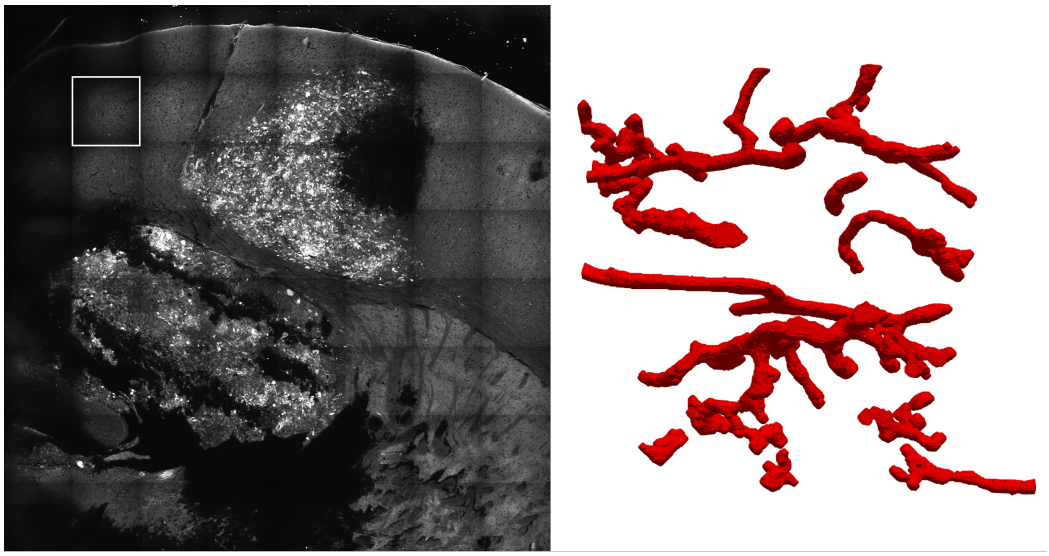

(a) (b)

Figure C.8: (a) shows the cross-sectional surface of the tumour cell reporter for the second slice of mouse 325 (tumour) with the tile B2 circled. (b) shows the reconstructed network at tile B2.

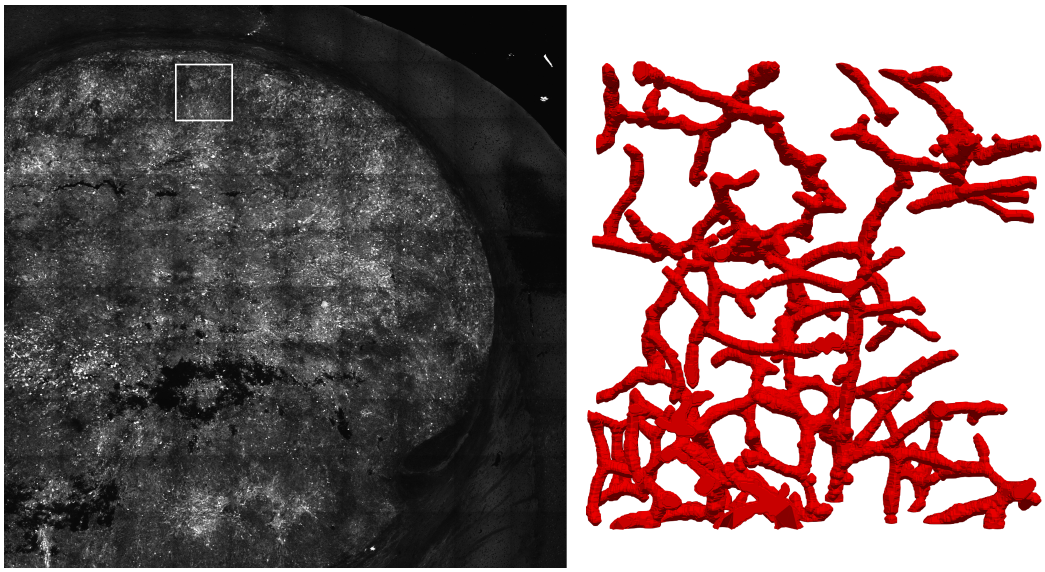

(a) (b)

Figure C.9: (a) shows the cross-sectional surface of the tumour cell reporter for the fourth slice of mouse 343 (tumour) with the tile B4 circled. (b) shows the reconstructed network at tile B4.

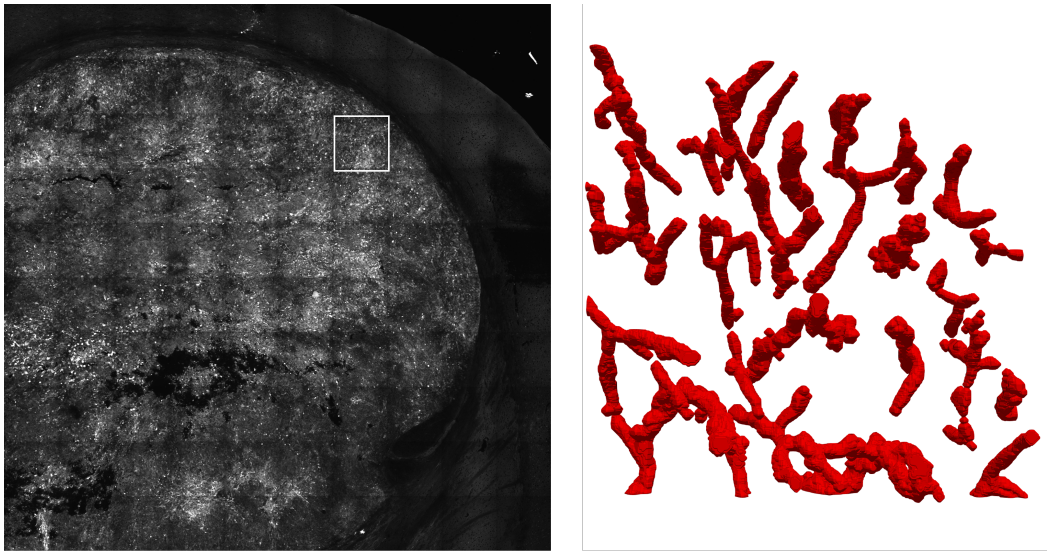

(a) (b)

Figure C.10: (a) shows the cross-sectional surface of the tumour cell reporter for the fourth slice of mouse 343 (tumour) with the tile C7 circled. (b) shows the reconstructed network at tile C7.

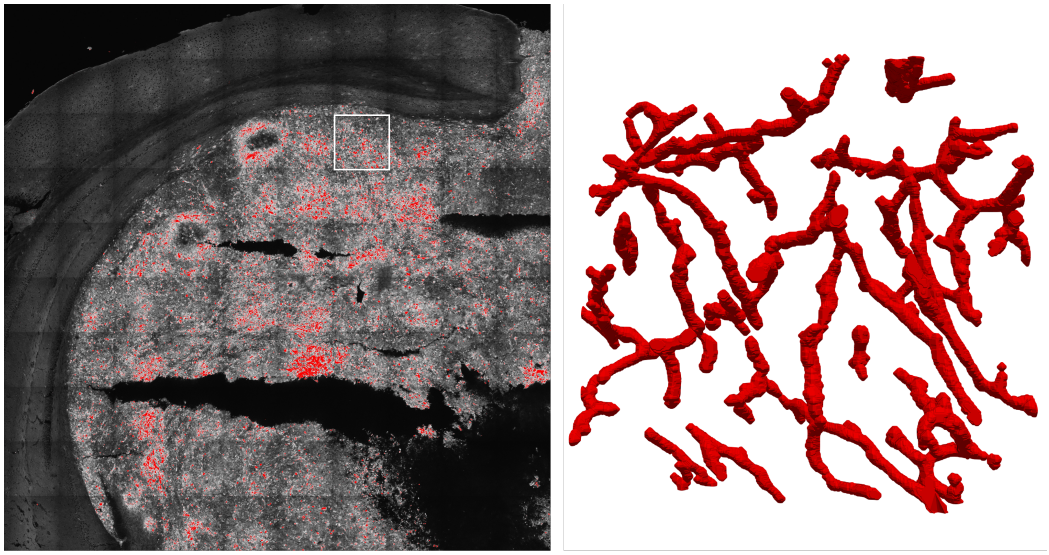

(a) (b)

Figure C.11: (a) shows the cross-sectional surface of the tumour cell reporter for the fifth slice of mouse 343 (tumour) with the tile C7 circled. (b) shows the reconstructed network at tile C7.

Table C.1: Phenotype p-value for every network pair.

Network pair		Phenotype p-value				
Network 1	Network 2	λ	Tissue-vessel distance	Minor diameter	Aspect ratio	Tortuosity
C-929-2-B5	C-323-3-B6	0.52	0.76	0.12	0.31	0.4
C-929-2-B5	C-323-3-F6	**p-value <0.05**	**p-value <0.05**	**p-value <0.05**	0.12	0.54
C-929-2-B5	GB-324-6-E6	**p-value <0.05**	**p-value <0.05**	0.94	0.55	**p-value <0.05**
C-929-2-B5	GB-324-3-D6	**p-value <0.05**	**p-value <0.05**	0.56	0.07	0.15
C-929-2-B5	GB-324-3-E7	**p-value <0.05**	**p-value <0.05**	0.61	**p-value <0.05**	0.95
C-929-2-B5	GB-325-1-J12	**p-value <0.05**	**p-value <0.05**	0.29	0.88	0.51
C-929-2-B5	GB-325-2-B2	0.22	0.32	0.19	**p-value <0.05**	0.44
C-929-2-B5	GB-343-4-B4	**p-value <0.05**	**p-value <0.05**	0.73	0.79	0.31
C-929-2-B5	GB-343-4-C7	**p-value <0.05**	**p-value <0.05**	0.07	0.09	0.06
C-929-2-B5	GB-343-5-C7	**p-value <0.05**	**p-value <0.05**	**p-value <0.05**	**p-value <0.05**	0.15
C-323-3-B6	C-323-3-F6	**p-value <0.05**	**p-value <0.05**	0.11	**p-value <0.05**	0.41
C-323-3-B6	GB-324-6-E6	**p-value <0.05**	**p-value <0.05**	0.29	0.11	0.08
C-323-3-B6	GB-324-3-D6	**p-value <0.05**	**p-value <0.05**	0.41	0.23	0.05
C-323-3-B6	GB-324-3-E7	**p-value <0.05**	**p-value <0.05**	0.3	0.07	0.3
C-323-3-B6	GB-325-1-J12	**p-value <0.05**	**p-value <0.05**	**p-value <0.05**	0.37	0.1
C-323-3-B6	GB-325-2-B2	0.31	0.45	0.08	**p-value <0.05**	0.38
C-323-3-B6	GB-343-4-B4	**p-value <0.05**	**p-value <0.05**	0.63	0.23	0.75
C-323-3-B6	GB-343-4-C7	**p-value <0.05**	**p-value <0.05**	0.27	0.15	0.23
C-323-3-B6	GB-343-5-C7	**p-value <0.05**	**p-value <0.05**	0.38	0.23	0.56
C-323-3-F6	GB-324-6-E6	0.54	0.3	0.06	0.35	0.25
C-323-3-F6	GB-324-3-D6	0.38	0.66	0.05	**p-value <0.05**	0.98
C-323-3-F6	GB-324-3-E7	0.87	**p-value <0.05**	0.15	**p-value <0.05**	0.55
C-323-3-F6	GB-325-1-J12	0.61	0.25	**p-value <0.05**	0.28	0.66
C-323-3-F6	GB-325-2-B2	0.76	**p-value <0.05**	**p-value <0.05**	**p-value <0.05**	0.65
C-323-3-F6	GB-343-4-B4	0.75	**p-value <0.05**	0.24	0.23	0.37
C-323-3-F6	GB-343-4-C7	0.94	0.1	0.74	**p-value <0.05**	0.27
C-323-3-F6	GB-343-5-C7	0.43	**p-value <0.05**	0.54	**p-value <0.05**	0.35
GB-324-6-E6	GB-324-3-D6	0.92	0.53	0.69	**p-value <0.05**	**p-value <0.05**
GB-324-6-E6	GB-324-3-E7	0.5	0.05	0.6	**p-value <0.05**	**p-value <0.05**
GB-324-6-E6	GB-325-1-J12	0.3	**p-value <0.05**	0.32	0.74	**p-value <0.05**
GB-324-6-E6	GB-325-2-B2	0.98	**p-value <0.05**	0.19	**p-value <0.05**	0.31
GB-324-6-E6	GB-343-4-B4	0.69	0.15	0.8	0.76	0.3
GB-324-6-E6	GB-343-4-C7	0.54	0.57	0.11	0.07	0.83
GB-324-6-E6	GB-343-5-C7	0.98	0.13	0.13	**p-value <0.05**	0.13
GB-324-3-D6	GB-324-3-E7	0.38	**p-value <0.05**	0.45	0.93	0.15
GB-324-3-D6	GB-325-1-J12	0.14	0.1	0.14	0.1	0.27
GB-324-3-D6	GB-325-2-B2	0.99	**p-value <0.05**	0.13	0.14	0.63
GB-324-3-D6	GB-343-4-B4	0.52	**p-value <0.05**	0.98	0.05	**p-value <0.05**
GB-324-3-D6	GB-343-4-C7	0.42	0.22	0.15	0.28	**p-value <0.05**
GB-324-3-D6	GB-343-5-C7	0.93	**p-value <0.05**	0.16	0.65	**p-value <0.05**
GB-324-3-E7	GB-325-1-J12	0.82	**p-value <0.05**	0.93	**p-value <0.05**	0.5
GB-324-3-E7	GB-325-2-B2	0.71	**p-value <0.05**	0.56	0.09	0.44
GB-324-3-E7	GB-343-4-B4	0.67	0.53	0.51	**p-value <0.05**	0.24
GB-324-3-E7	GB-343-4-C7	0.94	0.12	0.13	0.29	**p-value <0.05**
GB-324-3-E7	GB-343-5-C7	0.42	0.45	0.2	0.43	0.08
GB-325-1-J12	GB-325-2-B2	0.63	**p-value <0.05**	0.51	**p-value <0.05**	0.48
GB-325-1-J12	GB-343-4-B4	0.35	**p-value <0.05**	0.28	0.94	0.09
GB-325-1-J12	GB-343-4-C7	0.74	**p-value <0.05**	**p-value <0.05**	0.09	**p-value <0.05**
GB-325-1-J12	GB-343-5-C7	0.16	**p-value <0.05**	**p-value <0.05**	0.11	**p-value <0.05**
GB-325-2-B2	GB-343-4-B4	0.84	**p-value <0.05**	0.17	**p-value <0.05**	0.36
GB-325-2-B2	GB-343-4-C7	0.74	**p-value <0.05**	**p-value <0.05**	0.59	0.32
GB-325-2-B2	GB-343-5-C7	0.98	**p-value <0.05**	0.06	**p-value <0.05**	0.36
GB-343-4-B4	GB-343-4-C7	0.74	0.33	0.24	0.08	0.46
GB-343-4-B4	GB-343-5-C7	0.58	0.93	0.39	**p-value <0.05**	0.91
GB-343-4-C7	GB-343-5-C7	0.46	0.31	0.51	0.22	0.38

Bibliography

1. Abay, A. *et al.* Cross-sectional focusing of red blood cells in a constricted microfluidic channel. *Soft Matter* **16,** 534–543 (2020).
2. Acharya, T. *et al. Image Processing: Principles and Practice* (2005).
3. Alonso, C. *et al.* Time-dependent rheological behaviour of blood flow at low shear rate in narrow horizontal tubes. *BIORHEOLOGY* **26,** 229–246 (1989).
4. Antiga, L. *et al.* An image-based modeling framework for patient-specific computational hemodynamics. *Medical and Biological Engineering and Computing* **46,** 1097–1112 (2008).
5. Arnold, M. *et al.* Progress in cancer survival, mortality, and incidence in seven high-income countries 1995–2014 (ICBP SURVMARK-2): a population-based study. *The Lancet Oncology* **20,** 1493–1505 (Nov. 2019).
6. Aromando, R. F. *et al.* Angiogenesis in potentially malignant lesions and carcinomas during experimental oral carcinogenesis: a preliminary study in the hamster cheek pouch. *Anticancer research* **34,** 6381–6388 (2014).
7. Arzt, M. *et al.* LABKIT: Labeling and Segmentation Toolkit for Big Image Data. *Frontiers in Computer Science* **4** (Feb. 2022).
8. Azzi, S. *et al.* Vascular permeability and drug delivery in cancers. *Frontiers in Oncology* **3 AUG** (2013).
9. Bächer, C. *et al.* Clustering of microscopic particles in constricted blood flow. *Physical Review Fluids* **2,** 1–12 (2017).
10. Bader, S. B. *et al. Review cyclic hypoxia: An update on its characteristics, methods to measure it and biological implications in cancer* Jan. 2021.
11. Balogh, P. *et al.* Analysis of red blood cell partitioning at bifurcations in simulated microvascular networks. *Physics of Fluids* **30** (2018).
12. Balogh, P. *et al.* The cell-free layer in simulated microvascular networks. *Journal of Fluid Mechanics* **864,** 768–806 (2019).
13. Bankhead, P. *et al.* QuPath: Open source software for digital pathology image analysis. *Scientific Reports* **7** (Dec. 2017).

14. Barber, J. O. *et al.* Simulated two-dimensional red blood cell motion, deformation, and partitioning in microvessel bifurcations. *Annals of Biomedical Engineering* **36,** 1690–1698 (2008).
15. Batchelor. *An Introduction to Fluid Dynamics* (Cambridge University Press, 2000).
16. Bentzen, S. Theragnostic imaging for radiation oncology: dose-painting by numbers. *The Lancer Oncology,* 112–117 (2005).
17. Bergers, G. *et al.* Modes of resistance to anti-angiogenic therapy. *Nature Reviews Cancer* **8,** 592–603 (Aug. 2008).
18. Bernabeu, M. O. *et al.* Abnormal morphology biases haematocrit distribution in tumour vasculature and contributes to heterogeneity in tissue oxygenation. *Proceedings of the National Academy of Sciences* **117,** 27811–27819 (2020).
19. Bhatnagar, P. L. *et al.* A Model for Collision Processes in Gases. I. Small Amplitude Processes in Charged and Neutral One-Component Systems. *Phys. Rev.* **94** (1954).
20. Bocanegra Cifuentes, J. A. *et al.* Lattice boltzmann method applied to nuclear reactors-A systematic literature review. *Sustainability in Innovative Nuclear Fission/Fusion Systems and Related Fuel Cycles* **12** (2020).
21. Boucher, Y. *et al.* Microvascular Pressure Is the Principal Driving Force for Interstitial Hypertension in Solid Tumors: Implications for Vascular Collapse. *Cancer Research* **52,** 5110–5114 (1992).
22. Brehar, F. M. *et al.* The development of xenograft glioblastoma implants in nude mice brain. *Journal of Medicine and Life* **1** (2008).
23. Brizel, D. M. *et al. Tumor Oxygenation Predicts for the Likelihood of Distant Metastases in Human Soft Tissue Sarcoma1* tech. rep. (1996), 941–943.
24. Brown, J. M. *et al.* Exploiting tumour hypoxia in cancer treatment. *Nature Reviews Cancer* **4,** 437–447 (2004).
25. Cancer Research UK. *Cancer mortality statistics* Dec. 2020.
26. Cancer Research UK. *Cancer survival statistics* Dec. 2020.
27. Cancer Research UK. *Cancer statistics for the UK* Oct. 2022.
28. Cancer Research UK. *What is cancer?* Oct. 2022.
29. Cancer research UK. *Breast cancer survival* 2023.
30. Cancer research UK. *Prostate cancer survival* 2023.
31. Cancer research UK. *Survival* 2023.
32. Cao, Y. *et al.* Observation of Incipient Tumor Angiogenesis That Is Independent of Hypoxia and Hypoxia Inducible Factor-1 Activation. *Cancer research* **65,** 5498–5505 (2005).
33. Chauhan, V. P. *et al.* Angiotensin inhibition enhances drug delivery and potentiates chemotherapy by decompressing tumour blood vessels. *Nature Communications* **4** (2013).

34. Chen, M. *et al.* An Enhanced Spring-Particle Model for Red Blood Cell Structural Mechanics: Application to the Stomatocyte-Discocyte-Echinocyte Transformation. *Journal of Biomechanical Engineering* **139** (Dec. 2017).
35. Cheng Ng, Y. *et al.* Symmetry recovery of cell-free layer after bifurcations of small arterioles in reduced flow conditions: Effect of RBC aggregation. *American Journal of Physiology - Heart and Circulatory Physiology* **311,** H487–H497 (2016).
36. Clavica, F. *et al.* Red blood cell phase separation in symmetric and asymmetric microchannel networks: Effect of capillary dilation and inflow velocity. *Scientific Reports* **6,** 1–12 (2016).
37. Coupier, G. *et al.* Noninertial lateral migration of vesicles in bounded Poiseuille flow. *Physics of Fluids* **20** (2008).
38. Cribaro, G. P. *et al.* Three-dimensional vascular microenvironment landscape in human glioblastoma. *Acta Neuropathologica Communications* **9** (Dec. 2021).
39. d'Esposito, A. *et al.* Computational fluid dynamics with imaging of cleared tissue and of in vivo perfusion predicts drug uptake and treatment responses in tumours. *Nature Biomedical Engineering* **2,** 773–787 (2018).
40. De Haan, M. *et al.* Numerical investigation of the effects of red blood cell cytoplasmic viscosity contrasts on single cell and bulk transport behaviour. *Applied Sciences (Switzerland)* **8** (Sept. 2018).
41. Dewhirst, M. W. *et al.* Cycling hypoxia and free radicals regulate angiogenesis and radiotherapy response. *Nature Reviews Cancer* **8,** 425–437 (June 2008).
42. Dewhirst, M. W. *et al.* Transport of drugs from blood vessels to tumour tissue. *Nature Reviews Cancer* **17,** 738–750 (2017).
43. Dewhirst, M. W. *et al.* Rationale for hypoxia assessment and amelioration for precision therapy and immunotherapy studies. *Journal of Clinical Investigation* **129,** 489–491 (Jan. 2019).
44. Dewhirst, M. *et al.* Microvascular studies on the origins of perfusion-limited hypoxia. *British Journal of Cancer* **74,** 247–251 (1996).
45. Di Carlo, D. Inertial microfluidics. *Lab on a Chip* **9,** 3038–3046 (2009).
46. Doddi, S. K. *et al.* Three-dimensional computational modeling of multiple deformable cells flowing in microvessels. *Physical Review E - Statistical, Nonlinear, and Soft Matter Physics* **79** (Apr. 2009).
47. Doyeux, V. *et al.* Spheres in the vicinity of a bifurcation: Elucidating the Zweifach-Fung effect. *Journal of Fluid Mechanics* **674,** 359–388 (2011).
48. Dunn, J.-O. *et al.* Physiology of oxygen transport. *BJA Education* **16,** 341–348 (2016).
49. Enden, G. *et al. A Numerical Study of the Shape of the Surface Separating Flow Into Branches in Microvascular Bifurcations* in *Transactions of the ASME* **114** (1992), 398–405.

50. Enjalbert, R. *et al.* Compressed vessels bias red blood cell partitioning at bifurcations in a hematocrit-dependent manner: Implications in tumor blood flow. *Proceedings of the National Academy of Sciences* **118** (2021).
51. Evans, E. *et al.* Improved Measurements of the Erythrocyte Geometry. *Microvascular research* **4,** 335–347 (1972).
52. Fahraeus R. Die Strömungsverhältnisse und die Verteilung der Blutzellen im Gef äßsystem. Zur Frageder Bedeutung der intravasculären Erythrocytenaggregation. *Klin. Wochenschr.* **7,** 100–106 (1928).
53. Fahraeus R. The suspension stability of the blood. *Physiol Rev* **9,** 241–274 (1929).
54. Fahraeus R *et al.* The viscosity of the blood in narrow capillary tubes. *American Journal of Physiology* **96,** 562–568 (1931).
55. Faivre, M. *et al.* Geometrical focusing of cells in a microfluidic device: an approach to separate blood plasma. *Biorheology* **43,** 147–59 (2006).
56. Fang, L. *et al.* Flattened microvessel independently predicts poor prognosis of patients with non-small cell lung cancer. *Oncotarget* **8,** 30092–30099 (2017).
57. Fenton, B. M. *et al.* Nonuniform Red Cell Distribution in 20 to 100 um Bifurcations. *Microvascular research* **29,** 103–126 (1985).
58. Fouda, A. Y. *et al.* Utility of LysM-Cre and CdH5-Cre driver mice in retinal and brain research: An imaging study using tdtomato reporter mouse. *Investigative Ophthalmology and Visual Science* **61** (Mar. 2020).
59. Fredrich, T. *et al.* Tumorcode: A framework to simulate vascularized tumors. *European Physical Journal E* **41** (Apr. 2018).
60. Fry, B. C. *et al.* Estimation of Blood Flow Rates in Large Microvascular Networks. *Microcirculation* **19,** 530–538 (2012).
61. Fujiwara, H. *et al.* Red blood cell motions in high-hematocrit blood flowing through a stenosed microchannel. *Journal of Biomechanics* **42,** 838–843 (2009).
62. Fung, Y.-C. Stochastic Flow in Capillary Blood Vessels. *Microvascular research* **5,** 34–48 (1973).
63. Gagnon, L. *et al. Modeling of cerebral oxygen transport based on In vivo microscopic imaging of microvascular network structure, blood flow, and oxygenation* Aug. 2016.
64. Giarratano, Y. *et al.* Automated segmentation of optical coherence tomography angiography images: Benchmark data and clinically relevant metrics. *Translational Vision Science and Technology* **9,** 1–10 (2020).
65. Gillies, R. J. *et al.* Causes and Effects of Heterogeneous Perfusion in Tumors. *Neoplasia* **1,** 197207 (1999).
66. Goldman, D. Theoretical models of microvascular oxygen transport to tissue. *Microcirculation* **15,** 795–811 (2008).

67. Gompper, G. *et al.* Modeling microcirculatory blood flow: Current state and future perspectives. *Wiley Interdisciplinary Reviews: Systems Biology and Medicine* **8,** 157–168 (2016).
68. Gould, I. G. *et al.* Hematocrit distribution and tissue oxygenation in large microcirculatory networks. *Microcirculation* **22,** 1–18 (2015).
69. Grandchamp, X. *et al.* Lift and down-gradient shear-induced diffusion in red blood cell suspensions. *Physical Review Letters* **110,** 1–5 (2013).
70. Gray, L. H. *et al.* The Concentration of Oxygen Dissolved in Tissues at the Time of Irradiation as a Factor in Radiotherapy. *The British Journal of Radiology* **26,** 638–648 (Dec. 1953).
71. Greenhalgh, S. N. *et al.* Cre-ativity in the liver: Transgenic approaches to targeting hepatic nonparenchymal cells. *Hepatology* **61,** 2091–2099 (June 2015).
72. Griffith, B. E. *et al.* Immersed Methods for Fluid-Structure Interaction. *Annu. Rev. Fluid Mech. 2020* **52,** 421–448 (2019).
73. Grimes, D. R. *et al.* Oxygen consumption dynamics in steady-state tumour models. *Journal of the Royal Society, Interface / the Royal Society* **1** (2014).
74. Guckenberger, A. *et al. Theory and algorithms to compute Helfrich bending forces: A review* Apr. 2017.
75. Guibert, R. *et al.* A new approach to model confined suspensions flows in complex networks: Application to blood flow. *Transport in Porous Media* **83,** 171–194 (2010).
76. Guo, Z. *et al.* Discrete lattice effects on the forcing term in the lattice Boltzmann method. *Physical Review E - Statistical Physics, Plasmas, Fluids, and Related Interdisciplinary Topics* **65,** 1–6 (2002).
77. Hagenbach, E. Ueber die Bestimmung der Zähigkeit einer Flüssigkeit durch den Ausfluss aus Röhren. *Annalen der physik und chemie* **108,** 385–426 (1860).
78. Hagendoorn, J. *et al.* Onset of abnormal blood and lymphatic vessel function and interstitial hypertension in early stages of carcinogenesis. *Cancer Research* **66,** 3360–3364 (2006).
79. Hanahan, D. *et al. The Hallmarks of Cancer Review evolve progressively from normalcy via a series of pre* tech. rep. (2000), 57–70.
80. Hanahan, D. *et al. Hallmarks of cancer: The next generation* Mar. 2011.
81. Helmchen, F. *et al.* Deep tissue two-photon microscopy. *Nature Methods* **2,** 932–940 (Dec. 2005).
82. Hesketh, R. in *Introduction to Cancer Biology* 103–152 (Cambridge University Press, Feb. 2013).
83. Hesketh R. in *Introduction to Cancer Biology* 20–43 (Cambridge University Press, Dec. 2012).
84. Hill, S. A. *et al.* Microregional blood flow in murine and human tumours assessed using laser Doppler microprobes. *British Journal of Cancer* **74,** 260–263 (1996).

85. Hoskins, P. R. *et al. Cardiovascular Biomechanics* 1–462 (Springer International Publishing, Jan. 2017).
86. Hyakutake, T. *et al.* Numerical simulation of red blood cell distributions in three-dimensional microvascular bifurcations. *Microvascular Research* **97,** 115–123 (2015).
87. Hyakutake, T. *et al.* In vitro study on the partitioning of red blood cells using a microchannel network. *Microvascular Research* **140** (Mar. 2022).
88. Jain, R. K. Molecular regulation of vessel maturation. *Nature medecine* **9,** 685–693 (2003).
89. Jain, R. K. Determinants of Tumor Blood Flow: A Review. *CANCER RESEARCH* **48,** 2641–2658 (1988).
90. Jain, R. K. Normalizing tumour vasculature with anti-angiogenic therapy: A new paradigm for combination therapy. *Nature Medecine* **7** (2001).
91. Jain, R. K. Normalization of Tumor Vasculature: An Emerging Concept in Antiangiogenic Therapy. *Science* **307,** 58–62 (2005).
92. Jain, R. K. Normalizing tumor microenvironment to treat cancer: Bench to bedside to biomarkers. *Journal of Clinical Oncology* **31,** 2205–2218 (2013).
93. Jain, R. K. Antiangiogenesis Strategies Revisited: From Starving Tumors to Alleviating Hypoxia. *Cancer Cell* **26,** 605–622 (2014).
94. Jain, R. K. *et al.* Lessons from phase III clinical trials on anti-VEGF therapy for cancer. *Nature Clinical Practice Oncology* **3,** 24–40 (Jan. 2006).
95. Jain, R. K. *et al.* The Role of Mechanical Forces in Tumor Growth and Therapy. *Annual Review of Biomedical Engineering* **16,** 321–346 (2014).
96. Kamoun, W. S. *et al.* Simultaneous measurement of RBC velocity, flux, hematocrit and shear rate in vascular networks. *Nature Methods* **7,** 655–660 (2010).
97. Kannan, P. *et al.* Functional parameters derived from magnetic resonance imaging reflect vascular morphology in preclinical tumors and in human liver metastases. *Clinical Cancer Research* **24,** 4694–4704 (Oct. 2018).
98. Kaoui, B. *et al.* Lateral migration of a two-dimensional vesicle in unbounded Poiseuille flow. *Physical Review E - Statistical, Nonlinear, and Soft Matter Physics* **77** (Feb. 2008).
99. Kapur, J. N. *et al.* A New Method for Gray-Level Picture Thresholding Using the Entropy of the Histogram. *COMPUTER VISION, GRAPHICS, AND IMAGE PROCESSING* **29,** 273–285 (1985).
100. Katanov, D. *et al.* Microvascular blood flow resistance: Role of red blood cell migration and dispersion. *Microvascular Research* **99,** 57–66 (2015).
101. Kersaudy-Kerhoas, M. *et al.* Hydrodynamic blood plasma separation in microfluidic channels. *Microfluidics and Nanofluidics* **8,** 105–114 (Jan. 2010).
102. Kersaudy-Kerhoas, M. *et al.* Validation of a blood plasma separation system by biomarker detection. *Lab on a Chip* **10,** 1587–1595 (2010).

103. Kimura, H. *et al.* Flucuations in red cell flux in tumor microvessels can lead to transient hypoxia and reoxygenation in tumor parenchyma. *Cancer Research* **56,** 5522–5528 (1996).
104. Kolitsi, L. I. *et al.* Effects of artery size on the hydrodynamic diffusivity of red cells and other contained particles. *Physical Review Fluids* **4,** 113103 (2019).
105. Köry, J. *et al.* Dependence of cell-free-layer width on rheological parameters: Combining empirical data on flow separation at microvascular bifurcations with geometrical considerations. *Physical Review E* **105** (Jan. 2022).
106. Koumoutsakos, P. *et al.* The Fluid Mechanics of Cancer and Its Therapy. *Annual Review of Fluid Mechanics* **45,** 325–355 (2013).
107. Kruger, T. *et al. The lattice boltzmann method, principles and practice* **207,** 1–705 (Springer, 2017).
108. Krüger, T. *et al.* Efficient and accurate simulations of deformable particles immersed in a fluid using a combined immersed boundary lattice Boltzmann finite element method. *Computers and Mathematics with Applications* **61,** 3485–3505 (2011).
109. Krüger, T. *et al.* Crossover from tumbling to tank-treading-like motion in dense simulated suspensions of red blood cells. *Soft Matter* **9,** 9008–9015 (Oct. 2013).
110. Ladd, A. J. Numerical Simulations of Particulate Suspensions Via a Discretized Boltzmann Equation. Part 1. Theoretical Foundation. *Journal of Fluid Mechanics* **271,** 285–309 (1994).
111. Lanotte, L. *et al.* Red cells' dynamic morphologies govern blood shear thinning under microcirculatory flow conditions. *Proceedings of the National Academy of Sciences of the United States of America* **113,** 13289–13294 (Nov. 2016).
112. Lanzen, J. *et al.* Direct demonstration of instabilities in oxygen concentrations within the extravascular compartment of an experimental tumor. *Cancer Research* **66,** 2219–2223 (Feb. 2006).
113. Less, J. R. *et al.* Microvascular Architecture in a Mammary Carcinoma: Branching Patterns and Vessel Dimensions. *Cancer research* **51,** 265–273 (1991).
114. Lorensen, W. E. *et al.* Marching cubes: A high resolution 3D surface construction algorithm. *Computer Graphics* **21** (1987).
115. Lorthois, S. *et al.* Simulation study of brain blood flow regulation by intra-cortical arterioles in an anatomically accurate large human vascular network: Part I: Methodology and baseline flow. *NeuroImage* **54,** 1031–1042 (Jan. 2011).
116. Lorthois, S. *et al.* Simulation study of brain blood flow regulation by intra-cortical arterioles in an anatomically accurate large human vascular network. Part II: Flow variations induced by global or localized modifications of arteriolar diameters. *NeuroImage* **54,** 2840–2853 (Feb. 2011).
117. Losserand, S. *et al.* Migration velocity of red blood cells in microchannels. *Microvascular Research* **124,** 30–36 (July 2019).

118. Lücker, A. *et al.* The relative influence of hematocrit and red blood cell velocity on oxygen transport from capillaries to tissue. *Microcirculation* **24,** 1–12 (2017).
119. Lücker, A. *et al.* The Relation Between Capillary Transit Times and Hemoglobin Saturation Heterogeneity. Part 1: Theoretical Models. *Frontiers in Physiology* **9** (2018).
120. Lücker, A. *et al.* The relation between capillary transit times and hemoglobin saturation heterogeneity. Part 2: Capillary networks. *Frontiers in Physiology* **9,** 1–12 (2018).
121. Lykov, K. *et al.* Inflow/Outflow Boundary Conditions for Particle-Based Blood Flow Simulations: Application to Arterial Bifurcations and Trees. *PLoS Computational Biology* **11,** 1–13 (2015).
122. Mantegazza, A. *et al.* In vitro investigations of red blood cell phase separation in a complex microchannel network. *Biomicrofluidics* **14** (2020).
123. Mantegazza, A. *et al.* Local vs. Global Blood Flow Modulation in Artificial Microvascular Networks: Effects on Red Blood Cell Distribution and Partitioning. *Frontiers in Physiology* **11** (Sept. 2020).
124. Martin, J. D. *et al.* Improving cancer immunotherapy using nanomedicines: progress, opportunities and challenges. *Nature Reviews Clinical Oncology* **17,** 251–266 (Apr. 2020).
125. Marumoto, T. *et al.* Development of a novel mouse glioma model using lentiviral vectors. *Nature Medicine* **15,** 110–116 (Jan. 2009).
126. Mazzeo, M. D. *et al.* HemeLB: A high performance parallel lattice-Boltzmann code for large scale fluid flow in complex geometries. *Computer Physics Communications* **178,** 894–914 (2008).
127. McDonald, D. M. *et al.* Significance of blood vessel leakiness in cancer. *Cancer Research* **62,** 5381–5385 (2002).
128. Merlo, A. *et al.* A few upstream bifurcations drive the spatial distribution of red blood cells in model microfluidic networks. *Soft Matter* **18,** 1463–1478 (Feb. 2022).
129. Michiels, C. *et al.* Cycling hypoxia: A key feature of the tumor microenvironment. *Biochimica et Biophysica Acta - Reviews on Cancer* **1866,** 76–86 (2016).
130. Moschandreou, T. E. *et al.* Influence of tissue metabolism and capillary oxygen supply on arteriolar oxygen transport: A computational model. *Mathematical Biosciences* **232,** 1–10 (2011).
131. Naghavi, M. *et al.* Global, regional, and national age-sex specific mortality for 264 causes of death, 1980–2016: a systematic analysis for the Global Burden of Disease Study 2016. *The Lancet* **390,** 1151–1210 (Sept. 2017).
132. Nagy, J. A. *et al.* Why are tumour blood vessels abnormal and why is it important to know? *British Journal of Cancer* **100,** 865–869 (Mar. 2009).
133. Nash, R. W. *et al.* Choice of boundary condition for lattice-Boltzmann simulation of moderate-Reynolds-number flow in complex domains. *Physical Review E - Statistical, Nonlinear, and Soft Matter Physics* **89** (Feb. 2014).

134. Nia, H. T. *et al.* In vivo compression and imaging in mouse brain to measure the effects of solid stress. *Nature Protocols* **15,** 2321–2340 (Aug. 2020).
135. Nia, H. T. *et al.* Physical traits of cancer. *Science* **370** (2020).
136. Noguchi, H. *et al.* Shape transitions of fluid vesicles and red blood cells in capillary flows. *Proceedings of the National Academy of Sciences* **102,** 14159–14164 (2005).
137. Nozue, M. *et al.* Role of Tumor Vascular Architecture in Nutrient and Drug Delivery: An Invasion Percolation-Based Network Model. *Microvascular Research* **51,** 327–346 (1996).
138. Obrist, D. *et al.* Red blood cell distribution in simplified capillary networks. *Philosophical Transactions of the Royal Society A: Mathematical, Physical and Engineering Sciences* **368,** 2897–2918 (June 2010).
139. Ong, P. K. *et al.* Spatio-temporal variations in cell-free layer formation near bifurcations of small arterioles. *Microvascular Research* **83,** 118–125 (2012).
140. Padera, T. *et al.* Cancer cells compress intratumour vessels. *Nature* **427,** 695 (2004).
141. Palmer, G. M. *et al.* Optical imaging of tumor hypoxia dynamics. *Journal of Biomedical Optics* **15,** 066021 (2010).
142. Penta, R. *et al.* The role of the microvascular tortuosity in tumor transport phenomena. *Journal of Theoretical Biology* **364,** 80–97 (Jan. 2015).
143. Peskin, C. S. The immersed boundary method. *Acta Numerica* **11,** 479–517 (Jan. 2002).
144. Poiseuille, J. Recherches exp erimentales sur le mouvement des liquides dans les tubes de tres-petits diametres. *Mem. Acad. R. Sci. Inst. Fr.* **9,** 433–544 (1846).
145. Popel, A. *et al.* Microcirculation and hemorheology. *Annual Review of Fluid Mechanics,* 43–69 (2005).
146. Popel, A. S. THEORY OF OXYGEN TRANSPORT TO TISSUE. *Critical reviews in biomedical engineering,* 257–321 (1989).
147. Pretini, V. *et al.* Red blood cells: Chasing interactions. *Frontiers in Physiology* **10** (2019).
148. Pries, A. *et al.* Red Cell Distribution at Microvascular. *Microvascular research* **38,** 81–101 (1989).
149. Pries, A. R. *et al.* Generalization of the Fahraeus principle for microvessel networks. *American Journal of Physiology - Heart and Circulatory Physiology* **251** (1986).
150. Pries, A. R. *et al.* Blood flow in microvascular networks. Experiments and simulation. *Circulation research,* 826–834 (1990).
151. Pries, A. R. *et al.* Blood viscosity in tube flow: Dependence on diameter and hematocrit. *American Journal of Physiology - Heart and Circulatory Physiology* **263** (1992).
152. Pries, A. R. *et al.* Microvascular blood viscosity in vivo and the endothelial surface layer. *American Journal of Physiology - Heart and Circulatory Physiology* **289,** 2657–2664 (2005).

153. Pries, A. R. *et al.* Blood Flow in Microvascular Networks. In: Comprehensive Physiology. *Handbook of Physiology: Microcirculation,* 1–34 (2008).
154. Pries, A. R. *et al.* The shunt problem: Control of functional shunting in normal and tumour vasculature. *Nature Reviews Cancer* **10,** 587–593 (Aug. 2010).
155. Pskowski, A. *et al.* Investigation of red blood cell partitioning in an in vitro microvascular bifurcation. *Artificial Organs* (2021).
156. Pskowski, A. *et al.* Hematocrit skewness along sequential bifurcations within a microfluidic network induces significant changes in downstream red blood cell partitioning. *Biomicrofluidics* **16** (Dec. 2022).
157. Puig-De-Morales-Marinkovic, M. *et al.* Viscoelasticity of the human red blood cell. *Am J Physiol Cell Physiol* **293,** 597–605 (2007).
158. Quiros-Gonzalez, I. *et al.* Optoacoustics delineates murine breast cancer models displaying angiogenesis and vascular mimicry. *British Journal of Cancer* **118,** 1098–1106 (2018).
159. Rashidi, Y. *et al.* Red blood cell lingering modulates hematocrit distribution in the microcirculation. *Biophysical Journal* **122,** 1526–1537 (Apr. 2023).
160. Rasmussen, P. M. *et al.* Modeling the hematocrit distribution in microcirculatory networks: A quantitative evaluation of a phase separation model. *Microcirculation* **25** (Apr. 2018).
161. Reichel, F. *et al.* High-Throughput Microfluidic Characterization of Erythrocyte Shapes and Mechanical Variability. *Biophysical Journal* **117,** 14–24 (2019).
162. Rieger, H. *et al.* Integrative models of vascular remodeling during tumor growth. *Wiley Interdisciplinary Reviews: Systems Biology and Medicine* **7,** 113–129 (May 2015).
163. Rieger, H. *et al.* Physics of the tumor vasculature: Theory and experiment. *European Physical Journal Plus* **131,** 1–24 (Feb. 2016).
164. Robertson, A. *et al. Hemodynamical Flows* 63–120 (Birkhauser Basel, 2008).
165. Roman, S. *et al.* Going beyond 20 μm-sized channels for studying red blood cell phase separation in microfluidic bifurcations. *Biomicrofluidics* **10** (2016).
166. Russ, J. C. *et al. The Image Processing Handbook The Fifth Edition* 5th ed. (Taylor & Francis group, 2007).
167. Schindelin, J. *et al.* Fiji: An open-source platform for biological-image analysis. *Nature Methods* **9,** 676–682 (July 2012).
168. Schroeder, W. *et al. The Visualization Toolkit An Object-Oriented Approach To 3D Graphics* 4.1 (2018).
169. Seano, G. *et al.* Solid stress in brain tumours causes neuronal loss and neurological dysfunction and can be reversed by lithium. *Nature Biomedical Engineering* **3,** 230–245 (Mar. 2019).
170. Secomb, T. W. *et al.* Analysis of oxygen transport to tumor tissue by microvascular networks. *International Journal of Radiation Oncology, Biology, Physics* (1993).

171. Secomb, T. *et al.* Theoretical Simulation of Oxygen Transport to Brain by Networks of Microvessels: Effects of Oxygen Supply and Demand on Tissue Hypoxia. *Microcirculation* **7,** 237–247 (2000).
172. Secomb, T. W. Blood Flow in the Microcirculation. *Annual Review of Fluid Mechanics* **49,** 443–461 (2017).
173. Secomb, T. W. *et al.* Structural adaptation of normal and tumour vascular networks. *Basic and Clinical Pharmacology and Toxicology* **110,** 63–69 (2011).
174. Sevick, E. M. *et al.* Geometric Resistance to Blood Flow in Solid Tumors Perfused ex Vivo:Effects of Tumor Size and Perfusion Pressure1. *Cancer Research* **49,** 3506–3512 (1989).
175. Sevick, E. M. *et al.* Viscous Resistance to Blood Flow in Solid Tumors: Effect of Hematocrit on Intratumor Blood Viscosity. *Cancer Research* **49,** 3513–3519 (1989).
176. Sezgin, M. *et al.* Survey over image thresholding techniques and quantitative performance evaluation. *Journal of Electronic Imaging* **13,** 146–168 (Jan. 2004).
177. Shen, Z. *et al.* Inversion of hematocrit partition at microfluidic bifurcations. *Microvascular Research* **105,** 40–46 (2016).
178. Shen, Z. *et al.* Migration of a red blood cell in a permeable microvessel. *Medicine in Novel Technology and Devices* **3,** 100023 (2019).
179. Sherwood, J. M. *et al.* Hematocrit, viscosity and velocity distributions of aggregating and non-aggregating blood in a bifurcating microchannel. *Biomechanics and Modeling in Mechanobiology* **13,** 259–273 (2014).
180. Sherwood, J. M. *et al.* Spatial distributions of red blood cells significantly alter local haemodynamics. *PLoS ONE* **9** (2014).
181. Simonsen, T. G. *et al.* Vascular abnormalities associated with acute hypoxia in human melanoma xenografts. *Radiotherapy and Oncology* **105,** 72–78 (Oct. 2012).
182. Skala, M. C. *et al.* Longitudinal optical imaging of tumor metabolism and hemodynamics. *Journal of Biomedical Optics* **15,** 011112 (2010).
183. Skalak, R. *et al.* Strain Energy Function of Red Blood Cell Membranes. *Biophysical Journal* **13,** 245–264 (1973).
184. Smith, W. *et al.* Hypoxia imaging with [F-18] FMISO-PET in head and neck cancer: Potential for guiding intensity modulated radiation therapy in overcoming hypoxia-induced treatment resistance. *Radiotherapy and Oncology* (2011).
185. Stolz, B. J. *et al.* Multiscale topology characterizes dynamic tumor vascular networks. *Sci. Adv* **8,** 2456 (2022).
186. Stylianopoulos, T. *et al.* Causes, consequences, and remedies for growth-induced solid stress in murine and human tumors. *Proceedings of the National Academy of Sciences* **109,** 15101–15108 (2012).

187. Stylianopoulos, T. *et al.* Combining two strategies to improve perfusion and drug delivery in solid tumors. *Proceedings of the National Academy of Sciences* **110,** 18632–18637 (2013).
188. Stylianopoulos, T. *et al.* Coevolution of solid stress and interstitial fluid pressure in tumors during progression: Implications for vascular collapse. *Cancer Research* **73,** 3833–3841 (2013).
189. Stylianopoulos, T. *et al.* Reengineering the Physical Microenvironment of Tumors to Improve Drug Delivery and Efficacy: From Mathematical Modeling to Bench to Bedside. *Trends in Cancer* **4,** 292–319 (2018).
190. Sun, C. *et al.* Non-uniform plasma leakage affects local hematocrit and blood flow: Implications for inflammation and tumor perfusion. *Annals of Biomedical Engineering* **35,** 2121–2129 (2007).
191. Sweeney, P. W. *et al.* Modelling the transport of fluid through heterogeneous, whole tumours in silico. *PLoS computational biology* **15,** e1006751 (2019).
192. Tadeo, I. *et al.* Vascular patterns provide therapeutic targets in aggressive neuroblastic tumors. *Oncotarget* **7,** 19935–19947 (2016).
193. Tang, J. *et al.* Shear-induced diffusion of red blood cells measured with dynamic light scattering-optical coherence tomography. *Journal of Biophotonics* **11** (Feb. 2018).
194. Thomlinson, R. H. *et al.* The histological structure of some human lung cancers and the possible implications for radiotherapy. *British journal of cancer* **9,** 539–549 (1955).
195. Timm Krüger. *Computer simulation study of collective phenomena in dense suspensions of red blood cells under shear* PhD thesis (2012).
196. Tomaiuolo, G. Biomechanical properties of red blood cells in health and disease towards microfluidics. *Biomicrofluidics* **8** (Sept. 2014).
197. Tong, R. T. *et al.* Vascular Normalization by Vascular Endothelial Growth Factor Receptor 2 Blockade Induces a Pressure Gradient Across the Vasculature and Improves Drug Penetration in Tumors. *Cancer Research* **64,** 3731–3736 (2004).
198. Tripathi, S. *et al.* Microdevice for plasma separation from whole human blood using bio-physical and geometrical effects. *Scientific Reports* **6,** 1–15 (2016).
199. Vahidkhah, K. *et al.* Flow of Red Blood Cells in Stenosed Microvessels. *Scientific Reports* **6,** 1–15 (2016).
200. Valen-Sendstad, K. *et al.* Real-World Variability in the Prediction of Intracranial Aneurysm Wall Shear Stress: The 2015 International Aneurysm CFD Challenge. *Cardiovascular Engineering and Technology* **9,** 544–564 (Dec. 2018).
201. Varchanis, S. *et al.* How viscoelastic is human blood plasma? *Soft Matter* **14,** 4238–4251 (2018).
202. Vaupel, P. *et al.* Detection and characterization of tumor hypoxia using pO2 histography. *Antioxidants and Redox Signaling* **9,** 1221–1235 (Aug. 2007).

203. Wang, Z. *et al.* Motion of a spherical capsule in branched tube flow with finite inertia. *Journal of Fluid Mechanics* **806,** 603–626 (2016).
204. Wang, Z. *et al.* Path selection of a spherical capsule in a microfluidic branched channel: Towards the design of an enrichment device. *Journal of Fluid Mechanics* **849,** 136–162 (2018).
205. Welter, M. *et al.* Computational model for tumor oxygenation applied to clinical data on breast tumor hemoglobin concentrations suggests vascular dilatation and compression. *PLoS ONE* **11,** 1–42 (2016).
206. Yamamoto, K. *et al.* Study of the Partitioning of Red Blood Cells Through Asymmetric Bifurcating Microchannels. *Journal of Medical and Biological Engineering* (2019).
207. Yang, J. *et al.* Predicting bifurcation angle effect on blood flow in the microvasculature. *Microvascular Research* **108,** 22–28 (Nov. 2016).
208. Yazdani, A. *et al.* Sub-cellular modeling of platelet transport in blood flow through microchannels with constriction. *Soft Matter* **12,** 4339–4351 (2016).
209. Ye, T. *et al.* Red blood cell distribution in a microvascular network with successive bifurcations. *Biomechanics and Modeling in Mechanobiology* **18,** 1821–1835 (Dec. 2019).
210. Závodszky, G. *et al.* Cellular level in-silico modeling of blood rheology with an improved material model for red blood cells. *Frontiers in Physiology* **8** (Aug. 2017).
211. Zhou, Q. *et al.* Spatiotemporal Dynamics of Dilute Red Blood Cell Suspensions in Low-Inertia Microchannel Flow. *Biophysical Journal* **118,** 2561–2573 (May 2020).
212. Zhou, Q. *et al.* Association between erythrocyte dynamics and vessel remodelling in developmental vascular networks. *Journal of the Royal Society Interface* **18** (June 2021).
213. Zhou, Q. *et al.* Emergent cell-free layer asymmetry and biased haematocrit partition in a biomimetic vascular network of successive bifurcations. *Soft Matter* (2021).